

Limoges University

**École Doctorale Sciences et Ingénierie pour l'Information,
Mathématiques (ED 521)**

Laboratoire XLIM – Département RF-ELITE

Thesis to obtain the graduation of
Doctor of the Limoges University
High Frequencies Electronics, Photonics and Systems

presented and held by
Alexandre Gheno

December 15th 2017

**Printable and Printed Perovskites Photovoltaic Solar Cells for
Autonomous Sensors Network**

Thesis directed by Mr. Bernard Ratier and Mr Sylvain Vedraïne

JURY :

President

Mr. Yvan Bonnassieux, Professor, Ecole Polytechnique

Rapporteurs

Ms. Anne Blayo, Lecturer and researcher, Grenoble INP - Pagora

Mr. Stéphane Cros, Research Engineer, CEA Grenoble

Examineurs

Ms. Rose-Marie Sauvage, DGA, Paris

Mr. Bernard Ratier, Professor, Limoges University

Mr. Sylvain Vedraïne, Associate professor, Limoges University

Mr. Johann Bouclé, Associate professor, Limoges University

**École Doctorale Sciences et Ingénierie pour l'Information,
Mathématiques (ED 521)**

Laboratoire XLIM – Département RF-ELITE

Thèse pour obtenir le grade de

Docteur de l'Université de Limoges

Electronique des Hautes Fréquences, Photoniques et Systèmes

Présentée et soutenue par

Alexandre Gheno

Le 15 décembre 2017

**Cellules Solaires Photovoltaïques Pérovskites Imprimables et
Imprimées pour Réseau de Capteurs Autonomes**

Thèse dirigée par MM. Bernard Ratier et Sylvain Vedraine

JURY :

Président du jury

M. Yvan Bonnassieux, Professeur, Ecole Polytechnique

Rapporteurs

Mme. Anne Blayo, Enseignant-chercheur, Grenoble INP - Pagora

M. Stéphane Cros, Ingénieur de recherche, CEA Grenoble

Examineurs

Mme. Rose-Marie Sauvage, DGA, Paris

M. Bernard Ratier, Professeur, Université de Limoges

M. Sylvain Vedraine, Maître de conférences, Université de Limoges

M. Johann Bouclé, Maître de conférences, Université de Limoges

Droits d'auteurs

Cette création est mise à disposition selon le Contrat :

« **Attribution-Pas d'Utilisation Commerciale-Pas de modification 3.0 France** »

disponible en ligne : <http://creativecommons.org/licenses/by-nc-nd/3.0/fr/>



*“You haven't tried to confuse me with any scientific babble for the last couple of days
and that's a red flag to me.”*

GENERAL JACK O'NEILL

“Had to be me. Someone else might have gotten it wrong...”

MORDIN SOLUS

REMERCIEMENTS

Je remercie Bernard Ratier pour l'encadrement de ma thèse bien sûr, mais aussi pour les discussions que nous avons eues qui ont toujours été constructives et m'ont toujours amenées vers de nouvelles idées pour mes recherches. Un remerciement spécial pour Sylvain Vedraïne, ça a été un honneur d'avoir été un des premiers thésards qu'il ait encadré. Il a été extrêmement disponible, il a toujours pris le temps de m'expliquer les concepts scientifiques que je ne connaissais pas et m'aidait dans les complications qui gravitent autour d'une thèse. Encore merci à lui. Sans Johann Bouclé qui m'a expliqué comment le laboratoire fonctionnait et comment faire mes premières cellules solaires je ne serai pas allé bien loin et je le remercie tout autant. C'est avec ces trois personnes que j'ai eu aussi des discussions extrêmement intéressantes sur des sujets personnels ou non et c'était toujours un réel plaisir.

Merci à Rémi Antony qui m'a aidé pour les cours que je donnais et pour avoir réparé les machines que je cassais. Je remercie Thierry Trigaud et Bruno Lucas pour avoir été disponibles. Un grand merci à Marie-Laure Guillat pour toutes les tracasseries administratives dont elle s'est occupée. Merci à Rose-Marie Sauvage qui a suivi ma thèse pour la DGA.

Merci à Maria Mendez-Malaga qui, au CEA de Grenoble, m'a formé pour faire mes premières cellules solaires à pérovskite qui fonctionnaient vraiment !

Merci à mes petites sœurs Faustine et Béatrice, à mes parents Nicole et Tibère, à ma mamie Rosette et ma famille qui m'ont soutenu tout le long.

Maintenant c'est l'heure de remercier tous les gens que j'ai rencontré lors de ma thèse à XLIM dans l'équipe Elite. Sans eux ma thèse aurait été beaucoup moins amusante et épanouissante, et mon installation à Limoges beaucoup moins facile : de grands mercis à Agostino, Bilel, Cedric, Claudio, Hesham, Jean-Charles, Julien, Malika, Martin, Michelle, Raphaëlle, Richard, Safia, Sandy, Sudip, Thomas, Wisly, Yong et Youssef.

Durant ma thèse j'ai visité quelques régions de France (certaines très éloignées) avec mes poteaux de Papet' : Camille, Charlène, Charline, Clotilde, Marie-Catherine, Nicolas et Vivien. On a bien rigolé, je les embrasse ! Un coucou à mes amis du Lycée Berthollet et d'Annecy aussi, j'ai beaucoup pensé à eux durant ma thèse même si je n'ai pas su me rendre très disponible pour aller les voir.

Enfin je remercie Nadine et Michel pour leur accueil et leur amitié.

Et bien sûr je remercie Malorie, sans son soutien je n'aurais pas pu en faire autant.

SUMMARY

Droits d’auteurs	2
General introduction	9
I. Energy supplying for autonomous network of communicating devices.....	11
1. Photovoltaic as a credible energy source for nomad devices	11
2. Autonomous sensor network	13
i. Sizing the autonomous sensor	13
ii. The different solar cell technologies.....	16
3. Photovoltaic	18
i. Photovoltaic effect	18
ii. Photovoltaic as an energy supplier.....	20
4. Hybrid Organic-Inorganic Perovskites	20
i. 3D hybrid perovskite	20
ii. Optical and electronical properties	22
iii. Perovskite solar cell technology development.....	25
II. Experimental technics	28
1. Fabrication methods	28
i. Spincoating	28
ii. Drop-on-Demand Inkjet.....	29
2. Image management.....	38
i. Splat size and resolution	38
ii. Addressability and repeatability: conception of the image.....	39
3. Characterisations	40
i. Surface Energy	40
ii. Surface tension.....	44
iii. Viscosity	46
iv. Measurement of the bulk density	48

v.	Photovoltaic	48
III.	Toward a low annealing printable perovskite solar cell.....	52
1.	The reference and non-printable perovskite solar cell.....	52
i.	Objectives, strategy	52
ii.	Architecture.....	52
iii.	Best results	54
iv.	Fabrication	57
v.	Morphological features.....	62
vi.	Optical characterization and IPCE.....	63
vii.	Electrical measurements parameters.....	65
viii.	Stability issues	70
2.	WO ₃ -based perovskite solar cell.....	75
i.	Introduction and literature.	75
ii.	Fabrication	76
iii.	Best results	78
iv.	Optical, electrical and morphological features, IPCE.....	80
v.	Work Function.....	85
vi.	Optoelectronic properties.....	87
vii.	Stability issues	92
3.	UV protection of perovskite solar cells	96
i.	Introduction	96
ii.	Optical properties.....	97
iii.	Utilization of the down-shifting film for PCE enhancing.....	98
iv.	Beneficial effect of UV-protection on device stability.....	102
v.	Stability of the NITZ molecule.....	105
vi.	Conclusion	106
IV.	Printed perovskite solar cells.....	107

1.	Introduction	107
2.	Design of the printed solar cell.....	108
3.	Printed WO ₃ electron transporting layer.....	110
i.	WO ₃ nanoparticle ink	110
ii.	AFM and KPFM characterization.....	116
iii.	Perovskite solar cell with printed WO ₃ layer.....	117
iv.	Discussions on possible improvements.....	118
4.	Printing of the perovskite layer	118
i.	Perovskite ink	118
ii.	Printing optimisation.....	120
iii.	Thickness variation of printed perovskite layer.....	124
iv.	Surface energy and perovskite composition influence on wettability.	130
v.	Characterisation of printed perovskite layer.....	136
vi.	Perovskite solar cells with printed WO ₃ and printed perovskite layers....	139
5.	Printing of the hole transporting layer printing	141
i.	HTL ink requirements	141
ii.	Spiro-OMeTAD ink	142
iii.	Printing optimisation.....	143
iv.	Perovskite solar cells with three printed layers.....	144
v.	LBIC and LBIV	146
vi.	Cause of outstanding working cell.....	149
vii.	WO ₃ annealing temperature	154
6.	Perspectives for a printable top electrode.....	156
	General conclusion	158
V.	References and tables	160
1.	Figures table	160
2.	Tables table.....	164

GENERAL INTRODUCTION

3.	References	165
4.	Notations table	172
VI.	Acknowledgements	175
VII.	Résumé en français	176

General introduction

The objective of this work is to demonstrate the feasibility of the inkjet printing of the perovskite material for the application of photovoltaic devices. These printed perovskite solar cells are aimed to be used to supply energy to autonomous sensors, primarily used for the Internet of Things.

The first two sections will deal with the context and the literature about perovskite solar cells as well as presenting the experimental technics used for this work:

- The presentation of the context will set up the photovoltaic parameters objectives needed to supply in energy a network of autonomous sensors with perovskite solar cells. The physical explanation of the photovoltaic phenomenon will be also covered alongside the presentation of the functioning and literature of the perovskite solar cell technology.

- In the experimental technics the main fabrication methods used in this work will be investigated at the theoretical level. Spincoating technic and Drop-on-Demand inkjet printing technique will be presented and the physical models describing the rheological behaviour are deeply covered.

- The characterization technics for the rheological parameters of inks are also presented in this section with the classical electrical characterisation of solar cells.

The first result obtained for the reference perovskite solar cell made in the laboratory will be presented in the third section. In the same section, we will investigate the possibility to replace the conventional electron transporting layers, which are not printable and require high annealing temperatures, by the WO_3 material. This WO_3 layer is extensively investigated in this section: KPFM and ellipsometric measurements, optical characterization, and microscopic imagery has been conducted to qualify it. A large section of this section deals with the dynamic of the charge carriers between this layer and the perovskite layer, this discussion relies on the use of the spectrofluorimetry. The stability of perovskite solar cell will also be studied with the possibility to enhance it with down-shifting molecules.

The last section will cover in depth the inkjet printing of the perovskite solar cell inner layers. The experimental conditions and the results associated with the printing of the WO_3 , perovskite and Spiro-OMeTAD hole transport layer will be investigated and discussed. Investigations on the interactions between the ITO surface and the WO_3 ink is discussed, especially about the use of cleaning and surface treatment procedures. The printing of the

GENERAL INTRODUCTION

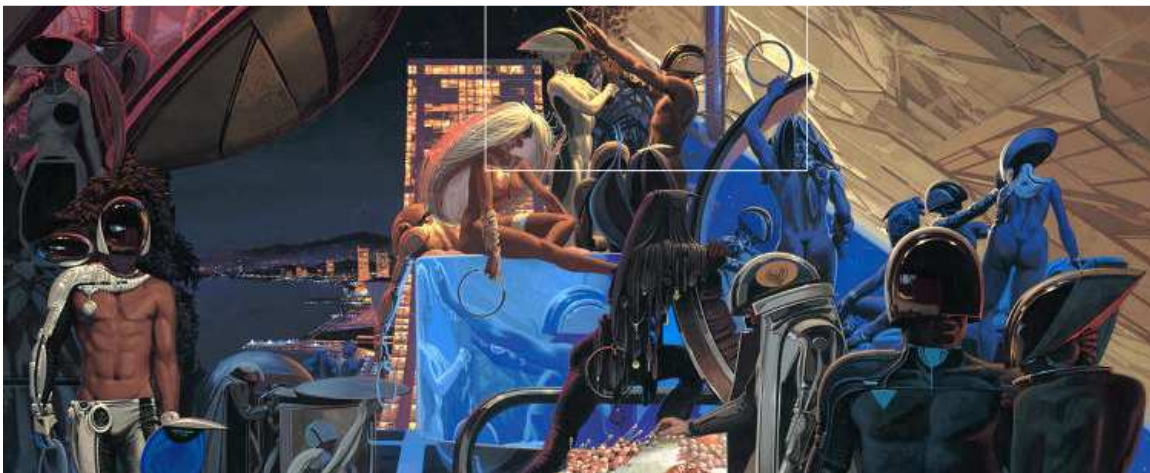
perovskite will be deeply covered: the optimisation of the perovskite ink is one of the main topic of the section with the control of the thickness of the printed wet layer.

I. Energy supplying for autonomous network of communicating devices

1. Photovoltaic as a credible energy source for nomad devices

A world where inanimate objects could communicate with each other, informing about their state or their whereabouts, was often described in the science-fiction and fantastic genre. The visions of this world are various depending of the atmosphere: in the Walt Disney's animated movie *Beauty and the Beast* [1] cups, teapots and furniture speak and sing altogether, it is the object for humoristic or musical interlude, however in the short-story *...That Thou Art Mindful of Him* written by Isaac Asimov in 1974 [2] little animals, like birds or insects, are replaced by autonomous basic robots, barely able to accomplish one simple task, but at the end ought to replace gradually every living being on Earth, including men. In a less apocalyptic point of view the novel 1984 *Neuromancer* [3], which is considered as a seminal work of the cyberpunk genre, William Gibson describes a very disturbing world where every object is connected and are speaking *via* the internet. Thanks to this technology, this fictional world is perfectly controlled by the states, the armies and the private organisations.

Let's us finish this short cultural review with a more positive thought. In the TV-Show *Star Trek* [4], created in 1966 by Gene Roddenberry, the communicating objects are used to teleport people with their badges used as a GPS marker or simply to save people thanks to this marvellous communicator able to diagnosis every possible medical condition and communicate with every electronic device. These communicating objects are thus essential, and precursor ideas are already developed in our current society.



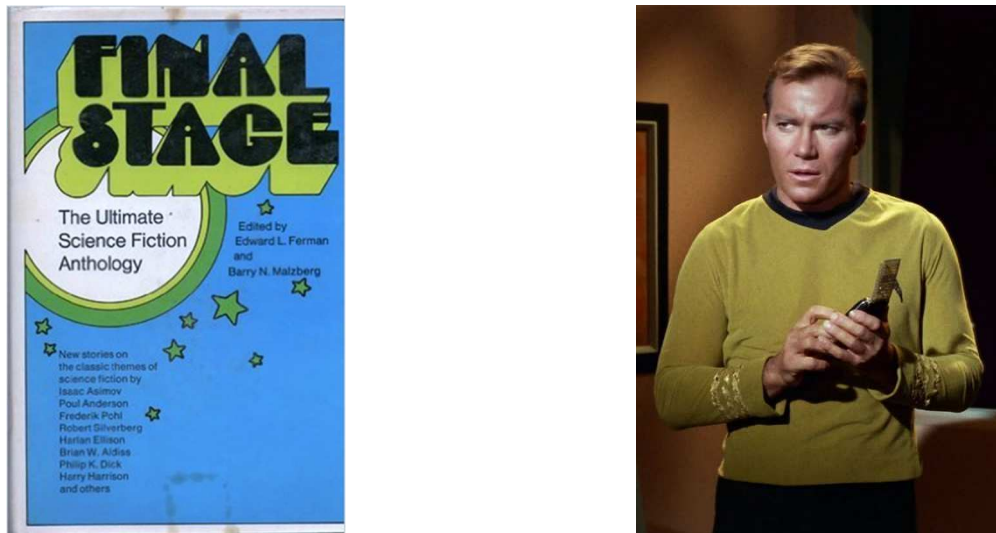


Figure I.1 – The future as seen by Syd Mead, the first publication of Asimov’s « ...That Thou Art Mindful of Him » and Captain James Tiberius Kirk using his omnipotent communicator.

Today this idea that every object could communicate between them and with the users has a concrete application: the Internet of Things (IoT) [5]. The implications of this concept are huge. In the commercial application IoT could help to monitor the behaviour of persons through space and time in order to send them custom sales or special offers. In the industry it will be a powerful tool to control closed and automated systems, like production process or supply chain. At the geographic scale it would give the opportunity to manage the energy consumption and to adjust its production and distribution, as well as helping the managing of person or cars flux. This shows how the Internet of Things could help to act on process of any kind. In this thesis we will focus on the other utilisation, more passive and simple: the information gathering. This simple version of IoT could be able to give information about the condition of a specific area, like its temperature, its humidity, the presence of an illumination source or the presence of sound. These application interest military organizations as well as public and private organisms which work into difficult conditions or not easily accessible areas. We will discuss about the particularities of these IoT on the next sections.

To give the possibility to an object to talk will need electronics: generally composed of a simple microcontroller, a sensor (designed to gather the interesting information) and an antenna to communicate. If science-fiction always dreamed of this kind of technology it never really explain how these electronics could work, especially what is its power source.

2. Autonomous sensor network

i. Sizing the autonomous sensor

One example of application of the IoT is an autonomous sensor network. An autonomous network is composed of hundreds of autonomous sensors, each of these sensors is able to gather information about the environment, such as temperature or composition of the atmosphere. The aim of this network is to monitor an area for security or sanitary purpose. Depending of the design and its component, a sensor could inform about the temperature or the composition of an atmosphere, thus detecting the presence of threats like radiological, chemical or biological attacks or hazards. This network could be droppable by plane on the area to survey or can be simply used indoor, anyway they must function in various and multiple conditions. Furthermore, each sensor is autonomous so it must possess its own power supply, these sensors are also potentially not-recoverable. This kind of network potentially interests military organizations as well as public and private organisms eager to evaluate risks before to intervene on battlefields or industrial accidents, or simply to monitor air contamination.

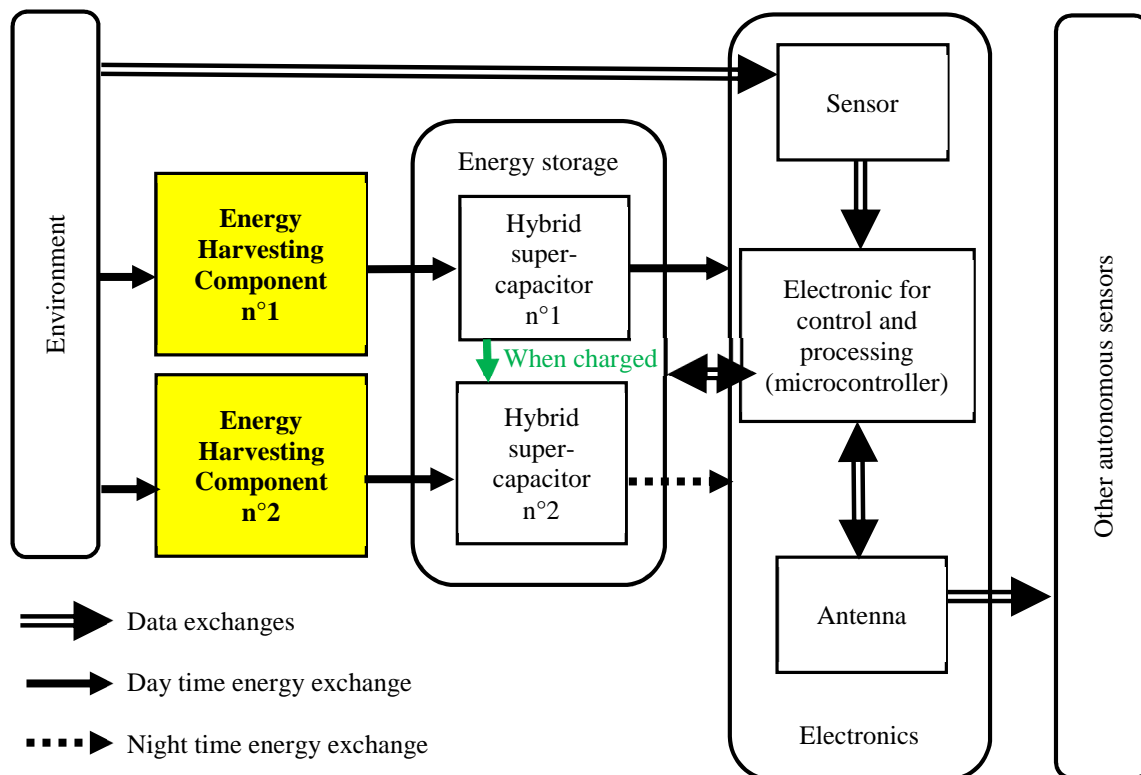


Figure I.2 – Schematic representation of an autonomous sensor

Each sensor is composed of three main part as presented in Figure I.2. The first part is the electronic one, containing the sensor itself whose role is to gather information such as the temperature, the humidity or the composition of an atmosphere. These data must be treated and

filtered to reduce the energy consumption during its sending through wireless communications. To do so the second part of the electronics is composed, for example, by a microcontroller consuming a very low level of energy, typically with operating voltages between 3 and 5 Volts. The last electronic component is the antenna allowing the sensor to communicate with the other sensors and eventually directly with the users.

The storage part has a particular functioning cycle because it must supply in energy to the sensor in every condition, furthermore it must be i) cheap and ii) small, as well as iii) efficient. In order to compete the third point the storage contains two Hybrid Super-Capacitors (HSC), one for the day and one for the night. During the day the hybrid super-capacitor n°1 is charged (via the Energy Harvesting Component n°1) during few minutes. When it is full, it is used to supply the electronics part of the sensor. The sensor uses this energy to gather the needed information (with the sensor), to process it (with the microcontroller) and to send it (with the antenna). When it is fully charged, the remaining energy is used to fill the hybrid super-capacitor n°2. Parallel to these operations the hybrid super-capacitor n°2 is continually filled during day in order to be used during night. During night the HSC n°2 is slowly used to supply all the sensor in energy. These operations are summarized in Figure I.3.

The energy harvesting part is composed of two Energy Harvesting Component (EHC). There are a lot of different possibilities to produce energy but the EHC must fulfil certain requirements which limit the number of possibilities. The main requirements is to possess a high power density. Indeed, the sensor must be small, around 10 cm² and cannot be heavier than an hundred grams. This constraint reduces the possibility, as the only light energy supplying component are batteries, photovoltaic solar cells, thermoelectric devices, tribo or piezoelectric devices (powered by wind and/or motion). Moreover these sensors should be usable for indoor application, which is an environment with potentially low solar energy or mechanical energy. One important aspect to consider is that some of the sensors could be used in some conditions where retrieval is not possible, therefore the environmental impact and pollutions must be reduced at its minimum. With these constraints and for long-term usage the best is not to use energy supplying solution only based on batteries [6]. Furthermore the sensor might be used during several weeks, and be used at any time without having to worry about finding an electrical plug to recharge its battery. Conventional batteries (alone) are thus suppressed from the list.

In term of energy requirements, an IoT sensor would need around 10 mW of power energy (see further to the detail of the calculus). Considering the size of a sensor (10 cm²), as

specified previously, some technologies for energy harvesting will have strong limitations. Tribo or piezoelectric is limited at $10 \mu\text{W}$, and as the sensor must be used in any place, potentially without wind or motion, the tribological devices are also not practicable. The same power level limitation would apply to ambient RF harvesting, some places can be also be deprived of artificial RF signal. Thermoelectric harvesting can only supply few tens of μW and need a high gradient in temperature which is almost never the case. At the end only the photovoltaic technology remains, which can harvest few hundreds of μW indoors and up to 100 mW outdoor [7].

From now on, EHC will be assimilated as photovoltaic solar cell.

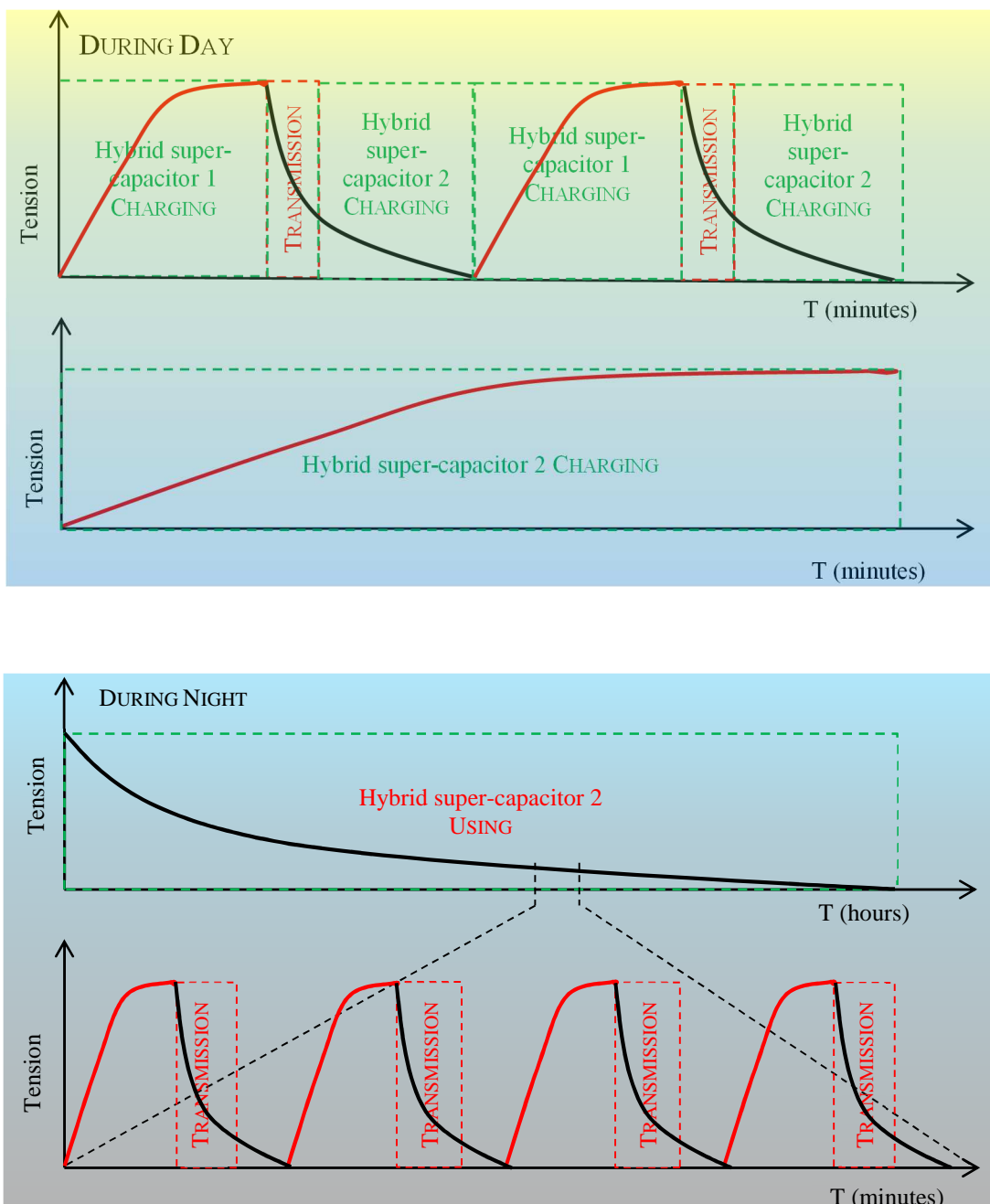


Figure I.3 – Schematic illustration of the energy management in the sensor.

The objective is therefore to print at low cost a solar cell to supply in energy the autonomous sensor. The first step is to know the electrical requirement for such equipment. As said previously, the sensor must be able to send data every 5 minutes during the day, and 20 minutes during the night. The energy would be stored in a 1 F supercapacitor or a 100 mAh battery. To charge 100 mAh during 6 h at least 16.7 mA is needed while 5 V is necessary to maintain the electronic component functioning. Knowing this sizing and the average performance published in literature, the objective to achieve for one perovskite solar cell is: around 1 V for the open-circuit voltage (0.83 V is enough to obtain the needed 5 V) and 16 mA.cm⁻² for the short-circuit current (J_{sc}). With 6 cells of 1 cm² by cell, connected in series, the autonomous sensor should work in the optimal conditions. Furthermore to allow the fabrication of solar cells on all substrate the maximum annealing temperature should be 130 °C. All the objectives are summarized on the Table I.1.

Photovoltaic parameters	
V_{oc} (mV)	830
J_{sc} (mA.cm ⁻²)	16
FF (%)	75
PCE (%)	10
Fabrication	
Surface (cm ²)	1
Back electrode (ITO or FTO)	Non-printable
ETL	Printed
Absorbing layer	Printed
HTL	Printed
Top electrode	Printable
Max annealing temperature	130°C

Table I.1 - Objectives for the printed solar cell.

ii. The different solar cell technologies.

To produce this solar cell a various number of technologies are already available, there are summarized in the Table I.2.

Type	Amorphous Silicon	Crystalline Silicon	Multi-junction	CIGS	Organic	Dyes	Perovskite
Current uses	Calculator, watches	Domestic, sensors	Cars, domestic		Commercialized for some applications (sensors, domestic)		Research
Best laboratory efficiency	5-7 %	10-20 %	40 %	20 %	10 %	10 %	20 %
Printable	No	No	No	Yes	Yes	Yes	Yes

Table I.2 - Available solar cell technologies

In term of photovoltaic performances the amorphous silicon, organic and dyes technology are not powerful enough. The best efficiencies obtained in laboratory are not high enough to promise a sufficient performance for an industrial fabrication. For our application, only the crystalline silicon, the multi-junction, the CIGS, and the perovskite technologies remain efficient enough. The crystalline Silicon and the multi-junction technologies remain too expensive to be used as solar cell on disposable sensors. The only left technologies are the CIGS and the perovskite which are both printable and allow a high PCE around 20 % in laboratory for surface areas lower than 1 cm².

Compared to CIGS one of the advantages of the perovskite are the availability of certain raw materials. Some CIGS are constituted by indium which is a rare material, however other technologies of CIGS use gallium instead of indium. The perovskites are only composed of carbon, hydrogen, nitrogen, iodine and lead which are very affordable materials and can be found very easily anywhere on Earth. The main advantage of perovskite is of course their low annealing temperature, once the CIGS layer is printed it needs to be sintered at 400 °C [8] while the perovskite only need an annealing at 90 °C. This allows the production of printed solar cells on flexible substrates, such as PET or PEN.

One other advantage of the perovskite is their high efficiency under low level of illumination. Organic solar cells with P3HT:PCBM reached a 7 % PCE under low light conditions [9]. Under LED lightings PCE over 20 % were reported for organic solar cells [10]. In the other hand, perovskite solar cells with PEDOT:PSS as hole transporting layer and C₇₀ as electron transporting layer were able to achieve a 22.5 % of efficiency for a 100 lux illumination [11] which corresponds to an overcast day. This result shows that perovskite material could open a path for new applications for indoor usage.

The presence of lead in the composition of perovskite is an issue in term of environmental contamination and safety during production. Several studies already investigate

the effect of lead during the production of Perovskite Solar Cell (PSC) and lead is commonly known to provoke lead poisoning [12]. Attempts to replace it by other metals, like tin, is in process but this solution is known to induced lower material stability, and therefore, at the end, higher probability of tin poisoning or lead poisoning in the case of mix-cations perovskite [13]. Compared to the consumption of electricity (and its impact on global environment for the preparation of the different materials of the PSC and its fabrication), the presence of lead is not critical [14]. At the end, in a PSC only 0.008 % of the cell is composed of PbCl_2 and 0.001 % of metallic Pb [14]. The RoHS (Restriction of the use of certain Hazardous Substances in electrical and electronic equipment) directive of the European Union is known as the “lead-free directive”, among other materials it restricts the use of lead in electronics sold in the EU [15]. This directive could be a brake in the development of perovskite photovoltaic panel in the UE, however the RoHS also restricts the use of cadmium but an exception has been created for CdTe thin-films PV modules. The same can be expected for perovskite photovoltaics considering their huge potential. If we exclude the legislative (considering an exception has been made) and the environmental (using perovskite solar cells for energy production compensates the environmental threat of lead) issues, the main effort to be done are in the production of PSC to protect the operators and in the recycling of the perovskite PV modules at the end of the life cycle [14].

3. Photovoltaic

i. Photovoltaic effect

The photovoltaic effect was first observed by French physicist Alexandre Edmond Becquerel in 1839, almost 200 years ago. His experience consisted in two electrodes made of platinum and copper in an acidic solution: when the liquid was exposed to light a current was spontaneously produced [16]. In 1883 the American inventor Charles Fritt created the first photovoltaic cell made with gold coated selenium, with a power conversion efficiency of 1%. In 1905 Albert Einstein published “On a Heuristic Point of View about the Creation and Conversion of Light” explaining the photovoltaic and photoelectric effects, from a quantum point of view, which has earned him the physic Nobel Prize in 1921. The first commercial silicon solar cell is created in 1954 by the Bell Labs, with a power conversion efficiency of 6%.

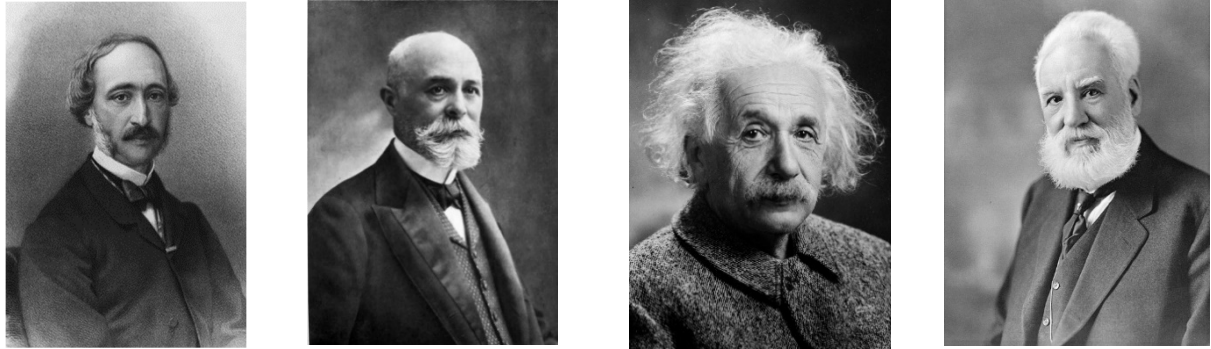


Figure I.4 – From left to right Alexandre Edmond Becquerel, Charles Fritt, Albert Einstein and Alexander Graham Bell

The photovoltaic effect happens when a material is under illumination (natural or artificial) and consequently photons are absorbed by the structure of the material. If the energy of the incoming photon is enough (depending of its wavelength) one of its electron from its outer orbital will escape from the attraction of the atom's nuclei. This electron will be free to move to another atom and its absence in the original atom will create a lack of negative charge: a hole. Considering the original atom it is now in an ionized state, this state can be exchanged with another atom in the neighbour and so forth. As a result we consider than, as the electron is a mobile negative charge carrier passing from atom to atom, the hole is a mobile positive charge carrier.

The movement of the electrons and holes (a pair of each bounded by Coulombian force is named an exciton) follows the rule of a Brownian motion. When a large amount of photons are absorbed by the material the same number of holes and electrons are created, which means that each charge carrier (negative or positive) has a great chance to meet his opposed charged entity and, therefore, to recombine. In order to produce a current it is needed to collect a maximum quantity of electrons and holes and to avoid recombination. However when an electric field is imposed to the material the holes and electrons are separated in two opposite direction, which favour the exciton dissociation mechanisms.

The solution to avoid recombination is therefore to engineer an inbuilt electric field thanks to a *pn* junction (n for negative and p for positive). For a crystal lattice, such as crystalline silicon, a *pn* junction can be created by the incorporation of impurities: a process called the doping. In order to produce p type silicon the most used acceptor used is boron, while the phosphorus is often used for the n-type silicon. As the interface between the p-doped material and the n-doped material the holes are attracted and move toward from the p-doped material to

the n-doped material in a diffusion mechanism. The electrons move in the other direction, from the n-type to the p-type zone. This will create a depletion region with an inbuilt electric field to help the extraction of the charges. Of course, the exciton spontaneously dissociates in crystalline silicon, as the Coulombic binding energy between the electron and the hole is in the order of the thermal energy. This is not always the case for disordered or organic semiconductors, as we will see later.

ii. Photovoltaic as an energy supplier

In one hand the need for electricity in 2025 will summit at 25000 TWh. In the other hand, each centimetre square of the earth surface receives during daytime, in average, 100 milliwatt of solar energy. If we had a device able to restrain only 10 % of this energy we only need to cover 31000 km² with these devices, this corresponds to a square with 176 km length sides, 0.006 % of the total earth surface area, the size of 10 French department of the size of the “Rhône” one.

4. Hybrid Organic-Inorganic Perovskites

i. 3D hybrid perovskite

Within the last five years, a new class of photovoltaic materials made an impressive arrival in the field of solar energy conversion: the organic-inorganic halide perovskites, or hybrid perovskites. The term perovskite was primary created for the CaTiO₃, discovered in 1839 by the German mineralogist Gustav Rose from a rock sample of the Ural Mountains. He gave the name *perovskite* as a tribute to the Russian count Alexeïevitch Perovski, who was also a respected mineralogist, having proposed in 1845 to found the *Русское географическое общество*, the Russian Geographical Society. The term perovskite was given then to the typical crystalline structure presented by the CaTiO₃. It is defined by a crystalline structure composed by three different species (A, B and X) forming the general ABX₃ formula, an ideal cubic structure (α phase, Pm3m space group) [17]. A and B are two cations of very different sizes and X an anion. In the ideal perovskite structure the big A⁺ cations are at the corners of a cube, the anions X⁻ are in the middle of each faces, and the little B²⁺ cations are in the middle of the octahedral sites formed by the anions X⁻.

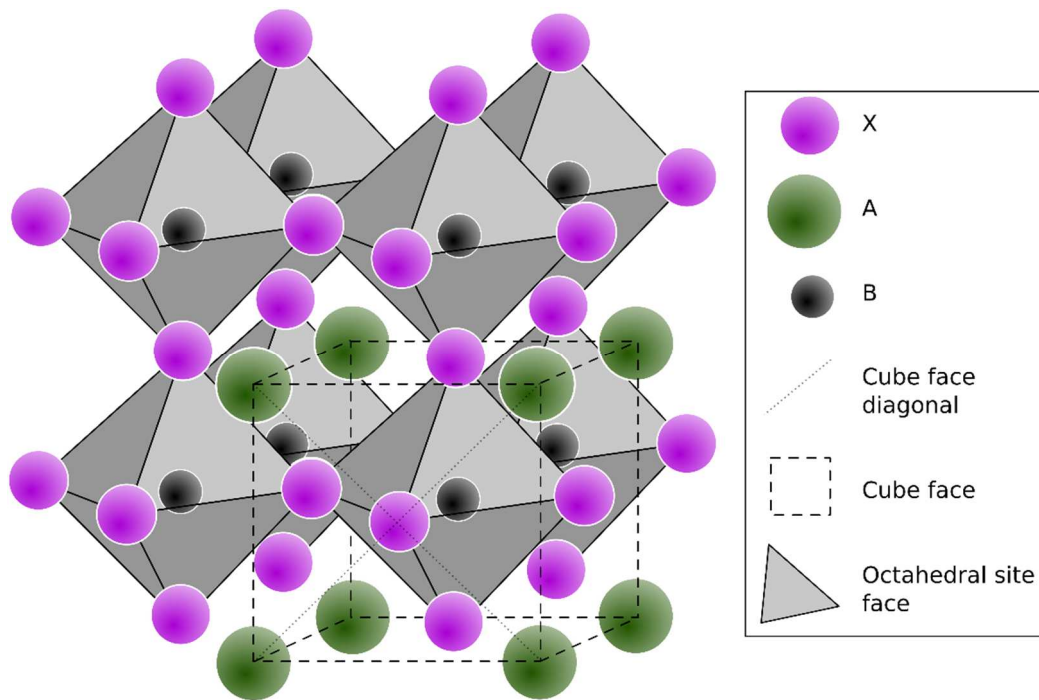


Figure I.5 - Generic perovskite structure.

In hybrid perovskites, the X anion is often a halide: an atom of fluorine (F), chlorine (Cl), bromine (Br) or iodine (I). The halide anion site can also be used by a mixture of different halide atoms, leading to mixed halide perovskites. In fact, by replacing chlorine by bromine, and then by iodine, the absorption spectrum shifts toward the red. The little B cations is usually lead (Pb). Tin (Sn) can also be used but the resulting material is found to be less stable as it can form SnI_4 inside the perovskite phase [18]. For the moment, lead is the favourite specie because of its higher electronegativity and a larger binding metal-anion-metal angle (which is good for high band gap absorption) [19]. These X anions and little cations B form the inorganic part of the hybrid perovskites. The organic part corresponds to the big cation A, it is played by an organic molecule. Methylammonium (CH_3NH_3^+) is commonly used and is sometimes replaced by ethylammonium ($\text{CH}_3\text{CH}_2\text{NH}_3^+$) or formamidinium ($\text{NH}_2\text{CH}=\text{NH}_2^+$). For example, formamidinium is used to reduce the absorption gap in order to increase the part of the light that is converted in current [20]. At last for the photovoltaic application the most investigated hybrid perovskites are $\text{CH}_3\text{NH}_3\text{PbI}_3$, or the mixed-halide compound $\text{CH}_3\text{NH}_3\text{PbI}_{3-x}\text{Cl}_x$, which is the main perovskite used for this thesis.

Under ideal conditions and to maintain the cubic structure, A, B, and X should be chosen related to their atomic radius, which must allow a tolerance factor t close to 1, following:

$$t = \frac{R_A + R_X}{\sqrt{2} \times (R_B + R_X)} \quad (1)$$

Where R_A , R_X , R_B are the ionic radii of corresponding ions. If the cubic symmetry is not respected the structure will be distorted while the crystal symmetry is lowered. In order to respect this condition and with these kind of perovskite where the B site is occupied by a Pb atom, which is already big, the A has yet to be bigger. The biggest atom that we can consider is Cs, but it is not big enough, and this is probably why organic molecules are employed to form more stable perovskites [21]. Theoretically, the perovskite crystal will exhibit a cubic structures if t is between 0.89 and 1. Furthermore, smaller t leads to lower-symmetry tetragonal (β phase) or orthorhombic structures (γ phase), whereas larger t ($t > 1$) could destabilize the three-dimensional network, forming a two-dimensional (2D) layer structure. In other words, if this organic molecule radius begins to be bigger than roughly 0.40 nm the perovskite becomes a 2D perovskite, forming more or less thick sheets of inorganic materials separated by organic sheet. Depending of the temperature and the composition, the perovskite can change its phase. As an example with the classical $\text{CH}_3\text{NH}_3\text{PbI}_3$ the α to β to γ phase transitions happen respectively at 330 K and 160 K [22].

ii. Optical and electronical properties

Now than the principal lines of perovskite are drawn, the explanations about photovoltaic properties is now approached. These explanations lay essentially on computational modelling and will focus on the work of Jacky Even et al [23].

In term of optical properties, the $\text{CH}_3\text{NH}_3\text{PbI}_3$ perovskite is characterized by an absorption spectrum between 460 and 760 nm, as figured in the Figure I.6. The direct gap transition from the first valence band maximum to the conduction band minimum, has a value of 1.7 eV [24] and around 1.6 eV for $\text{CH}_3\text{NH}_3\text{PbI}_{3-x}\text{Cl}_x$ perovskite [25]. From this value we can predict where the absorption peak is on an absorption spectrum with:

$$E = \frac{hc}{\lambda} \quad (2)$$

With h the Planck constant and c the light velocity in vacuum, we find 775 nm. A close value can be found in the absorption spectrum with the presence of a peak around 770 nm [26]. The linear absorption coefficient of hybrid perovskite has been calculated at $5.7 \times 10^4 \text{ cm}^{-1}$ [26].

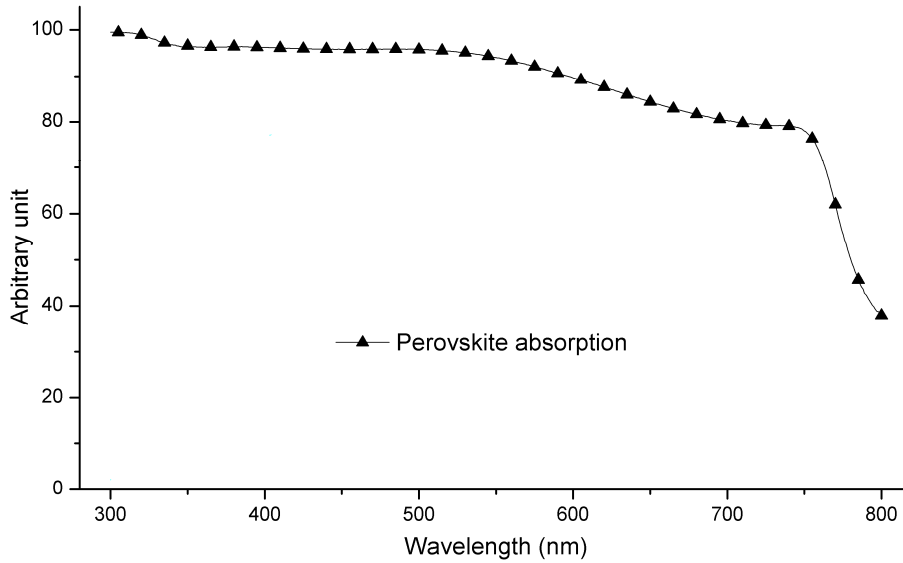


Figure I.6 - Absorption Spectrum of $\text{CH}_3\text{NH}_3\text{PbI}_{3-x}\text{Cl}_x$ perovskite

The absorbance α from the transmission T of the perovskite film can be computed with the following equation:

$$\alpha = -\frac{1}{d} \log(T) \tag{3}$$

Where d is the thickness of the layer (here, 2 microns). The absorbance and the optical gap E_g can be linked by the Tauc equation [27] :

$$\alpha h\nu = B^2(h\nu - E_g)^r \tag{4}$$

Where $h\nu$ is the incident photon energy, B is a parameter corresponding to the band tailing and r a parameter with a specific value: 2 for indirect allowed transitions, 3 for indirect forbidden transitions, $1/2$ for direct allowed transitions or $1/3$ for direct forbidden transitions.

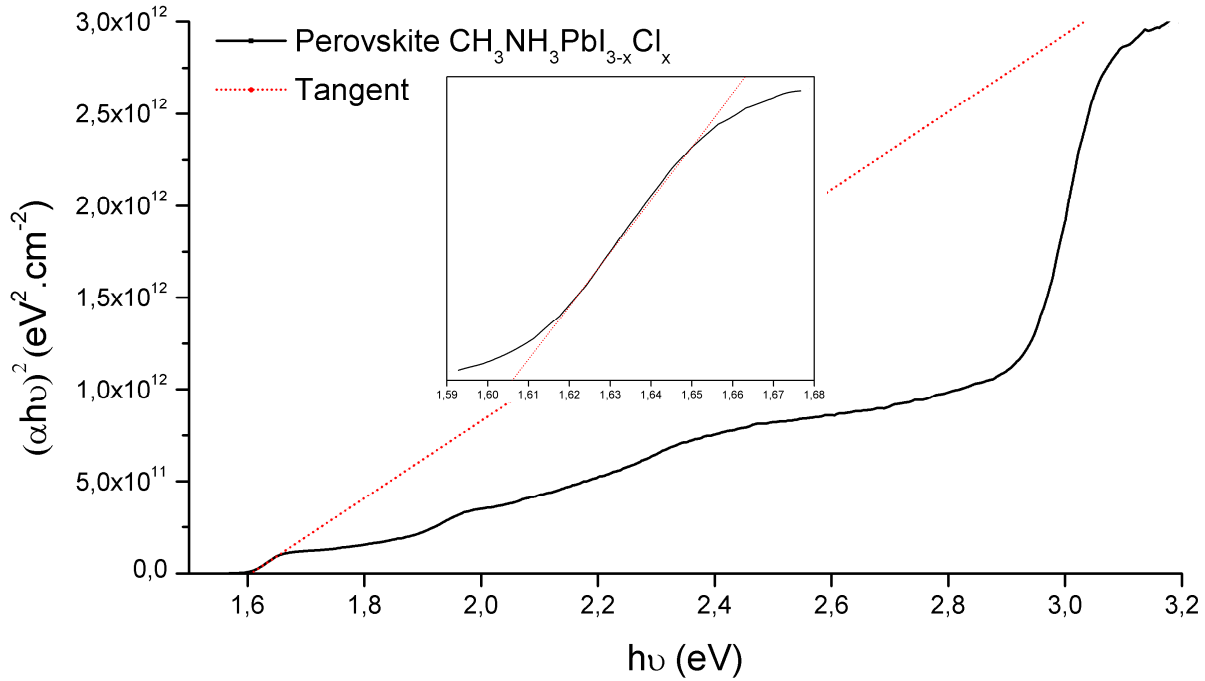


Figure I.7 - Tauc fit for $\text{CH}_3\text{NH}_3\text{PbI}_{3-x}\text{Cl}_x$ layer

As said previously the hybrid perovskite possess a direct gap transitions, $1/2$ is therefore the value of r . The value of E_g can be then calculated by extrapolating the linear region of the curve with the following equation (Figure I.7):

$$(\alpha h\nu)^{\frac{1}{r}} = f(h\nu)$$

The value of E_g is found at the intersection of the abscise and the tangent. We find for the $\text{CH}_3\text{NH}_3\text{PbI}_3$ -perovskite a value of 1.6 eV.

It is possible with photoluminescence technics to extract some interesting optoelectronic properties values. For a $\text{CH}_3\text{NH}_3\text{PbI}_3$ perovskite layer the fitted charge carrier lifetime has been calculated around 4.5 ns [26] and 9.6 ns [28] while in the $\text{CH}_3\text{NH}_3\text{PbI}_{3-x}\text{Cl}_x$ material the lifetime of the charge carrier calculated at XLIM was 238 ns [29] and confirmed at 273 ns by Stranks et al. [28]. Here we see the beneficial effect of the presence of chlorine, even if it is not clearly explained. With its higher charge carrier lifetime, the $\text{CH}_3\text{NH}_3\text{PbI}_{3-x}\text{Cl}_x$ perovskite produces much longer diffusion lengths of the holes and electrons, with values respectively around 1200 nm and 1000 nm against 100nm and 130 nm for $\text{CH}_3\text{NH}_3\text{PbI}_3$ [26, 28]. This will have an interesting consequence in term of solar cell fabrication, particularly because the $\text{CH}_3\text{NH}_3\text{PbI}_3$.

$x\text{Cl}_x$ allows to produce a thicker and less homogeneous layer with a simple methodology, while the $\text{CH}_3\text{NH}_3\text{PbI}_3$ perovskite asks to be prepared in a sequential fabrication which is not suitable for printing technologies. However the $\text{CH}_3\text{NH}_3\text{PbI}_3$ remains more performant than the $\text{CH}_3\text{NH}_3\text{PbI}_{3-x}\text{Cl}_x$ [30]. Halide perovskites are also characterized by high carrier diffusion length for about one micron, effective mobilities of roughly $10 \text{ cm}^2 \cdot \text{V}^{-1} \cdot \text{s}^{-1}$ while the exciton binding energy value is still being investigated, it has been reported between approximately $\sim 40 \text{ meV}$ [31] and 6 meV [32].

Computational modelling is able to evaluate the band structure of the hybrid perovskite. It has been demonstrated that it is possible to link the electronic structures of the ideal cubic crystal structure of the perovskite and that it is of its room temperature tetragonal phase [33]. It appears that such structure leads to a direct band-gap structure. Furthermore a spin-orbit coupling lower the band-gap value for more than 0.8 eV [23], leading to theoretical predictions in line with experimental values.

iii. Perovskite solar cell technology development

Direct Architecture

The perovskite solar cell technology profits of the solid-state dye sensitized solar cell (sDSSC) technology previously designed in 1998 by Grätzel and al. [34], the power conversion efficiency (PCE) was 0.74% . After much improvements in architecture and composition the

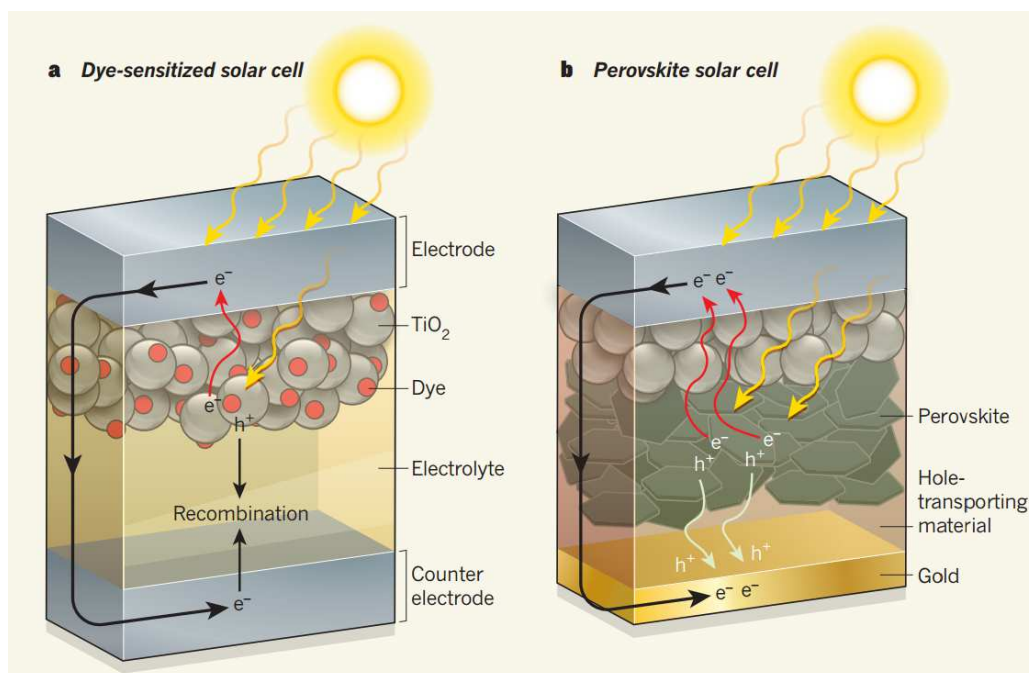


Figure I.8 - The evolution of perovskite solar cells from the dye sensitized solar cells technology [113]

most commonly used sDSSC is composed of TiO₂ mesoporous layer sensitized with an organic dye called D102 [35] and a solid electrolyte as hole transporting layer (Figure I.8), the conversion efficiency of these kind cells are around 4 %.

In the other hand, the photovoltaic behaviour of inorganic perovskites was already reported in 1956 [36] on BaTiO₃, however it is only in 2006 that we saw the first application of a hybrid perovskite as the active layer of solar cells. Hybrid perovskite were then used as photosensitizers in dye sensitized solar cells demonstrating 2.2 % efficient devices under full sun illumination condition [37] before achieving 3.8 % in 2009 [38]. The solar cells performances were however highly unstable and deteriorated within a few minutes. In 2012 occurred the real breakthrough: two publications reported efficiencies up to 10 % [39, 40], constituting the first uses of the perovskite as sensitizers of the mesostructured electron transporting layer TiO₂. Since these reports, a lot of progress has been made in the composition, fabrication, and post-processing of the different layers that compose these PSC. Today, certified state-of-the-art performance are reported at 21.02 % by a common work of the Ecole polytechnique fédérale de Lausanne and the Australian company Dyesol and 22,1% by the Korea Research Institute of Chemical Technology with the university of Ulsan, and several groups demonstrated efficiencies over 19% illustrating the strong potentialities of perovskite materials among thin film technologies [41, 42]. All these PCE evolutions are presented in the NREL chart [43] of the Figure I.9.

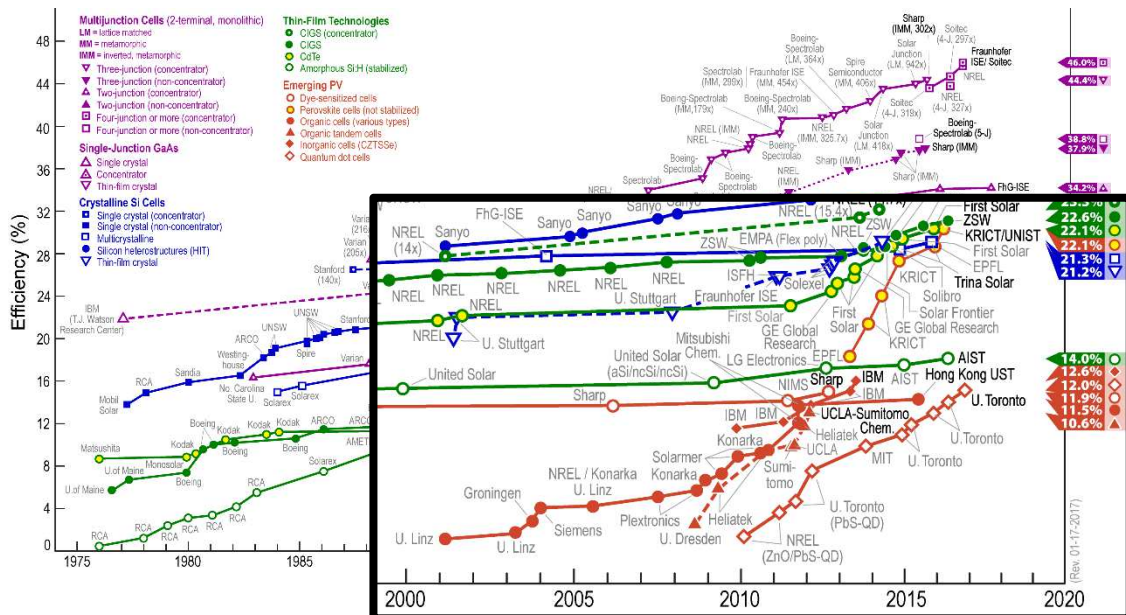


Figure I.9 - Chart of the best photovoltaic research-cell efficiencies (January 2017)

This rapid and outstanding evolution of performance is thus mostly of the precedent DSSC technology and its progress in the fabrication and process of the TiO₂ layers as well as that of the hole transporting layer organic molecule Spiro-OMeTAD.

II. Experimental technics

1. Fabrication methods

i. Spincoating

The spincoating method was used in this work to produce and optimize the reference TiO₂ perovskite solar cells. It was then used for optimization of the new layers and the different characterizations conducted on these new perovskite solar cells. Spincoating is a way to produce a uniform thin liquid film on small rigid flat substrate. This process is divided in three stages: deposition, spinning and evaporation

The first stage consists in depositing an excess of liquid on an immobile or a slowly spinning substrate. The amount of liquid is far more than the coating actually needs, provoking a loss of matter.

In the second stage the spinning of the substrate begins and the liquid flows radially outward, driven by the centrifugal force generated by the rotating substrate. This stage can last few seconds or several minutes. The substrate rotates as several thousand revolutions by minutes. During the spinning the liquid flows against the gas surrounding the original drop. After a moment the liquid occupies all the free surface of the substrate. At the perimeter of the substrate accumulates all the unwanted matter in the form of a swelling that eventually break into droplets. In the rest of the surface the thickness of the liquid film reaches an initial thickness h_0 . The equation linking the evolution of the thickness of the film with times and rotation speed before the evaporation step is [44]:

$$h(t) = \frac{h_0}{\sqrt{1 + \frac{4}{3} \frac{\rho \omega h_0^2 t}{\eta}}} \quad (5)$$

Here ρ is the density of the liquid, ω the angular velocity, and η the dynamic viscosity. As the film thins the resistance against the flow and the evaporating rate increase resulting in a decrease of the liquid flow. This means that the final thickness depends also of the nature of the gas surrounding the layer and of the vapour pressure of the liquid in this gas since the evaporation of the solvent can begin during the spincoating.

The last stage depends of the nature of the spincoated liquid, some require a annealing to simply evaporate the solvents, some to sinter the metallic particle and other just need an evaporation at room temperature.

Spincoating is an efficient method to produce homogenous film because two forces balance in the liquid during the spinning: the centrifugal forces that drives the liquid out and the resisting viscous forces that lead the liquid toward the interior of the substrate.

ii. Drop-on-Demand Inkjet

Presentation

Once the fabrication of the TiO₂ reference perovskite solar cells with spincoating was mastered, our objective was to produce the perovskite solar cells with a printing technique. In XLIM the only printing technics which is available is Drop-on-Demand (DOD) Inkjet, this technology will be presented in this section.

DOD Inkjet is a masterless printing technology. This means that this technology does not need a master. This master consists on a substrate commonly etched with the image to print. This substrate carries the ink and transfer it to the printed surface: this is case for gravure with the gravure cylinder, the offset printing with the offset plate, the screen-printing and its screen, and, at last, the flexography and the rubber plate. This kind of printing processes is call digital printing. With inkjet we can find in this group electrophotography (also known as xerography or laser-printing), ionography, magnetography. The main advantages of this kind of printing is that the image to print can be changed for every substrate allowing a more flexible printing strategy, which is very comfortable for R&D objectives.

The main principle in inkjet is to jet little droplets through nozzles and to drop them on the substrate. There are a lot of technologies to eject droplet but here, we will focus on the one used by the Dimatix Materials Printer DMP-2850 [45] used in the thesis: the piezoelectric technic. The “Drop-On-Demand” term means that droplet are jet only when necessary, contrary to Continuous Ink Jet where drop are continuously jetted, and are deflected by an electric field (meaning that the ink must be electrically charged).

Piezoelectric jetting

The principle is to deform a piezoelectric element which is in front of the nozzle, separated by a flexible and hermetic vibration plate and the ink chamber. The deformation of the piezoelectric element will create a variation of the ink volume, this variation will provoke

the ejection of a drop (Figure II.1). Other architecture are possible, with piezoelement on both side of the ink chamber, around it or with each ink chamber separated by a piezoelectric bulkhead.

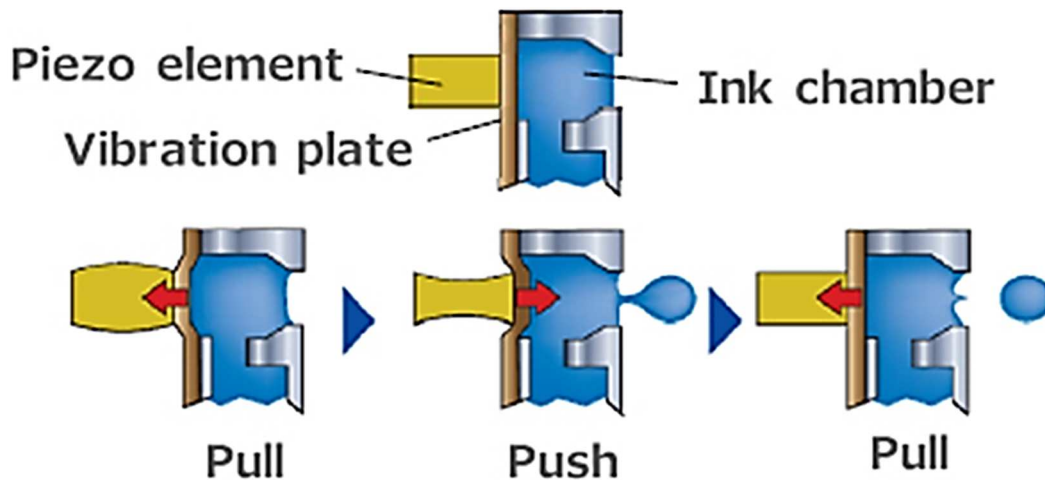


Figure II.1 - Piezoelectric element deformation provoking the droplet jetting

The way the piezo electric deforms will change how the drop is ejected. The piezo element is deformed by applying a voltage. The waveform of the voltage signal can be changes in order to tune the jetting parameters. The shape of this waveform is the one presented in the Figure II.2. The first negative *voltage 1* will deform the size of the piezo element, pulling it in the opposite direction of the nozzle. The volume of ink is then increased, this first modification of the piezoelement plays a major role in the size of the drop. Indeed the bigger is this *voltage 1*, the bigger the deformation of the piezoelement will be, the bigger will be the drop. We will see later (in the following *jetting condition* section) how the size of the drop, more specifically its weight (i.e. its inertia) can ease the jetting or restrain it. Of course the size of the drop plays an important role in the size of the splat on the substrate, and the final thickness of the layer. Depending on the viscosity and the density of the liquid it can be necessary to adjust the *Holdtime 1*, to let the time (or not) to the ink to fill the new volume of the ink chamber. The *voltage 2* will decrease the size of the ink chamber pushing the ink in the only free direction: toward the nozzle. Indeed the ink cannot go back in the canal since it is continually fill with ink up to the ink cartridge itself. This voltage can be held during few milliseconds (*holdtime 1*) to enhance jetting quality. The *voltage 2* value will be also important for the drop size. For each ink it is needed to customise the shape of the waveform. The waveform can be heavily modified by extending the length of the different step, adding a slope rate between ejection phases or a negative voltage bias can be added.

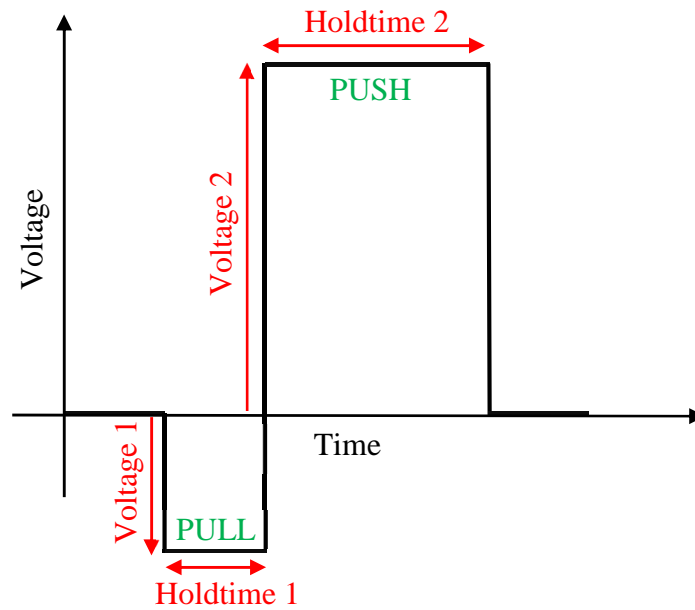


Figure II.2 - Piezoelement jetting waveform

Jetting condition

The final objective is to jet an ink in good and repeatable conditions. These conditions are visually represented in the Figure II.3 and are:

- a jetted ink forming a unique drop (without satellites droplets)
- without any tail (the head of the drop and its tail must merge)
- following a straight trajectory
- without clogging the nozzle

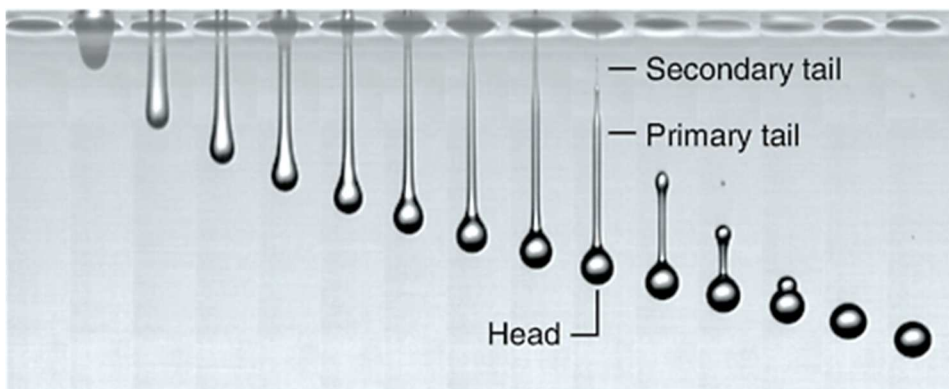


Figure II.3 - example of a good and repeatable jetting: forming a unique drop, without droplets, in a straight trajectory and with tails retracting into the drop's head. [111]

To know if a liquid is correctly jettable with an inkjet system, a number of ink parameters must be checked. In the general case the ink viscosity should be between 1 mPa.s (water viscosity at 20°C) and 30 mPa.s and its surface tension should be between 24 and 40

mN.m^{-1} [46]. In the specific case of our inkjet printing machine it is advised to keep the viscosity between 10 mPa.s and 12 mPa.s which is a pretty narrow gap, it is possible to use lower viscosity ink but to the detriment of the jetting performances (i.e. repeatability). The surface tension should be between 28 and 33 mN.m^{-1} .

In the general case, inkjet inks must be engineered in order not to clog the nozzle. If the ink is a suspension of particles, the particles should not be bigger than $1/10^{\text{th}}$ of the nozzle diameter ($1/100^{\text{th}}$ for the case of the DMP-2850 10 pl cartridge, that is to say $0.2 \mu\text{m}$). It is also mandatory to avoid evaporation of the ink in the nozzle during the non-printing steps. To do so the solvent must have a high boiling point. It is possible to do a mix of solvent to increase this temperature while trying to keep the rheological properties of the ink.

Viscosity, surface tension, particle size and boiling point temperature are a quick way to evaluate the usability of a solution in an inkjet system. However good rheological parameters, coupled with the density and limited nozzle size cannot, sometimes, guarantee a good jettability of the ink. In order to predict in a more efficient way what are the appropriate jetting mathematical models have been designed. This work has been made by Derby and Reiss, and summarized by Derby in a review in 2010 [47] and will be described here.

The jettability of the ink is linked to the Reynolds (Re) number which express the ratio between the inertial forces and the viscous forces. The value of this ratio express if the strain we apply on the ink is enough to overpass the liquid viscosity. If Re is superior to one we consider than the ink is jettable.

$$Re = \frac{v\rho a}{\eta} \quad (6)$$

Where v is the jet speed, ρ the bulk weight of the ink, η the dynamic viscosity and a a characteristic dimension of the studied flow, here it is the drop diameter than we can approximate by the diameter of the nozzle. Re depends of the speed of the drop v , which is not accessible before having try a first printing.

A solution to determine a velocity is to calculate the ejection speed. This speed corresponds to the minimum speed that allows the drop to overcome the barrier that the surface energy of the air/liquid interface represents. To do so we use the Weber (We) number, which must be superior to 4.

$$We = \frac{v^2 \rho a}{\gamma} > 4 \quad (7)$$

Here γ is the surface tension of the ink. From this equation it is possible to calculate the minimum velocity needed to eject a drop:

$$v > \sqrt{4 \frac{\gamma}{\rho a}} \quad (8)$$

Moreover, almost the same expression for the minimum speed for drop ejection can be found from a different calculus. In considering that the ejection of the drop is possible when the kinetic energy overcome the surface energy of the air/liquid energy we have:

$$\frac{1}{2} m v^2 > \gamma S \quad (9)$$

Where the mass m of the spherical drop can be write as $m = \rho \frac{3}{4} \pi \left(\frac{a}{2}\right)^3$ and S the section of the nozzle exposed to the air by $S = \pi \left(\frac{a}{2}\right)^2$, and we found :

$$v > \sqrt{3 \frac{\gamma}{\rho a}} \quad (10)$$

In practice we used the expression determined with We (8) to calculate this minimum drop velocity.

To know if the jet will be composed of only one drop and without any satellites droplets the number of Ohnesorge (Oh) is calculate (this number is sometimes expressed with $Z=1/Oh$). When this number is between 0.1 and 1, there will not have any satellite droplets. The smaller Oh is, bigger will be the number of droplets, when Oh is too big it is difficult to jet a drop.

$$Oh = \frac{\sqrt{We}}{Re} = \frac{\eta}{\sqrt{\gamma \rho a}} \quad (11)$$

Is it possible to summarize this calculations in one graph (Figure II.4). In this graph for each speed reachable by the drop the We and Re are calculated and reported. This graph helps to select the speed that allow the print condition to be in the “Printable fluid” area. This graph allow us to see in what conditions the jetting may be problematic (with a fixed size drop) and help to engineer the ink:

- When Re is too low (<1), the solutions could be to reduce the viscosity in using a co-solvent with a lower viscosity.
- When Re is too high (>20), increasing the viscosity in using a long chain glycol additive (the chemical family possesses viscosity between 10 and 50 mPa.s) is an often used solution.
- When We is too low (<4), since this number is proportional to the square to the speed this case is rarely seen, the solution being to reduce the surface tension with a non-ionic surfactant.
- For this three cases the density can be adjusted, however this will change both number at the time.

At last, it is important to note that since the density, the viscosity and the surface tension are temperature dependents it is possible to tweak the ejection parameters by adjusting the temperature of the nozzle. Indeed these three rheological parameters decrease with the increasing of the temperature, viscosity being the more sensible parameters. However, in doing so, the temperature should not be too close to the boiling point of any co-solvent which could provoke the clogging of the nozzle.

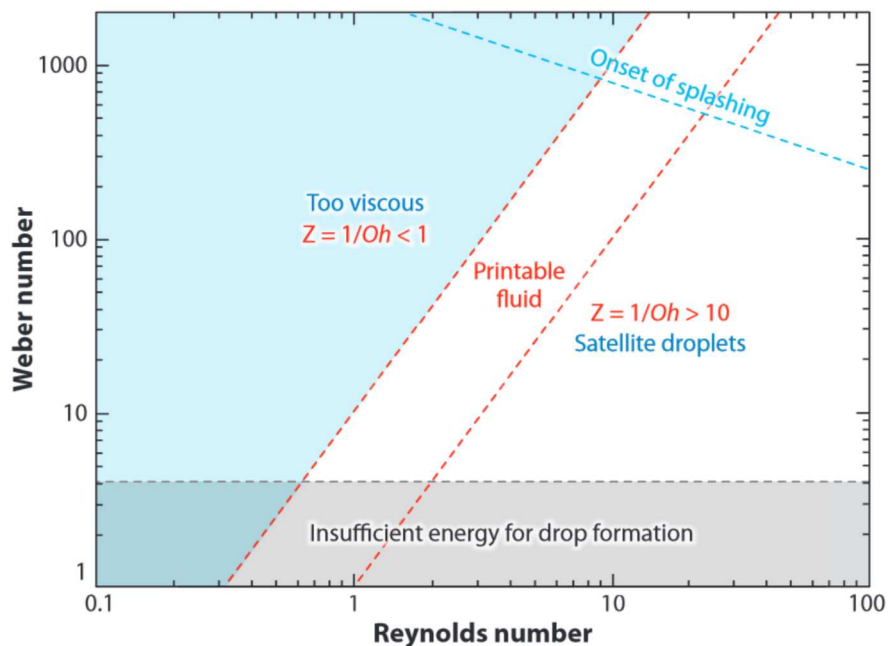


Figure II.4 - Re/We graph for ink jettability [46]

Here we see that when the Weber is very high it is possible that the drop splash instead of forming a uniform film. This splashing is due to the interaction between the arriving drop and the surface, which is the subject of the next section.

Drop/ surface interaction

For Stow & Hadfield [48] an ejected drop falling on a surface can splash when:

$$\sqrt{We} \times \sqrt[4]{Re} > 50 \tag{12}$$

This inequality can be used to determine when the speed of the jetted drop will likely provoke splashing at the surface. However please note that the empirical law was established for distilled water, more specifically for speed lower than the one attributed to inkjet ($\sim 3 \text{ m.s}^{-1}$ against inkjet jetting speed between 5 and 40 m.s^{-1}) and bigger drop than the inkjet drop (2 mm diameter against only 20 μm for inkjet drops).

Without this splashing we can determinate 3 phases describing the deposition phase of the drop on the printed surface, summarized in the Figure II.5.

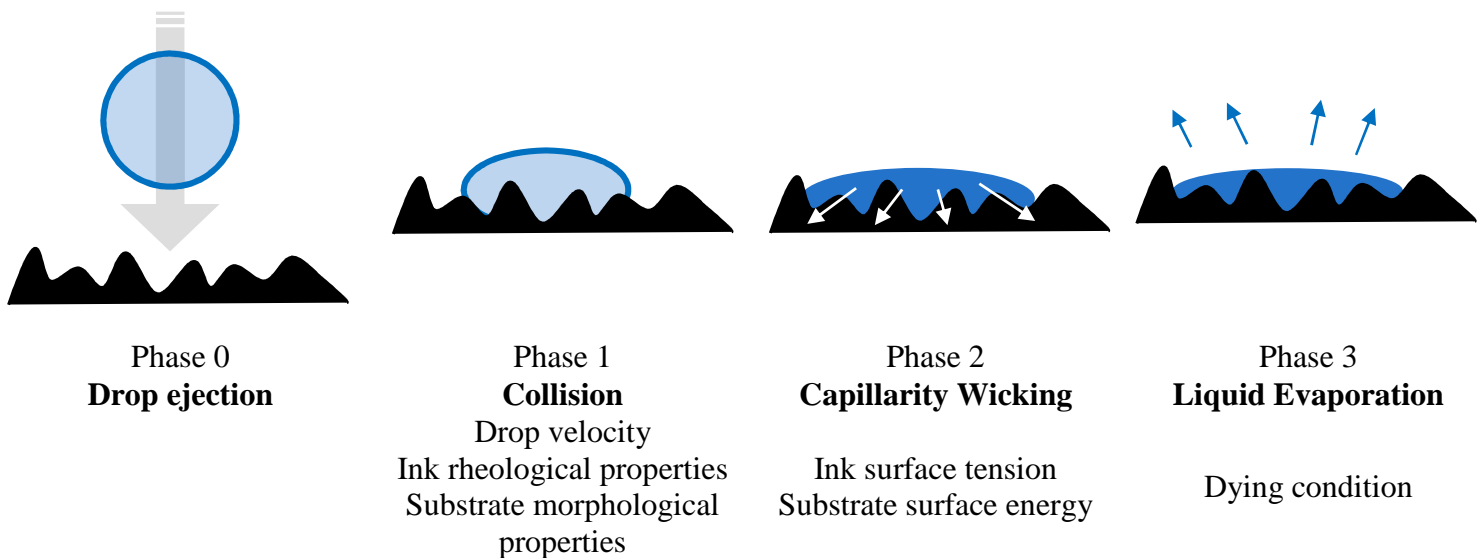


Figure II.5 - Interaction phases between drop and surface.

The phase 1, the collision, is when the splashing can occur if the roughness is too big compared to the drop size, or if the drop velocity is too high. Rheological proprieties of the ink also play an important role. If the surface tension and viscosity are too high drop may rebound or partial rebound. A low viscosity or a low surface tension will provoke the splashing as seen is the Stow & Hadfield inequality (12). A good spreading will be the result of an ink surface tension compatible with the surface energy of the surface and a viscosity suitable with the shear imposed to the drop when it collides the surface, shear related to the speed of the drop. The different collision possibilities are summarized in the Figure II.6. Please note that phase 1 could be subdivided under 3 other phases, indeed upon impact the drop is crossed by fluctuations due to residual kinetic energy and it needs some times to reach stabilization.

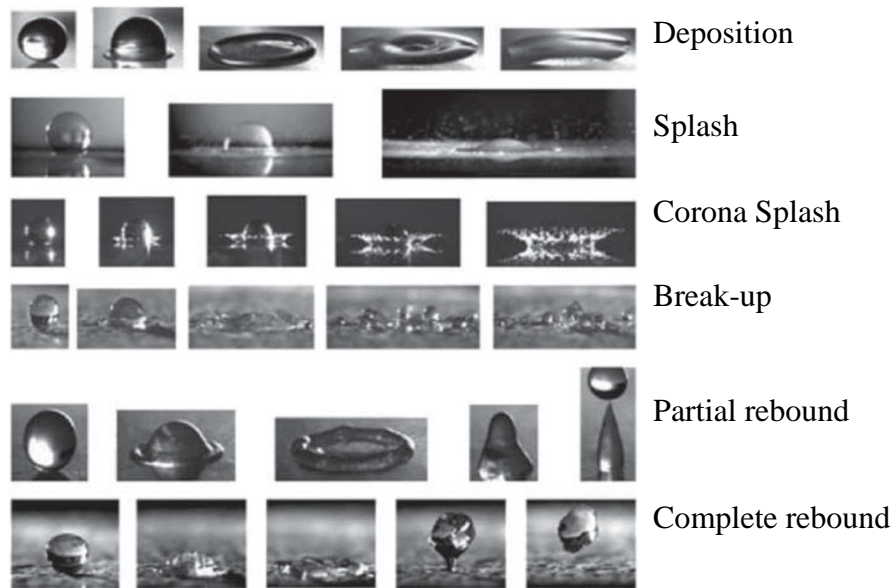


Figure II.6 - A variety liquid drop impact on to a surface [112, 45]

The phase 2 (Figure II.6) is the phase where most of the final spot size is determined. This phase is the most sensitive to the surface tension of the ink and its affinity with the surface energy. When a drop is deposited on to a surface (Figure II.7) the shape of the drop depends on the interaction energy between the surface and the liquid (γ_{LS}), between the gas surrounding the drop and the liquid (γ_L) and between the gas and the surface (γ_S). The angle θ formed by the vectors γ_{LS} and γ_L is called the contact angle and it used to determinate the quality of the wetting:

- When θ is close to 0° the wetting is complete
- Between 0 and 90° the wetting is partial
- For contact angle above 90° and lower 180° this corresponds to a partial dewetting.
- For $\theta=180^\circ$ the liquid forms a perfect spherical drop

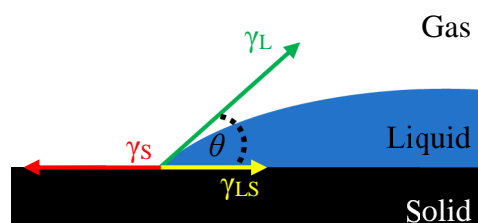


Figure II.7 - Interaction forces at the gas/surface/liquid interfaces

Depending of the intensity and the affinity of this interactions the drop will more or less be spread. The theory, and the practical measurements of the contact angle, will be presented further in the section II.3. If the substrate is porous the liquid will flow in it during this phase.

That means that if the objectives is to impregnate a substrate the liquid should be choose to avoid its premature evaporation. This phase can last from a few hundred of nanoseconds for the case of non-porous and smooth substrate, up to tenth of seconds for substrate like paper.

The phase 3 begins when the flow of liquid (parallel to the substrate or in its porous structure) has stopped. This is the drying phase, depending of the concentration in materials, the boiling point of the solvent, its vapour pressure the drying stage can take several minutes to few hours.

In order to apprehend the problematic of drying we will focus only on the evaporation of one drop containing only one liquid. As the height of liquid is maximum at the middle of the drop and decrease when approaching the edge and since the evaporation rate is the same everywhere then the drying is quicker in the edge (since there is less liquid). This phenomenon will create flows from the surface of the drop toward the edge of the drop. Depending of the evolution of the viscosity during drying these flows might be able to follow the flow of evaporation inside the drop. If not the edge will be completely dry before the rest of the drop. This can produce heterogeneous film if this situation happens relatively soon in the drying.

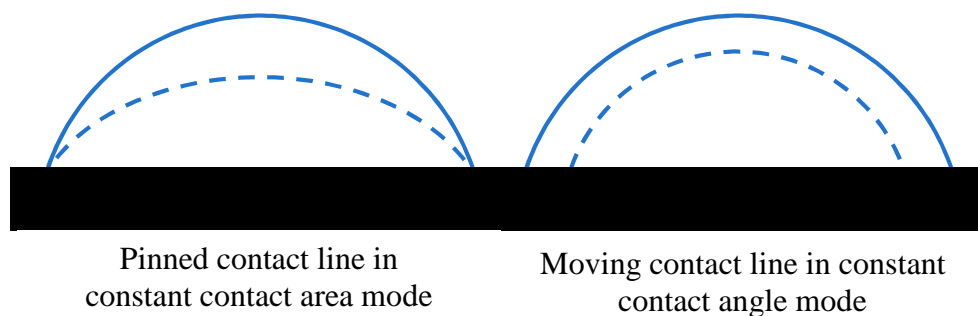


Figure II.8 - Drying mode and contact line moves

Furthermore, if the surface energy of the substrate is high the drop cannot reduce its size as the liquid dry, this is the case of the pinned contact lined with a decreasing contact angle. At the contrary when the surface energy is low the reducing size of the drop will be proceeded at constant contact angle (Figure II.8). Both can produce good homogeneous films, but, since the drop size is reduced in the second case, this can produce dewetting between droplets and at the edge of the printed layer.

2. Image management

i. Splat size and resolution

In order to control the size, thickness and shape of a printed layer the first step is to measure the size of one dry drop printed on the previous layer. This measurement is effectuated by optical microscope. This size is called the splat size. Once the splat size is known, it is possible to calculate the minimum space between each drop-centre to promote coalescence, which is equal to the diameter of one splat size.

Once established, we can calculate the resolution needed to have each drop side by side. For this resolution, the thickness of the final layer will be close to the thickness of one drop. Indeed there is no overlapping between each drop. To calculate the resolution we must calculate the number n of drop: we can take the case of one rectangle with a length of x and a height of y (Figure II.9). To print this rectangle we use drops with a splat size of $2r$, each drop being separated from another of a drop spacing of d .

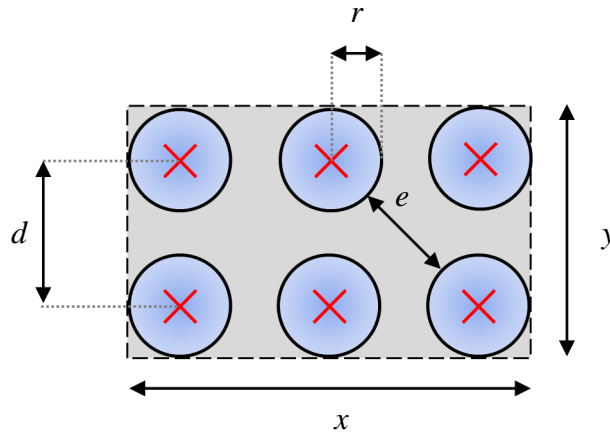


Figure II.9 - Drop disposition on a rectangle

We have then, with n_x and n_y the number of drop respectively at the length and height:

$$\begin{cases} n = n_x n_y \\ x = 2r + (n_x - 1)d \\ y = 2r + (n_y - 1)d \end{cases} \quad (13)$$

Which gives for the total number of drops:

$$n = \left(\frac{x - 2r}{d} + 1 \right) \left(\frac{y - 2r}{d} + 1 \right) \quad (14)$$

With:

$$e = \sqrt{2}d - 2r \quad (15)$$

The resolution r is usually given in dpi, (Dot Per Inch) and is calculated this way:

$$r = \frac{n_x}{x/2.54} = \frac{n_y}{y/2.54} \quad (16)$$

During printing some nozzles can clog, thus reducing the number on drop effectively deposited on the substrate. It is interesting to know how many drop were actually printed, in taking the same value for the ratio between the number of open nozzle and desired nozzle and the ration between the effectively ejected drop and the theoretical number. The drop spacing d can be adjust in a second printing to print the good number of drop, i.e. the same quantity of matter i.e. the same thickness, with less nozzle.

ii. Addressability and repeatability: conception of the image

The addressability is the minimum drop spacing possible between 2 drops (or between dots for other printing technics). When printing different colour layers in an image for a graphic objective, for example for a photography, it is very important to make sure the horizontal registering respected. Meaning that the different layers not supposed to overlap should be side by side. However, if an overlapping occurs it can be invisible for the human eye. At best, with a good contrast and luminosity, the human eye can perceive details occupying $1/3000^{\text{th}}$ radian of its field of view, which corresponds to approximately $100 \mu\text{m}$. Typically, the addressability must be around 0.1 mm for most practical application.

To print electronic devices, this horizontal registration must be taken more seriously: two layer side by side which are not meant to touch, must absolutely not touch. It could for example create short-circuit.

For the inkjet printing machines used in this thesis this minimum addressability is $5 \mu\text{m}$ [45]. These limitations must be taken into account when designing the architecture of the solar cells ought to be printed. Each pattern must be horizontally separated by at least $5 \mu\text{m}$, smaller gap cannot be fabricated and will provoke coalescence of the normally separated drops.

This position repeatability is also crucial when the objective is to print layers on top of others. Each layers must absolutely be on top of the previous, without touching for example the substrate, or even more seriously, the layer beneath the layer on which the printing is done. The Dimatix Materials Printer DMP-2850 has a repeatability of $\pm 25 \mu\text{m}$ between layers of different materials. This repeatability must be taken into account for the design of patterns of different layers printed side by side, the gap between them must be at the minimum of $50 \mu\text{m}$. This also

means that superposing layer will not be perfectly superposed and two layers separated by a third layers can come in contact. One strategy is to print smaller layer as the layers superposed layer after layer, but this is not always possible.

3. Characterisations

i. Surface Energy

Surface energy is a broadly researched topic [49] : inside a phase (solid, liquid or gas) every molecules endures the attraction from the other molecules surrounding here. The molecules pushed away from one another by the thermal agitation, in the overall phase all movements cancel each other statistically.

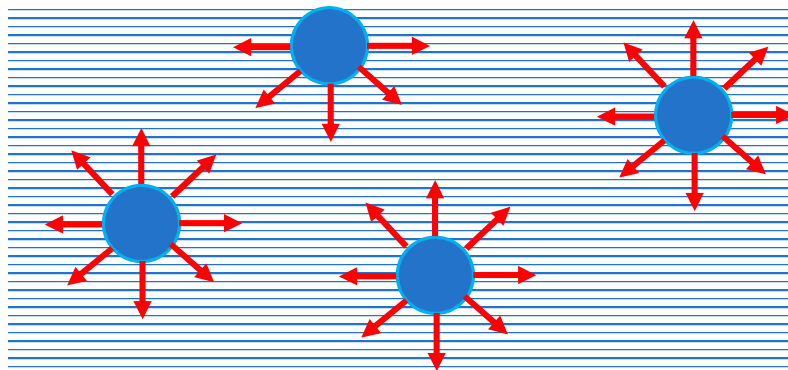


Figure II.10 - Schematic reorientation of the forces acting on the internal and superficial molecules

At the contrary at the surface of the phase each molecules endures an asymmetric pull toward the interiors of the phase, the attraction toward the exterior is weak. Therefore, the phase will tend to minimize the energy of the interface with the other exterior phase, to form a sphere as seen with liquid in zero gravity condition. In reality the Brownian movement, and the different flows in the phase (if the phase is a liquid or a gas), imply that the surface is continuously renewed by different molecules. This energy is the cohesion energy that allow a liquid phase to keep its integrity. It is usually expressed in $\text{mN}\cdot\text{m}^{-1}$ and can be interpreted as the force needed to break a film of a certain length of this liquid.

For a solid the dangling bonds at the surfaces, the morphological defaults, the crystalline structure and other external graft specie are all kind of sources of this surface energy representing the abilities that the solid has to stick to liquids.

Young equation

For a drop deposited on to a surface (Figure II.7) its shape depends on the interaction energy between the surface and the liquid (γ_{LS}), between the gas surrounding the drop and the

liquid (γ_L) and between the gas and the surface (γ_S). The angle θ formed by the vectors γ_{LS} and γ_L is called the contact angle and it used to determinate the quality of the wetting. When the thermodynamic equilibrium state is reached it is possible to write the Young equation :

$$\begin{aligned}\vec{\gamma}_S + \vec{\gamma}_{LS} + \vec{\gamma}_L &= 0 \\ \gamma_S &= \gamma_{LS} + \gamma_L \cos \theta\end{aligned}\quad (17)$$

From this equation is possible to predict the wettability of a specific liquid on a specific surface in calculating the angle θ (Figure II.7), thanks to the already known values of γ_L of specific liquid (water, ethylene glycol and diiodomethane) and of γ_S of specific surfaces. The calculation of surface energy is possible from the measurements of contact angle. Here will be presented one method of calculation.

Owens-Wendt-Rabel and Kaelble method

In this method, the liquid/solid interface energy value can be calculated from the value of surface energy of the solid and tension surface of the liquid and with the polar and dispersion component of each of these two energy, the formula being:

$$\gamma_{LS} = \gamma_L + \gamma_S - 2 \left(\sqrt{\gamma_L^P \gamma_S^P} + \sqrt{\gamma_L^D \gamma_S^D} \right) \quad (18)$$

The dispersive component γ_i^D takes into account the electrostatic attraction, H-H, van der Walls bounding for example, the polar γ_i^P component represents the attraction due to the polar nature of the molecules of the solid and the liquid.

When using the equation (17) with the equation (18) we have:

$$\gamma_{LS} = \gamma_L + \gamma_S - 2 \left(\sqrt{\gamma_L^P \gamma_S^P} + \sqrt{\gamma_L^D \gamma_S^D} \right) \quad (19)$$

With:

$$\gamma_i = \gamma_i^D + \gamma_i^P \quad (20)$$

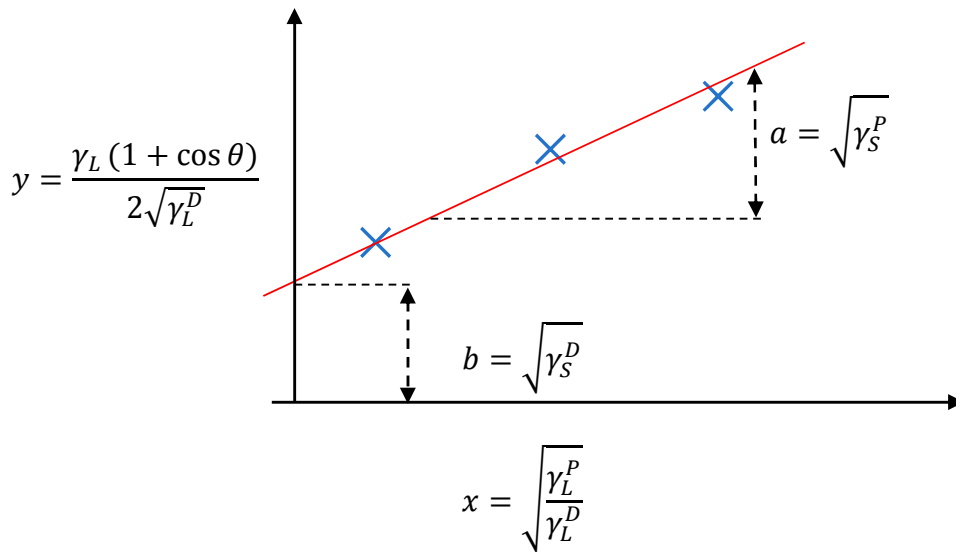
From the equations (17) and (19), we found:

$$\gamma_L (1 + \cos \theta) = 2 \left(\sqrt{\gamma_L^P \gamma_S^P} + \sqrt{\gamma_L^D \gamma_S^D} \right) \quad (21)$$

This equation allows to compute γ_S of a specific solid in measuring the contact angle of the drops of 3 different known reference liquids deposited on the substrate. Alternatively it is possible to calculate γ_L with the use of 3 different known reference substrate. The method is to express the precedent equation under the $y=ax+b$, for computing γ_S we have:

$$\frac{\gamma_L (1 + \cos \theta)}{2\sqrt{\gamma_L^D}} = \sqrt{\gamma_S^P} \times \sqrt{\frac{\gamma_L^P}{\gamma_L^D}} + \sqrt{\gamma_S^D} \quad (22)$$

After having measuring the contact angle is it possible to draw the $y=f(x)$ graph with 3 points (the 3 different reference liquids), and to extract a and b with a linear regression:



For computing γ_L we have:

$$2\sqrt{\frac{\gamma_S^D}{\gamma_S^P}} = \frac{\gamma_L}{\sqrt{\gamma_L^D}} \times \frac{1 + \cos \theta}{\sqrt{\gamma_S^P}} - 2\sqrt{\frac{\gamma_L^P}{\gamma_L^D}} \quad (23)$$

With :

$$y = 2\sqrt{\frac{\gamma_S^D}{\gamma_S^P}} \quad a = \frac{\gamma_L}{\sqrt{\gamma_L^D}} \quad x = \frac{1 + \cos \theta}{\sqrt{\gamma_S^P}} \quad b = -2\sqrt{\frac{\gamma_L^P}{\gamma_L^D}}$$

Wettability envelop

The wetting envelop is a graph which is used to determine which kind of liquid will have a perfect wettability on a specific surfaces. This is the condition when $\theta=0$, so from the equation (21) we obtain:

$$\gamma_L^D + \gamma_L^P = \sqrt{\gamma_L^P \gamma_S^P} + \sqrt{\gamma_L^D \gamma_S^D} \quad (24)$$

The polar and dispersive components of the liquid surface energy can be used in a coordinate system as functions. Hence, we have for the R parameter for the geometric consideration:

$$R = \sqrt{(\gamma_L^D)^2 + (\gamma_L^P)^2} \quad (25)$$

$$R \cos \varphi = \gamma_L^P \quad (26)$$

$$R \sin \varphi = \gamma_L^D \quad (27)$$

In putting the equations (26) and (27) into the equation (24), we have:

$$R \cos \varphi + R \sin \varphi = \sqrt{R \gamma_S^D \cos \varphi} + \sqrt{R \gamma_S^P \sin \varphi} \quad (28)$$

When this equation is resolved to express R as function of φ we find:

$$R(\varphi) = \left(\sqrt{\gamma_S^D \cos \varphi} + \sqrt{\gamma_S^P \sin \varphi} \right) / (\cos \varphi + \sin \varphi) \quad (29)$$

As the polar and dispersive components cannot be negative we consider only the value of φ between 0° and 90° . Finally we have these two expressions for the dispersive and polar components.

$$\gamma_L^P = \cos(\varphi) \times R(\varphi) = \cos \varphi \times \left[\left(\sqrt{\gamma_S^D \cos \varphi} + \sqrt{\gamma_S^P \sin \varphi} \right) / (\cos \varphi + \sin \varphi) \right] \quad (30)$$

$$\gamma_L^D = \sin(\varphi) \times R(\varphi) = \sin \varphi \times \left[\left(\sqrt{\gamma_S^D \cos \varphi} + \sqrt{\gamma_S^P \sin \varphi} \right) / (\cos \varphi + \sin \varphi) \right] \quad (31)$$

The obtained graph is represented in the Figure II.11, here the liquid 1 will wet correctly the surface while the liquid 2 will provoke a dewetting:

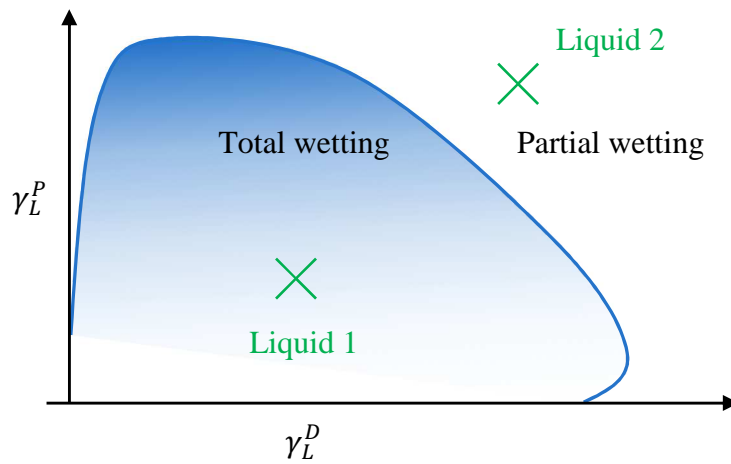


Figure II.11 - Wetting envelop look

ii. Surface tension

To measure the surface tension of a liquid the most used technique is the pendent drop method (Figure II.12). The setup is to capture the image of a drop pending from a vertical needle on a syringe, the drop is formed by the pressure of the piston. When the drop is the heavier possible, that is to say just before it falls, the capture is taken and the edge of the drop is numerically analysed.

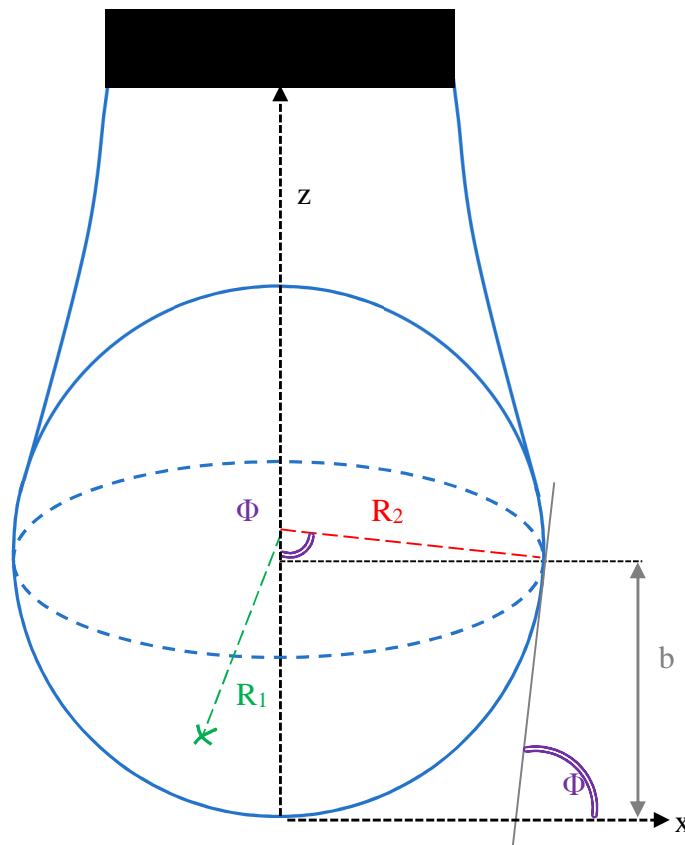


Figure II.12 - Drop schematisation for surface energy measurement

The analysis method is to determine the half bottom part of the drop forming a perfect hemisphere. This hemisphere has a height named b in (Figure II.12) and surface at its maximum height forms an angle Φ with the horizontal. The angle is reported to determine the radius R_2 between the any points of top of the hemisphere and the vertical axis of the drop and to the radius R_1 between any points of the hemisphere (excepted at the top) and the vertical axis. Of course when Φ approaches 90° the value of R_1 and R_2 are the almost the same and the bottom of the drop forms a perfect hemisphere.

The difference of pressure between the two phases, the liquid and the atmospheres, separated by a curved interface is given by the Young-Laplace equation, in function of the surface tension γ :

$$\Delta P = P_{int} - P_{ext} = \gamma \left(\frac{1}{R_1} + \frac{1}{R_2} \right) \quad (32)$$

At the vertex (lowest point of the drop) the shape of the drop can be approach as being a perfect sphere, therefore $R_1=R_2=R$:

$$\Delta P_0 = \frac{2\gamma}{R} \quad (33)$$

From Pascal law along the z axis where $\Delta\rho$ is the difference between the densities of the two phases in contact, we have:

$$\Delta P(z) = \Delta P_0 \pm \Delta\rho g z = \frac{2\gamma}{R} + \Delta\rho g z \quad (34)$$

From every point above the vertex we have $R_2=x/\sin \Phi$, from the equation (32) it gives:

$$\frac{\Delta P}{\gamma} = \frac{1}{R_1} + \frac{\sin \Phi}{x} \quad (35)$$

The equality of the equations (34) and (35) leads to:

$$\frac{1}{R_1} = \frac{2}{R} \pm \frac{\Delta\rho g z}{\gamma} - \frac{\sin \Phi}{x} \quad (36)$$

With this equation it is possible to calculate γ from the shape analysis of the drop, and from the known density of each phases.

iii. Viscosity

Definition

The viscosity is the propriety of a fluid to resist to shear stress and flow. This measurable physical value is called the dynamic viscosity η and corresponds to the shear stress when a shear rate to the fluid.

The dynamic viscosity η can be defined in the ideal situation where the fluid is trapped between two horizontal plate, one is fixed the other is moving horizontally with a constant speed u (the Couette flow, Figure II.13).

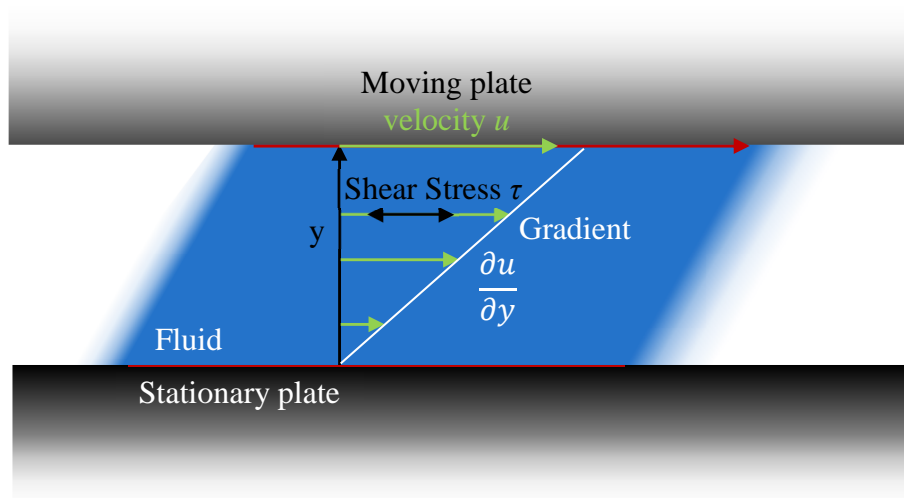


Figure II.13 - Laminar shear of fluid between two plates: Couette flow

Here, each layer of the fluid will flow slower than the one on top of it: friction between them will provoke resistance against their relative motion. Therefore a force F applied on the top plate is needed to keep it in motion, it is proportional to the contact area A between the plate and the fluid:

$$\vec{F} = \eta A \frac{\partial \vec{u}}{\partial y} \quad (37)$$

Fluids with a fixed value of dynamic viscosity, meaning that η is independent from $\frac{\partial \vec{u}}{\partial y}$ (rate of shear strain), are called Newtonian fluids. Most inkjet ink are Newtonian but some are none. The shear-thickening will have a viscosity increasing with a shear strain, contrary to the shear-thinning fluids. Thixotropic fluids become less viscous after a certain time of stressing (contrary to the rheopectic), this is the case of liquids containing particles with a high aspect ratio (solutions with long polymer chains for example).

Measurements

For the viscosity measurements of the ink used in this theses we used an *A&D SV-A series Tuning Fork Vibro Viscosimeter* [50]. Two thin parallel plates are forced to vibrate at their resonant frequency of 30 Hz within the sample fluid. Viscosity is then calculated based on the proportional relationship between the viscous resistance of the sample fluid and the amount

of electric current required to maintain the sensor plates at a constant vibration. The advantage is that this measurement needs only 2 ml of the solution. The drawback is that this measurement is performed under fixed shear strain, we must assumed that the tested inks are Newtonian.

iv. Measurement of the bulk density

As there is no access to measure the density of a fluid a methodology has been designed by using water, a micro-balance and a pipette:

- The first step is to measure the temperature of the water and to determine the density of water thanks to reference table
- With the pipette set on a 100 μl volume water is taken and weighted several times
- The correct value of taken volume of water is calculated from the mean value of measured water and the reference density of water
- With the pipette set on a 100 μl volume the liquid to measure is taken and weighted several times.
- From the correct value of taken volume and the correct value of weight of the liquid to measure the density is calculated by divided the weight by the volume (kg/m^3).

v. Photovoltaic

JV characterisation

Through the imposition of a voltage sweep and the measurements of the photocurrent of a solar cell it is possible to obtain different electronic parameters. During this measurement the solar cells is exposed to a simulated solar light. This simulated solar light is provided by a lamp equipment and the emitted light spectrum follows the AM 1.5 G norm, its illumination power P_{lum} is of $100 \text{ mW}\cdot\text{cm}^{-2}$. This spectrum corresponds to the actual solar spectrum light received on earth surface at a 45° latitude as represented as AM 1.5 Global curve in the Figure II.14.

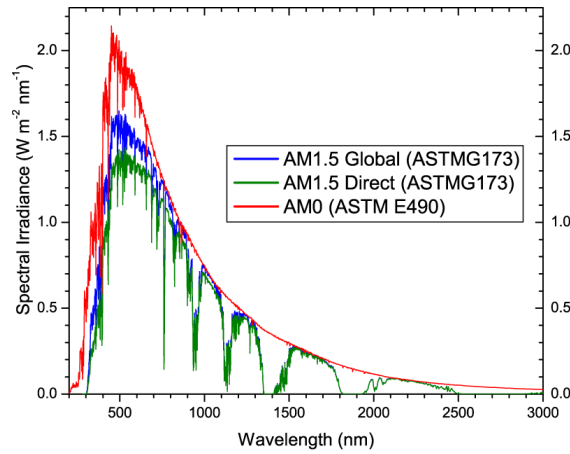


Figure II.14 - The AM1.5 Global spectrum is designed for flat plate modules, AM1.5 for solar concentrator, the AM0 is the extraterrestrial solar spectra

From the JV curve the short-circuit current J_{SC} and the open-circuit voltage V_{OC} can be easily extracted, as well as the point of maximum power P_{max} . The Power Conversion Efficiency (PCE) or efficiency η is expressed in percentage, A being the surface area of the solar cell:

$$PCE = \frac{P_{max}}{P_{lum} \times A} \times 100 \quad (38)$$

The fill factor (FF) can be also calculated and is expressed in percentage. The higher the value of FF is the more ideal is the tested solar cell, low FF means that the cells might have current leaks, charge recombination. It could be due to bad quality of material, charge being stocked at the interface for example, it is a great indicator of the overall quality of the cell.

$$FF = \frac{P_{max}}{J_{SC} \times V_{OC}} \times 100 = \frac{J_{max} \times V_{max}}{J_{SC} \times V_{OC}} \times 100 \quad (39)$$

From the value of the slope of the $J(V)$ curve at V_{OC} and J_{SC} it is possible to calculate respectively the series resistance R_S and the shunt resistance R_{SH} .

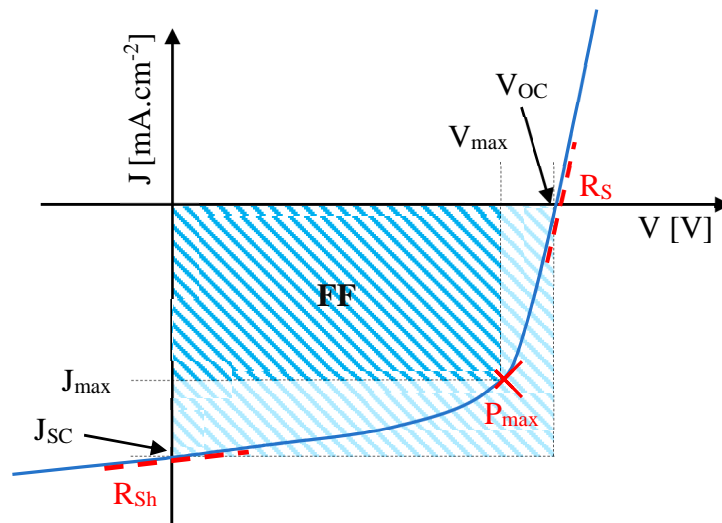


Figure II.15 - $J(V)$ curve schematic representation of an illuminated photovoltaic cell

The JV measurement can be done with two voltage sweep directions: in the *forward* scan the scan is proceed from the negative voltage to the positive voltage, the *backward* scan is done from the positive bias to the negative bias. In the case of the perovskite solar cell the photovoltaic performances are most often determined in the JV backward scan. More explanation about this will be given in the section III.1. **Erreur ! Source du renvoi introuvable.** about electrical measurement parameters. During these measurements the cell was masked in order to correctly determine the surface area and not to make any errors in the current density. Furthermore the intensity of light is adjusted by using a mismatch factor to compensate the discrepancy between the simulated spectrum of the solar lamp and the spectrum of the sun.

IPCE

Incident photon to converted electron (IPCE) is the method to analyse the efficiency of photovoltaic solar cell. The objective of the measurements is to know the efficiency of conversion of the energy of each photon onto electrical energy. In this experiments a monochromatic filter (with a xenon white lamp) isolate each wavelength, the shape of the illuminated zone on the photovoltaic cell is a small area of roughly 2 mm of diameter. The illumination power is first measured before the actual measurements with a silicon calibration cell whose wavelength sensibility is known. With this calibration the power of illumination P_{lum} of each wavelength is known. From the calibration and the measurements of the electric power P_{elec} for each wavelength we have:

$$ICPE(\lambda) = \frac{P_{elec}(\lambda)}{P_{lum}(\lambda)} = \frac{R}{hc/\lambda} \times \frac{\left(q \times \frac{electrons}{cm^2.s}\right)^2}{\frac{photons}{cm^2.s}} \quad (40)$$

With the R the impedance of the measuring instrumentation, q the charge of an electron, h the Planck constant, c the light velocity. The boundary of the wavelength are adjustable as well as the delay between each wavelength and the bandwidth $\Delta\lambda$.

Mismatch factor

As the spectrum of the solar simulator is not perfectly the same as the true solar irradiance spectrum the evaluation the PCE of a solar cell can be over or under estimated. Furthermore, the $IPCE(\lambda)$ depends of the illumination wavelength which increases the discrepancy between the measured PCE and the true PCE. A methodology has been designed to control and compensate this discrepancy [51, 52, 53].

The solution to correct this imprecision is to equalize the photogenerated current under the theoretical AM 1.5 G spectrum and the same current under the used solar simulator:

$$ICPE(\lambda) = \frac{I_{cell}^{SoSim}}{I_{cell}^{AM1.5G}} = \frac{\int E_{SoSim} S_{cell} d\lambda}{\int E_{AM1.5G} S_{cell} d\lambda} = 1 \quad (41)$$

Where :

- E_{SoSim} is the irradiance spectrum of the used solar simulator
- $E_{AM1.5G}$ is the irradiance spectrum of the sun for the AM 1.5G norm.
- S_{cell} is the sensibility of the solar cell to characterize

This condition happens in evaluating the mismatch factor M , which takes into account another term, S_{ref} , the sensibility of the calibration device sensor:

$$M = \frac{\int E_{AM1.5G} S_{ref} d\lambda}{\int E_{SoSim} S_{ref} d\lambda} \times \frac{\int E_{SoSim} S_{cell} d\lambda}{\int E_{AM1.5G} S_{cell} d\lambda} \quad (42)$$

The computing of the M factor (for one system constituted of one cell, one calibration sensor and a solar simulator) allows to correct the calibration of the solar simulator in order that the illumination power received by the solar cell is close from the one delivered by the AM1.5G irradiance spectrum.

III. Toward a low annealing printable perovskite solar cell

1. The reference and non-printable perovskite solar cell

i. Objectives, strategy

The industrialisation and commercialisation of a new photovoltaic technology require that it presents a high efficiency, a good stability and a low cost of fabrication. The perovskite solar cells match the first requirements and the second point is the subject of several studies across the world. The third point is important to consider for the case of disposable autonomous sensors.

The strategy of this thesis has been to develop a protocol for the printing of the PSC starting from a speciality of the laboratory XLIM: the DSSCs made from TiO₂ electron transporting layer (ETL). This structure is called “direct architecture” [54]. From this technology the strategy is to replace the non-printable layer by printable and low-temperature annealable layers. In order to facilitate the printing step of the perovskite solar cells the inner layers (ETL, perovskite and HTL) was designed to be fabricated by exclusively liquid solution with one deposition for each layer. For the perovskites it is possible to use different approach, for example via evaporation or chemical deposition, or with liquid deposition in two step [34] (see section IV.4.iv).

The comparison of the PSC performances is not easy: there are a lot of different perovskite solar cells version, direct or indirect architecture, with or without mesoporous TiO₂, with or without chlorine or with different solvent, concentration, additives etc.. In the literature, the cell architecture which was the closer of the one of our cells was the one of Wojciechowski et al. [55]: the best PCE obtainable is around 15.9 %, this corresponds to a V_{oc} of 1 V, a J_{sc} of 21.5 mA.cm⁻² and a 71 % FF, for a 10 mm² solar cell.

ii. Architecture

The first cells produced were composed of an electrode in FTO, of a dense TiO₂ as ETL, CH₃NH₃PbI₃ perovskite as absorbent layer, Spiro-OMeTAD as HTL and gold as top electrode. The first results were not as good as expected: the solar cells were shunted. After having add a TiO₂-mesoporous layer (TiO₂-mp) and changed the CH₃NH₃PbI₃ perovskite for CH₃NH₃PbI_{3-x}Cl_x (Figure III.2) we obtained our first working cells, and this is the same architecture that we kept as a reference for most of the comparisons.

In this direct architecture the cell is illuminated from the back electrode in FTO, having firstly cross through the glass substrate. The light then goes through the two ETL layers of TiO_2 to be absorbed by the hybrid photovoltaic (Figure III.2). The band gap of the $\text{CH}_3\text{NH}_3\text{PbI}_{3-x}\text{Cl}_x$ perovskite is of 1.7 eV, with an electronic affinity and an ionization potential respectively at -3.7 eV and -5.4 eV [24]. Each absorbed photon will provoke the promotion of one electron in a higher energy band, creating one electron-hole pair. The hole is extracted by the hole-transporting layer Spiro-OMeTAD valence band (-5.22 eV [19]), since it cannot go to the one of TiO_2 which is too high. The electron is transported toward the FTO electrode by the TiO_2 layer (-4.2 eV [19]).



Figure III.2 - Schematic representation of the TiO_2 reference perovskite solar cell direct structure

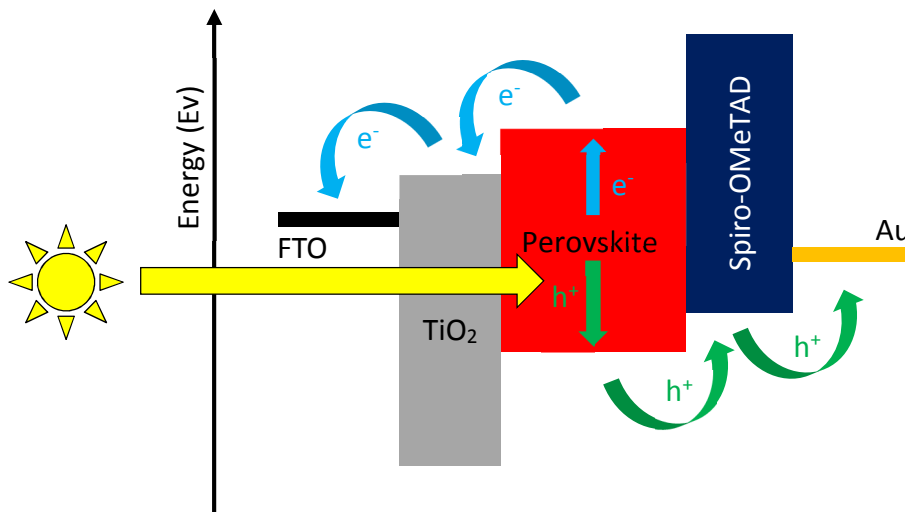


Figure III.2 - Working principle of perovskite solar cell in direct architecture

This first PCE were around 0.14 %. It was very low but we knew that we were on the good path since we got our first photoconversion, this convinced us that the overall architecture was correct but architecture defect, or bad post treatment (for example annealing of the layer), was responsible of this low PCE. One of the most important aspect to look upon is the way the

layers are stacked, each layer must be in contact with the previous one and the next one but should never touches the other layers. This will provoke recombinations between holes and electrons. After few adjustments on the architecture, with bigger overlapping layer to protect the previous one the PCE was enhanced to 0.74 %. The final architecture of a 20 mm² active area perovskite solar cell is presented in Figure III.3.

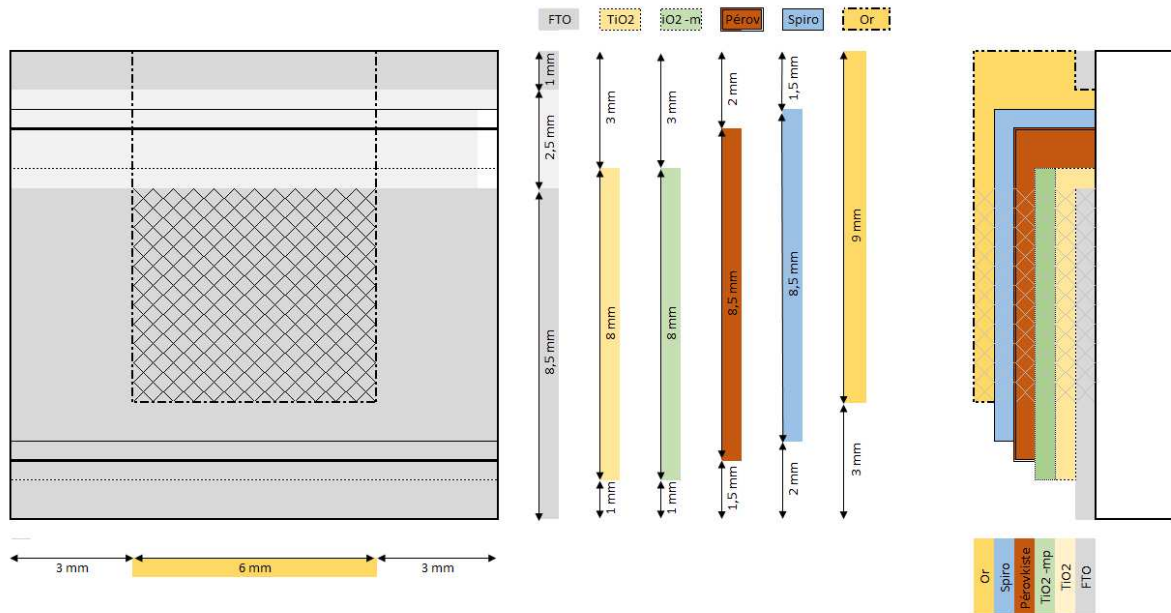


Figure III.3 - TiO₂-based perovskite solar cell fabrication design (vertical scale not respected)

iii. Best results

After much improvements, particularly in the perovskite spincoating and annealing conditions and in the post-treatment of the TiO₂ (explained further in the III.1.iv. section), and a better master of the overall production the best result obtained was a PCE of 15.3 %. The FF was of 68 %, while the V_{oc} was at 949 mV and the J_{sc} at 23.6 mA.cm⁻². The JV curve of this best cell is represented in Figure III.4, and its aspect is in Figure III.7. The JV measurements conducted under dark conditions (Figure III.5) highlights the quality of the TiO₂-based PSC with no current until 650 mV. The performances of this best solar cell are very close to the maximum performances for this kind of architecture when comparing to the typical result of the literature. The evolution of the TiO₂-based PSC performances through time is presented in Figure III.6.

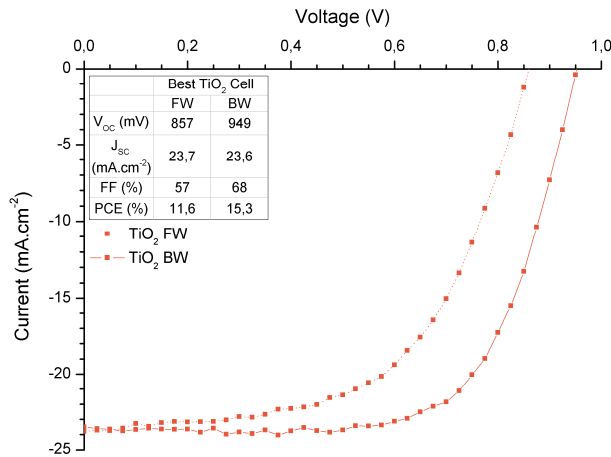


Figure III.4 - JV curves of the best TiO₂-based PSC : backward (BW) measurements is from 1.5 V to -0.1 V and forward (FW) is from -0.1 V to 1.5V

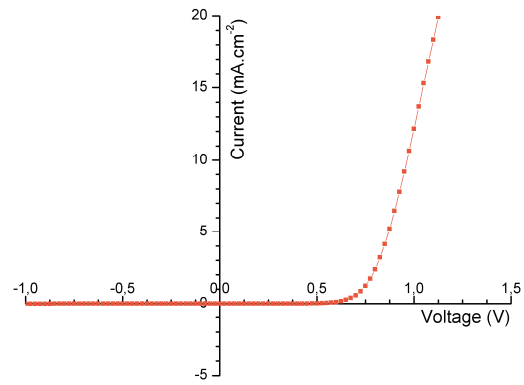


Figure III.5 - JV curve in dark of a perovskite solar cell

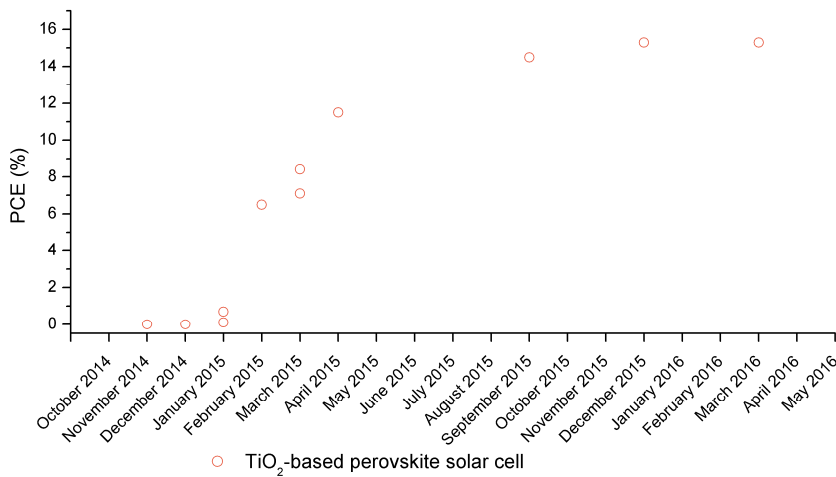


Figure III.6 - PCE evolution of the best perovskite solar cells

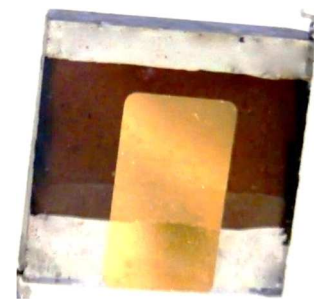


Figure III.7 - A TiO₂-based perovskite solar cell

From this point we can compare this 15.3 % performances with the objectives of the Table I.1. The photovoltaic parameters of the TiO₂-based perovskite solar cells are superior to the objectives. The open-circuit voltage is 14 % higher than the voltage objectives. The short-circuit current, which is the most important parameter to charge the batteries, is 47 % higher than the one of the objectives. The result is a very high PCE compared to the objectives.

For each batch of produced TiO₂-based perovskite solar cells not all perovskite solar cells will be at this maximum of 15.3 %, the repartition of the performances will be in reality between 7 % and this maximum of 15.3 % PCE. It happens that one or two cells of a batch of 12 cells presented a short circuit. Furthermore, some batches will be better than others and the mean PCE of each batch can be greatly different from another.

To have a better idea of which value of PCE that can be expected when producing TiO₂-based perovskite solar cells we computed the photovoltaic performances of an “**Average best TiO₂ cell**”. This mean value takes into account all the cells produced with a PCE higher than 9 % (in backward measurements). The chosen value of 9 % is arbitrary. We think that a PCE over 9 % means that the perovskite solar cell is working properly, furthermore, every time a batch of TiO₂-based PSC produced working solar cells (some batch produced just non-working cells) the minimum PCE of working solar cells was around 9 % (non-working solar cells are still present, yet). The mean PCE of the average best TiO₂-based PSC is 10.2 %, the mean J_{sc} is 19.01 mA.cm⁻², the mean V_{oc} is 860 mV, and the mean FF is 64 %, there are summarized and compared with the objectives in the Table III.1. In a controlled environment with an industrial fabrication method these are the value that can be expected at the minimum for this kind of TiO₂-based PSC.

	OBJECTIVES	BEST TiO ₂ CELL	AVERAGE BEST TiO ₂ CELLS
Photovoltaic parameters			
V _{oc} (mV)	830	949	850 (± 6)
J _{sc} (mA.cm ⁻²)	16	23.6	19.21 (± 3.11)
FF (%)	75	68	64 (± 9)
PCE (%)	10	15.3	10.26 (± 1.73)
Fabrication			
Active area	1 cm ²		20 mm ²
Electrode (ITO or FTO)	Non-printable		Non-printable
ETL	Printed		Non-printed
Perovskite	Printed		Non-printed
HTL	Printed		Non-printed
Top electrode	Printable		Non-printable
Max annealing temperature	130°C		450 °C

Table III.1 - Comparison between the objectives and the TiO₂-based perovskite solar cell

As it is, the TiO₂ PSC are already completing the photovoltaic parameters objectives. They can produce enough power to supply in energy an autonomous sensor. The effort must be now focused on the fabrication steps. Only the perovskite layer and the HTL are printable and annealable below 130 °C: the TiO₂ is here the principal issue as it is not easily jettable (particularly the mesoporous TiO₂), but the most important aspect is that it must be annealed at 500 °C. The second issue is the size of the cell which is 5 times smaller than wished.

iv. Fabrication

This section presents first the protocol to produce TiO₂-based PSC, which is used as a reference cell. Then follow different aspects about this fabrication.

Protocol

In this section the fabrication of reference TiO₂-based perovskites solar cell will be detailed.

Three days before the spincoating of the TiO₂ layers the dense TiO₂, the mesoporous TiO₂ and the Spiro-OMeTAD solutions are prepared as follow:

The dense TiO₂ solution is prepared with 15.4 µl of titanium (IV) isopropoxide in 1 ml of ethanol, then 1 µl of HCl 37 % (one little drop) is added and the solution is put to be stirred until its use. The mesoporous-TiO₂ solution is prepared with 210 mg of mesoporous TiO₂ paste [56] in 700 mg of ethanol, the solution is then put to be stirred until its use. For the Spiro-OMeTAD solution, in a nitrogen glovebox 106 mg of Bis(trifluoromethane)sulfonimide lithium salt (Li salt) is added in 200 µl of acetonitrile. Separately, in ambient condition, 73.2 mg of Spiro-OMeTAD is added to 1 ml of chlorobenzene, then 17.5 µl of the lithium salt/acetonitrile solution is added followed by 28,8 µl of 4-tert-Butylpyridine (tBP). This yellow-coloured solution is then put to be stirred up until its use. Before their spincoating the dense TiO₂ solution and the Spiro-OMeTAD must be filtered with a 0.2 µm PTFE filter.

For the FTO etching the first step is to cover the non-etched parts (8.5 mm on the bottom, and 1 m at the top, as figured in the Figure III.3) with duct tape. Then a cotton buds impregnated with a 37% HCl water solution is covered with zinc powder. The cotton buds is rubbed on the non-covered part of the FTO, the FTO layer takes a brown colour then after a few rubbing the rubbed part become transparent again, the etching is finished. The substrate is immediately soak in water to stop the chemical reaction. The duct tape is removed and the substrate is cleaned in acetone, iso-propanol then ethanol in an ultrasonic bath during 20 min for each solvent.

The day of the spincoating of the TiO₂ layers a 70°C solution of TiCl₄ is prepared in adding 220 µl of TiCl₄ in 100 ml of distilled water at 5°C and then mixing it with 100 ml of distilled water à 100°C. The produced solution must be clear, like water, any slight white tint indicates a bad preparation.

Just before the deposition of the first TiO₂ layer the FTO surface of the substrates is treated by UV/ozone during 20 minutes. The TiO₂ spincoating on FTO is then proceed at 4000

rpm (rotations per minute), with an acceleration of $1000 \text{ rpm}\cdot\text{s}^{-1}$, for 10 seconds. The layer is partially removed at both side of the cell by using a swab and ethanol and annealed at 450°C during 20 minutes, once cooldown the substrates are put in 100 ml of the TiCl_4 solution at 70°C during 30 minutes, then rinsed with water and ethanol and annealed at 450°C for 20 minutes. The resulting thickness is 15 nm (measured by ellipsometry).

The mesoporous TiO_2 is spincoated at 5000 rpm ($2000 \text{ rpm}\cdot\text{s}^{-1}$) during 60 seconds. The layer is partially removed at both side of the cell by using a swab and ethanol. The layer is then annealed at 325°C for 30 minutes, then at 375°C for 5 minutes, then 450°C for 15 minutes and finally 500°C for 30 min. Once cooldown the substrates are put in 100 ml of the TiCl_4 solution at 70°C during 30 minutes, then rinsed with water and ethanol and annealed at 450°C for 20 minutes. The thickness of the mesoporous layer is of 250 nm (measured by ellipsometry and profilometry).

The day of the spincoating of the perovskite the perovskite solution is prepared in adding 252 mg of methylammonium iodide ($\text{CH}_3\text{NH}_3\text{I}$, $158.9 \text{ g}\cdot\text{mol}^{-1}$, MAI) in 600 mg of N,N-Dimethylformamide ($0.948 \text{ g}\cdot\text{mol}^{-1}$, DMF). Once the MAI is correctly dissolved in the DMF, 147 mg of PbCl_2 ($278.2 \text{ g}\cdot\text{mol}^{-1}$) and 5.4 μl of diiodooctane ($\text{ICH}_2(\text{CH}_2)_6\text{CH}_2\text{I}$, $1.84 \text{ g}\cdot\text{ml}^{-1}$, DIO) are added. The solution is stirred during at least 1 hour at 90°C . The resulting solution has a weight concentration in perovskite of 40 %, and a weight concentration of DIO of 1 %. The molar ratio between MAI and PbCl_2 is 3:1, thus to benefit the formation of $\text{CH}_3\text{NH}_3\text{PbI}_{3-x}\text{Cl}_x$ with the lower x (i.e. the lowest amount of chlorine).

Before the spincoating the TiO_2 coated substrates are heated to 90°C as well as the 0.2 PTFE filtered perovskite solution. The spincoating is proceed under nitrogen atmosphere: 5000 rpm, with a $2000 \text{ rpm}\cdot\text{s}^{-1}$ acceleration, for 20 seconds. Then the substrate rests motionless in the spincoater, under nitrogen atmosphere, for 20 seconds. The perovskite layer is then directly annealed under ambient atmosphere at 90°C for 2 hours. 15 minutes before the end of the annealing the layer is removed from each side of the cell by using a swab and DMF while the substrate are still on the hot-plate. On top of the perovskite layer (once the substrate is cooled) the filtered Spiro-OMeTAD is spincoated at 2000 rpm ($2000 \text{ rpm}\cdot\text{s}^{-1}$) during 20 seconds. The layer is removed from each side of the cell by using a swab and chlorobenzene. The thickness of the perovskite and Spiro-OMeTAD layer is difficult to measure because the mesoporous TiO_2 is very rough and porous, as well as the perovskite layer itself. The perovskite layer has a thickness of around 200 nm and the thickness of Spiro-OMeTAD is around 100 nm (measured

with a profilometer on glass). Under a 10^{-6} mbar vacuum a 100 nm thick gold electrode is evaporated at $0.1 \text{ \AA}\cdot\text{s}^{-1}$.

Ambient condition effects: N₂

As seen in the protocol of the previous section the spincoating phase is processed under N₂ atmosphere. A commercial perovskite solution (with a composition very close of what we used thereafter) [57] was spincoated to produce TiO₂-based PSC. For 3 cells the perovskite layers were spincoated under normal atmosphere and for 3 other cells the perovskite layers were spincoated under nitrogen atmosphere. All cells were annealed at 90°C during 120 minutes under normal atmosphere. The results are summarized in the Figure III.8. The presence of the nitrogen atmosphere tends to enhance the value of the J_{SC} by $1 \text{ mA}\cdot\text{cm}^{-2}$. This increase is slightly higher than the standard deviation value ($0.53 \text{ mA}\cdot\text{cm}^{-2}$). The modification of the FF is more noticeable: in normal atmosphere the FF is at 50 % in average and is increased at 57 % with nitrogen atmosphere but the high standard deviation of 7 points forces us to be cautious on the interpretations. This results in the increase of the PCE by 1.08 point (SD: 0.53 point) which correspond to an increase of 26 %.

The presence of N₂ atmosphere could have an impact of the evaporation rate of the DMF solvent. A lower evaporation rate could reduce the rate of perovskite crystallization, and thus promotes bigger perovskite crystal domain. This can be explained by a lower vapour pressure in nitrogen atmosphere than in normal atmosphere, also, the atmospheric pressure in the spincoater could be higher when the nitrogen atmosphere is applied.

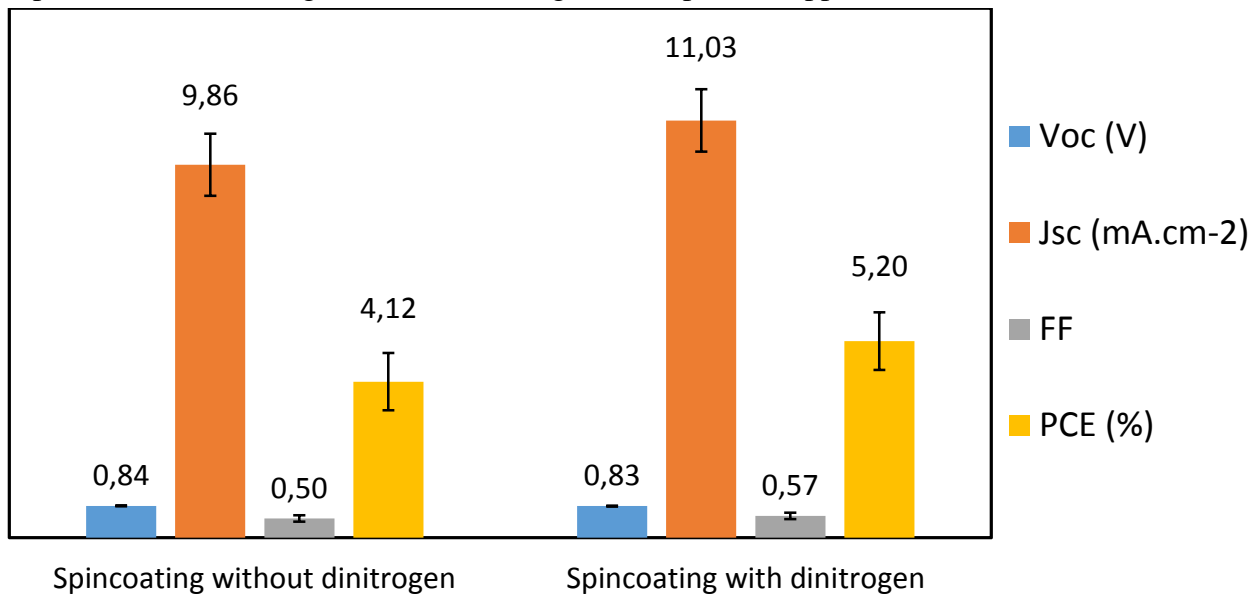


Figure III.8 - PSC performances measured in backward JV depending of the atmosphere during perovskite spincoating

A more possible explanation is that the perovskite crystallisation is sensible to humidity [58] and since the nitrogen atmosphere is totally dry this could enhance the crystallisation. In the objectives to print the perovskite layer this method could be very useful to control the evaporation of the DMF, or at least the crystallisation quality of the perovskite. We are not able to print under nitrogen atmosphere, therefore, all the following perovskite printing will be done under normal atmosphere. That means that perovskite printing is subject to atmospheric changes, like temperature and relative humidity variation through the seasons. That also means that all the performances of printed PSC shown in this thesis could be enhance in the future by simply printing under nitrogen atmosphere.

Ambient condition effects: humidity

In the previous section the effect of N₂ atmosphere during spincoating was investigated. This was link to the perovskite sensibility relative humidity level in atmosphere. The effect of humidity during the annealing is also known. For some authors a dry atmosphere is the best to anneal perovskite layers [58], for others the best relative humidity level is around 30 % [59]. In our process since we have no control on the level of humidity we just did the measurements. During most of the year, from October to April the relative humidity level is lower than 45 %. When summer hits and the temperature rises the relative humidity can increase up to 90 %. This can be clearly seen in the Figure III.6 where no increase in the PCE was made during summer 2015. Atmospheric conditions could have a detrimental effect on photovoltaic performances, for our protocol the best humidity range seems to be under 45 %. This can be improved with a controlled atmosphere with a steady relative humidity level.

Compact TiO₂ layer solution

At the beginning of this thesis the compact TiO₂ layers was processed via spray technic with this recipe for the TiO₂ solution (noted TiO₂ recipe 1):

- 250 mg of acetylacetone in 355 mg de titanium IV isopropoxide, this solution is then added in 5 ml of absolute ethanol.

The results are presented in the Table III.2 and are here for PSC with CH₃NH₃PbI_{3-x}CL_x perovskite and a mesoporous TiO₂.

Two other TiO₂ solutions where tested but this time with spincoating technics:

- The TiO₂ recipe 2 : 380 µl of acetylacetone in 5 ml of ethanol followed by the adding of 650 µl de Ti (IV) isopropoxide

- The TiO₂ recipe 3 : 15.4 µl of titanium (IV) isopropoxide in 1 ml of ethanol, then 1 µl of HCl 37 %.

The results are also presented in the Table III.2. The main difference of photovoltaic performances se due do the use of the spincoating instead of the spray TiO₂ fabrication. Both recipe 2 and recipe 3 allow the fabrication of PSC with photovoltaic performances close to one another. However, the average V_{OC} is higher for the recipe 3 and the electrical parameters of the best cell is higher also for the recipe 3. As seen is the protocol section this TiO₂ fabrication proceeding with the recipe 3 has been chosen for the future works.

Electrical paramaters	Spray			Spincoating					
	TiO ₂ recipe 1			TiO ₂ recipe 2			TiO ₂ recipe 3		
	Average (2 cells)	SD	Best cell	Average (2 cells)	SD	Best cell	Average (3 cells)	SD	Best cell
V _{OC} (mV)	289	266	733	549	283	831	862	16	877
J _{sc} (mA.cm ⁻²)	0.42	0.4	1	13.0	0.4	13.4	13.4	1.6	15.3
FF (%)	26	13	54	40	11	51	44	22	48
PCE (%)	0.08	0.2	0.46	3.1	2.2	5.3	4.8	2.3	6.5

Table III.2 - TiO₂ fabrication proceeding effect on the electrical parameters of TiO₂-based PSC

TiCl₄ treatment influence

As specified in the protocol section, the TiO₂ layers (dense and mesoporous) are treated by a bath in an aqueous solution of TiCl₄. This treatment reduces the oxygen vacancies of the TiO₂ [60] and, therefore, enhances the surface of the TiO₂.

In a first attempt to assess the utility of this treatment six PSC with TiO₂ layers were processed with two different conditions:

- Three PSC with a TiCl₄ treatment of the mesoporous TiO₂. Two of the cells did work.
- Three PSC without a TiCl₄ treatment of the mesoporous TiO₂, all three cells were working

For both conditions the dense TiO₂ remained untreated. The results are summarized in the Table III.3. The main effects of the TiCl₄ treatment are the increase of the V_{OC} and the J_{sc}. The V_{OC} is considerably increased from 479 mV to 650 mV. The J_{sc}, despite a high standard deviation, has been efficiently enhanced. This increase can be clearly seen in the result of the

best cells of both conditions, from 2.5 to 15.8 mA.cm⁻². This treatment has allowed the increase the PCE to almost 10 %.

Here, we can comment the result. Without the TiCl₄ treatment the average PCE is lower than the previous result found for the TiO₂ recipe 2 or TiO₂ recipe 3. It is possible that this batch was not correctly produced but the TiCl₄ treatment could compensate the overall bad quality of the PSC. This treatment was then adopted for both compact and mesoporous TiO₂ layers.

Electrical parameters	WITH TiCl ₄ TREATMENT			WITHOUT TiCl ₄ TREATMENT		
	Average (2 cells)	SD	Best cell	Average (3 cells)	SD	Best cell
V _{oc} (mV)	650	54	708	479	168	711
J _{sc} (mA.cm ⁻²)	9.6	5.9	15.8	4.4	2.7	2.5
FF (%)	52	20	83	44	20	79
PCE (%)	3.46	3.4	9.24	0.82	0.5	1.40

Table III.3 - TiCl₄ treatment effect on the electrical parameters of TiO₂-based PSC

v. Morphological features

AFM characterization were conducted on the surface of the mesoporous TiO₂ and are presented in the *Figure III.9* and in the *Figure III.10*. In putting the lowest point of the TiO₂ mesoporous layer at 0 nm the highest height is around 80 nm while the roughness (RMS) is 8 nm. The particle size is around 20 nm, as specified by the TiO₂ mesoporous furnisher [56]. As for the perovskite the surface is way more heterogeneous: the mean thickness is calculated at 170 nm, which is close from the 200 nm measured with the profilometer, however the difference between the lowest and highest point is at around 400 nm. This measurement highlights one particularity of the perovskite layer: the coverage on top of the TiO₂ mesoporous layer is not efficient. This observation can also be made from simple optical microscopy, the two pictures of the *Figure III.11* were taken from PSCs with 10 % PCE and the result is visually different, the coverage of the perovskite seems not to be detrimental to the performances.

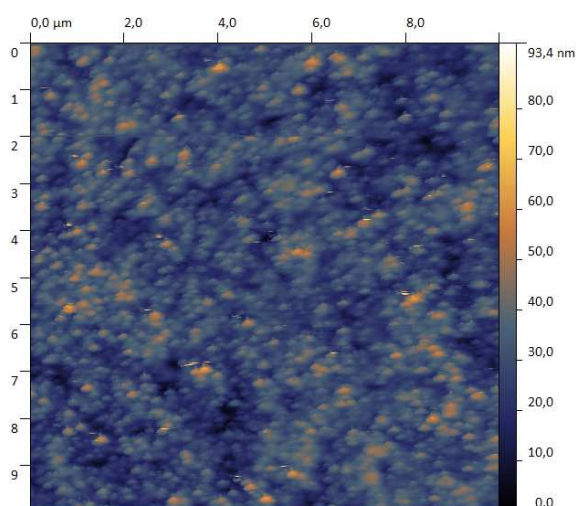


Figure III.9 - TiO_2 -mp surface AFM characterization

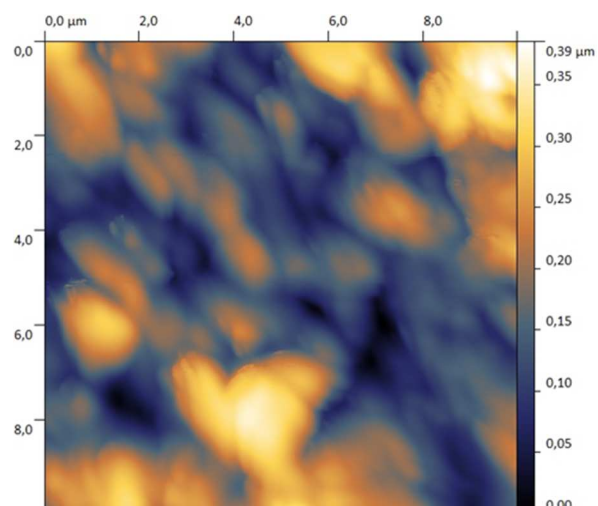


Figure III.10 - $\text{CH}_3\text{NH}_3\text{PbI}_{3-x}\text{Cl}_x$ perovskite surface AFM characterization

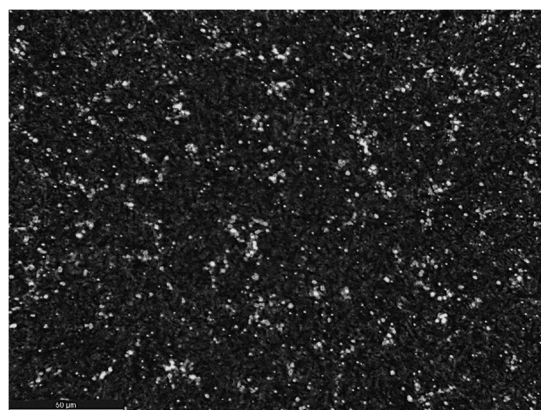
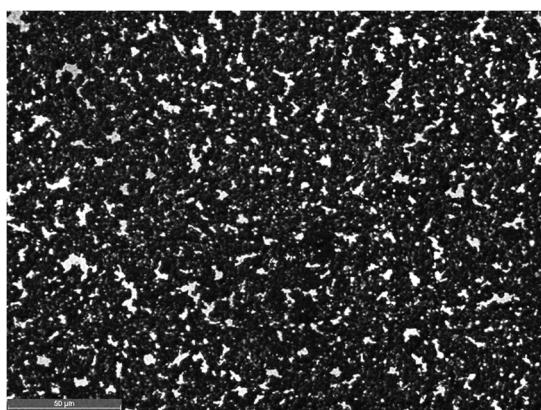


Figure III.11 - Two different shots of optical microscopy of the perovskite layer from comparable perovskite solar cell.

vi. Optical characterization and IPCE

Optical characterization

The UV-Visible spectrometry was conducted on the TiO_2 layers, on the perovskite layer and on the TiO_2 /perovskite/Spiro-OMeTAD stacking in order to determine, for example, the transparency of the TiO_2 , which could be useful to compare with a replacement ETL. The measurements are summarized in the Figure III.12. For perovskite spincoated on glass, the layer already absorbs 90 % to 100 % of the light between 350 nm and 750 nm, showing the absorption efficiency of 1 μm thick layer of perovskite.

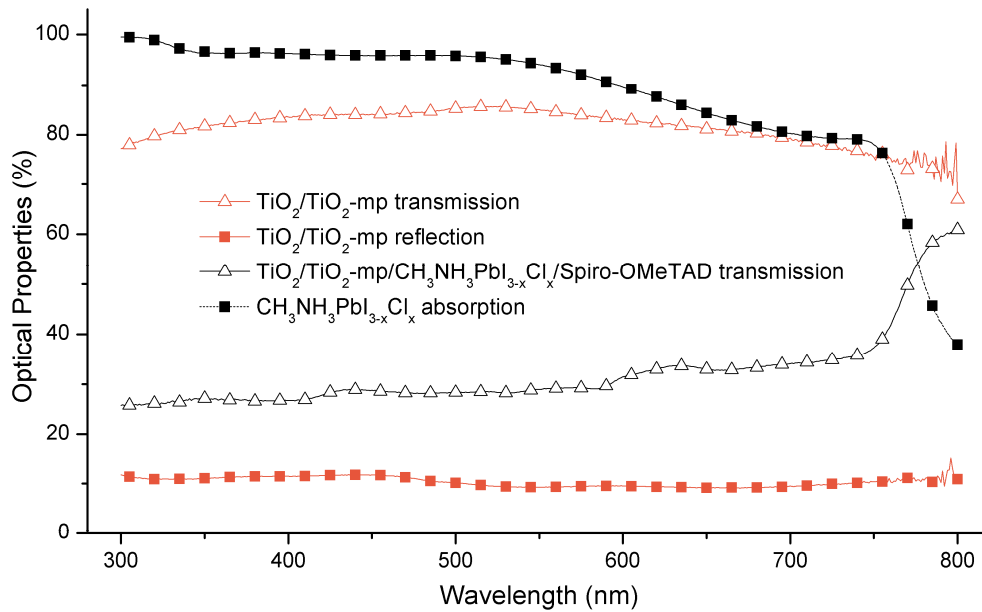


Figure III.12 - Post-annealing UV-Visible transmission and reflection spectra for compact and mesoporous TiO_2 on glass, absorption of $\text{CH}_3\text{NH}_3\text{PbI}_{3-x}\text{Cl}_x$ on glass.

IPCE

In order to determine the efficiency of photo-conversion of the perovskite solar cell in function of the wavelength light Incident-Photon-to-electron Conversion Efficiency (IPCE, or External Quantum Efficiency, EQE) characterizations were performed. In this characterization the cell is illuminated by a white lamp, between the lamp and the cell a monochromator which allows the selection of a particular wavelength, for each wavelength the photogenerated current is measured. The integration of the current curve gives the maximum current that can produce a solar cell. The IPCE of a TiO_2 perovskite solar cell is presented in the Figure III.13. It shows that the perovskite layer is the more efficient between 350 nm and 750 nm. Most of the light absorbed in this 400 nm bandwidth is converted into current, the light which is not converted in electron has been absorbed by the other layer or is reflected outside of the cell. Part of the electron-hole pair recombines in the perovskite itself, these recombinations also provoke a decrease of the measured current in the IPCE characterization.

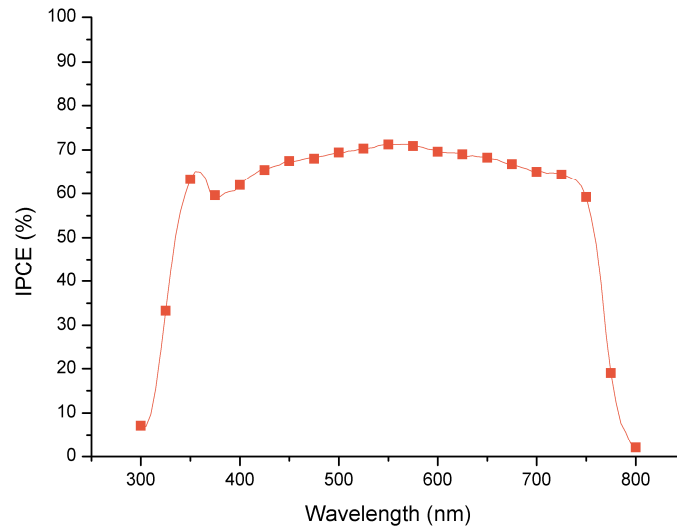


Figure III.13 - IPCE of a TiO₂- based perovskite solar cell

Once integrated this curve predicts a maximum short-circuit current of 16.9 mA.cm⁻² which is 30 % lower than the one observed in the JV characterisation (Figure III.4).

Mismatch factor

The mismatch factor calculated for the TiO₂-based PSC and for the solar simulator and the calibration sensor that we used (the details are in the section II.3.v.) is at 0.83. This value of mismatch factor has been used for all the other JV characterisation of this work because of the difficulty to evaluate the IPCE of the WO₃-based PSC.

vii. Electrical measurements parameters

Hysteresis

As stated in the section II.3.v about photovoltaic characterisation it is possible to do the JV polarisation with a voltage sweep from negative tension to positive tension (forward), or in the other direction (backward). In the case of perovskite solar cells there is a difference between this two directions: the backward measurement gives better photovoltaic parameter measurements, as seen in the Figure III.14.

This phenomenon could be due to mobile charge carriers in the perovskite layer. These mobile charge carriers could be I⁻ [61], Pb²⁺ and CH₃NH₃⁺ [62] or vacancies of these ions in the perovskite structures [62]. When no tension is applied, an inbuilt electrical field is imposed by the work function difference between the ETL and the HTL. This electrical field displaced the anions and can partially screens them. When a positive polarisation is imposed this effect is increased, all the anions move closer to the ETL. This corresponds to an increase of the positive carrier population near the TiO₂ and an increase of the negative carrier population near the Spiro-OMeTAD. This provokes a modification in the band structure of the perovskite solar cell and easing the transport of the hole toward the Spiro-OMeTAD and the electrons through the TiO₂. This effect reduces the value of the electrical potential needed to force the charge carrier to go through their respective collection layers. When a forward scan is imposed to the cell, that is to say when a positive bias is imposed to the cell, the V_{OC} will be lower than when the backward scan is imposed. This can be clearly seen in the Figure III.14 and the mechanism is schematized in the Figure III.15.

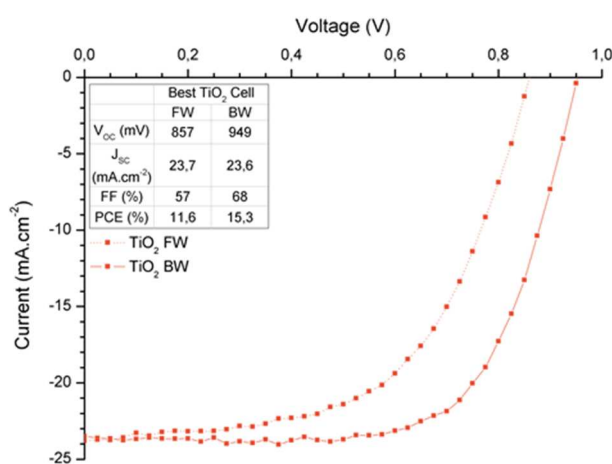


Figure III.14 - JV curves of the best TiO₂-based PSC: backward (BW) measurements is from 1.5 V to -0.1 V and forward (FW) is from -0.1 V to 1.5V

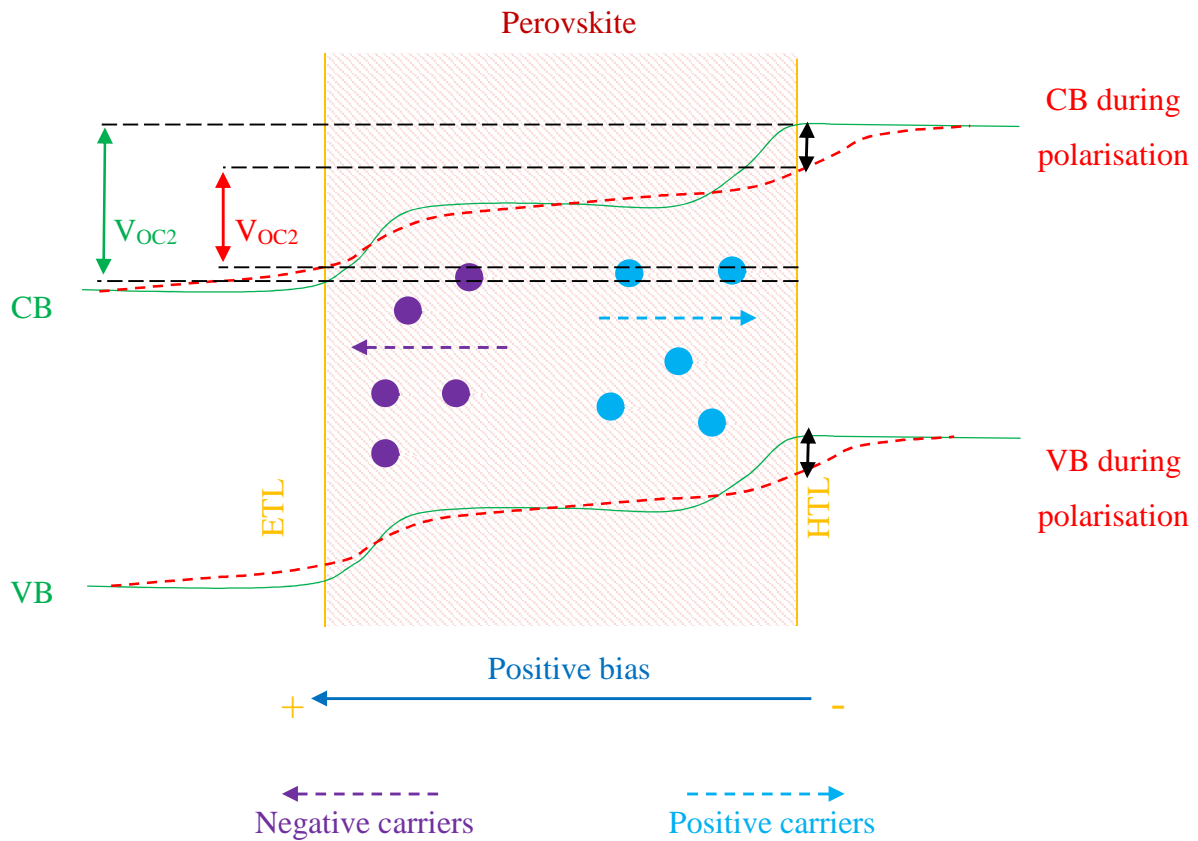


Figure III.15 - Influence of moving charge carriers on band energies of a perovskite thin film.

Voltage sweep starting point

For the forward scan the first voltage value imposed to the perovskite solar cell will also determine the value of the measured performances. This can be even seen with low-efficient PSC in the Figure III.16. When a very low negative starting point is chosen the J_{sc} is extremely reduced. This results in a lower PCE. This phenomenon has probably the same origin than the

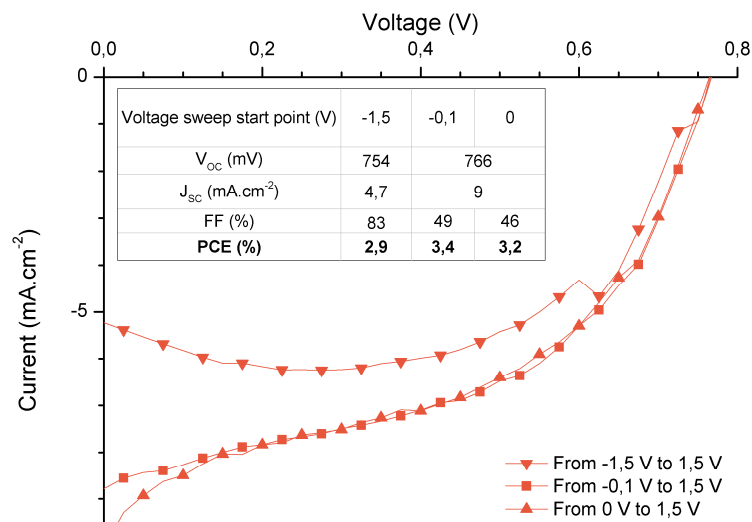


Figure III.16 - Influence of the voltage sweep starting point on the forward scan

hysteresis. In this case the screening of the electrical field would be so effective that the charge collection will be dramatically reduced if the polarisation level is high and maintained during a long time. To limit the S shape visible at the V_{OC} it is preferable to start the voltage sweep on the lowest positive polarisation, like 0 V. However the acquisition software does not correctly identify the J_{SC} if the sweep start at 0 V (as seen in the table of the Figure III.16) so every JV characterizations has been made between -0.1 V and 1.5 V.

Delay

One of the electrical parameter is the delay between each imposition of voltage. This delay can have consequences on the final result. Indeed, the longer the delay is the longer the JV characterization takes. Furthermore, since there are several ions in the perovskite layer, depending of their mobilities and diffusion coefficients choosing short delays could help to reduce their effect and to obtain the photovoltaic parameters which are the closest of the true working state of the PSC. For example, and with no polarisation, at 320 K, the diffusion coefficient of I^- and $CH_3NH_3^+$ were respectively estimated at $10^{-12} \text{ cm}^2.\text{s}^{-1}$ and $10^{-16} \text{ cm}^2.\text{s}^{-1}$ [62].

For this measurement three cells were characterized with the JV characterization at different delay, 0 ms, 100 ms, 250 ms, 500 ms and 1000 ms. For each cell and for each voltage the maximum value of current was used as reference and the other delay value was compared to. Then, for each value of delay the mean for each compared current was calculated, this generated the curves presented in the Figure III.17. In the forward measurement, it seems that delay value higher than 250 ms will provoke very similar curves. In the backward measurement the effect of the delay is much visible. The J_{SC} and V_{OC} decrease as the delay increases. The delay that gives the best PCE is 250 ms but a strong S shape is visible between 0 V and 0.4 V, this create an error in the calculation of the FF, explaining the high PCE. The most interesting delay to choose would be 0 ms. Indeed the J_{SC} and V_{OC} is the higher and the shape of the curve is well defined. However, the equipment is not as fast as 0 ms and we do not know what is the exact value of minimum possible delay. Furthermore, in the backward measurements this very low delay tends to generate high standard deviation. Therefore, in order to know the exact value of the delay, and thus to have repeatability, the value of 100 ms has been chosen for most of the measurements. This has the side effects to slightly reduce the J_{SC} by 10 % and the V_{OC} by 3 %.

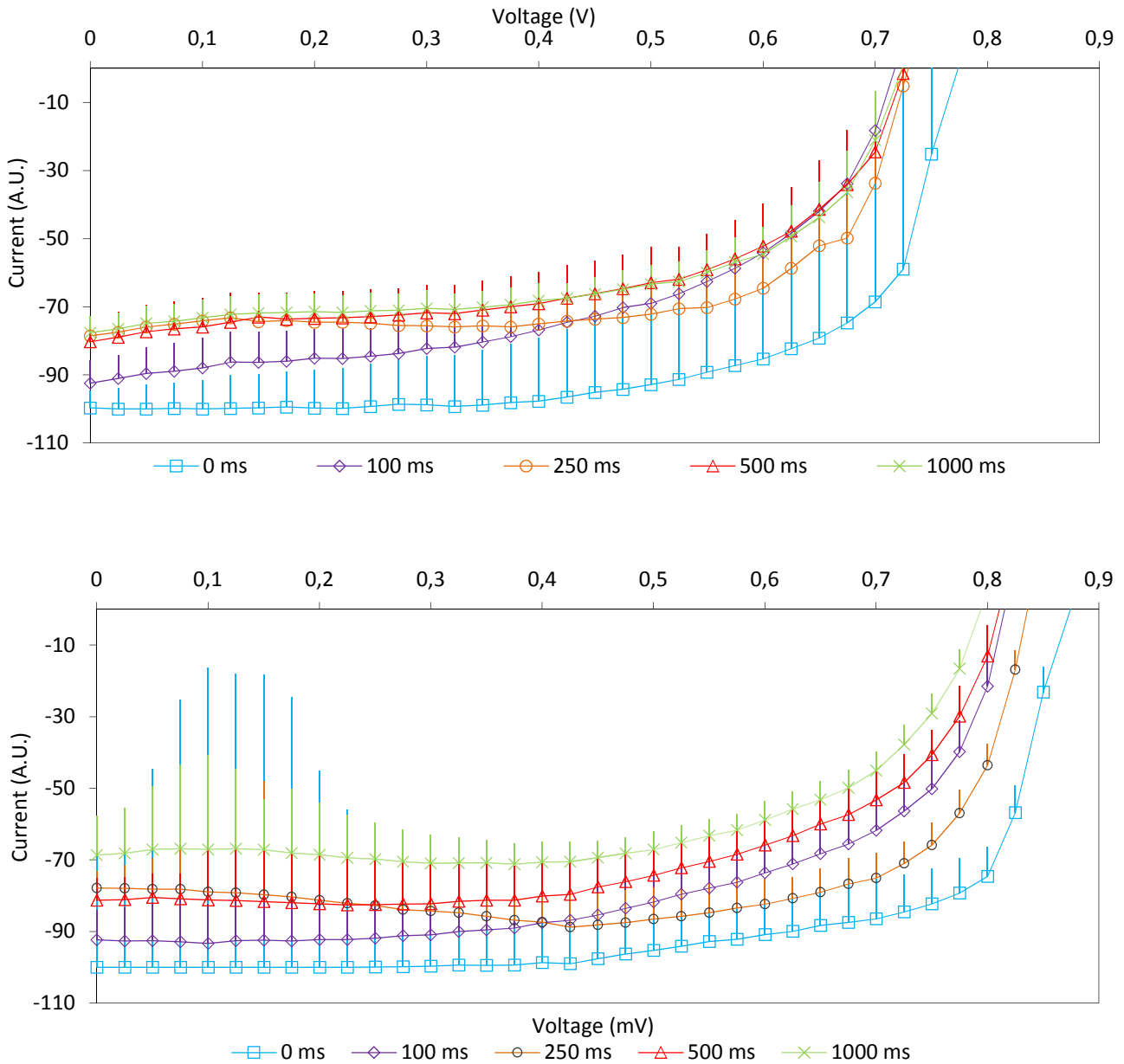


Figure III.17 - Forward (top) and backward (bottom) JV curves depending of the delay between voltage imposition values. For clarity only the positive standard deviation values are displayed

Illumination level

These perovskite solar cells are aim to be used to gather energy for autonomous sensors which can be used indoor. Thus, we measured the efficiency of one cell with low level of illumination, the results are summarized in the Figure III.18.

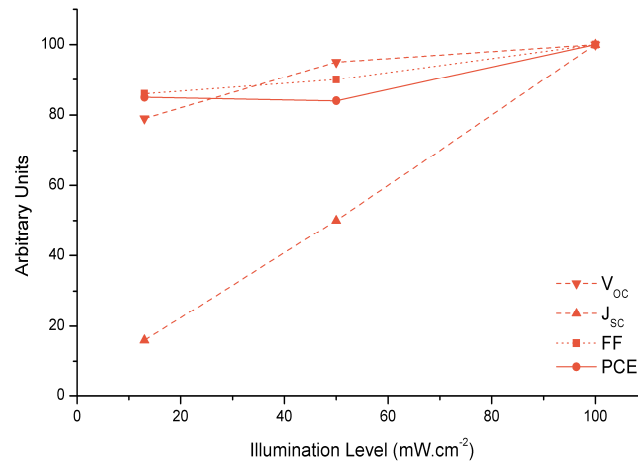


Figure III.18 - Short-circuit current, open-circuit voltage, FF and PCE depending of the illumination level

As expected the J_{SC} increase is directly link to the increase of illumination level with almost a linear law. The V_{OC} loses only 10 % of its maximum value when the level of illumination is only at 10 $W.cm^{-2}$. As for the PCE when the level of illumination is around 10 $W.cm^{-2}$ the remaining efficiency is at 85 % of its maximum, this is a good point because it means that the cell is still efficient even with a very low level of illumination. For a 10 % PCE cell we can hope to have an 8.5 % conversion efficiency when used indoor. The limitation would be the low current which could be not high enough to load the super-capacitor or batteries and to operate all the electronics of the sensor in the same time. When the electronic operations are idle, the low current could be also not enough to charge entirely the batteries.

viii. Stability issues

One of the most commented aspect on perovskite solar cells are their stability when illuminated or even when stored in the black. Several article already explored this aspect [63, 64] and we begin to understand what the mechanics of deterioration are. Our work allowed us to write an article about the stability of PSC [29]. In this section we will summarized the principal result and main interpretation of the deterioration mechanisms.

The deterioration occurs when the perovskite layer is in contact with moisture of the atmosphere, as schematized in the Figure III.19. The first step is the diffusion of water into the perovskite. In a second step this water reacts with the $CH_3NH_3PbI_{3-x}Cl_x$ to create H^+ and I^- . During illumination the UV light have also a role which is not clear but we know that it can be absorbed by the TiO_2 layers to generate a electron-hole pairs.

For Snaith et al. the hole will be collected by the Spiro-OMeTAD but the electron could react with adsorbed oxygen at the TiO_2 surface on the oxygen vacancies [64]. In detail, the explanation of the Snaith team is that oxygen vacancies of the TiO_2 mesoporous layer, combined with an exposure to UV-containing light can explain the poor stability of PSC produced and characterized in the absence of atmospheric oxygen (while keeping in mind that the ITO and FTO TCL are known to absorb UV below 300 nm, yet transmit between 300 and 400 nm). In this case, the solar cells whose TiO_2 layer is produced under nitrogen atmosphere and then encapsulated were less stable under illumination than the ambient-air-produced and not-encapsulated ones, or even than the simply UV-filtered and encapsulated ones. The mesoporous TiO_2 layer naturally hosts oxygen vacancies, especially at its surface, in the form of Ti^{3+} sites [65]. When exposed to ambient atmosphere after production and annealing, these vacancies are spontaneously filled with O_2 molecules. Under illumination using a UV-containing-light, an electron-hole pair is generated in the TiO_2 (step 3). The photo-generated hole recombines with electron at the O_2 site, desorbing the oxygen [66]. This leaves a free electron and an oxygen vacancy site at the TiO_2 surface. The free electron will eventually combine with a hole from the doped Spiro-OMeTAD HTL. TiO_2 layers produced under nitrogen exhibit native oxygen vacancies and if a cell based on such layers is encapsulated, O_2 will never have the opportunity to diffuse through the layers (either from the top electrode or through lateral diffusion pathways) to fill and passivate these vacancies. However, if the cell is not encapsulated, and after a certain amount of time, oxygen will passivate the vacancies until it is desorbed again by the UV-induced hole generated under (unfiltered) solar illumination. A potential solution to address this issue would be to cut the UV contribution in the illumination spectrum, so that oxygen vacancies remain passivated. The report by Snaith et al. finally points out that these vacancies are supposed to be at the origin of the fast degradation of cells based on TiO_2 layers processed under nitrogen atmosphere.

We think that this mechanism is limited in the case of our TiO_2 -based perovskite solar cells and that the exciton just recombines in this third step. Indeed our TiO_2 is treated with a TiCl_4 bath and this greatly reduce the oxygen vacancies of the TiO_2 [60]. The fourth step is the closing of the loop, the water continues to add up and to degrade the perovskite layer.

This path for the reaction of the adsorbed O_2 has been also reported by Wang et. Al [67] (in the case of $\text{CH}_3\text{NH}_3\text{PbI}_{3-x}\text{Cl}_x$) where HI (produced by the degradation of $\text{CH}_3\text{NH}_3\text{I}$) reacts with the O_2 to form water as follow:

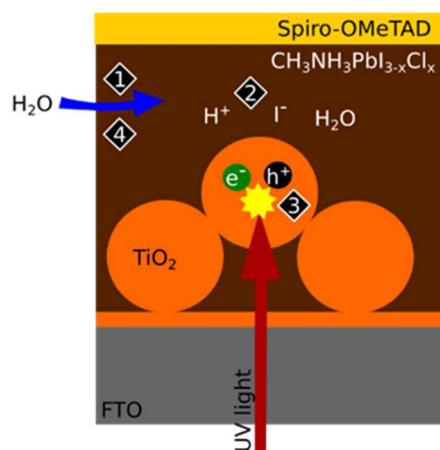
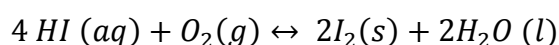
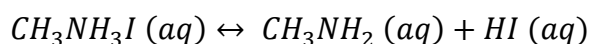
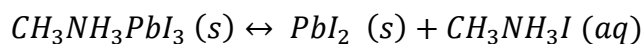


Figure III.19 - Summarizing scheme of degradation in PSC

The presence of water can be directly seen in the steady-state photoluminescence spectra shown in the Figure III.20. Although both ETL sample are associated with a highly quenched perovskite PL emission in the 740-800 nm range, they exhibit some structuration. In general, two main contributions centred at 770 and 790 nm are evidenced. The steady-state PL spectra of the TiO₂-based PSC show a trend: two days after the production the peak at 770 nm is very weak but its signal significantly increased after 9 days of storage in the dark and under ambient conditions. This trend, which has already been identified in the literature is supposed to be correlated with the presence of water into the perovskite crystal. [68] The penetration of water molecules in the perovskite layer is usually accompanied by a blue-shift of the free exciton emission, going from 790 nm to 770 nm. From the steady-state PL spectra we can conclude that the fresh TiO₂-based perovskite solar cells contain only few water molecules after their production, but that moisture is in fact absorbed throughout the storage.

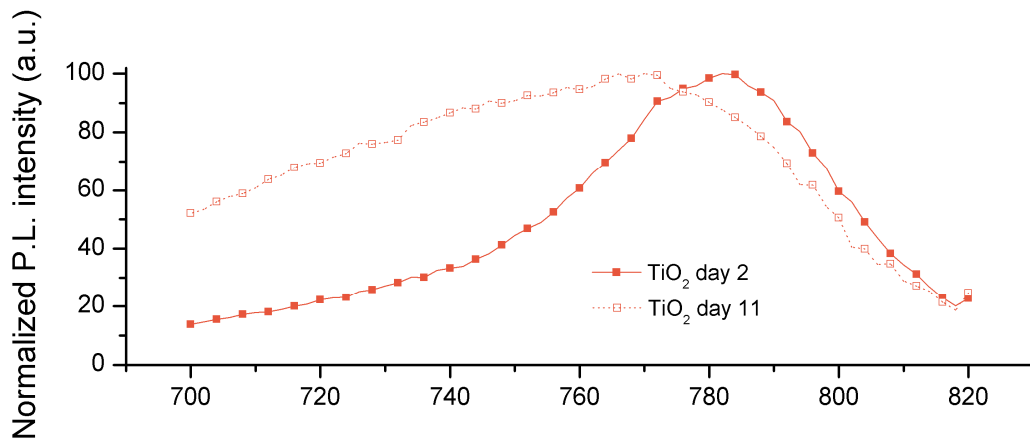


Figure III.20 - Steady-state PL measurements of perovskite layers 2 days and 11 days after the production on TiO_2 ETL

When perovskite solar cells are exposed to illumination over a long period of time they deteriorate, the reason is the photo-bleaching of the perovskite. This can be seen in the Figure III.21 where the PCE of the cell is at 10 % of its initial value after 5 hours of exposition. We observe a little increase of the PCE after these 5 hours, this is mostly due to an increase in the FF and this increase tends to disappear after another 10 hours. Removing the UV from the light source improves the stability of the PSC during the 10 first hours. It seems that the UVs have a detrimental influence on the perovskite solar cells and need to be removed with encapsulation if we want to produce more stable perovskite solar cells.

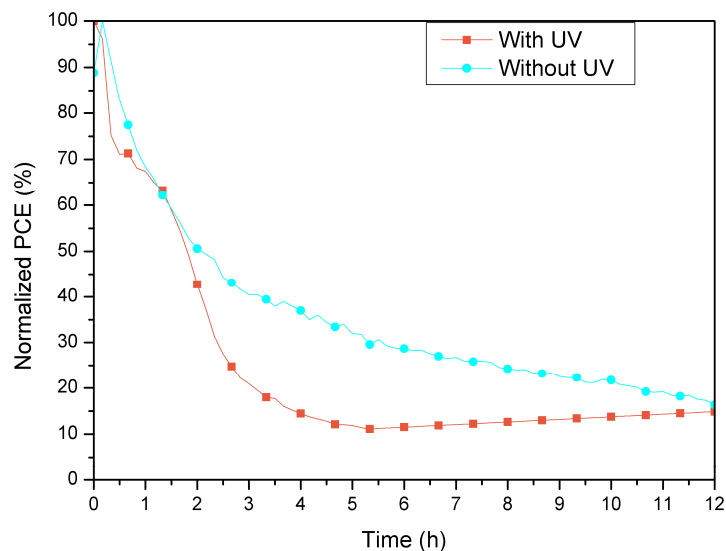


Figure III.21 - Stability of TiO_2 -based perovskite solar cells

TiO₂-based PSC stored in black during few days tend to have different deterioration. At the day of the production the cells all work with similar photovoltaic parameters as presented in Figure III.22, for example the mean PCE is (with backward JV measurement) 10.2 % with a low standard deviation of 0.6 %. When stored 9 days in dark in ambient atmosphere this means PCE decreases to 5.8 % with a standard deviation of 2.4. This trends in the decrease of the photovoltaic parameters is easy to generalize since some cells will be working better after this storage and other will lost all their efficiency. The parameters who are the most sensitive to storage are the J_{SC} and the FF. As stated previously this is probably due to the reaction with the humidity of the atmosphere. Pin-holes on the metallic top electrode, or local in-homogeneities in the perovskite or HTM layers would result in various degree of active layer degradation upon oxygen and moisture exposure [69]. Furthermore, Spiro-OMeTAD is responsible of antagonist effects which complicates the interpretation of the poor dark room stability of the PSC. Indeed, the presence of the dopants in this HTL is thought to be responsible for the poor stability of the perovskite solar cells and at the same time the Spiro-OMeTAD needs to be doped by atmospheric oxygen to function properly [70, 71].

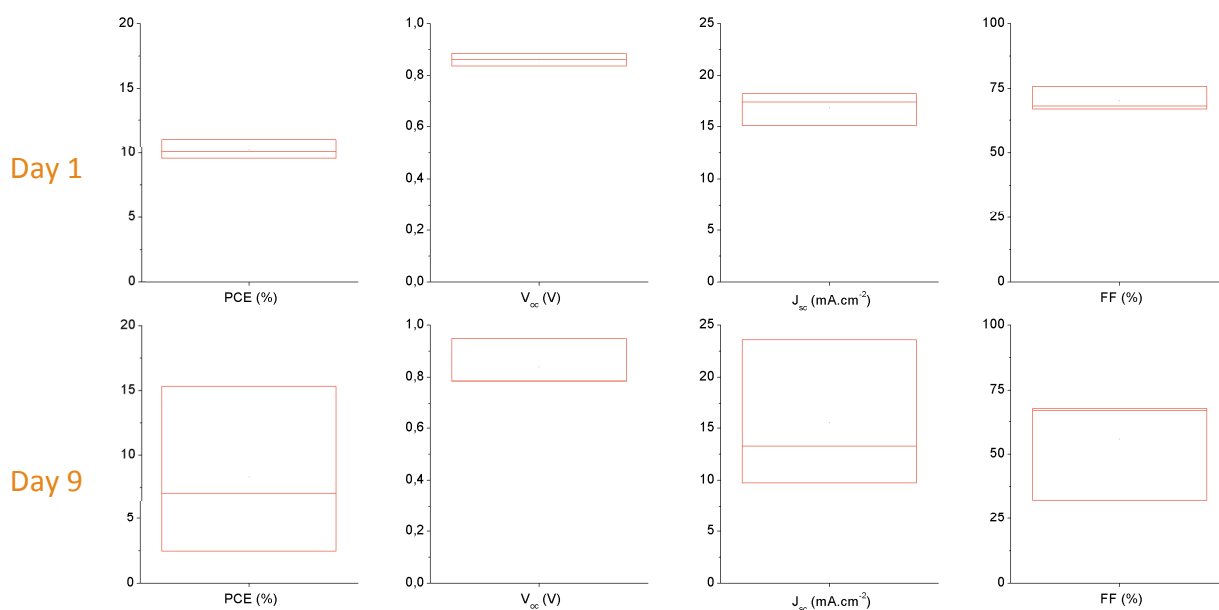


Figure III.22 - Backward JV measurements for TiO₂-based PSC at their production day and 9 days later.

2. WO₃-based perovskite solar cell

i. Introduction and literature.

As said in the first section the goal is to produce a solar cell with printing technics and suitable for all substrate. One possibility is to replace the TiO₂ layer by WO₃. Indeed the TiO₂ layers are annealed at 450°C which is incompatible with the polymer substrates and the mesoporous layer cannot be produced via inkjet printing. Furthermore, it is important to create a mesoporous - or at least rough - layer in order to provoke a good shape definition and layer stacking precision for the following perovskite inkjet-printing step [72, 73]. To summarize the material that would replace the TiO₂ must be jettable, at least slightly rough and annealed under 130 °C maximum.

There are many alternative: SnO₂ [74, 75], ZnO [76, 77] Al₂O₃ [19]. For these materials the stability are not systematically tested and still need annealing temperature slightly above 130 °C. Here, we propose to the use of tungsten oxide (WO_x or WO₃), this oxide is already commercially available in a printable nanoparticle alcoholic solutions, allowing the production of a mesoporous and rough layer, and has been already used with success as an interface layer in organic solar cell [78, 79, 80].

The first used of WO₃ with PSC happened in 2014: nano-structured high temperature annealed WO₃ structures were synthesized on another WO₃ compact layer [81]. Different shapes were tested, such as nanorods, nanosheets or simply nanoparticles in order to create a mesoporous ETL. Power conversion efficiency (PCE) reached 3.80 % for the nano-sheets WO₃ based perovskite solar cell, improved to 11.2 % when coated with the classical ETL TiO₂ via a TiCl₄ chemical treatment. Low-temperature annealed WO_x was then tested. In this case, the oxide was synthesized from a solution of WCl₆ in N-propanol [82]. The 150°C annealed WO_x was then covered with CH₃NH₃I_xCl_{3-x} and the produced solar cells owned a mean PCE of 8.99 % when the TiO₂ reference cells was able to reach the 8.78 %. Even if these solar cells showed a relatively small active area (0.06 cm²) and were entirely produced in a nitrogen glove box, this remains the first significant demonstration of the true potential WO_x as an alternative to TiO₂. The authors made the statement that such good performances could be improved by suppressing the charge recombination events at the WO_x/perovskite interface. This idea was put in practice by another research team which proposed the utilization of a self-assembled monolayer (SAM) of fullerene coated directly on the low temperature annealed WO₃ layer [83]. The WO₃ reference cell, without any SAM, produced a short-circuit current density (J_{SC}) of

21.8 mA.cm⁻², with an open-circuit voltage (V_{OC}) of 750 mV and a fill factor (FF) of 65.3%, resulting in a PCE of 10.7% which was at the moment the best bare-WO₃-based PSC. The cell with SAM on top of WO₃ was even able to reach an impressive PCE of 14.9 % [83]. The augmentation of PCE is related to a huge raise of V_{OC} up to 1.02V, when the J_{SC} and FF were almost unchanged at 21.9 mA.cm⁻² and 66.5% respectively.

From this bibliographic study we saw that the WO₃ ETL would be able the production of printed perovskite solar with a PCE of 10 %. The next sections will present the main feature of these WO₃-based perovskite solar cells.

ii. Fabrication

WO₃ solution

The solution used is a solution of WO_x nanoparticle from the company Avantama (former Nanograde) [84]. The nanoparticles as a mean size of 16 nm, and the known main solvent is 2-propanol, and the weight concentration is 2.5 % (Figure III.23). The information from the manufacturer specifies that the viscosity is 2 mP.s and the work function of the resulting layer is 5.5 eV.



Figure III.23 - WO₃ nanoparticle solution used for PSC fabrication

Architecture and design

The design for the production of the WO₃-based perovskite solar cells is adapted from the design of the perovskite solar cell with TiO₂ as presented previously Figure III.3. This design is presented in the Figure III.24.

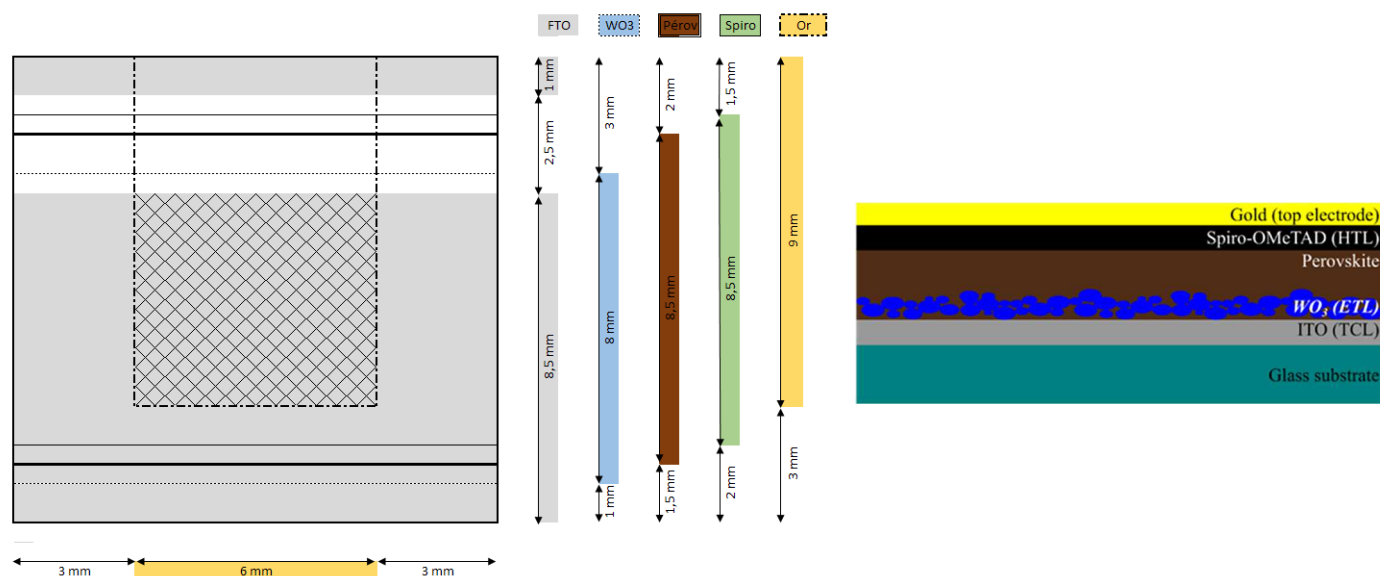


Figure III.24 - WO₃-based perovskite solar cell fabrication design (vertical scale not respected)

Fabrication routine

In this section only the WO₃-based perovskites solar fabrication steps which differs from the one of the reference TiO₂-based PSC will be detailed. The step of the preparation of the perovskite solution and Spiro-OMeTAD is the same. The ITO etching part is strictly the same than for the FTO. However, the cleaning and preparation of the cells are slightly different. The first solvent to be used to clean is acetone, then it is ethanol, isopropanol. After the cleaning the ITO surface is treated with UV/ozone during 20 minutes and the substrate are soaked again in iso-propanol and put in an ultrasonic bath during 20 minutes and finally dried.

The WO₃ solution is agitated with an ultrasonic probe for one minute with sequences of agitation of 5 seconds separated by sequence of non-agitation of 5 seconds. This solution is then put in an ultrasonic bath during 20 minutes.

The WO₃ is spincoated on FTO at 2000 rpm with an acceleration of 2000 rpm.s⁻¹, for 10 seconds. The layer is then annealed at 110°C during 10 minutes.

Before the perovskite spincoating the WO₃ coated substrates are heated at 90°C as well as the 0.2 PTFE filtered perovskite solution. The spincoating is proceed under nitrogen

atmosphere: 2000 rpm, with a $2000 \text{ rpm}\cdot\text{s}^{-1}$ acceleration, for 20 seconds. Then the substrate rests motionless in the spincoater, under nitrogen atmosphere, for 20 seconds. The perovskite layer is then directly annealed under ambient atmosphere at 90°C for 2 hours. On top of the perovskite layer (once the substrate is cooled) the filtered Spiro-OMeTAD is spincoated at 2000 rpm ($2000 \text{ rpm}\cdot\text{s}^{-1}$) during 20 seconds. Under a 10^{-6} mbar vacuum a 100 nm thick gold electrode is evaporated at $0.1 \text{ \AA}\cdot\text{s}^{-1}$.

iii. Best results

The best result obtained for a WO_3 -based PSC (with a spincoated ETL) is a PCE of 9.5 % in backward measurement. This corresponds to a V_{OC} of 710 mV, a J_{SC} of $20.7 \text{ mA}\cdot\text{cm}^{-2}$ with a FF of 58 %, the JV curve is represented in Figure III.25. When the dark characterisation (Figure III.26) of the WO_3 -based PSC is compared to the one of the TiO_2 -based PSC (Figure III.5) the main difference is less defined and the threshold voltage is more difficult to determine, it is around 650 mV, against 750 mV for the TiO_2 -based PSC. The best performances for WO_3 -based PSC was obtained in 6 months. The optimisation of the WO_3 -based PSC profited from the elaboration of the TiO_2 -based PSC, the evolution of PCE is represented in the Figure III.27.

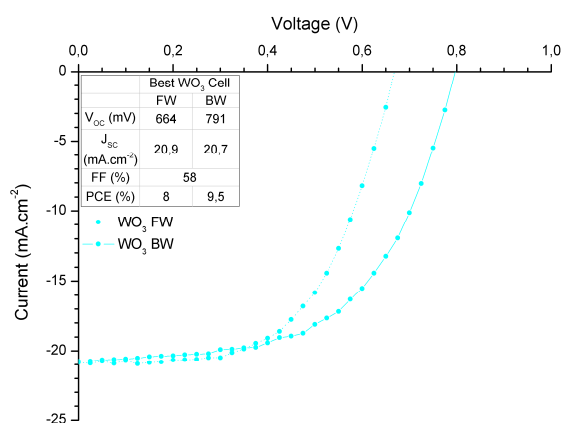


Figure III.25 - JV curves of the best WO_3 -based PSC : backward (BW) measurements is from 1.5 V to -0.1 V and forward (FW) is from -0.1 V to 1.5V

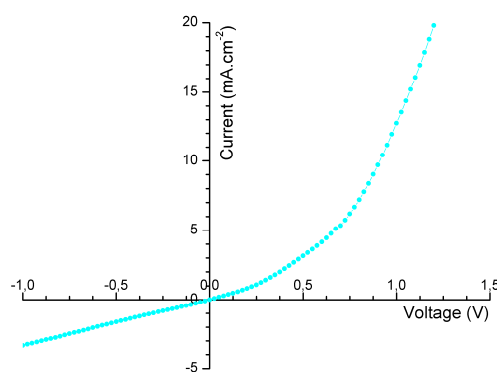


Figure III.26 - JV curve in dark of a perovskite solar cell

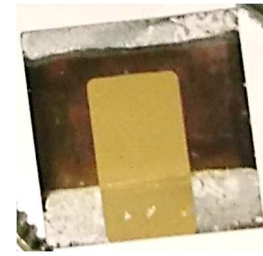
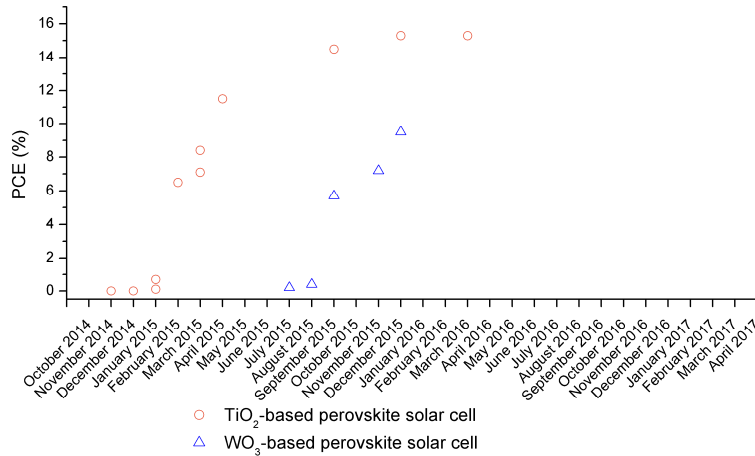


Figure III.27 - PCE evolution of the best perovskite solar cells

Figure III.28 - A WO₃-based perovskite solar cell

Compared to the objectives, described in the Table III.4, the best performances of the WO₃-based PSC are in the desired range. We calculated the average best WO₃-based PSC, this time only the cells with a PCE superior to 6 % (in the backward measurement) were retained. The average best WO₃-based PSC PCE is 7.19 %. This PCE seems pretty low compared to the PCE of the objectives, however the J_{SC} is superior to the current of the objective. This aspect is crucial because the current is the most important electrical parameter to enhance the super-capacitor loading speed. The V_{OC} is pretty low compared to the objective, it is still high enough yet to operate the sensor if the solar cells are disposed in series.

As for the fabrication side, the evolution toward the objectives is positive. Now three layers on five are printable while with the TiO₂-based PSC only two were printable. Furthermore the maximum temperature used is now of 110 °C. All substrates are now usable like polyethylene terephthalate (PET), polyethylene naphthalate (PEN) or even cardboard and paper.

iv. Optical, electrical and morphological features, IPCE

	OBJECTIVES	BEST TiO ₂ CELL	BEST WO ₃ CELL	AVERAGE BEST WO ₃ CELLS
Photovoltaic parameters				
V _{oc} (mV)	830	949	791	720 (± 70)
J _{sc} (mA.cm ⁻²)	16	23.6	20.7	18.39 (± 3.57)
FF (%)	75	68	58	54 (± 6.3)
PCE (%)	10	15.3	9.5	7.19 (± 1.4)
Fabrication				
Active area	1 cm ²	20 mm ²	20 mm ²	
Electrode (ITO or FTO)	Non-printable	Non-printable	Non-printable	
ETL	Printed	Non-printed	Printable	
Perovskite	Printed	Non-printed	Printable	
HTL	Printed	Non-printed	Printable	
Top electrode	Printable	Non-printable	Non-printable	
Max annealing temperature	130°C	450 °C	130°C	

Table III.4 - Comparison between the objectives, the TiO₂-based and WO₃-based PSC*Absorption*

The UV-Visible spectrometry was also conducted on the WO₃ thin layers, and the measurements are summarized in the Figure III.29. Interferences effects are visible with the waves in the measurements of the reflection and transmission of the WO₃ film. These are due to the low thickness of the WO₃ film, measured with ellipsometry at around 50 nm (see next section). The transmission of the WO₃ film is between 80 % and 90 % above 350 nm. This point is very important to guarantee a good absorption of the perovskite layer.

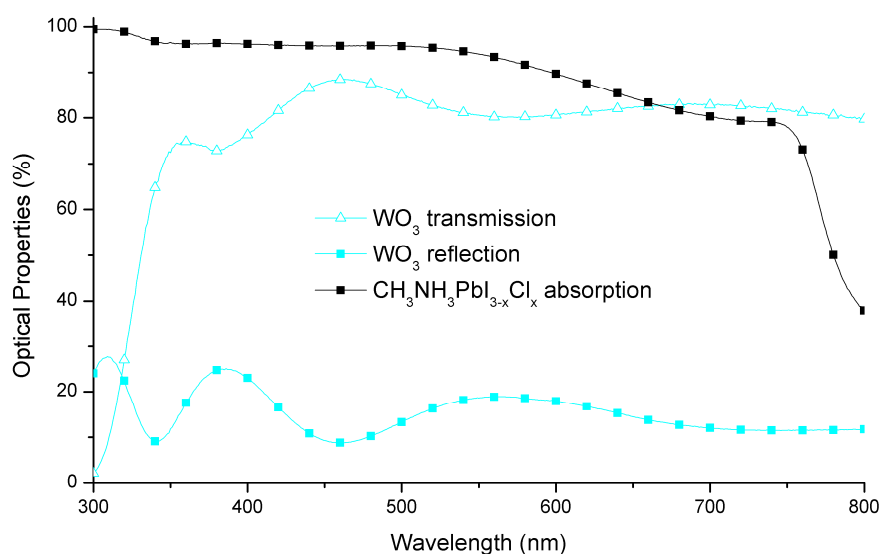


Figure III.29 - Post-annealing UV-Visible transmission and reflection spectra for compact and mesoporous WO₃ on glass, absorption of CH₃NH₃I_xCl_{3-x} on glass.

UV-visible spectrometry was also conducted on the PSC itself to determine the absorption efficiency of the PSC depending of their ETL, this measurement takes into account the total absorption of the glass, the ITO or FTO, the ETL and the perovskite. The additional absorptions of the HTL in Spiro-OMeTAD and the top electrode in gold are not measured here. The curves are represented in the Figure III.30. The TiO₂-based PSC shows a better absorption between 300 nm and 550 nm while the WO₃-based PSC, and the perovskite absorption gap around 780 nm is way more visible on TiO₂ than on WO₃, this could indicates a lower perovskite quality in the case of WO₃-based PSC. This could also be due to the higher diffusion of a rougher perovskite layer.

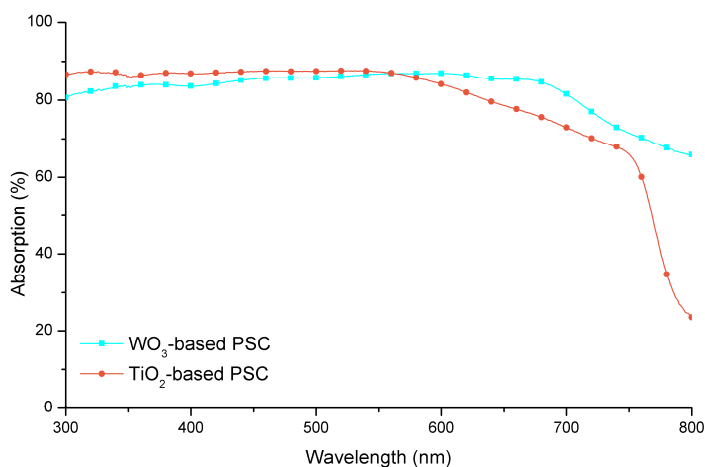


Figure III.30 - UV-visible absorption spectra for PSC with WO₃ or TiO₂ as ETL (without the gold top electrode)

IPCE

The measurement of the IPCE is not an easy to do on WO₃-based perovskite layer. In fact, the acquisition of the photo-current is not working properly. The origin of this problem is not well-known but seems to be intrinsic to the perovskite layer, indeed this happens also sometime with some TiO₂-based PSC. In the case of the WO₃-based PSC the integrated current from the IPCE is dramatically lower than the J_{SC} measured on the JV characterisation, 0.5 mA.cm⁻² against 15 mA.cm⁻². In order to produce an IPCE we corrected the measured IPCE in order to have a 15 mA.cm⁻² integrated current. This increases the noise in the signal, as visible in the Figure III.31. If we compare the IPCE of WO₃-based PSC based with the IPCE of TiO₂-based PSC the same peak is visible around 350 nm.

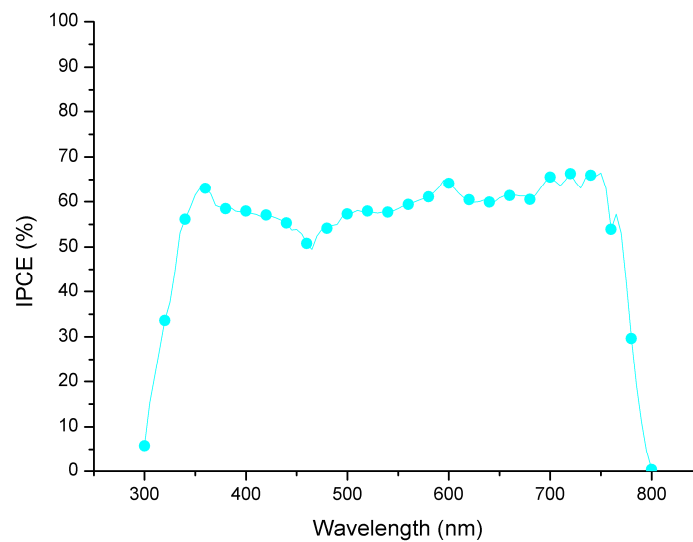


Figure III.31 - IPCE of a WO₃- based perovskite solar cell

Illumination level

As for the TiO₂-based PSC, the effect of the illumination level on the photovoltaic parameters of WO₃-based PSC has been evaluated, and are summarized in the **Erreur ! Source du renvoi introuvable.**

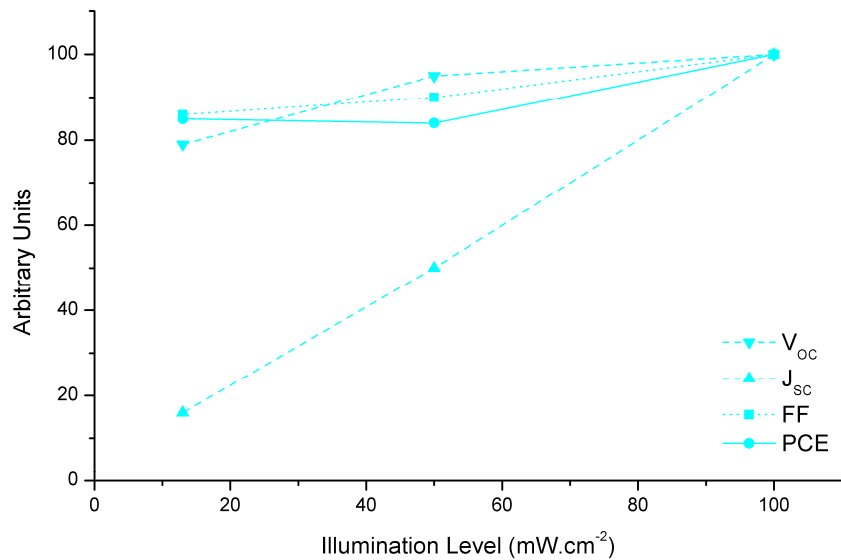


Figure III.32 - Short-circuit current, open-circuit voltage, FF and PCE depending of the illumination level

The result for the WO₃-based PSC are very close from the result for the TiO₂. As expected the J_{SC} is directly proportional to the illumination level. The PCE remains stable when the illumination level is reduced, at around 13 mW.cm⁻² the PCE is about 86 % of its maximum (at 100 mW.cm⁻²). Again, as for the TiO₂, this is a good point to use WO₃-based PSC could be used inside buildings or in low-level illumination situation, for example at dawn or at dusk.

Ellipsometry

Ellipsometry was conducted on WO₃ film to determine its thickness, porosity and optical properties. Thickness has been measured at exactly 54 nm, and the porosity at 30 %. As the mean size of the nanoparticle of WO₃ is 16 nm the average number of nanoparticle superposed in the film is 3. The minimum of porosity for a stacking of sphere is 26 %, if we consider that the WO₃ nanoparticle can be seen as sphere then the porosity of this WO₃ is low. With a value around 30 % that means that in the film there is some nanoparticle vacancy. These vacancies could play an important role for the printing of the perovskite layer on top of the WO₃ layer. The Figure III.33 presents the refractive and extinction index of the WO₃ layer.

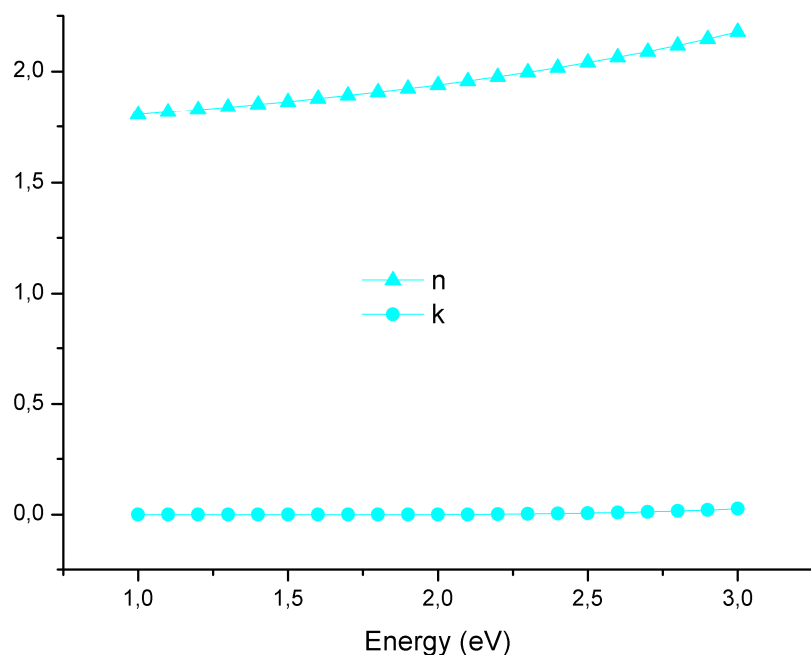


Figure III.33 - Refractive (n) and extinction (k) index of the WO₃ layer depending of the radiation energy

Morphology features

AFM characterization was conducted on spincoated WO₃ film, the picture is in the Figure III.34. The particle can be clearly seen and their size is around 20 nanometres. The roughness (RMS) is 4 nanometres, which is low but still comparable with the 8 nm RMS roughness of the mesoporous TiO₂. The most interesting feature to see is that the coverage of the ITO by the WO₃ layer is not perfect. Indeed the deepest region of the AFM characterisation is around 44 nanometres deep which is very close from the actual thickness of the film. This means that the perovskites layer will be in some places in contact with the ITO layer which can create recombination between holes and non-collected electrons.

As for the perovskite layer the optical microscopy indicates us that the coverage ratio is not good. Several pinholes are visible through this 200 nm thick layer. This pinholes will create contact between the Spiro-OMeTAD and the WO₃ layer. However this situation, even if it is not desirable, is not detrimental as demonstrated in the next section about work function.

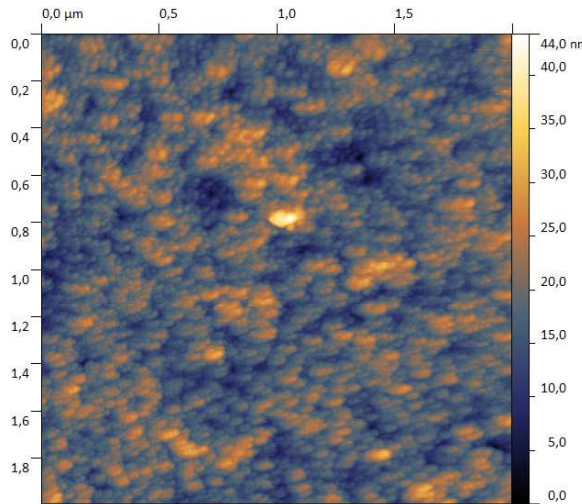


Figure III.34 - WO₃ surface AFM characterization

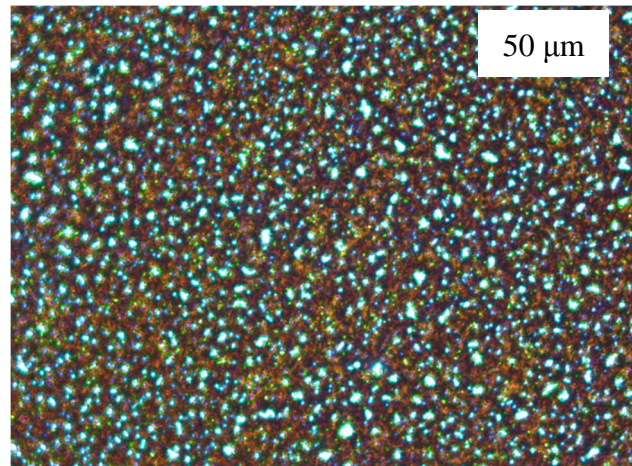


Figure III.35 - Optical microscopy of CH₃NH₃PbI_{3-x}Cl_x perovskite spincoated on a WO₃ layer

v. Work Function

In order to understand the functioning of the perovskite solar cell, it is possible to measure the work function of the ETL layers and to compare it with the work function of the perovskite layer. With the work function value it is possible to evaluate the quality of the charge transfer mechanisms at the interface. To do so, we conducted a HD-Kelvin-probe Force Microscopy KPFM measurements on the layers. It is worth noting that the measurements were performed under ambient atmosphere, in the dark and without HTL. These conditions are different from real operating conditions under light exposure. However, such measurement can provide valuable preliminary information on the energetic configuration of the selective contacts. Also, reference materials such as gold, ITO and FTO were initially tested in order to evaluate the relevance of our estimations with regard to the literature. The result is presented in the Table III.5.

The WF of both ITO and FTO are measured here at 4.9 eV and 4.8 eV respectively, for these materials these WF values are commonly reported in the literature [85, 86]. This validation of our experimental WF value data enabled us to evaluate the WF of the two ETL deposited on ITO or FTO or glass. The first observation is that the WO₃'s WF (5.4 eV) is higher than the TiO₂'s (5.2 eV). In fact, our measured value of the WO₃ WF (deposited on glass) is very close to the one communicated by the provider of the WO₃ solution which is 5.5 eV [84]. When the layer are deposited on the respective transparent conductive layer (FTO or ITO) the value of their WF tends to be decreased. For the WO₃ the new value of WF is 5.0 eV while for the TiO₂ the new WF is now below the WF value of FTO, at 4.5 eV. This means that the sole

knowledge of the value communicated by the producer is not enough to properly choose an ETL.

CONTROL LAYERS	MEASURED WORK FUNCTION (eV)
ITO	-4.9
FTO	-4.8
STACKING	MEASURED WORK FUNCTION (eV)
Glass/CH ₃ NH ₃ I _{3-x} Cl _x	-5.0 ± 0.2
Glass/WO ₃	-5.4
Glass/ITO/WO ₃	-5.0
Glass/ITO/WO ₃ /CH ₃ NH ₃ I _{3-x} Cl _x	-5.0 ± 0.2
Glass/TiO ₂ /TiO ₂ -mp	-5.2
Glass/FTO/TiO ₂ /TiO ₂ -mp	-4.5
Glass/FTO/TiO ₂ /TiO ₂ -mp /CH ₃ NH ₃ I _{3-x} Cl _x	-5.0 ± 0.2

Table III.5 - Work function measurements with KPFM technique

These differences in WF could give us an insight on the reason of the lower V_{OC} of the WO₃-based PSC, indeed, the V_{oc} is expected to be closely related to the absolute difference between the WF of the ETL and HTL, as illustrate in the Figure III.13. While the V_{OC} of the TiO₂-based PSC can reach more than 1100 mV [41, 42] that of WO₃-based devices is not expected to exceed 800 mV. The experimental V_{OC} measured for our TiO₂-based PSC (950 mV) seems to indicate that some significant loss mechanisms occur in our devices, such as charge recombination, these losses being probably less important in the case of TiO₂-based devices.

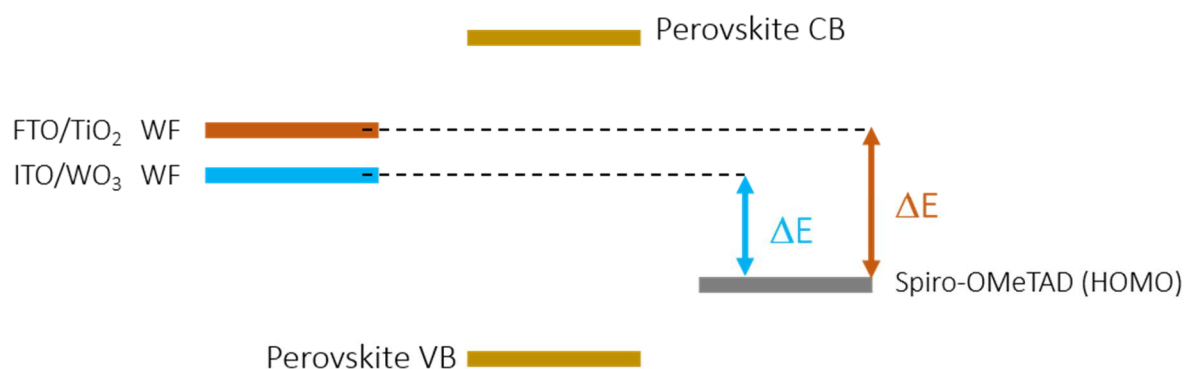


Figure III.36 - Illustration of the existence of a correlation between the values of the ETL WF and the V_{OC} of the PSC

As said previously the WF of WO₃ align with the one of ITO while this is not the case of the TiO₂ with the FTO, here the gap between each WF is about 0.5 eV. If we compare this gap of 0.5 eV and the actual 150 mV differences between the V_{oc} we observe a discrepancy. Indeed the WF of the perovskite is very close of the WF of the WO₃, which means that the

electron does need a lot of energy to overcome the energy barrier E_b to pass between each layer, almost 0 eV. If we consider the WF very close from the electronic affinity $e\chi$ we have in fact:

$$E_b = e\chi_{Perov} - e\chi_{WO_3} \quad (43)$$

But in the case if the TiO₂ layer, the value of E_b is of 0.5 eV which is in contradiction with a higher V_{OC} . We think that the measurements of the TiO₂ WF are distorted because of its roughness comparatively to the size of the KPFM tip (30nm). The measured WF is in fact an average between the actual TiO₂ and a voltage created by a capacitance between TiO₂, air (created by the porosity), and the tip itself. Moreover this interpretation can be modified by the existence of a built-in electrical field in the perovskite layer during illumination.

vi. Optoelectronic properties

One of the aspect to look is these devices are the photoluminescence (PL) of the perovskite material and the effect of the ETL, WO₃ or TiO₂, on charge extraction or excitation recombination time. The steady-state PL measurements can give is an insight of the quality of the perovskite layer and a comparison of the quenching in different conditions. Meanwhile, the time-resolved PL decay measurements will provide information on the mechanisms mainly governed by the interfacial charge transfer processes (electron transfer), leading to a relevant assessment of the general trends of the charge transfer efficiency of our ETLs.

Steady-state photoluminescence

For this characterisation perovskite layers were illuminated at 509.2 nm and the photoluminescence emissions count was observed between 700 nm and 820 nm. The comparison has been made between a simple layer of perovskite spincoated on top of a glass substrate and annealed at 90°C, and with perovskite layers processed in the same conditions that of a complete PSC fabrication, except no HTL or top electrode was deposited. The 509.2 nm excitation was performed under the same direction than the solar illumination, that is to say through the glass and through the ETL before to be absorbed by the perovskite layer. This illumination condition aim to simulate the true functioning of the PSC and to help discriminate the charges transfer mechanisms occurring at the interface. The delay between each wavelength is 600 ms and the step is 2 nm while the photons count was performed 4 times and added up, the resulting curves are presented in the Figure III.37.

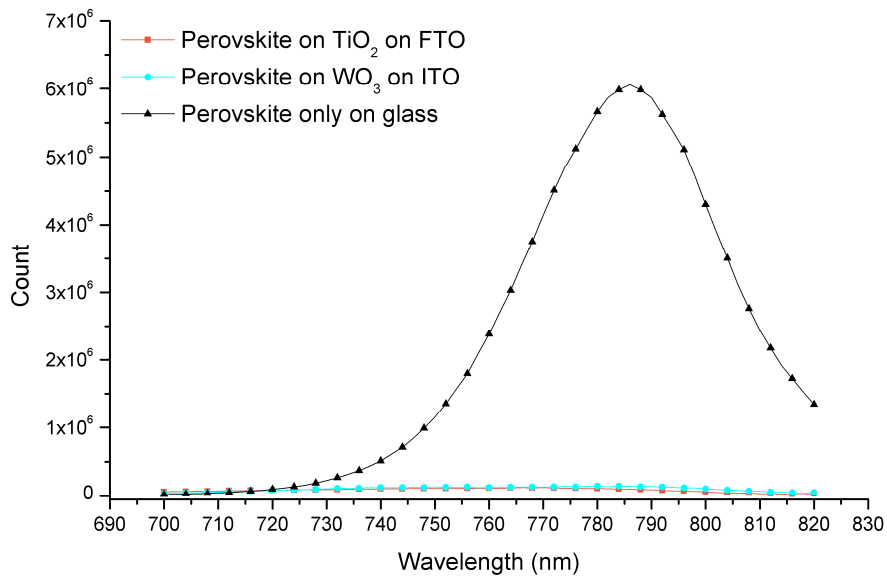


Figure III.37 - Steady-state PL measurements of perovskite layers on ETL and on their respective transparent conductive layer

The comparison between the peak intensity of the PL of the perovskite with or without an ETL indicates that with no ETL a large number of the exciton recombines in radiative mechanism. That means that, as expected, the TiO₂ promote non-radiative mechanisms like electron extraction. As for the WO₃, when compared to the TiO₂ the difference is not meaningful but we see that this new layer would be a good ETL.

Time-resolved PL decay

In order to discriminate the effect of both ETL time-resolved PL decay (TPLD) was performed on the same perovskite layers 3 days and 11 days after their production (with a storage in ambient atmosphere and in dark). For this characterisation each perovskite layer was illuminated with a 509.2 nm laser and the time before a radiative recombination (at 780 nm) was measured. These measurements are summarized in the Figure III.38, for the sake of reading the curve for the perovskite alone is not represented, as its decay time is extremely lengthy and would appear as a flat signal. In this graph, the instrument response function (IRF) is also represented, this IRF curve represents the minimum time resolution of the detector. As seen in the decay graphs the quenching of the charges are more effective on TiO₂ as the slope of the decay curve is steeper in this case.

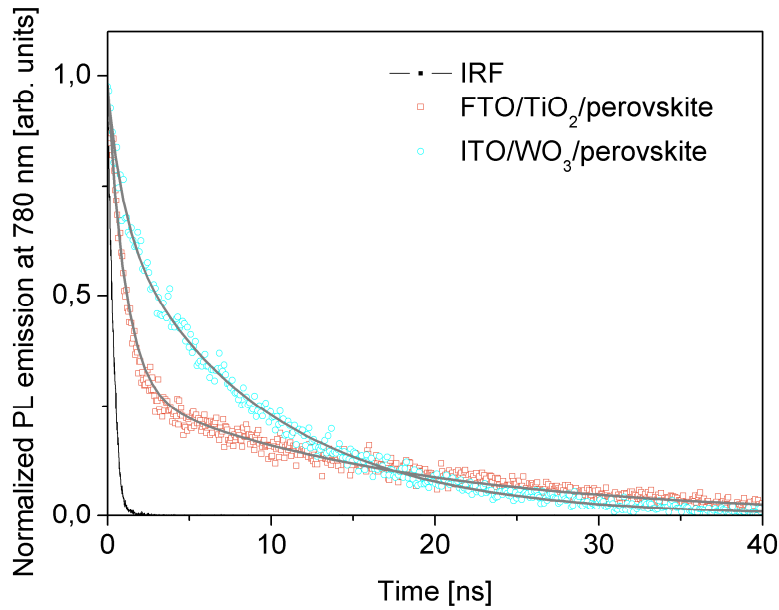


Figure III.38 - TRPLD curves of perovskite layers on ETL on their respective TCL

In order to have a more quantitative analysis we performed an exponential fitting of the raw data. More precisely, bi-exponential decay functions was used for the measurements for perovskite on ETL and a mono-exponential decay function was used for the perovskite layer on glass, the results are represented is the Table III.6:

$$y(t) = a + a_1 e^{-\frac{t}{\tau_1}} \quad (44)$$

$$y(t) = a + a_1 e^{-\frac{t}{\tau_1}} + a_2 e^{-\frac{t}{\tau_2}} \quad (45)$$

		a_1	τ_1 (ns)	a_2	τ_2 (ns)	τ_a (ns)	η_{CT} (%)	$k_{CT} \times 10^{-8}$ (@ $t = 0s$) (ns)
On glass		-	-	661	238.1	238.1	-	-
On TiO₂	Day 3	3965	1.1	329	16.6	2.29	99.0	6.6
	Day 11	3312	1.2	304	16.3	2.47	99.0	6.3
On WO₃	Day 3	1377	1.2	780	9.8	4.31	98.2	3.3
	Day 11	722	1.8	778	10.3	6.2	97.3	2.3

Table III.6 - Life time constants of perovskite on the different ETL and on glass

With τ_1 and τ_2 corresponding to the decay time constants, and a_1 and a_2 to the amplitude of both components respectively. The radiative recombination of free excitons is reported in various reports to be relatively long-lived for $CH_3NH_3PbI_{3-x}Cl_x$, either deposited using physical

vapour deposition or solution processed [28]. In the presence of the ETL, a fast (τ_1 in the order of 1-2 ns) and a slow (τ_2 in the order of 10-20 ns) components are observed for both TiO_2 and WO_3 -based PSC. Both ETL exhibit quite different morphology, the TiO_2 mesoporous is principle thicker (in the order of 200 nm) and much more porous (around 60% of porosity) while the WO_3 layer is only 50 nm with a 30 % porosity. Consequently, the amount of perovskite material deposited on TiO_2 is expected to be slightly larger than that deposited on WO_3 . Such trend is confirmed by the UV-visible absorption spectra of both samples (Figure III.30), especially for the domain of excitation a 509.2 nm. In order to compensate this difference in absorption the PL data were normalized with regard to the optical density of the films at the excitation wavelength (509 nm). Moreover, it was reported that all photo-generated charge carriers can reach the interface with the ETL, due to large charge diffusion lengths of hybrid perovskite up to 1 μm [28]. In these conditions, PL decays are representative of the ability of the ETL to efficiently collect photo-generated electrons from the perovskite layer. Here, we clearly evidence that the fast component is slightly shorter for TiO_2 compared to WO_3 for both fresh (3 days) and aged samples (11 days). These observations are consistent with the larger photocurrents evidenced for full devices measured under full sun where the contribution of the perovskite absorption is found to be larger on TiO_2 . The slow component is however found to be slower for TiO_2 than WO_3 . Such observation could be a consequence of thicker perovskite layer in this case, through a signature of delayed charge transfer events following charge diffusion to the interface. With only a minor increase of all time constants, aged devices show a similar trend, which indicates that no drastic influence of aging conditions on charge transfer mechanisms can be observed. In order to get a more quantitative picture of the transient behaviour of the samples, we have computes the weighted average PL lifetime τ_a [87] and the charge transfer efficiency η_{CT} of the ETL:

$$\tau_a = \frac{a_1\tau_1 + a_2\tau_2}{a_1 + a_2} \quad (46)$$

$$\eta_{CT} = 1 - \frac{\tau_a^{\text{perovskite on ETL}}}{\tau_a^{\text{perovskite on glass}}} \quad (47)$$

The results show that both layers efficiently collect photo-generated electrons from the perovskite film. Such observation is consistent with the PL quenching seen in Figure III.37 and with similar calculated charge transfer efficiency previously reported [88]. Considering the

similar order of magnitudes evidenced, the charge transfer rate (k_{CT}) is a better indicator to quantify the efficiency of the considered ETL. A suitable procedure consists to evaluate the natural logarithm of the ratio of the PL decay of the perovskite on ETL layers to the PL decay of the perovskite on glass. The time-dependent charge transfer rate is therefore given by [87] :

$$k_{CT}(t) = -\frac{d}{dt} \left(\ln \left(\frac{PL_{perovskite\ on\ ETL}}{PL_{perovskite\ on\ glass}} \right) \right) \quad (48)$$

$k_{CT}(t)$ are plotted in Figure III.39, showing an absolute order of magnitude of $\sim 10^8\ s^{-1}$, comparable with that of efficient photo-electrochemical systems such as TiO_2 -based dye-sensitized solar cells [87].

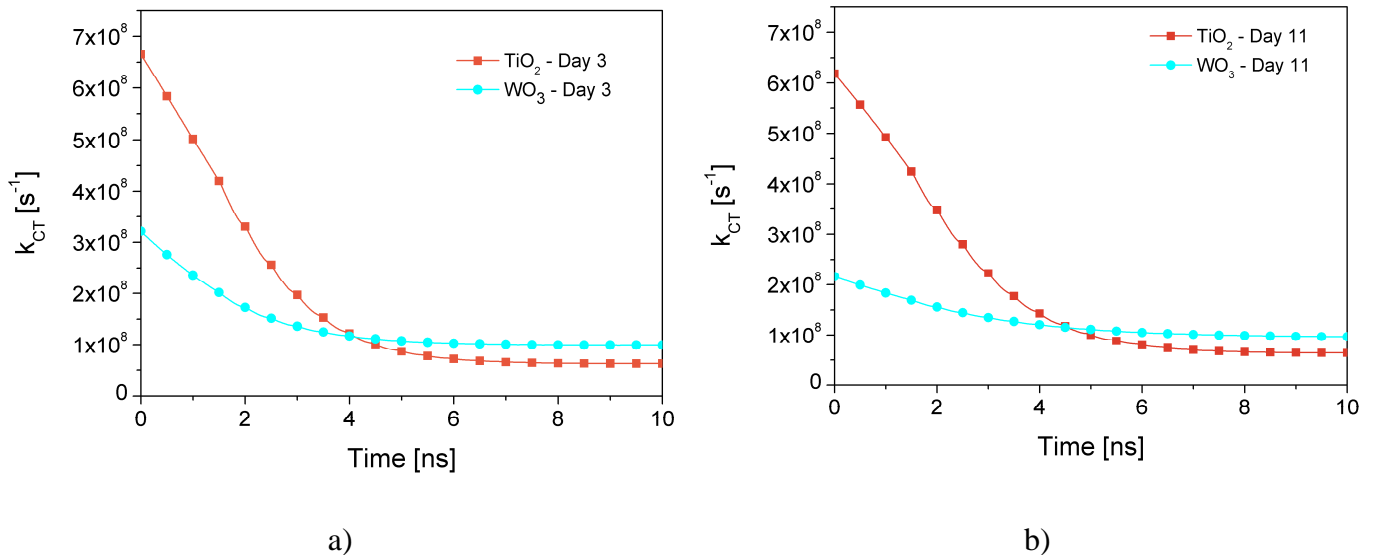


Figure III.39 - k_{CT} curves of perovskite layer on TiO_2 and WO_3 , after 3 days (a) and 11 days (b)

From these data, the charge transfer rate of TiO_2 remains twice larger than that of WO_3 , confirming that the layer remains a better electron acceptor for the perovskite layer, both for fresh and aged devices. A rapid electron injection to TiO_2 reduces radiative charge recombination in the perovskite, leading to efficient current generation. Upon aging during one week in the dark and under ambient conditions, k_{CT} remains almost unchanged. This exploitation of TRPL have as main result that the charge transport kinetics (including either non-radiative recombination, electron transfer, and interface charge trapping) are not modified upon storage in dark and ambient atmosphere, as long as the Spiro-OMeTAD HTL is not involved.

vii. Stability issues

Stability

The modification of one layer, the two TiO₂ layers (dense and mesoporous) being replaced by one layer of WO₃, have of course an impact on performances and on stability. In this section we will focus on the principal results and main interpretation concerning the stability of the WO₃-based PSC comparatively to that of TiO₂-based PSC.

As shown previously the WO₃ layer absorbs mainly in the UV part of the illumination spectrum (Figure III.29), below 350 nm. Moreover we know the influence of UV light exposure on large gap metal oxide materials (like WO₃), such optical absorption could also play an important role regarding device operation, aging and degradation. Indeed a simple comparison with the well-known UV-absorption behaviour of TiO₂, particularly when formed as a mesoporous layer, is possible. This behaviour has been described in the previous III.1.viii. section on TiO₂-based PSC stability

We propose that similar mechanisms associated with the presence of this oxygen vacancies mechanism occur within the WO₃ layer. Indeed, WO₃ is known to present oxygen vacancies associated with W⁵⁺ and W⁶⁺ sites [89]. Furthermore, the density of oxygen vacancies have been found directly dependent on the processing temperature of the films: the hotter it is heated the more it gets oxygen deficiencies [89]. Anyhow the annealing of WO₃ is necessary to completely remove the solvent and to obtain a good film homogeneity. In addition, depending of the method used for the production of the commercial WO₃ nanoparticle suspension, more oxygen vacancies can be produced if the synthesis was made under nitrogen atmosphere. In our process the WO₃ layer is formed just before the perovskite deposition since its electric properties tend to degrade when exposed to air humidity. The presence of a large amount of unpassivated oxygen vacancies would then induce a fast deterioration of the WO₃-based solar cells under unfiltered solar illumination, compared to TiO₂-based system. Moreover, WO₃ layer absorbs much more in the UVs than the TiO₂ even if it is thinner, which means that if our hypothesis is exact, the effect of UV on the oxygen vacancies is much more intense on WO₃. However; the more oxygen vacancies they are the more conductive is the WO₃ layer [90], thus the presence of the oxygen is beneficial for the overall performances, as long as the PSC is not exposed to UV containing light.

It is also possible to link the presence of the oxygen vacancies into the WO₃ with the results from the PL measurements showing the presence of water in the perovskite layer (Figure

III.40). As said previously the shifting of the peaks toward 770 nm reveals the presence of water. Comparatively to the TiO₂-based PSC the water is present as soon as 2 days after the production, indicating that water is already present in the WO₃ layer, or at least diffuse very quickly is the case of WO₃-based vacancy. Indeed, oxygen vacancies could also provoke water adsorption at the interface of the WO₃. Additionally, water molecules be produced trough the reaction of the WO₃ with hydrogen atoms forming H₂O molecules [91, 63]

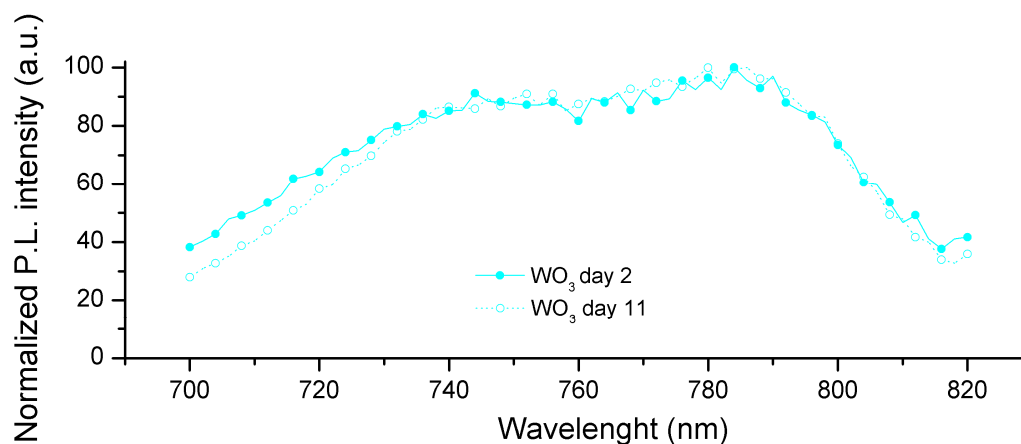
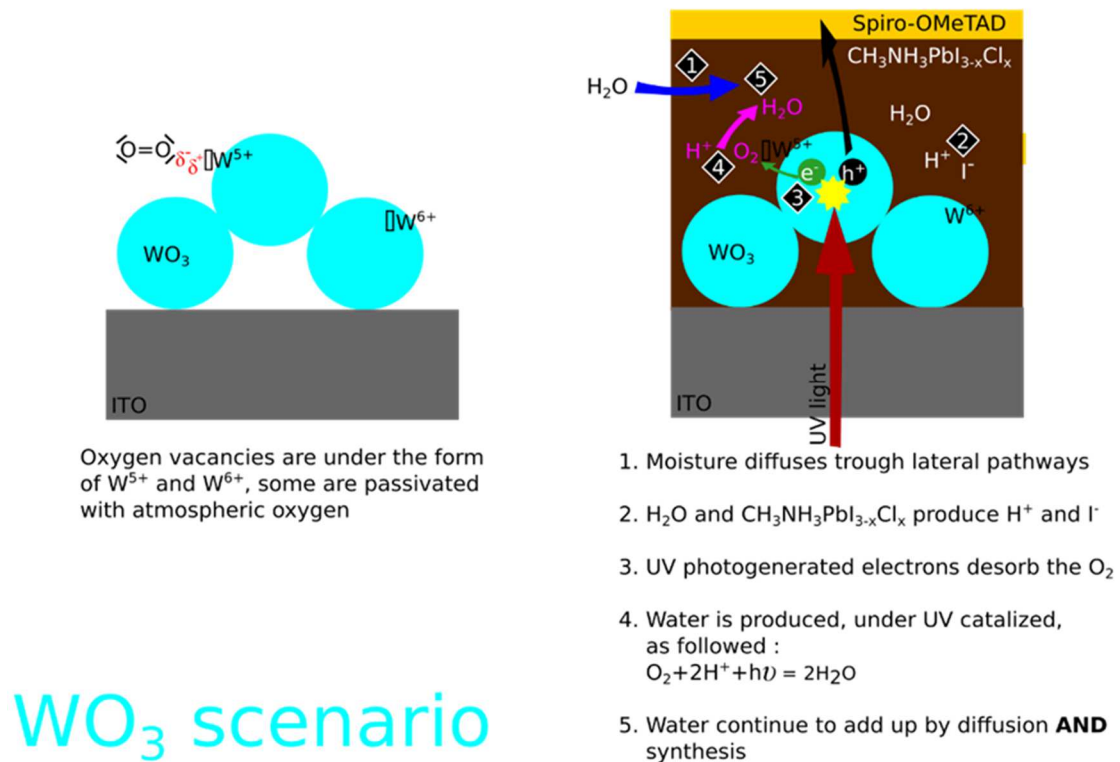


Figure III.40 - Steady-state PL measurements of perovskite layers 2 days and 11 days after the production on WO₃ ETL

Consequently, a reaction between WO₃, perovskite and water is proposed and resumed in the Figure III.41: this reaction being catalysed by the photo generation of excitons into the WO₃ following the UV exposure and the consecutive desorption of oxygen. Before the spincoating of perovskite, H₂O could be already present in the WO₃ layer, due to the presence of the O₂ vacancies and explaining the non-evolving shape of the PL spectra. Indeed, a non-covalent bound is created between oxygen of the O₂ and electron vacancy of the W⁵⁺ and W⁶⁺. After the spincoating of the perovskite the first step of degradation is the water diffusion from the non-protected sides of the perovskite layer. Production of water could also be occurring within the perovskite layer, as it may contain H⁺, resulting from the perovskite degradation by ambient humidity [92]. This H⁺ would react with O₂ at the surface of the WO₃ whose desorption would be facilitated by the production of electron by UV absorption of the WO₃. Moreover, WO₃ is known to be an efficient insertion material, which can therefore carry additional protons into its structure constituting another source of hydrogen species [93]. Tungsten oxide is also expected to actively produce reactive oxygen species (ROS), and exhibits a strong photocatalytic activity [94, 95]. Two mechanisms occur in the same time: the degradation by moistures absorption, again, and by water synthesis at the WO₃ surface due to the presence of a limited amount of oxygen vacancies. This should produce a bi-exponential decay in

photovoltaic performances whom one of the constant is correlated with the number of available passivated oxygen vacancies. If the cells are properly encapsulated the number of available passivated oxygen vacancies should tend to zero after few hours of exposition, resulting in a degradation comparable to the one of the TiO₂-based PSC.

To summarize (Figure III.42), ambient moisture can induce the degradation of the perovskite layer, forming H⁺ ions (step 1 then step 2). These ions would react with passivated oxygen vacancies in the WO₃ to form more water, this last reaction being catalysed under UV light (step 3 and step 4). The degradation of the perovskite layer is also likely to be enhanced in the case of WO₃, considering its high reactivity with oxygen species, as mentioned previously.



WO₃ scenario

Figure III.41 - Summarizing scheme of degradation in PSC

The same way that the perovskite of the TiO₂-based is sensible to photo-bleaching the same phenomenon occurs for the WO₃-based PSC. This can be seen in the Figure III.42 where the PCE of the cell is at 10 % of its initial value after 2 hours of exposition of UV-containing light and 4 hours when UV are suppressed from the light. This proves again the detrimental effect of the UV and that its suppression would be one of the key to improve the stability of the PSC. Of course, comparatively to the TiO₂-based PSC the WO₃-based PSC are less stable, since the reference TiO₂ PSC are at 10 % of its initial performance after 12 hours of illumination.

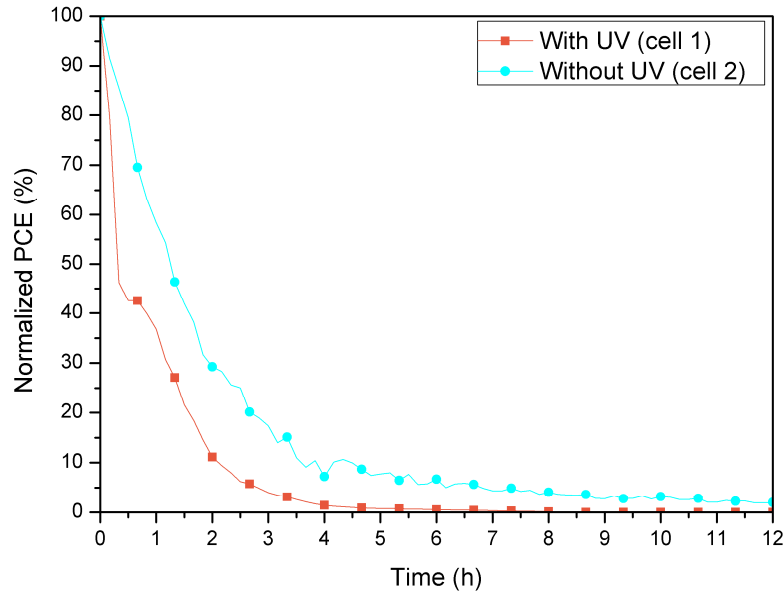


Figure III.42 - Stability of TiO₂-based perovskite solar cells

TiO₂-based PSC stored in black during few days tend to have different deterioration. At the day of the production the cells all work with similar photovoltaic parameters as presented in Figure III.43, for example the mean PCE is (with backward JV measurement) 4.5 % with a high standard deviation of 3 points. When stored 9 days in dark in ambient atmosphere this mean PCE increases to 7.5 % with a standard deviation of 1.0 points. This shows a trend: an increase of PCE and a decrease in the standard deviation for all WO₃-based PSC. All WO₃-PSC exhibits the same photovoltaic performances after 9 days of storage in ambient atmosphere and in dark. The J_{SC}, the V_{OC} and the FF behaviour toward storage is of course the same. Spiro-OMeTAD needs to be doped by atmospheric oxygen to function properly [70, 71] and could be one of the origin of the increase in PCE but does not explain alone the difference with TiO₂-based PSC which are less stable toward storage, even if these cells contains also this HTL.

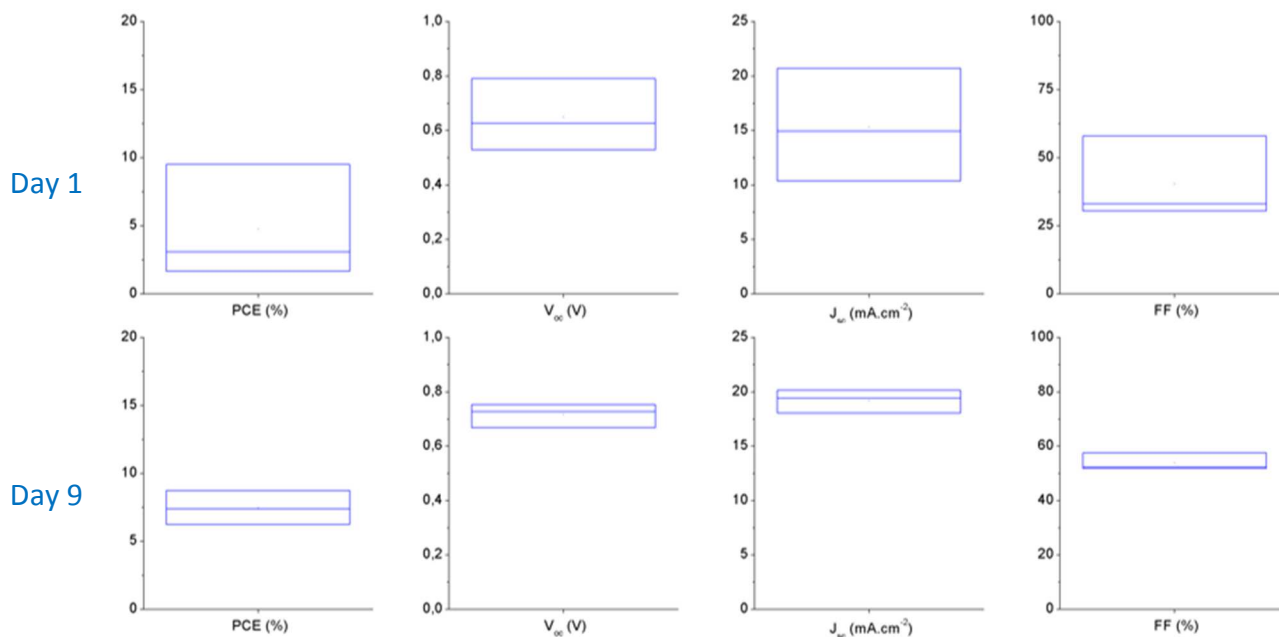


Figure III.43 - Backward JV measurements for WO_3 -based PSC at their production day and 9 days later.

3. UV protection of perovskite solar cells

i. Introduction

In this section we propose to evaluate the effect of a luminescent downshifting molecule to enhance the performances of PSC while protecting them from the ultraviolet (UV). The goal of this work is to use a S-tetrazine (NITZ, Figure III.44) molecule in a down-shifting layer in order to protect our PSC from UV light and to re-emit in the visible spectrum to enhance the PCE of the PSC or, at least, to compensate the loss in absorbed light.

Figure III.44 - NITZ molecule

This strategy has been already used several times: by Komarala et al. [96] who used a spray deposition of SHMP (sodium hexametaphosphate) capped $\text{YVO}_4:\text{Eu}^{3+}$ nanophosphor layer. This specie is excited in the UV mostly between 200 and 310 nm and emits in the red at 614 nm. This layer deposited on the back of PSC with $\text{CH}_3\text{NH}_3\text{PbI}_3$ as sensitizer and TiO_2 as

ETL allowed to enhance the PCE from 7.42 % to 7.92 %. After a 12 h exposition 52 % of the initial PCE remain, against 35 % for the control PSC (without $\text{YVO}_4:\text{Eu}^{3+}$ layer). More recently Bella et al. [97] used a classical organic fluorescence brightener in a fluoropolymeric capping layer. This molecule is excited around 370 nm and emits at 440 nm and is used on top of a PSC whose photoactive layer is a mix-halide formamidinium perovskite which almost does not absorb under 400 nm. This structure increased the average PCE from 17.31 % to 18.67 %. However, this is not clear if these molecules really improve the long-time stability of the devices since the fluoropolymer layer is already very efficient to stabilize the PSC [98].

ii. Optical properties

In order to measure the optical properties and to use the NITZ molecules polystyrene film containing the NITZ molecule has been produced on quartz substrate. A solution of toluene with a weight concentration of 20 % in PS (polystyrene from Sigma-Aldrich with an average molecular weight of 192000) and 0.3 % in NITZ is prepared and then spincoated on the quartz substrate at 6000 rpm and dried 5 min at 90°C in air. The produced film has a weight concentration is NITZ of 1.5 % and a thickness on 1.2 μm .

Different optical measurements are presented in the Figure III.45, please note that to ease the reading all values have been normalized. NITZ molecule, taken alone is solution, has a main excitation range between 250 and 375 nm with a maximum at 350 nm, which is well placed as it is entirely below the visible light range, in the near-UV region. The emission range of the molecule (excited at 350 nm) is found between 525 nm and 650 nm with a maximum at 580 nm, which is also ideally placed since it is where the perovskite active layer absorbs and photo-generates the most (the absorption spectrum of the perovskite active layer can be found in Figure S1 in the ESI). This photoluminescence is due to a $\pi \rightarrow \pi^*$ transition [99]. It is worth noting that this molecule also has a way less sensitive excitation domain around 550 nm due to a $n \rightarrow \pi^*$ transition [99]. The optical transparency of the NITZ:PS film is found to be very high in the visible range, over 350 nm, with more than 91% transmission. A transmission drop down to 45% occurs around 375 nm, where the molecule absorbs light.

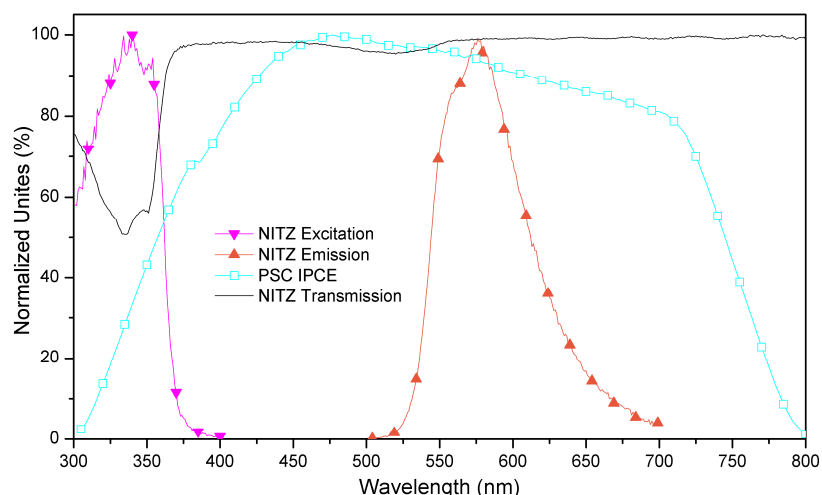


Figure III.45 - Excitation (magenta line) and emission (orange line) spectrum of NITZ molecule, PS/NITZ film transmission (black line). IPCE spectrum (cyan line) of our PSC.

This down-shifting layer was subsequently evaluated using our reference TiO_2 -based PSC which are composed of a FTO (fluorine doped tin oxide) in transparent conductive layer (TCL) covered by a dense TiO_2 layer and a mesoporous TiO_2 layer playing the role of ETLs. The photo-active layer is based on the reference methylammonium lead iodide chloride ($\text{CH}_3\text{NH}_3\text{PbI}_{3-x}\text{Cl}_x$) perovskite and the HTL is Spiro-OMeTAD layer doped by Li-TFSI and tert-butylpyridine. A gold top electrode is finally evaporated under vacuum, leading to the final structure FTO/ TiO_2 / TiO_2 -mp/ $\text{CH}_3\text{NH}_3\text{PbI}_{3-x}\text{Cl}_x$ /Spiro-OMeTAD/gold. In a similar way, the WO_3 -based PSC are designed with structure ITO/ WO_3 / $\text{CH}_3\text{NH}_3\text{PbI}_{3-x}\text{Cl}_x$ /Spiro-OMeTAD/gold where the WO_3 layer, deposited from spin-coating from a commercial suspension, plays the role of low-temperature ETL.

iii. Utilization of the down-shifting film for PCE enhancing

Five PSC with TiO_2 as ETL were exposed during 9 minutes under an AM 1.5 G100 $\text{W}\cdot\text{m}^{-2}$ solar simulator with a 0.20 cm^2 aperture mask. Between the PSC and the light source were disposed alternatively every minute a quartz substrate with only a PS film or a quartz substrate with a NITZ-embedded-PS film. Every minute a current density / voltage characteristics (or JV curve). This experimentation was designed to discriminate two independent phenomena: the actual effect of the down-shifting filter, and the natural PCE evolution of the cell under illumination and electric solicitations. Figure III.46 shows the mean evolution of the PCE comparatively to the PCE of the previous minute of the TiO_2 -based PSC, as well as the standard deviation. The first point of the graph corresponds to the quartz substrate

covered by a pristine PS film only, noted as Q. The second point corresponds to the use of the NITZ down-shifting film (noted N), and so on.

The Figure shows that using a down-shifting layer to enhance the PCE of our PSC is not efficient. A slight positive influence of the strategy is only seen after 5 minutes of exposure. Before this point, the use of a NITZ-loaded layer tends to lower the overall device efficiency. We also note that the standard deviation remain significant, so that it is difficult to conclude even if the positive trend seen after a few minutes is reproducible. Despite this observation, we now investigate the reasons of this negative influence of the down-shifting layer in order to guide further developments in this field.

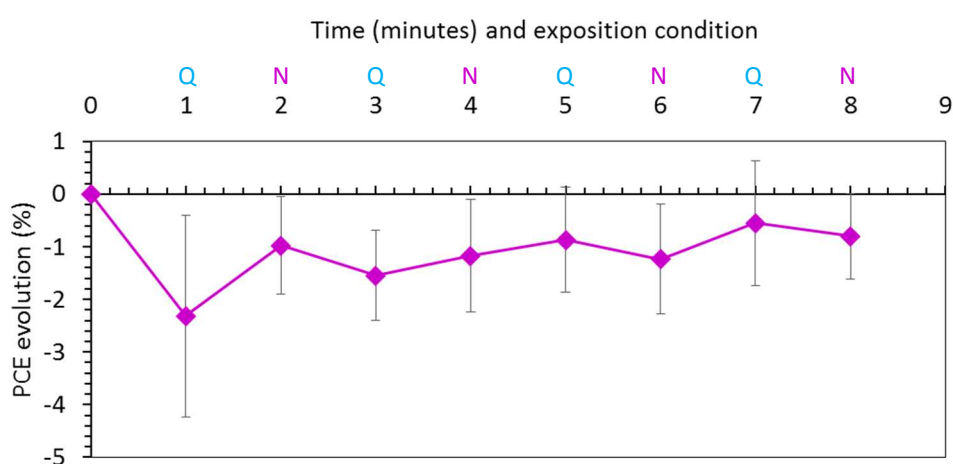


Figure III.46 - Mean evolution of PCE of 5 PSC during nine minutes under an AM 1.5 100 W.m^{-2} illumination, being alternatively exposed to UV-containing light (Q) and NITZ-filtered light (N)

Incident-Photon-to-electron Conversion Efficiency (IPCE) measurements were conducted on TiO_2 -based PSC (Figure III.47) by placing either a NITZ-embedded PS film or a bare PS film between the tungsten continuous light source and the PSC. For this graph the value was normalized from the IPCE value at 650 nm of the TiO_2 -based PSC and from the IPCE value of the same cell with the NITZ whose photo-generated current (at 650nm) was reduced by 5 % to reproduce the 95 % transmission of the NITZ film at 650 nm (Figure III.45). At wavelengths in the excitation range of the NITZ (around 340 nm), the IPCE of the device is lower using NITZ than without, due to the direct absorption of incident photons by the down-shifting molecules, reducing the corresponding amount of photons able to be converted into charge carriers in the perovskite active layer. It can be noted that the reemission of the NITZ layer at this wavelength seems to not be sufficiently efficient to cover the direct absorption of the NITZ. We will now explain that in deeper.

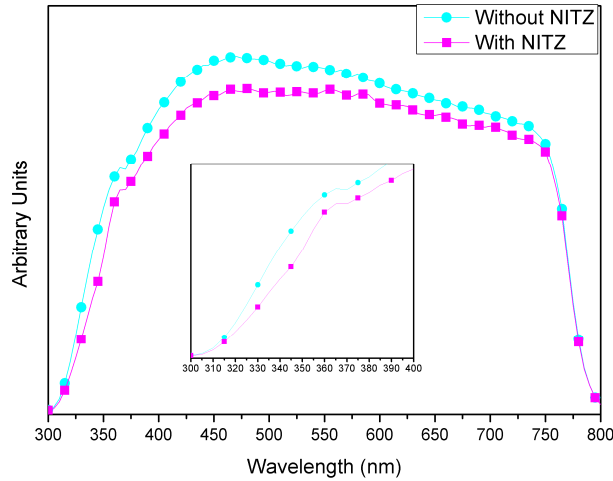


Figure III.47 - IPCE of TiO₂ PSC with or without NITZ film

We can summarize this problematic by defining a ratio X taking into account QY of the down-shifting layer and the efficiencies of the PSC in the excitation spectrum and emission spectrum of the down-shifting molecule:

$$X = QY \times \int_{\lambda_{exc}} R \times \frac{\int_{\lambda_{emi}} \frac{P_{elec}(\lambda)}{P_{lum}(\lambda)} d\lambda}{\int_{\lambda_{exc}} \frac{P_{elec}(\lambda)}{P_{lum}(\lambda)} d\lambda} \quad (49)$$

Where P_{elec} is the electric power produced by the PSC in function of wavelength, P_{lum} is the illumination power of the lighting source in function of the wavelength. Last is defined either for λ_{emi} the emission domain of the down-shifting molecule (i.e. 475 – 550 nm), and λ_{exc} its excitation domain (i.e. 250 – 375 nm). The R factor is present in this formula in order to take account of the NITZ emission which do not have a preferred direction (50% is emitted in the wrong direction) and the limit angle of refraction (total reflexion limit) between the polystyrene film and the quartz substrate. For example the refractive index of PS at 520 nm is 1.6, according to the literature, and the quartz refractive index was fixed at 1.55 giving a limit angle of 75.6°. We can evaluate the R factor at 520 nm to be given by $0.5 \times \frac{75.6}{90} = 0.42$.

When X is superior to one then the energy produced by the system PSC/down-shifting layer is greater than the one produced by the PSC alone and the use of this down-shifting material is relevant. To help identify the situation a graphical representation of this equitation is presented in the Figure III.48. This graphical representation indicates that the most important factor is the PSC efficiency in the excitation range of the down-shifting molecule. Indeed, under certain condition the use of a down-shifting layer is relevant even with an EQY of 15 % of the

down-shifting molecule, but the IPCE in the excitation range must not be higher than 35 % in this case. Here, the NITZ EQY is around 30 % as measured by photoluminescence spectroscopy with an integrating sphere, and the IPCE of our perovskite device without NITZ is in average of 30% in the excitation range of the NITZ. To be really efficient on this kind of PSC, such down-shifting material should have an EQY higher than 85%. This simple evaluation can thus quite easily explain our experimental results in terms of PCE evolution with and without the down-shifting layer. Nevertheless, even if this layer is not able to efficiently improve the J_{sc} of perovskite solar cells, they still act as a UV-filter where a part of the UV light is recycled for the generation of photo-current, which is a useful advantage compare to a standard UV filter. The gain of a down-shifting UV filter is close to its EQY (for light emitted towards the active layer) of reemission in the good direction. This corresponds, in our case, to 15% of useful reemission, in a spectral range where the perovskite has in average 70% of IPCE. This effect is therefore completely significant, if it can also have a positive impact on device stability, as we discuss in the following sections

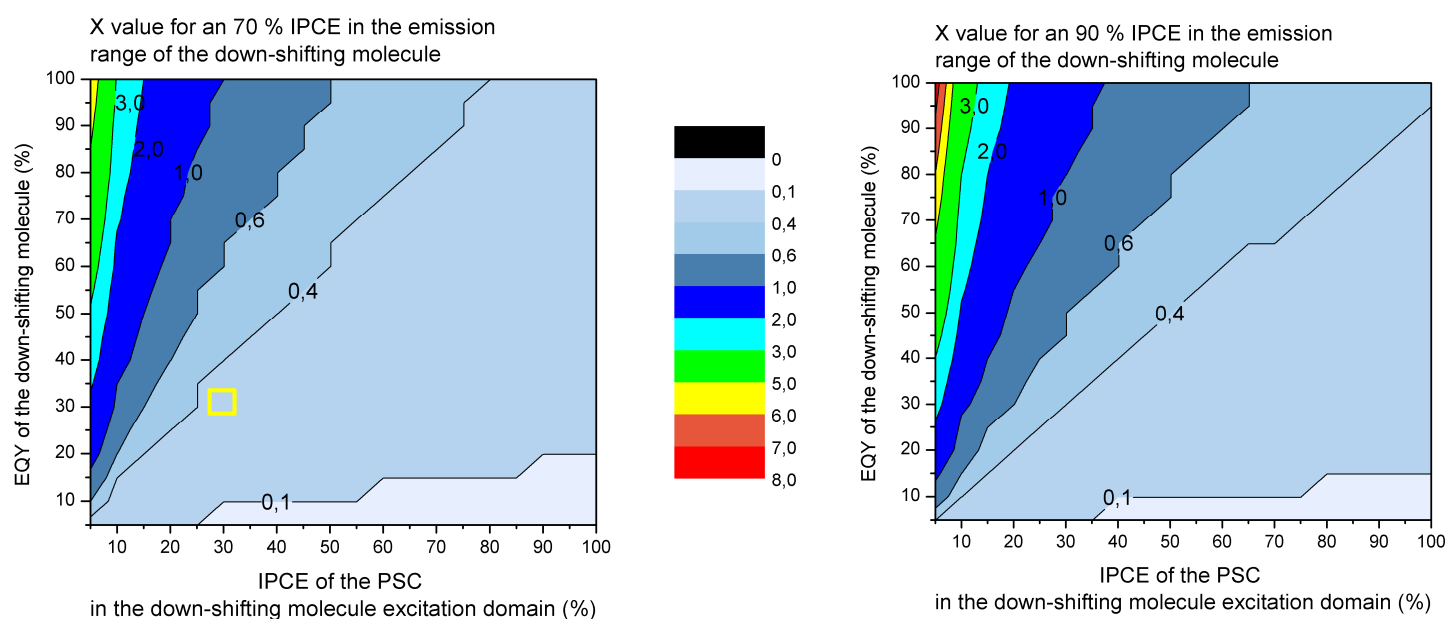


Figure III.48 - Graphical representation of the X calculation for two value of the IPCE of the PSC (70 and 90 %) in the emission range, depending of the efficiency (from 5 to 100 %) in the excitation range and the EQY. The situation of our PSC/NITZ system is framed in yellow.

The utilisation of the NITZ molecule to enhance the PCE of the P3HT:PCBM organic solar cells has already been proven to be efficient: the PCE has been increased by 6%. In the case of these organic solar cells its IPCE at 550 nm is 70 % and 5 % at 350 nm. Therefore, the

X value for this system is 4.3 showing that the strategy to use NITZ for P3HT:PCBM is efficient.

iv. Beneficial effect of UV-protection on device stability

The use of NITZ does not enhance the PCE of our PSC, however, since it absorbs UV and re-emits the energy in the visible range, it should be able to help stabilizing the solar cell operation and protect them against UV-induced deterioration. In order to assess the relevance of this strategy, three TiO₂-based PSC and three WO₃-based PSC with comparable photovoltaic parameters (Table III.7) were exposed during more than 14 h to simulated solar illumination, using a class A solar simulator whose irradiance spectrum is given as SI in Figure S2. For each cell, different conditions were used condition: UV-filtered (only the quartz substrate with pristine PS and a UV filtering glass), non-UV-filtered (only the quartz substrate with pristine PS is used in this case) and NITZ-protected (with the polystyrene film embedded with NITZ on quartz).

Electron Transporting Layer	TiO₂			WO₃		
	<i>A</i>	<i>B</i>	<i>C</i>	<i>1</i>	<i>2</i>	<i>3</i>
Cell number						
PCE (%)	8.6	9.6	8.6	7.5	7.7	7.5
J_{sc} (mA.cm⁻²)	17.7	15.3	15.6	21	18.3	20
V_{oc} (mV)	857	831	796	724	700	663

Table III.7 - Photovoltaic parameters of PSC before the stability measurements

The evolution of power conversion efficiencies of the devices based on TiO₂ and WO₃ ETL are summarized in Figure III.55. The TiO₂-based PSC are a little more stable when protected from UV radiation (with UV filtering glass or NITZ), particularly in the first five hours. When the TiO₂-based PSC are UV-protected the PCE drops to 40 % of its initial value after 3 h of exposition while the PCE of the not-UV-protected TiO₂-based PSC remains at 30 % of its initial value. However all three cells drop 30 % of the initial PCE after 6 h of exposition. Analysing in detail the different photovoltaic parameters (from Figure III.49 to Figure III.54) reveals that the short-circuit current (J_{sc}) is sensitive towards UV, UV-protected TiO₂-based PSC (with UV filtering glass or NITZ) keep 65 % of the J_{sc} initial value after 3 hours of exposition while the not-UV-protected TiO₂-based PSC only keeps 50 % of its initial photocurrent. The main difference of evolution between the three cells is clearly seen in the evolution of the fill factor (FF). Which increases by 10 points during the first two hours of exposure to UV. This could indicated that UV tends to stabilize the PSC in the first hours of exposure. The open-circuit voltage (V_{oc}) dropped for all TiO₂ PSC around 70 % of its initial

value after 6 h of exposition, following a rather linear trend, indicating that the only electrical parameters sensitive to the UV are finally J_{SC} and FF.

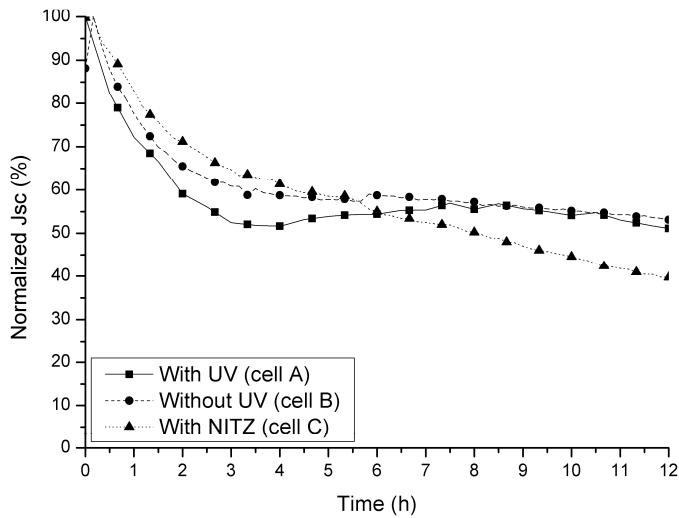


Figure III.49 - J_{SC} of TiO_2 -based PSC protected with UV filter (without UV), with NITZ or not UV-protected (with UV)

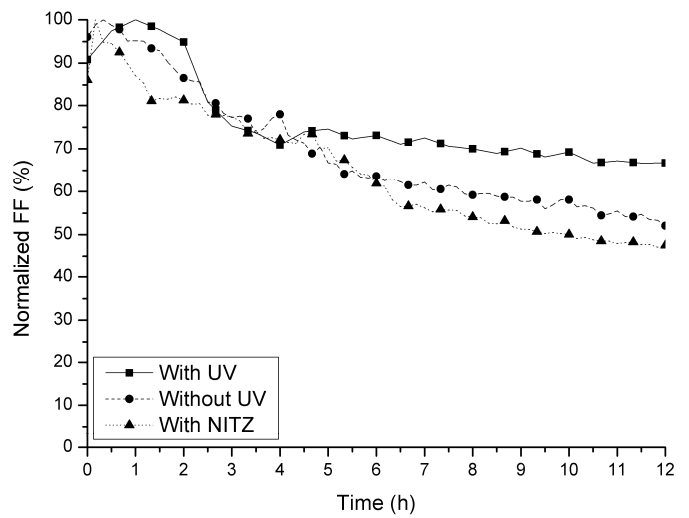


Figure III.50 - FF of TiO_2 -based PSC protected with UV filter (without UV), with NITZ or not UV-protected (with UV)

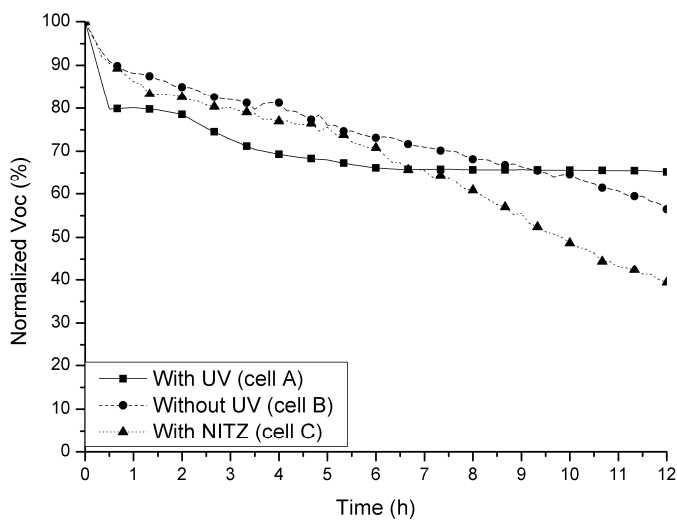


Figure III.51 - V_{OC} of TiO_2 -based PSC protected with UV filter (without UV), with NITZ or not UV-protected (with UV)

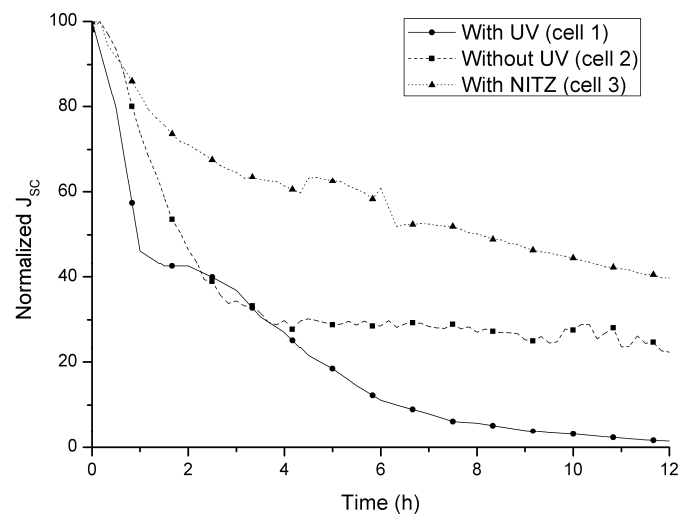


Figure III.52 - J_{SC} of WO_3 -based PSC protected with UV filter (without UV), with NITZ or not UV-protected (with UV)

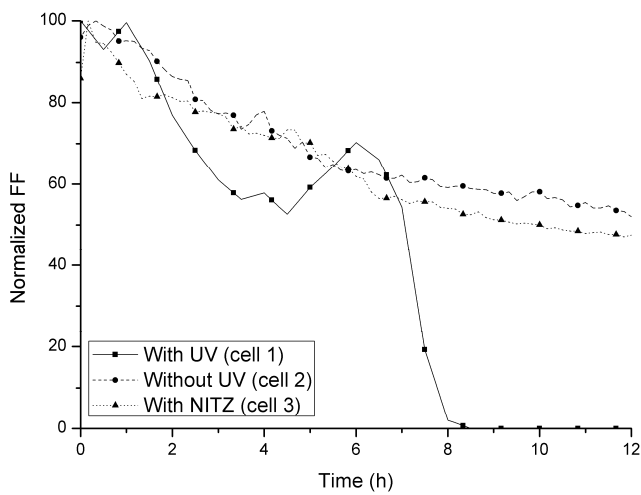


Figure III.53 - FF of WO_3 -based PSC protected with UV filter (without UV), with NITZ or not UV-protected (with UV)

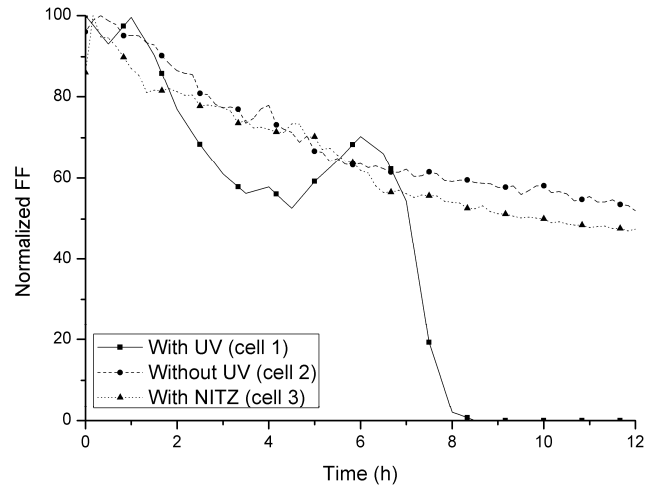


Figure III.54 - V_{OC} of WO_3 -based PSC protected with UV filter (without UV), with NITZ or not UV-protected (with UV)

The results for WO_3 -based PSC are more promising. Indeed, the PCE of the WO_3 -based cells decays slower when protected from UV with the NITZ film compared to the cells which are not protect of the UV, showing that UV is apparently detrimental to their light stability, as previously suggested in our previous article [29]. This is confirmed by the fact that the WO_3 -based PSC is slightly more stable when protected of the UV with the UV filter glass. With a NITZ film or UV-protected the PCE drops to 15 % of its initial value after 3h of exposition while the non-UV-protected WO_3 -based PSC PCE drops at the same level after 1h30 of exposition. This result also shows that although while the strategy of using a NITZ down-shifting film is not efficient to enhance the PCE of the WO_3 -based PSC, , it can at significantly helps their stability, while partially compensating the efficiency loss due to the use of an UV light filter.

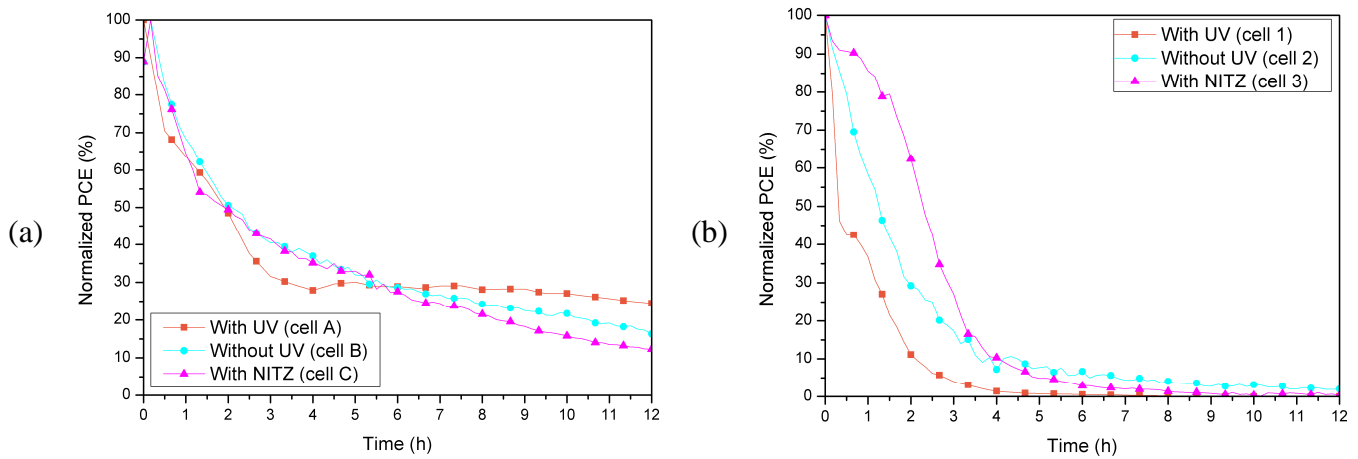


Figure III.55 - PCE of PSC protected with UV filter (without UV), with NITZ or not UV-protected (with UV) with TiO₂ (a) and WO₃ (b) as ETL

The beneficial effect of the protection from the UV for the WO₃-based PSC can be linked with the mechanisms exposed in the section III.2.vii (about the stability of the WO₃-based PSC). In fact since the UV are suppressed the adsorbed gaseous O₂ as the WO₃/perovskite interface cannot leave the oxygen vacancies and do not react to form water. As a result the WO₃-based PSC are more stable.

v. Stability of the NITZ molecule

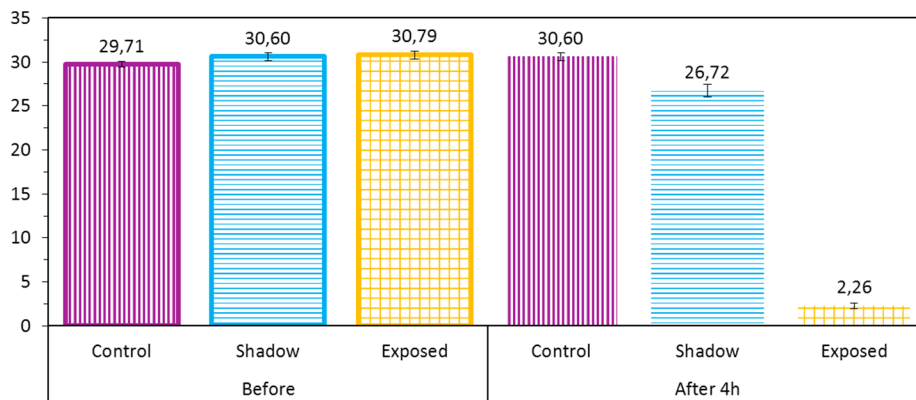


Figure III.56 - EQY of NITZ film after 4 h of solar light exposition

The difficulty to improve the PCE with our strategy lead us to study the stability of the NITZ molecule itself in terms of emission quantum yield (EQY) measured by photoluminescence spectroscopy using an integrating sphere. Nine quartz substrates were spincoated with NITZ-embedded PS films. Three of them were exposed during four hours under a 1 sun irradiance (AM1.5G, 100 mW.cm⁻²), three others were left aside in the dark but at the same temperature than the exposed cells (50°C), and the three remaining devices (the control substrates) were left in ambient condition.. Before and after the four hours, the EQY of each cell was calculated. The corresponding data are summarized in Figure III.56. These

measurements reveal that the NITZ films are unstable when exposed to solar illumination under ambient conditions. A photo-bleaching is indeed observed after the light exposure, and the EQY drops from 30 to 3 % only. The NITZ film seems also quite sensitive to temperature since the films unexposed to light lost 4 points of EQY, while the control sample fully retains his EQY. Our optical transmission measurements of the NITZ cells show that the films still absorb UV light even if the emission is very low. In the present case, the NITZ specie is not more efficient than a classical UV filter.

vi. Conclusion

Through JV measurements and IPCE characterization we showed that NITZ can temporarily act as a down-shifting and UV-protecting layer for $\text{CH}_3\text{NH}_3\text{PbI}_{3-x}\text{Cl}_x$ perovskite solar cells which already absorb and photo-generate in the UVs. Indeed, the EQY of this down-shifting specie is not high enough to increase the photovoltaic properties but can effectively recover a part of the absorbed UV light. The NITZ could be further investigated with different perovskites, like mix-halide or mix-cation hybrid perovskite, more fitted in terms of absorption spectrum. Our modelling shows that a good active layer candidate for this use should present an average IPCE lower than 10% in the spectral range of 250 and 375 nm. The specie presents a photo and thermal degradation after a 4 h of continuous exposition when used with polystyrene. In the present state, further experimentation is mandatory to find more suitable polymeric substrate and solvent which could allow a greater stability once deposited on film. The NITZ molecule has yet a great potential since its gap between its excitation domain and emission domain is very broad, almost 300 nm. We also confirm that cutting the UV from the incoming light tends to be beneficial for the stability of WO_3 -based devices, meaning that the WO_3 is way more sensitive to UV than the classical TiO_2 layer. Finally, this latter achievement allows to emphasize on the importance to protect some architecture of PSC from the UV, with a preferential use of a downshifting protection in order to compensate the J_{SC} loss when the UV light is cut.

IV. Printed perovskite solar cells

1. Introduction

The spincoating fabrication of a perovskite solar cell with 3 printable layers (ETL, perovskite and HTL) is now mastered. This cell, as resumed in the Table IV.1, match the objective in term of photovoltaic performances. The next step is the actual printing of the 3 inner layers.

	OBJECTIVES	BEST WO ₃ CELL COMPARISON
Photovoltaic parameters		
V _{oc} (mV)	830	791
J _{sc} (mA.cm ⁻²)	16	20.7
FF (%)	75	58
PCE (%)	10	9.5
Fabrication		
Active area	1 cm ²	20 mm ²
Electrode (ITO or FTO)	Non-printable	100 %
ETL	Printed	50 % (printable)
Perovskite	Printed	50 % (printable)
HTL	Printed	50 % (printable)
Top electrode	Printable	0 %
Max annealing temperature	130°C	100 %

Table IV.1 - Comparison between the objectives and spincoated printable WO₃-based PSC

The overall strategy was to replace gradually, from the bottom to the top, each spincoated layer by an inkjet printed layer. This strategy has been chosen since the printing of each layer depends of the surface of the previous layer. Once a layer is printed its surface energy, its thickness as wells as its roughness can vary from that of its spincoated version. Therefore, this gradual strategy is a good choice to correctly optimize the printing of each layer depending of the previous layer.

The first step was obviously to replace the spincoated WO₃ ETL by a printed WO₃ layer and to continue to process the 2 other layers by spincoating. After optimisation of the ETL printing the next step would be to go for the printing of the perovskite, on top of the printed ETL, while spincoating the Spiro-OMeTAD. The last step is of course the printing on the Spiro-OMeTAD on top of the printed WO₃ and printed perovskite.

Among the steps of printing optimisation this section will develop the ink characterization and formulation, the ejection parameters and wettability of each ink. Morphological characterisation like AFM or optical will be addressed. The photovoltaic parameters for each printed perovskite solar cell (with 1, 2 or 3 printed layers) will be measured as well as optoelectronic measurements. The stability and photo-degradation behaviour principles for printed WO₃-based PSC are considered as identical that for the spincoated WO₃-based PSC, and thus, will not be studied.

2. Design of the printed solar cell

The spincoated perovskite solar cell surface area is 20 mm², this size is limited by the gold electrode. The objective for the printing of the perovskite solar cell should be to reach larger active area, close to 1 cm². In order to also have a gradual strategy the active area was slightly increased to 0.33 cm², and this size is still limited by the size of the evaporated gold electrode which has been not changed. However, instead on printing the layers on all the width of the substrate (12 mm) it has been decided to print a smaller area. The printed WO₃ and perovskite layers have the same size (0.64 cm²) and the same position. The 0.42 cm² Spiro-OMeTAD area in contact with the perovskite layer is smaller in order to reduce the probability of contact between the HTL and the ITO. The HTL has been design to overlap the perovskite layer where the ITO is etched: this precaution has been taken to be sure that the gold does not touch the ITO or the WO₃ and in order to have a smoother offset for the evaporated gold between the superposition of the ITO, WO₃ and perovskite (more than 1.5 μm in total) and the bare glass surface. This HTL could be easily expanded to 0.54 cm². With a bigger gold electrode the active area could be extended to 0.42 cm².

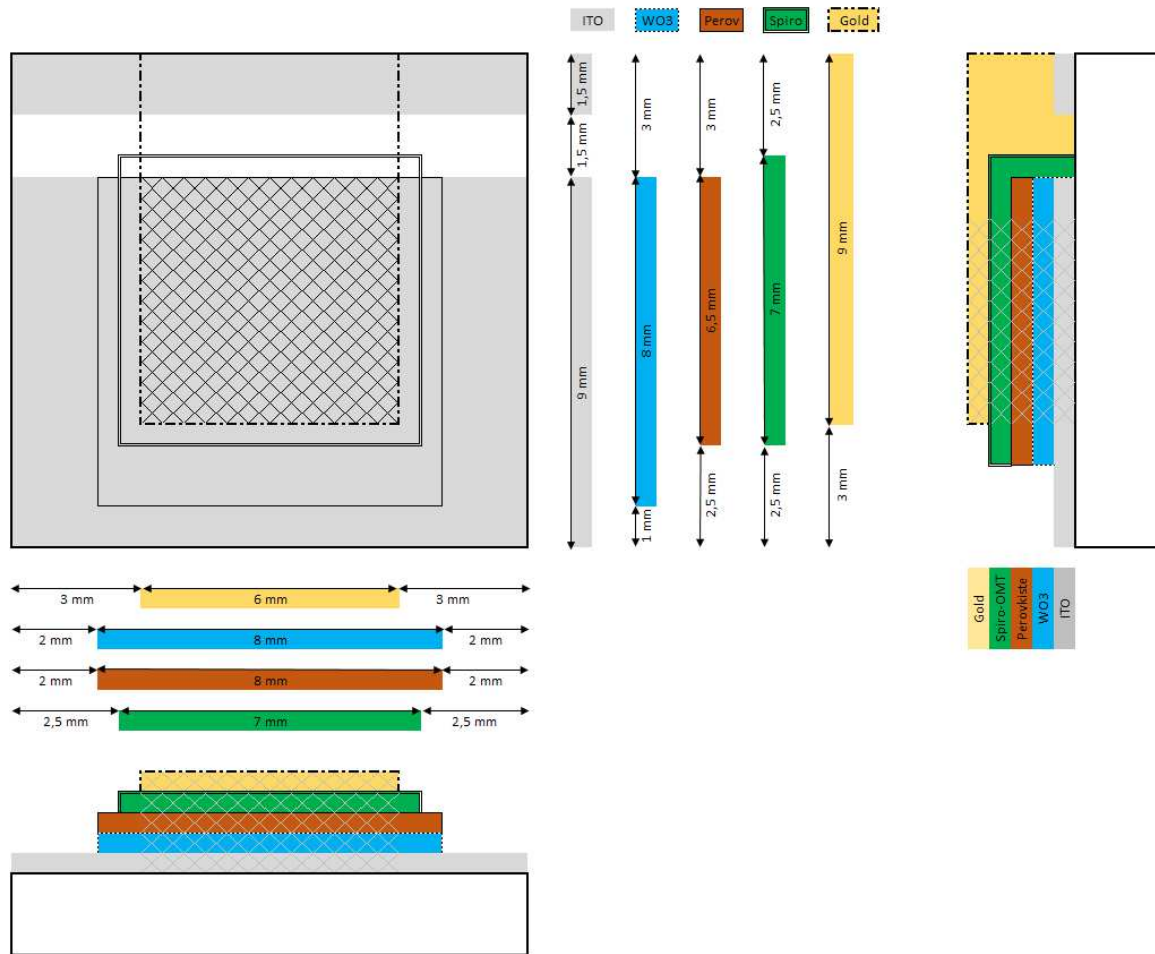


Figure IV.1 - Printed WO₃-based perovskite solar cell fabrication design (vertical scale not respected)

The strategy to keep small area was chosen for two main reasons. The first is that in order to fabricate a solar cell it is necessary to manually etch the ITO. For the printing this etching must be very accurate since the printing machine cannot adapt the printing for each substrate. The minimum size of the etching cannot be in practice inferior to 1.5 mm (since the etching is manual), a 1.5 mm band of ITO must remain at the top and 1 mm of non-printed ITO at the bottom, both for the electrical contact during measurement. At the end the maximum printable area is 0.75 mm², without considering the security margin in order that, for example, the gold and the WO₃ does not touch. This etching could be in the future however be realized by lithography in order to increase the surface.

The second reason is to ease the printing. Indeed the bigger the print area is, the higher is the probability that nozzles clog during printing. In choosing small area first we focus on optimisation of the printing and will try to increase progressively the printed area.

3. Printed WO₃ electron transporting layer

i. WO₃ nanoparticle ink

The printed WO₃ ink is very close from the WO₃ nanoparticle suspension used for the spincoating. The ink was fabricated by the same company, Avantama, but the production has stopped, and no more information is available. The WO₃ nanoparticle weight concentration is about 2.5 % and the solvent is also the isopropanol, an unknown amount of ethylene glycol is added to increase its viscosity. The size of nanoparticles, 16 nm, is suitable for inkjet printing because it is inferior to 1 μm (which is 1/10 of the nozzle size).

Rheological parameters

The viscosity of the WO₃ ink has been measured at 9.2 mPa.s at 26 °C (and 8.9 mPa.s at 30°C). Both bulk density and surface tension were measured at 22 °C and were respectively at 930 kg.m⁻³ and 18.4 mN.m⁻¹ (with the pendant drop method).

In order to determine the polar γ_L^P and dispersive γ_L^D components of the surface tension of the WO₃ ink the contact angle of WO₃ ink droplets was measured on a Teflon surface. The average value was measured at 56.8° (±1.7°) while the surface energy dispersive component γ_S^D of the Teflon surface was measured at 14.5 mN.m⁻¹ and the polar component γ_S^P was set at 0 mN.m⁻¹ (the real measured value is 0.3 mN.m⁻¹). The Owens-Wendt-Rabel and Kaelble equation coupled with the Young equation (equation (21) and the fact that the polar component of Teflon is equal to zero give us the next equation:

$$\gamma_L (1 + \cos \theta) = 2 \left(\sqrt{\gamma_L^D \gamma_S^D} \right) \quad (50)$$

The equation is easily solvable and we find a dispersive component estimated at 14.01 mN/m⁻¹ and a polar at 4.39 mN.m⁻¹.

Jettability

From these different characterisations we can evaluate the jettability of this ink. Since this ink has been already optimized for jetting, and is produced by a third party, we will not try to modify it.

However, the jettability of this ink is not insured. Indeed, we can compute the minimum speed required for ejection from the Weber equation (7), in taking 10 μm for a , we find $v > 2.8$ m.s⁻¹. This results in a Reynolds number (6) at 2.84, for an optimum jetting the Re value should

be higher than 1. However, the computation of Ohnesorge number (11) with a value at 0.70, smaller than the maximum of 1, allows us to foretell the good jetting of the ink.

Ejection parameters

As said before the WO_3 ink was not modified in order to keep it as the manufacturer deliver it, indeed the fabrication of this kind of ink tends to change and we did not want to change the optimisation of the ink for each new bottle. The ejection is difficult to stabilize at first, and new cartridge must be used every two printings.

The ejection voltage was around 30 V and was often change between 29 V and 33 V, depending of the batch and the used cartridge. The applied waveform at the piezoelectric elements of the nozzles is presented in the Figure IV.2. The first step in the waveform is the withdrawal of the piezoelectric and last for about 19 μs . The first push stays for 3 μs and creates the head of the drop as seen in the Figure IV.3.a. The second push helps the tails to catch up the head (Figure IV.3.b). The total time period of the wave form is 55.6 μs , which allows a maximum jetting frequency of 18 kHz. For the actual printing of the WO_3 ink the jetting frequency was set at 1 kHz to stabilize the printing and to avoid clogging of the nozzle, and more specifically to give the time to the ink to stabilize in the nozzle between each jetting. As such, the volume of each drop is 1.2 pl, which corresponds to a drop diameter of 13 μm . The final speed of the drop is 2.95 $\text{m}\cdot\text{s}^{-1}$, very close from the previously computed speed.

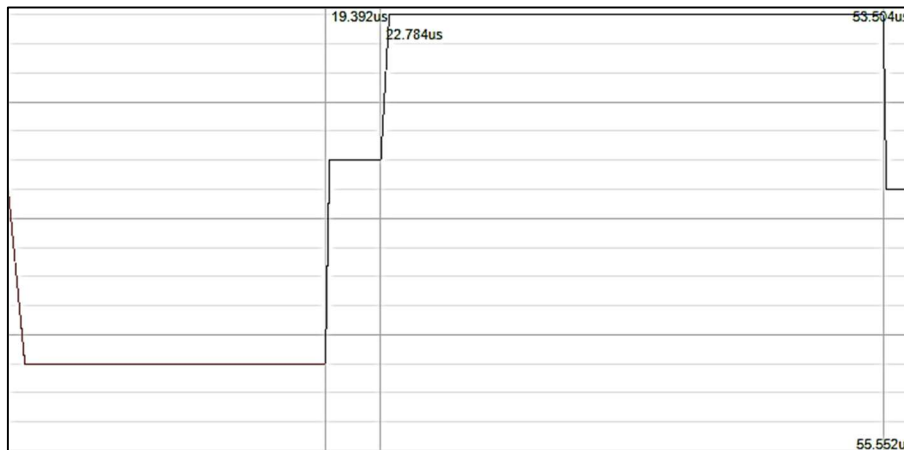


Figure IV.2 - Waveform applied for the WO_3 ink ejection

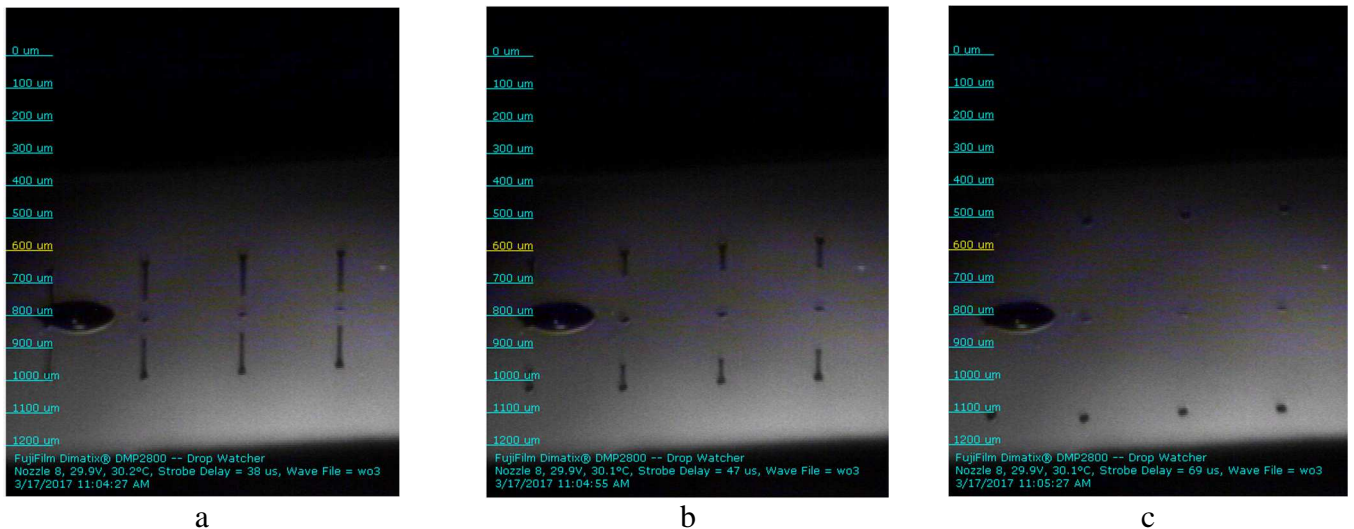


Figure IV.3 - Drop profiles of the WO_3 ejection through time, from the beginning of the jetting (a), to the intermediate step (b) then to the final drop (c)

Printing parameters

Once the ejection parameters were set the next optimisation was about printing parameters. The thickness to obtain is around 50 nanometres like in the case of the spincoated WO_3 . This is a low thickness for inkjet printing which is normally superior to 100 nm, at best [100]. This means that (1) the printing must be done in one time, a second pass is not feasible, (2) the drop spacing must be low compared to the splat size; (3) each default in printing will result in a contact between perovskite and ITO, the default must be minimized, which is more difficult with only one pass.

In order to have a starting point for the drop spacing we can estimate the size of the splat as being roughly the same size as the droplet. The chosen cartridge jets 10 pl droplets, for a spherical droplet this corresponds to a diameter of roughly 100 μm . A more precise estimation would be to print droplets of WO_3 on the ITO in making sure that the droplet does not touch each other, which has been done in this work.

The mean diameter of WO_3 splats on the ITO, after a 110 $^\circ\text{C}$ annealing, is 43.6 μm ($\pm 1.4 \mu\text{m}$). This is relatively small compared to the predicted 100 μm . This reduced size of splat is due to dewetting. Indeed, as said previously the value for the WO_3 the dispersive component is estimated at 14.01 $\text{mN}\cdot\text{m}^{-1}$ and the polar at 4.39 $\text{mN}\cdot\text{m}^{-1}$. Which means that the polar component is not negligible compared to the dispersive one. The ITO surface without any treatment has a polar component of 8.0 $\text{mN}\cdot\text{m}^{-1}$ and a dispersive one at 25.3 $\text{mN}\cdot\text{m}^{-1}$ (measured with the contact angle measurements technique), it may be possible to increase this low polar component in order to increase the wettability of the ink.

One strategy to enhance the wettability of the ink is to increase the surface energy of the ITO with surface treatment and cleaning with selected solvent. The normal treatment used for the spincoating of WO_3 to put the ITO substrate in a succession of 20 min ultrasonic bath of acetone, ethanol and isopropanol. This treatment has been adapted for WO_3 printing. After such treatment, an increase of the splat size is observed from $43.6 \mu\text{m} (\pm 1.4 \mu\text{m})$ to $101.6 (\pm 3.1 \mu\text{m})$. In order to slightly increase the wetting quality UV/ozone treatment was performed. This treatment removes O_2 and other organic molecules adsorbed on the ITO surface. After the same wet cleaning (acetone, ethanol, isopropanol, UV/ozone) the splat size is increased to $107.1 (\pm 3.1 \mu\text{m})$. Unfortunately, we know from the spincoated WO_3 layer for spincoated PSC that the UV treatment is detrimental for the efficiency, avoiding the cell to function properly. The solution is to follow the UV treatment by a final ultrasonic bath in isopropanol. In doing so we keep a mean splat size of 104.7 , slightly smaller than at the end of the UV treatment with a standard deviation of $2.9 \mu\text{m}$. The results are summarized in Figure IV.4.

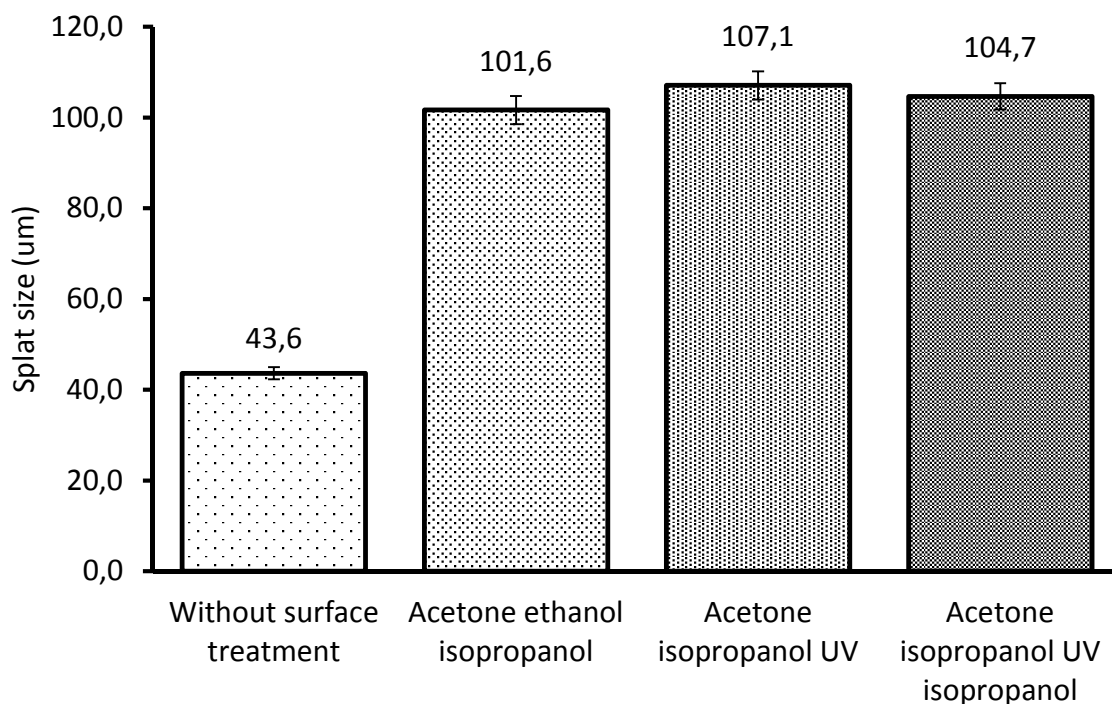


Figure IV.4 - Splat size of WO_3 printed on ITO depending of the surface treatment

With contact angle measurements of three reference liquids (water, diiodomethane and ethylene glycol) the surface energy of the ITO in the OWRK model (section II.3.i), before and after the treatment, was measured. Before the acetone/ethanol/isopropanol/UV/isopropanol treatment the dispersive component is at 25.3 mN.m^{-1} and the polar component is at 8.0 mN.m^{-1} , as said previously. After the selected treatment (acetone, ethanol, isopropanol, UV, isopropanol), the dispersive component is very slightly increased to 27.9 mN.m^{-1} , the improvement is very high for the polar component with a new value at 25.2 mN.m^{-1} . From these

values we can compute the wetting envelop of the ITO with or without treatment, this is shown in the Figure IV.5. As we can see the wetting envelop is larger after the treatments, confirming its effectiveness.

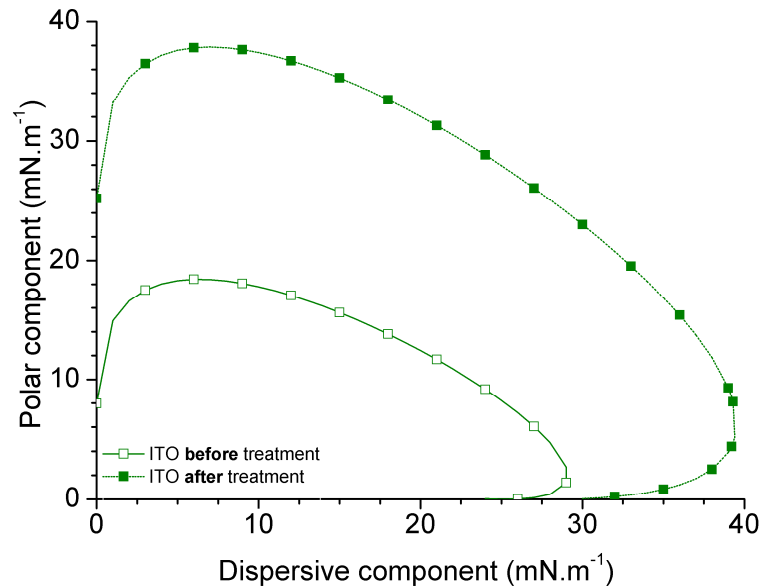


Figure IV.5 - Wetting envelope of the ITO before and after the acetone/ethanol/isopropanol/UV/isopropanol treatment

WO₃ has already been used in XLIM as a printed layer for organic solar cell by Jean-Charles Obscur [78], therefore we began by set a very close printing parameter already used: a drop spacing of 45 μm . The quality of printing is improved after the surface treatment as we can easily see in the Figure IV.6 and Figure IV.7. Without the treatment the droplets do not fuse and created separated lines at best, and separated drop at worst. This clearly shows the dewetting issue.

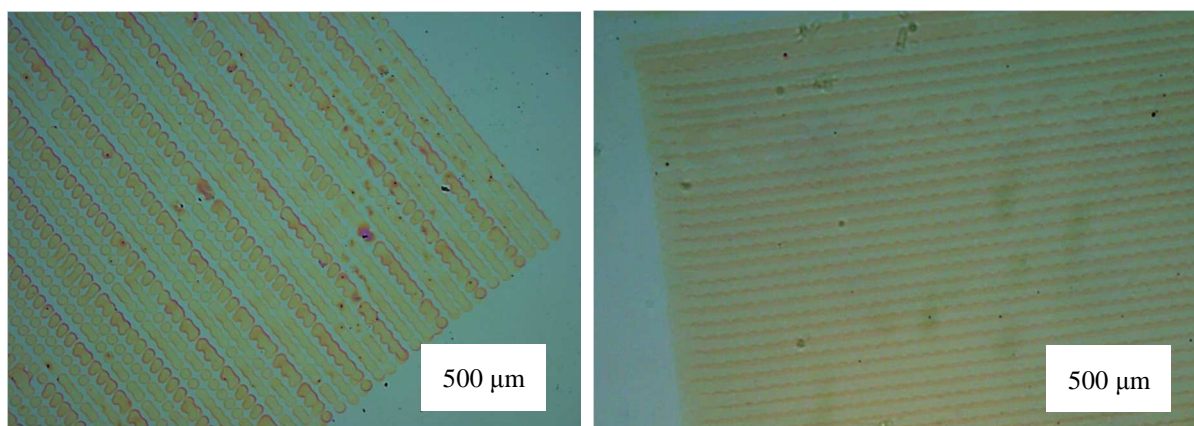


Figure IV.6 - WO₃ layer printed on ITO **before** treatment

Figure IV.7 - WO₃ layer printed on ITO **after** treatment

Perovskite solar cells were made with printed WO₃ layer with different dropspacing and thickness of this printed layer was measured with a Dektak profilometer, the results are resumed in the Figure IV.8. The best efficiencies were obtained for a drop spacing of 45 μm, which corresponds to a thickness of 70 nanometres which is thicker than the 50 nm spincoated WO₃ layers. Later, to print the perovskite layer on top of the printed WO₃ the drop spacing of the printing of the WO₃ has been adjust to 50 μm because of a new bottle of WO₃ nanoparticle solution, with these new conditions the thickness was 60 nm.

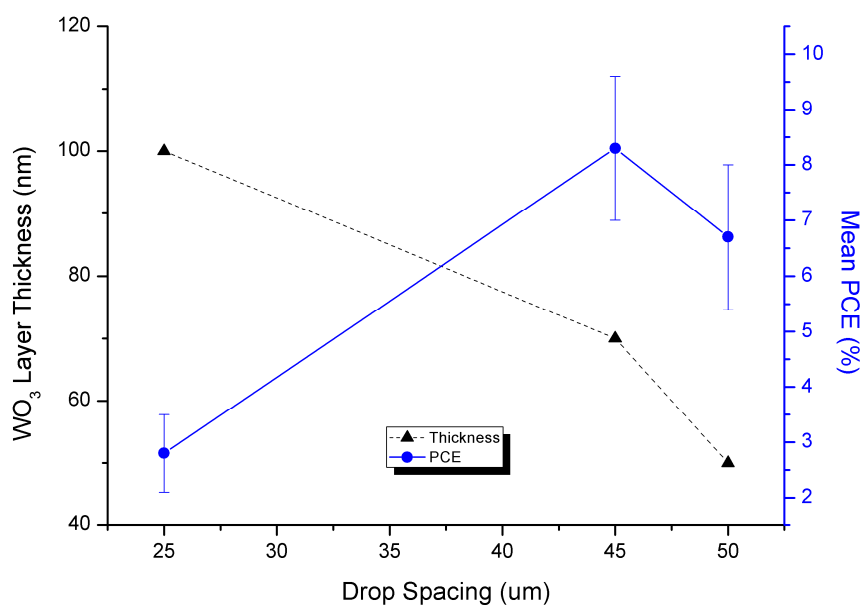


Figure IV.8 - Drop spacing optimisation with perovskite solar cell.

ii. AFM and KPFM characterization

KPFM characterization was conducted to evaluate the work function of the WO₃ layer once printed. This measure was effectuated on a WO₃ layer printed on ITO and is reported in the Table IV.2. The measured work function is now at -4.8 eV for printed WO₃ layer, this could be due to the thicker layer in the case of printed layer (60 nm against 50 nm).

Control layers	Measured work function (eV)
ITO	-4.9
FTO	-4.8
Stacking	Measured Work Function (eV)
Glass/CH ₃ NH ₃ I _{3-x} Cl _x	-5.0 ± 0.2
Glass/WO ₃	5.4
Glass/ITO/Spincoated WO ₃	-5.0
Glass/ITO/Printed WO₃	-4.8
Glass/FTO/TiO ₂ /TiO ₂ -mp	-4.5

Table IV.2 - Work function measurements with KPFM technique

AFM characterisation on printed layer was conducted and is visible in the Figure IV.9. The highest point is around 60 nm which is in fact the measured thickness which indicated that some areas are not covered by WO₃. The roughness (RMS) is 8 nm which is higher than for the spincoated layer (4 nm).

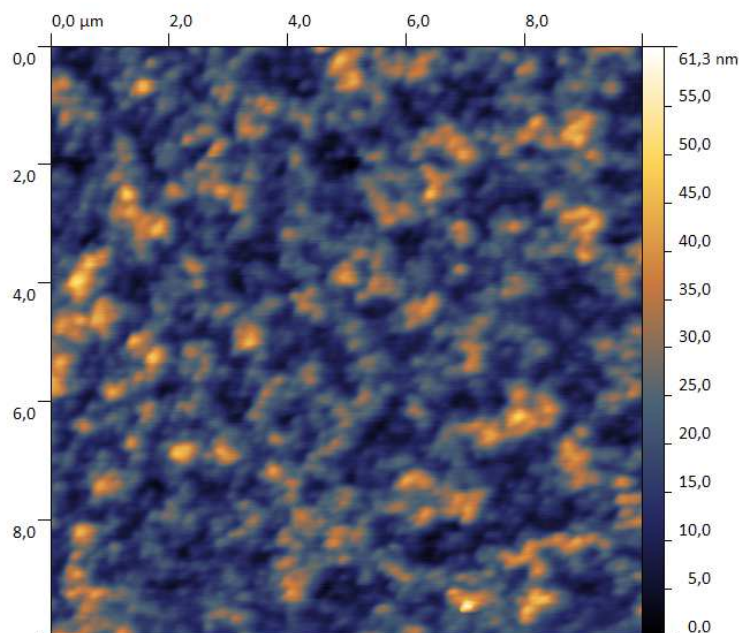


Figure IV.9 - AFM characterization of printed WO₃ layer.

iii. Perovskite solar cell with printed WO₃ layer.

The perovskite solar cells with a printed WO₃ layer was made following the same process than exposed in the section in WO₃-based PSC (III.2.ii) for the perovskite, Spiro-OMeTAD and gold layer. The WO₃ layer was printed as specified in the previous layer, with especially a drop spacing of 45 μm.

The best efficiency obtained was 9.3 %, with a V_{OC} of 797 mV, a J_{SC} 20.2 mA.cm⁻² and a FF of 57 % and is presented in the Figure IV.10. The fabrication for this kind of PSC was rapidly mastered and the champion cell was quickly obtained two months after the first try (Figure IV.11).

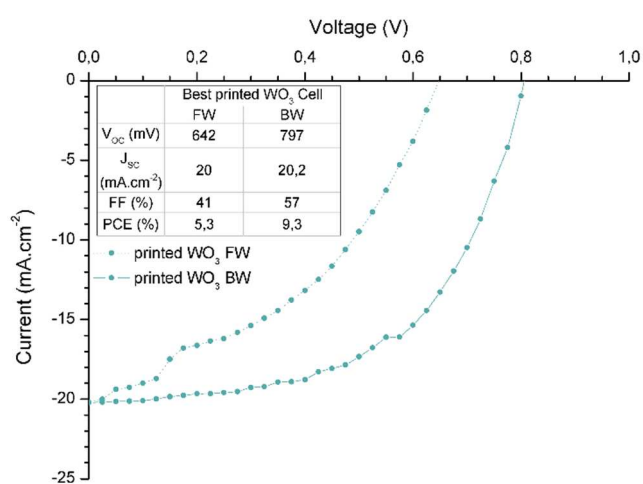


Figure IV.10 - JV curves of the best WO₃-based PSC with printed WO₃

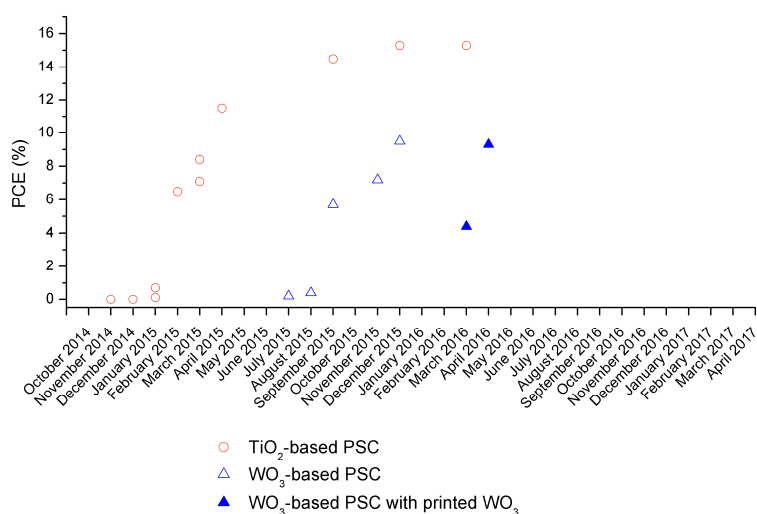


Figure IV.11 - PCE evolution of the best perovskite solar cells

Compared to the objectives one more step has been realized. WO₃ is now fully printed and allows the production of PSC with efficiency up to 9.3 %, the results are summarized in the Table IV.1.

		OBJECTIVES	BEST WO ₃ CELL
Photovoltaic parameters			
V _{oc}	(mV)	830	797
J _{sc}	(mA.cm ⁻²)	16	20.2
FF	(%)	75	57
η	(%)	10	9.3
Fabrication			
Active area		1 cm ²	20 mm ²
Electrode (ITO or FTO)		Non-printable	100 %
ETL		Printed	100 % (printed)
Perovskite		Printed	50 % (printable)
HTL		Printed	50 % (printable)
Top electrode		Printable	0 %
Max annealing temperature		130°C	100 %

Figure IV.4 - Comparison between the objectives and WO₃-based PSC with printed WO₃

iv. Discussions on possible improvements

One limitation is the low stability of the printings from the jetting point of view that force to change the nozzles head every two printings. In order to enhance the quality of the jetting one solution is to look at the *Oh* number. In this case the *Oh* number of the WO₃ is in the good range but the value of 0.7 is relatively close to the maximum of one. In practice the jetting of the WO₃ was often erratic and this can be due to a bad stability of the ink. Particular an evaporation of the solvent (the isopropanol) which can increase the viscosity of the ink and increase the value of the *Oh* number.

From the user's point-of-view, who has not the access to the fabrication of the ink, the best solution is to decrease the *Oh* number by lowering its viscosity by adding solvent, isopropanol in this case.

4. Printing of the perovskite layer

i. Perovskite ink

The perovskite solution is the most important ink to optimize, the strategy was to start from the solution used for the spincoated PSC. As a reminder, here the composition of the 40 % weight concentration perovskite solution:

The perovskite solution is prepared in adding 252 mg of methylammonium iodide ($\text{CH}_3\text{NH}_3\text{I}$, 158.9 g.mol^{-1} , MAI) in 600 mg of N,N-Dimethylformamide (0.948 g.mol^{-1} , DMF). Once the MAI is correctly dissolved in the DMF, 147 mg of PbCl_2 (278.2 g.mol^{-1}) and $5.4 \mu\text{l}$ of diiodooctane ($\text{ICH}_2(\text{CH}_2)_6\text{CH}_2\text{I}$, $1,84 \text{ g.ml}^{-1}$, DIO). The solution is stirred during at least 1 hour at 90°C . The resulting solution has a weight concentration in perovskite of 40 %, and a weight concentration of DIO of 1 %. The molar ratio between MAI and PbCl_2 is 3:1, thus to benefit the formation of $\text{CH}_3\text{NH}_3\text{PbI}_{3-x}\text{Cl}_x$ with the lower x (i.e. the lowest amount of chlorine).

After optimisation (IV.4.iii) the perovskite concentration was increased to 50 %:

With this new formulation, the perovskite solution is prepared in adding 593 mg of methylammonium iodide ($\text{CH}_3\text{NH}_3\text{I}$, 158.9 g.mol^{-1} , MAI) in 940 mg of N,N-Dimethylformamide (0.948 g.mol^{-1} , DMF). Once the MAI is correctly dissolved in the DMF, 347 mg of PbCl_2 (278.2 g.mol^{-1}) and $10.1 \mu\text{l}$ of diiodooctane ($\text{ICH}_2(\text{CH}_2)_6\text{CH}_2\text{I}$, $1,84 \text{ g.ml}^{-1}$, DIO). The solution is stirred during at least 1 hour at 90°C . The resulting solution has a weight concentration in perovskite of 40 %, and a weight concentration of DIO of 1 %. The molar ratio between MAI and PbCl_2 is 3:1, thus to benefit the formation of $\text{CH}_3\text{NH}_3\text{PbI}_{3-x}\text{Cl}_x$ with the lower x (i.e. the lowest amount of chlorine).

Rheological parameters

The viscosity of the 50 % weight concentration perovskite solution is of the ink has been measured at 10.6 mPa.s at 26° . Both bulk density and surface tension were measured at 22°C and were respectively at 1430 kg.m^{-3} and 19.3 mN.m^{-1} . If the surface tension is slightly under the 25 mN.m^{-1} , the viscosity is in the good range.

Jettability

From these different characterisations we can evaluate the jettability of this ink. We can compute the minimum speed required for ejection from the Weber equation (7), in taking $10 \mu\text{m}$ for a , we find $v > 2.3 \text{ m.s}^{-1}$. This value of ejection results in a Reynolds number (6) at 3.13, for an optimum jetting the Re value should be higher than 1. The computation of Ohnesorge number (11) confirm this conclusion, with a value at 0.63 in the middle of the jettable [0.1;1] range.

ii. Printing optimisation

Printing requirements

The formation of the perovskite is promoted at 90°C in wet condition. In colder temperature the PbI_2 is formed before the $\text{CH}_3\text{NH}_3\text{PbI}_{3-x}\text{Cl}_x$ hybrid perovskite, this also happens when the solvent begins to dry. Indeed, when the solvent evaporate the concentration rises and hits its maximum (around 50 %), and as the PbI_2 is less soluble than $\text{CH}_3\text{NH}_3\text{I}$ the PbI_2 precipitates at the surface of the printed substrate. Therefore, the printed layer must remain wet until it is annealed.

The best parameters for the printing of the perovskite film would be:

- High speed of printing: fast printing will allow to keep a wet film
- Large drops: the larger the drop the faster will be the printing. Of course as the jettability of the ink is related to the drop size there is, depending of the jetting condition, a maximum size.
- Low temperature to reduce the evaporation rate.
- Lower thickness to reduce the flow of the film during printing (see section IV.4.iii)

Ejection parameters

The ejection voltage was around 33 V, depending of the batch and the used cartridge. The cartridge temperature was set at 50°C. The waveform applied at the piezoelectric elements of the nozzles is presented in the Figure IV.12. The first step in the waveform is the withdrawal of the piezoelectric and last for about 27 μs and is very subtle. The only push stays for 18 μs and create the drop as seen in the Figure IV.13. The total time period of the wave form is 100 μs , which allows a maximum jetting frequency of 10 kHz. For the actual printing of the perovskite ink the jetting frequency was set at 1 kHz to stabilize the printing and to avoid

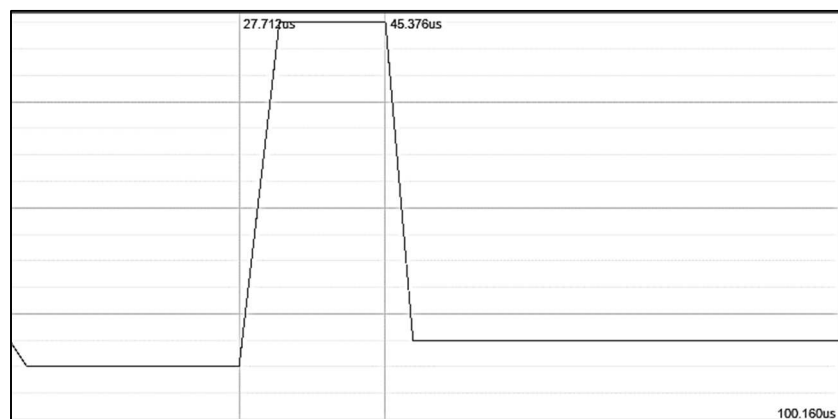


Figure IV.12 - Waveform applied for the perovskite ink ejection

clogging of the nozzle, and more specifically to give the time to the ink to stabilize in the nozzle between each jetting. The resulting diameter of the perovskite ink droplets is $10.3 \mu\text{m}$, that is to say a volume of 4.7 pl . The final speed of the drop is $5.1 \text{ m}\cdot\text{s}^{-1}$, which is twice the speed calculated previously. This difference could not be explained by the higher temperature use for the printing. Indeed to reach this speed the density should be divided by at least 3 and the surface tension multiplied by 3 (which is not possible since the surface tension normal evolution is to decrease when the temperature increases).

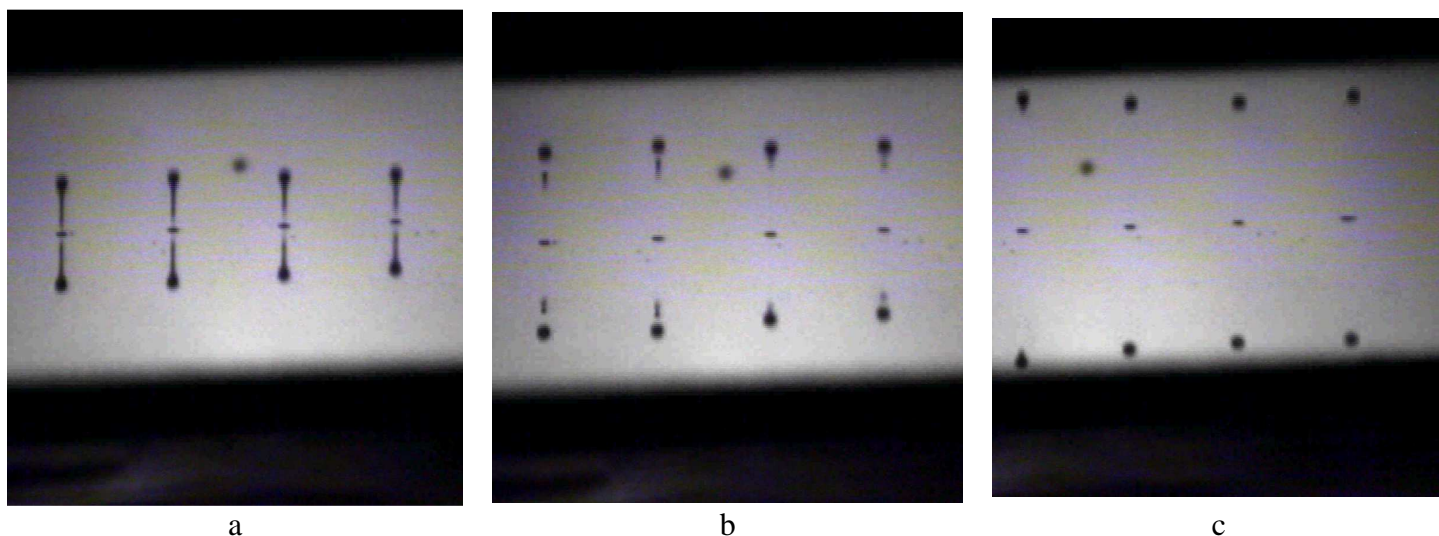


Figure IV.13 - Drop profiles of the perovskite ink ejection through time, from the beginning of the jetting (a), to the intermediate step (b) then to the final drop (c)

Splat size

Measuring the splat size of the printed droplets of perovskite is not easy as the droplets dry quickly after deposition. Therefore two sizes of splat were considered: with a simple drying at ambient temperature and with a 2h annealing time at 90°C in ambient atmosphere. The optical microscopy characterization of both conditions are seen in the Figure IV.14 and Figure IV.15, this pictures has been taken for a printing with a drop spacing of $200 \mu\text{m}$.

The average diameter of the perovskite droplets dried at ambient temperature is $132.3 \mu\text{m}$ ($\pm 7.7 \mu\text{m}$), the mean size for the droplets annealed at 90°C is $117.1 \mu\text{m}$ ($\pm 5.7 \mu\text{m}$). Several observations can be made. First, the larger average splat size for the droplets dried at ambient temperature indicates that the perovskite droplets tend to spread on the WO_3 if enough time is given. This time is relatively short, indeed the droplets dry in less than 30 seconds. Second, the higher standard deviation for the dried droplets is only the statistical translation for a feature which can be easily seen: the droplets present a non-regular circular shape. These shapes are due to the dewetting of the perovskite ink on the ITO in places where there is no WO_3 or a very

thin layer of WO_3 . This is confirmed by the average splat size on ITO in the same condition which is $57.8 \mu\text{m} (\pm 2.1 \mu\text{m})$. In conclusion, the spreading of the perovskite ink is enhanced on the WO_3 layer and when given time the splat size of the perovskite ink splat increases. These two behaviours will play a critical role in the quality of the printing, this will be discussed in next sections.

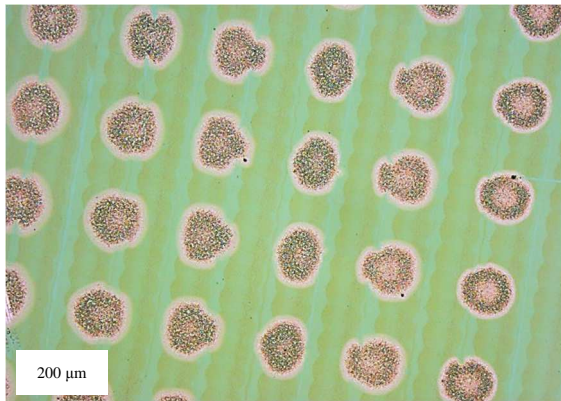


Figure IV.14 - perovskite printed drops annealed at **ambient temperature**

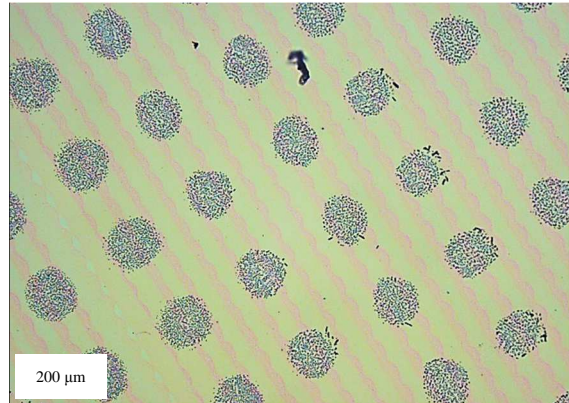


Figure IV.15 - perovskite printed drops annealed at **90°C**

Printing parameters

For a drop volume of $4.66 \times 10^{-15} \text{ m}^3$, theoretically the height of the sphere cap formed by the drop is 0.9 nm. If the perovskite layer was printed with a drop spacing of $117 \mu\text{m}$ (the diameter of one splat) the height of the annealed film would be nearly half of one nanometre (with a weight concentration of 50%). In order to have a perovskite thickness of 200 nm, we must at least print a wet layer of 400 nm. For a surface of 0.64 cm^2 this correspond to a volume of $2.6 \times 10^{-11} \text{ m}^3$. For this volume and a number of 5500 drops this corresponds to a drop spacing of $108 \mu\text{m}$. In practice, with a drops pacing of $108 \mu\text{m}$ the film is already dry before the end of the printing because the thickness of the wet film is too low and the DMF evaporates quickly.

Weight concentration		1 layer			2 layers			3 layers		
Drop spacing (um)	Mean PCE (%)	SD	Best PCE (%)	Mean PCE (%)	SD	Best PCE (%)	Mean PCE (%)	SD	Best PCE (%)	
										40%
	20	0,0	0,0	0,0			0,0	0,0	0,0	
	25	0,6	0,2	0,8						
	35	0,6	0,0	0,6	4,8	0,7	5,6			
	45				4,6	1,2	6,2			
	55	3,9	2,0	5,5	4,3	0,4	4,7	5,2	1,1	6,2
		1 layer			2 layers					
Drop spacing (um)	Mean PCE (%)	SD	Best PCE (%)	Mean PCE (%)	SD	Best PCE (%)	Mean PCE (%)	SD	Best PCE (%)	
										30%
	35	3,7	1,3	5,2	0,2	0,2	0,5			
	45				3,6	1,4	5,0			
		1 layer								
Drop spacing (um)	Mean PCE (%)	SD	Best PCE (%)	Mean PCE (%)	SD	Best PCE (%)	Mean PCE (%)	SD	Best PCE (%)	
										50%
	35	4,4	1,9	7,6						
	40	0,0	0,0	0,0						

Table IV.3 - PCE of PSC with printed WO₃ layer and printed perovskite layer, depending of the drop spacing of the perovskite printing and perovskite weight concentration, PCE measured with a AM 1.5 G 100 mW.cm⁻² illumination source, masked at 0.20 cm².

Therefore, several drop spacing values, several number of printed overlapping layers and different concentration of perovskite were tried in order to determine the best printing parameters to use. The results are presented in the following Table IV.3. When the printing of the perovskite is not stable and reproducible the number of working cell is often only of one cell for three printed cells. This first criteria indicated us which drop spacing values to exclude. The other criteria was a good compromise between the highest mean PCE of the working cells, the lowest standard deviation and the value of the best obtained PCE. The best mean efficiencies

with lowest standard deviation were obtained with one printed layer for a 40 % weight concentration and for a drop spacing of 55 μm and the smaller drop spacing was detrimental for the efficiency. When a greater number of layers are printed the mean efficiencies are superior to 4.3 % with a maximum at 5.2 %. Here we see two antagonist conclusions: using smaller dropspacing will increase the quantity of perovskite matter but will be reduce the efficiencies, increasing the number of layer will increase the quantity of perovskite matter and increase the mean efficiency. The difference between these two situations are the printing time, in one situation a greater quantity of perovskite is printed in one time when in the other situation the larger quantity of perovskite is deposited in several step. In the first condition the wet film is thick and as explained in the next section this creates flows in the layer and in the end a low film quality. In the last condition the solvent has time to dry between each layer printing and the thickness of the wet film at the end is reduced. A deeper analysis is addressed in the next section.

From this finding an ink with a higher concentration was tested: 50 % in weight of perovskite. With a drop spacing of 35 the best efficiencies was obtained at 7.6 % with a mean efficiency at 4.4 %. This parameter has been chosen for its ability to produce cells with a highest PCE.

iii. Thickness variation of printed perovskite layer

Phenomena

To illustrate the problematics of the perovskite printing this section will present one of the phenomena that occur when the printings is not stabilized. This phenomenon is due to the thickness variation across the printed perovskite layer and the result be seen in the Figure IV.16. In this picture we can identify two main features: some white shapes in the vertical direction and a colour variation from black to brown. Of course these features are detrimental to the functioning of the PSC: the white shapes are areas with a lack of perovskite creating contact between WO_3 and the Spiro-OMeTAD and possibly with the gold electrode. The variation of colour reflects a variation of thickness which is also a problem, indeed in order to print larger area the thickness of printed Spiro-OMeTAD should precisely adjusted in order to correctly cover even the thicker perovskite area which is not of course easily doable. In order to obtain a

homogenous thickness layer and to remove these white shapes this section will explain the causes of the phenomena.

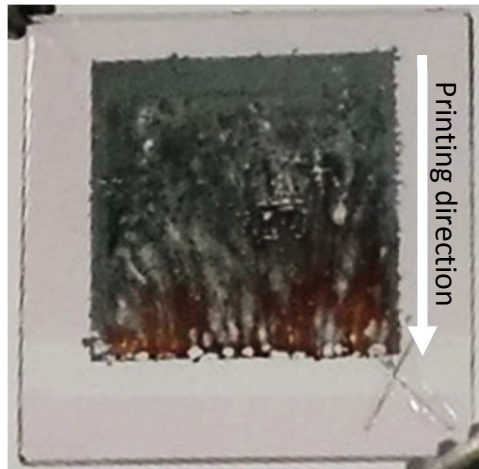
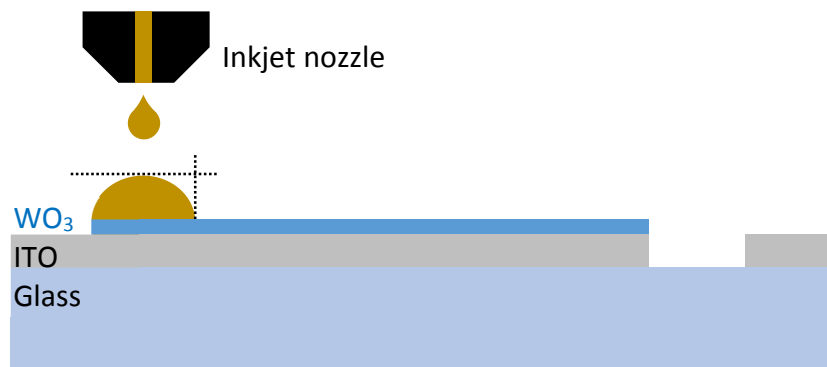


Figure IV.16 - Not stabilized printing of printed perovskite layer on printed WO_3 layer

The steps leading to this bad quality of printing are detailed in the Figure IV.17:

- The first step (a) is the printing of the first lines of droplets, depending of the number of nozzles the number of simultaneously printed lines lies between 2 and 6 nozzles. The dotted lines symbolize the height and width of the printed lines.
- During the second step (b), which takes place between the printing of the first lines and the printing of the second row, the lines have the time to spread. The line of ink spreads on the WO_3 layer and not on the ITO side (this is demonstrated further in the section IV.4.iv)
- In the third step (c), as the drop spacing is $35 \mu\text{m}$, the second lines is printed on 70 % on the last line of droplets. At the beginning of this step the new lines of ink are not stabilized, furthermore the surface contact between this second lines and the WO_3 is smaller than the one between the first lines and the same layer. As a result, the coalescence of the second lines toward the first lines is provoked. More specifically, a light dewetting occurs and the ink excess at the top of the second line in displaced toward the first lines, only the boundary layer of the ink film stays on the printed WO_3 layer.
- The fourth step (d) between the printing of the second and third line presents the resulting shape profile of the perovskite film.

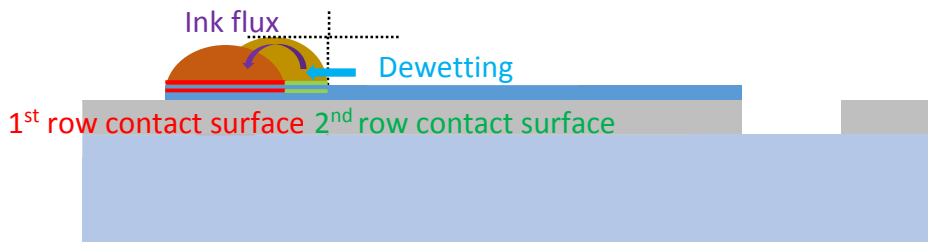
- The fifth step (e) represents the profile of the film after completion of the printing. The film is thicker at the beginning of the printing and thinner at the end.
- The sixth step (f) is the annealing of the film at 90°C. All across the perovskite film the evaporation rate is identical, but since the thickness is not homogenous the thinner part will be dry quicker. As a result, the concentration of the precursors is not constant through the layer. The concentration will be higher in the thinner part and lower in the thicker part. This gradient creates a precursor flux from the end to the beginning area. Moreover, during drying the faster evaporation of the solvent in the thinner part created a moving front from the end to the beginning area. This front push forward some of the liquid and increase the heterogeneity of the annealed layer.



a) Printing of the first lines of droplets



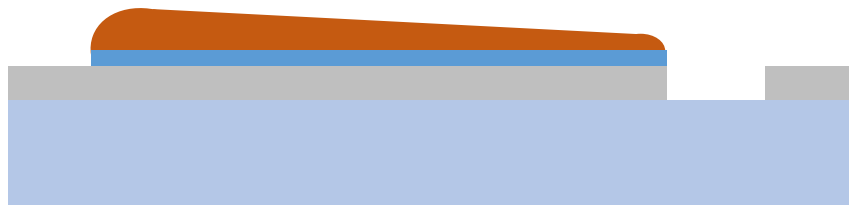
b) Spreading of the first rows



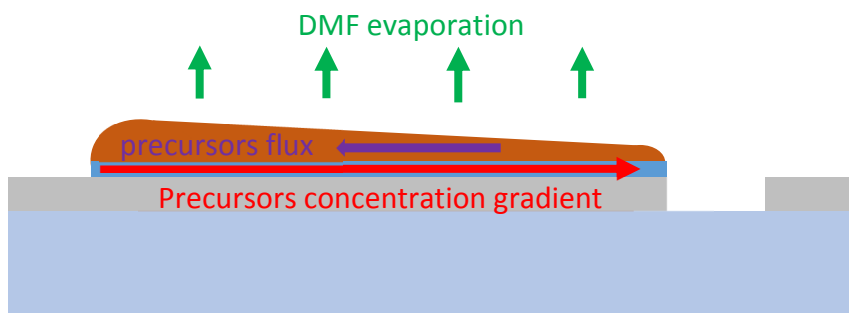
c) Printing of the second rows of droplets



d) Final state of the droplets after fusion



e) Profile of the perovskite film after printing



f) Annealing at 90°C after the completed printing

Figure IV.17 - Profile view of the substrate and steps of the perovskite printing (vertical and horizontal scales not respected)

This flows of precursors and this moving front creates these white shapes oriented from the end to the beginning area of the printing. Furthermore, the precursors flux speed is probably not the same for both precursor (PbCl_2 and $\text{CH}_3\text{NH}_3\text{I}$), some areas would then lack of one precursors which provokes this change of colour. Of course the variation of thickness also explains the variation of colour, from brown to black.

The hypothesis was that the viscosity of the ink was too low or the thickness of the wet film was too high. In order to reduce the height of the film two solution was investigated: using high drop spacing with 40 % and 30 % perovskite weight concentration, and as demonstrated previously this solution was not satisfactory. To increase the viscosity was the other solution and is developed in the next section, as well as the characterisation of the other inks with different perovskite weight concentration.

Ink optimisation

To increase the viscosity one solution is to modify the concentration of hybrid perovskite, as resumed in the Table IV.4. By modifying the weight concentration of the ink the viscosity is modified from 2.3 to 10.6 mPa.s, the minimum being close to 0.92 mPa.s which is the viscosity of the pristine DMF. The value of surface tension maximum is found to be for a perovskite weight concentration of 40 %. The exact maximum of surface tension has not been investigated since its variation is not significant between 30 % and 50 % of perovskite weight concentration. 50 % is the maximum concentration reachable giving the solubility of the precursors. One observation to make is that the diiodooctane additive seems to play a surfactant role by reducing the surface tension.

Perovskite weight concentration	30 %	40 %	50 %
Diiodooctane weight concentration	0 %	1 %	1 %
Density (kg.m^3)	1250	1340	1430
Viscosity (mPa.s)	2.3	8.8	10.5
Surface tension (mN.m^{-1})	18.5	21.2 21.9 ^a	19.3
Minimum ejection speed (m.s^{-1})	2.43	2.51	2.32
Re	13.2	3.8	3.1
Oh	0.15	0.52	0.63

Table IV.4 - Ejection parameters of the perovskite inks depending of the $\text{CH}_3\text{NH}_3\text{PbI}_{3-x}\text{Cl}_x$ weight concentration. ^a Surface tension of the perovskite ink without diiodooctane

The first effect of this perovskite ink optimization is the reduction of the Re number: from the 30 % perovskite concentration with a Re value of 13.2 (too high to have a stable jetting) to 3.1 which is in the working range. The 40 % concentration ink is already jettable and the first printed perovskite layer was in fact used but the printing was not stable (as demonstrated previously). The other effect of the concentration increase is the enhancing of the Oh number to approach the middle of the [0.1;1] range.

Other optimisation tries

Other optimisations were tried to increase the viscosity of the perovskite. In a perovskite ink with a weight concentration of 30 % polyethylene glycol (PEG) was added. The objective was to increase the viscosity of the ink in order to reduce the previous problematics. The viscosity and the surface tension of the ink were measured for different value of PEG concentrations (Figure IV.18). The viscosity of the ink increased from 2.3 to 3.9 mPa.s when the weight concentration of PEG increased from 0 to 10 %. More precisely the viscosity increase is the most sensible up to 5 % weight concentration of PEG into the perovskite ink. The surface tension does not evolve with the PEG concentration. This new value of viscosity increases the Oh from 0.15 to 0.23 which enhance the stability of the jetting.

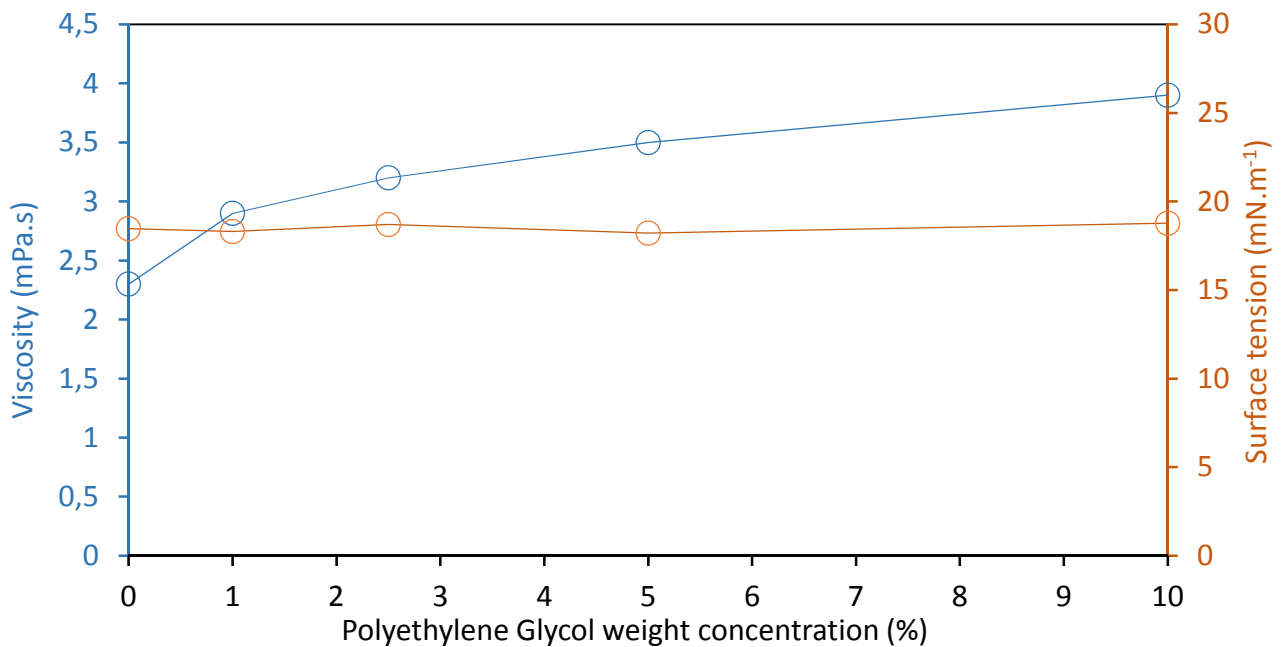


Figure IV.18 - PEG influence on viscosity and surface tension on 30 % weight concentration perovskite ink.

Perovskite solar cells were made using printed WO_3 layer and printed perovskite with 30 % weight concentration with a weight concentration of 1% for DIO and 5 % for PEG. Unfortunately, upon annealing the perovskite layer presented a yellow colour, and the cells were not working properly showing only short circuit behaviour.

Other solution could be to change part of the solvent of the perovskite ink. One of the most used solvents for perovskite are dimethyl sulfoxide (DMSO) and *gamma*-butyrolactone (GBL) which have a higher viscosity than the one of the DMF. The GBL possesses a viscosity of 1.7 mPa.s while the DMSO is at 2 mPa.s, twice as big as the viscosity of the DMF. Furthermore, in order to reduce the rate of evaporation it would be a good idea to choose a solvent with a lower vapor pressure. At 20°C DMF is at 3.77 mbar, DMSO at 0.6 mbar and GBL at 1.5 mbar. Thus, in replacing part of the DMF by one of these two solvents it will naturally increase the viscosity and reduce the evaporation rate allowing a better homogeneity of the thickness while keeping a lower average thickness. Finally in order to reduce again the evaporation rate the printing could be conducted in an atmosphere already saturated with the chosen solvents.

iv. Surface energy and perovskite composition influence on wettability.

This final section will deal with the role of chlorine in the perovskite. The chlorine is used as a second halide in the composition of the hybrid perovskite. First we will speak about the current state of the art about the two main fabrication methods and about the effect of chlorine in the perovskite formation. The second part will show the result of this work and hypothesis about one of the possibly revealed role of chlorine.

Literature

The simplest possible hybrid perovskite is $\text{CH}_3\text{NH}_3\text{PbI}_3$, as such this composition was the first to be intensely used in research. With this kind of perovskite fabrication method is the sequential deposition [101], also known as “two-step”. Essentially this method consists in the spincoating of a first solution of PbI_2 in isopropanol, a short annealing at 90 °C forms at the surface a first layer of PbI_2 . The second step is the soaking of the substrate in a CH_3NH_3 solution, often in DMF. During this soaking the perovskite forms, turning the colour of the film from yellow to brown, an annealing of 2 hours at 90°C finishes the perovskite formation. With this technic PSCs over 15 % PCE are easily obtained [101].

The one-step method is the other strategy. This technic is the one used in this thesis and has been chosen to ease the printing step as the soaking step of the previous method is not

doable in the inkjet method, at least not with the used printing machine. The one-step method performs well with the use of chlorine in the perovskite but a $\text{CH}_3\text{NH}_3\text{PbI}_3$ perovskite solution would produce layer with low quality and low performances [102]. The chlorine can come from the use of $\text{CH}_3\text{NH}_3\text{Cl}$ (instead of $\text{CH}_3\text{NH}_3\text{I}$) or in the case of this work from PbCl_2 (instead of PbI_2).

The true role of chlorine in the formation of perovskite is not confirmed but several hypothesis already exists, of course the chlorine could play a beneficial role for multiple explanations:

- The use of $\text{CH}_3\text{NH}_3\text{Cl}$ allows a better control of the perovskite formation process [102], more precisely in facilitating the evaporation of CH_3NH_3^+ in excess at low annealing temperature [103].
- The chlorine improves the interface between the perovskites and the carrier transport layer, however does not improve crystal morphology [104].
- The chlorine tends to concentrate at the interface between the perovskite layer and the ETL, increasing the binding energy of both film [105].
- At the interface the chlorine modifies the interface electronic structures. More precisely it leads to an interfacial coupling between the lead p and the titanium d conduction band states and favourites higher electron injection [105].
- At last, the chlorine would tend to enhance the formation of a p-i-n structures easing charge extraction [106].

Furthermore, several studies shows the absence of chlorine, or at least the low amount, at the end of the annealing. From XRD data the conclusion is that the Cl incorporation is about 3-4% [25]. Other data suggest that the Cl incorporation is very weak at the surface with a molar ratio (relative to the iodine) inferior to 0.07 but relatively high at 0.40 near the ETL surface [107].

Wettability interpretation

The use of chlorine for the one-step fabrication leads us to hypothesis the possible influence of chlorine on the wettability of the perovskite ink. For this experimentation only contact angle measurements was used to compute the surface energy components, dispersive and polar, in the OWRK model. Three solvents were used as reference liquids:

- Diiodomethane (DIM)
- Ethylene glycol (EG)

- Water

The software used for this characterisation has for the reference liquid the value of dispersive and polar component presented in the Table IV.5.

LIQUID	DIM	EG	H ₂ O
Dispersive component (mN.m ⁻¹)	50.8	19.0	21.8
Polar component (mN.m ⁻¹)	0	3.0	51.0

Table IV.5 - Tension surface components of the reference liquids

These three liquids were used to determine the surface energy of both mesoporous-TiO₂ layer and WO₃ layer (respectively on FTO and ITO) as well as to determine the surface energy of five materials used as reference surfaces:

- Teflon
- PVDF (Polyvinylidene fluoride)
- PMMA (Poly(methyl methacrylate))
- PS (polystyrene)
- Inox

For information here (Table IV.6) are the measured value of contacted angle for each reference liquids on the reference surfaces.

		SURFACES				
		Teflon	PVDF	PMMA	PS	Inox
LIQUIDS	DIM	82.6 ± 2.3	51.2 ± 2.1	32.3 ± 1.3	32.4 ± 1.7	47.0 ± 2.4
	EG	94.5 ± 1.4	56.1 ± 1.7	48.8 ± 0.9	59.7 ± 1.0	50.6 ± 1.8
	H ₂ O	108.0 ± 2.0	75.7 ± 1.2	68.2 ± 2.2	92.0 ± 2.2	73.4 ± 2.8

Table IV.6 - Contact angle of reference liquids on reference solid.

From this contact angle values a linear regression was effectuated to compute the polar and dispersive component for our reference surfaces, the results are presented in the Table IV.7 alongside comparison with known value of the literature. No source or comparison has been found for inox steel.

SURFACE	Teflon	PVDF		PMMA	PS		Inox
COMPUTED SURFACE ENERGY							
Dispersive component (mN.m ⁻¹)	15.5	27.6		35.8	42.7		39.8
Polar component (mN.m ⁻¹)	0.3	6.0		5.6	0.4		6.4
LITERATURE REFERENCES							
Dispersive component (mN.m ⁻¹)	22.0	23.3	31.3	35.8	41.2	41.4	-
Polar component (mN.m ⁻¹)	0.3	7.0	5.4	4.4	0.8	0.6	-
Reference	[108]	[109]	[110]	[109]	[109]	[110]	-

Table IV.7 - Surface energy for reference surfaces.

The next step was to measure the contact angle of 4 different perovskite inks on the five reference surface materials. Each solution is composed of a perovskite weight concentration of 40 % in DMF, and with a molar ratio of 3:1 for the CH₃NH₃I and PbX₂ (X=I,Br,Cl). These four perovskite are:

- CH₃NH₃PbI₃ (I ink)
- CH₃NH₃PbI_{3-x}Cl_x (C ink)
- CH₃NH₃PbI_{3-x}Cl_x with 1% wt DIO (D ink)
- CH₃NH₃PbI_{3-x}Br_x (B ink)

The results are summarized in the Table IV.8. The clearest result is that chlorine decreases the contact angle on PVDF and Inox while the contact angle on the other surfaces remain in the range of the standard deviation measurement. This confirms the beneficial effect of chlorine in improving a better wettability and thus inducing a better crystal perovskite formation and a better impregnation in porous material like mesoporous TiO₂. On the other hand, the use of DIO will decrease the wettability in increasing the overall surface tension of the ink (as seen previously) promoting the behaviour to form a drop instead of forming a film. When bromide is used instead of chlorine the contact angle increases on all surfaces

		SURFACES				
		Teflon	PVDF	PMMA	PS	Inox
PEROVSKITE INK	I	68.8 ± 0.8	23.3 ± 0.7	20.3 ± 1.6	28.4 ± 0.8	46.0 ± 1.2
	C	67.7 ± 2.0	18.9 ± 1.3	23.8 ± 1.6	30.9 ± 1.6	38.6 ± 1.9
	D	71.4 ± 1	24.3 ± 1.0	23.4 ± 1.3	30.4 ± 1.4	41.3 ± 2.8
	B	73.6 ± 2.1	23.1 ± 1.5	25.0 ± 1.1	34.1 ± 1.5	42.2 ± 1.6

Table IV.8 - Contact angle of perovskite ink on reference surfaces.

In order to have a better comprehension of this mechanism and its consequence in term of perovskite ink spreading and perovskite formation, the component and dispersive part of the surface energy of each ETL (TiO_2 and WO_3) and of the surface tension of each ink has been computed. To do so the contact angles of the three reference liquids were measured and the surface energy of each solid was computed by linear regression (see the explanation in section II.3.i). The results are summarized in the Table IV.9.

SURFACE	TiO_2	$\text{TiO}_2\text{-mp}$	WO_3
Dispersive component (mN.m^{-1})	26.2	30.0	26.7
Polar component (mN.m^{-1})	38.9	33.7	36.7

Table IV.9 - Surface energy of the ETLs

The three ETL are very close from one another, especially the dense TiO_2 and WO_3 layers. Indeed as these two layers are very thin (respectively 20 and 50 nm) the surface energy of ITO and FTO has probably on strong influence on the surface energy of each ETL.

In measuring the contact angle of the drop of the 4 perovskite inks on the 5 reference surface materials followed by a linear regression (with the OWRK model) the dispersive and polar components of the surface tensions of these inks were estimated (Table IV.10).

PEROVSKITE INK	I	C	D	B
Dispersive component (mN.m ⁻¹)	36.8	34.6	34.9	33.3
Polar component (mN.m ⁻¹)	3.9	5.1	5.9	7.7

Table IV.10 - Surface tension component of the perovskite inks.

From these values of polar and dispersive components of the ETL and of the surface tension of ink it is possible to draw the wetting envelope of each ETL as well as indicate the position of each ink in this diagram (Figure IV.19). In this diagram the wetting envelop of the dense TiO₂ layer is not represented for two reasons: (1) the perovskite inks are never in contact with this layer (2) the WO₃ wetting envelop is very similar and was kept alone for the ease of reading.

Several conclusions can be made from this diagram:

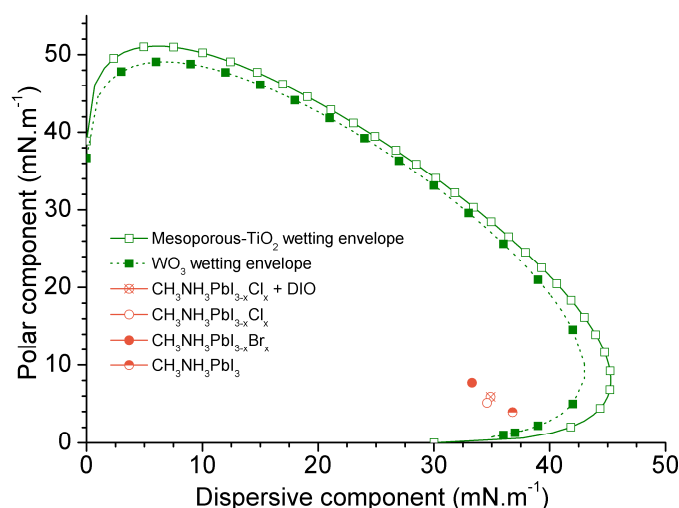


Figure IV.19 - Wetting envelope of the ETL and wettability of various perovskite inks

- The WO₃ and mesoporous-TiO₂ are very close in term of wetting envelop. Each perovskite ink have a very good predicted wettability on the two surfaces, independently of their composition. We can see this effect in the section IV.4.ii when the splat of the perovskite ink is reported to be 132 μm for a drop size of only 10 μm.
- The position of each ink in the diagram is unique. In comparing the iodine-based perovskite and the chlorine-based perovskite we see that the position of the chlorine-based perovskite point is further inside the wettability envelope. This

could indicate us that for porous material the impregnation of the ink would be slightly better. Thus chlorine would improve the wettability of the ink in certain conditions. This effect of chlorine has already been observed previously in the Table IV.8 when the contact angle is reduced for PVDF and Inox which are the reference material with the higher dispersive component.

- The DIO tends to slightly decrease the wettability of the chlorine-based perovskite, as already observed in the result of the Table IV.8.

One hypothesis to explain the better wettability of the chlorine-based perovskite ink was that chlorine was more electronegative than iodine (3.16 against 2.66 on the Pauling scale) thus increasing the polarity of the components of the ink (namely the methylammonium halide). The increase in polar component of the perovskite ink surface tension can be seen in the Table IV.10. In order to test this hypothesis, the same experiments were conducted in replacing the chlorine by bromine which possess an intermediate electronegativity at 2.96. The results indicated that the polar component of bromine-based perovskite is stronger than for the chlorine-based ink which contradicts our first hypothesis.

In conclusion the use of chlorine tends to increase the wettability of the perovskite ink compared to ink containing only iodine. This has been demonstrated by contact angle measurements and wettability envelope and compatibility calculation. The origin of this behaviour is unknown for the moment and the effect of electronegativity can be ruled out. At last, the effect of diiodooctane (DIO) is not clear and does not seem to play a significant role in wettability.

v. Characterisation of printed perovskite layer

Morphology

The thickness of the printed perovskite film has been measured with a profilometer at 1.8 μm . Interestingly, for a printed layer with a drop spacing of 35 μm with droplets volume of 4.7 picolitre, a 50 % weight concentration perovskite ink and a 0.64 cm^2 surface the predicted height is of 1.8 μm . That indicates us that the printing of the perovskite is stable since all the desired matter is ejected and no nozzles clog during printing. This thickness is very high compared to the 200 nm for the spincoated perovskite on the WO_3 layer, however this high thickness is not detrimental to the efficiency of the perovskite cell (see further).

The Figure IV.20 presents the picture of the printed perovskite layer taken with an optical microscope. The high thickness of the printed perovskite layer is visible in this picture

as holes in the perovskite layer are barely visible and no transmitted light is visible through the layer. The roughness of the perovskite, estimated from the AFM data (Figure IV.21) is 83 nm (RMS). The difference between the deepest and the highest points is 462 nm, this indicates that the coverage is good since the thickness is 1.8 μm .

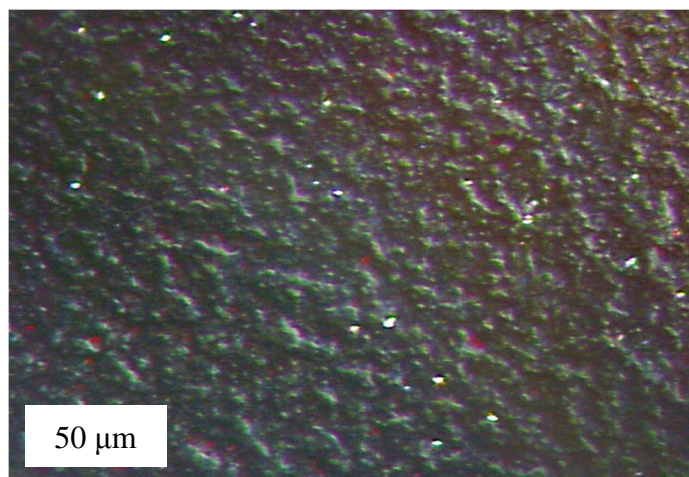


Figure IV.20 - Optical microscopy picture of printed perovskite layer on printed WO_3 layer.

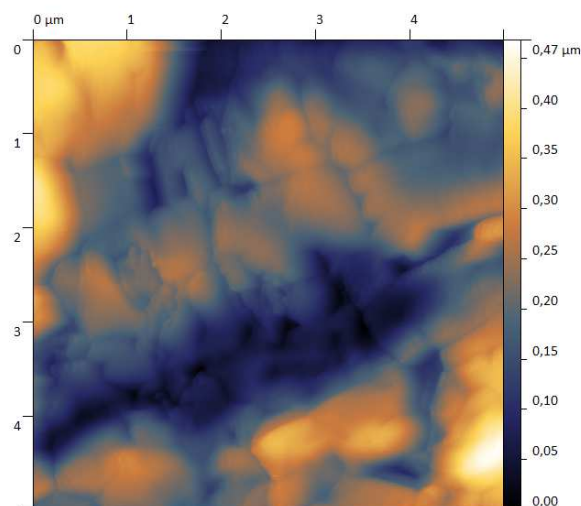


Figure IV.21 - AFM characterization of the printed perovskite layer.

PL and TPLRD

For the steady-state PL characterisation the printed perovskite layers were illuminated at 509.2 nm and the photoluminescence emissions count was observed between 700 nm and 820 nm and is presented in the Figure IV.22. The curve shows a well-defined peak centred at 790 nm. This is a similar shape than the one observed for the perovskite layer on TiO_2 ETL (Figure III.20), the second peak around 750 nm related to the presence of water is not visible confirming again the very good quality of the film. This absence of water can be the result of a thicker perovskite layer protecting most of the layer from being in contact with humidity.

Time-resolved PL decay measurement was performed on the printed perovskite layers rapidly following the printing. For this characterisation the perovskite layer was illuminated with a 509.2 nm laser and the time before a radiative recombination (at 780 nm) was measured. This measurement is summarized in the Figure IV.23.

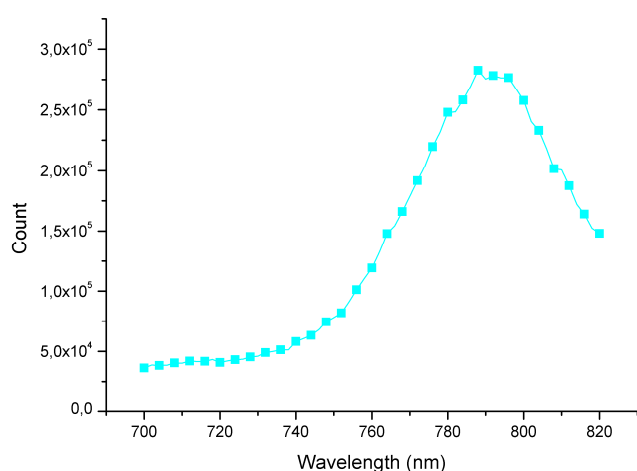


Figure IV.22 - Steady-state PL measurements of the printed perovskite layers on printed WO₃ layer

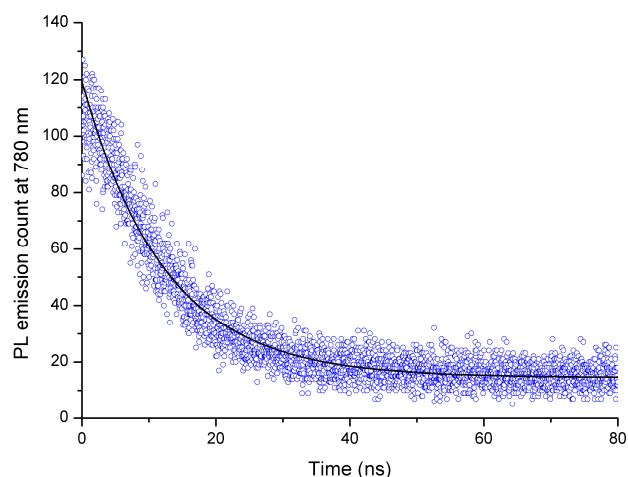


Figure IV.23 - TRPLD curves of the printed perovskite layer on printed WO₃ layer.

Exponential fitting on the time-resolved PL decay on the printed perovskite was performed to determine the decay time constant. All mathematical explanations have already been developed in the section III.2.vi. The results are presented in the Table IV.11 where the previous result for spincoated perovskite and WO₃ layers are also reported.

	a_1	τ_1 (ns)	a_2	τ_2 (ns)	τ_a (ns)	η_{CT} (%)
Spincoated perovskite on spincoated WO ₃	3965	1.1	329	16.6	2.3	99
Printed perovskite on printed WO ₃	105	12.3	-	-	12.3	94.8

Table IV.11 - Life time constants of printed and spincoated perovskite on WO₃ both spincoated and printed.

The average decay time constant τ_a of the printed perovskite layer photoluminescence value is 12.3 ns against 2.3 ns for the spincoated perovskite layer. The comparison here is difficult since the thickness of the printed perovskite layer is nine times stronger than for the spincoated layer. This could indicate that the emissive recombination of exciton occurs later for the printed layer or that the quenching of the electron is less efficient in this printed layer. However, the electrons photo-generated at the surface layer could be too far away from the WO₃ layer to be collected provoking a lower quenching efficiency. The charge transfer efficiency decreasing from 99 % to 94.8 % illustrated this loss in quenching efficiency.

XRD

XRD was conducted to characterize and determine the quality of the perovskite layer printed on a printed WO₃ layer (Figure IV.24). This printed perovskite layer shows a crystal

structure with two distinctive (110) and (220) diffraction peaks at 12.2° (\blacktriangle) and 28.3° (\blacktriangledown) [111]. The peak at 12.7° (\blacklozenge) is associated to PbI_2 [103] and this peak is very small, indicating the overall good quality of this printed perovskite layer.

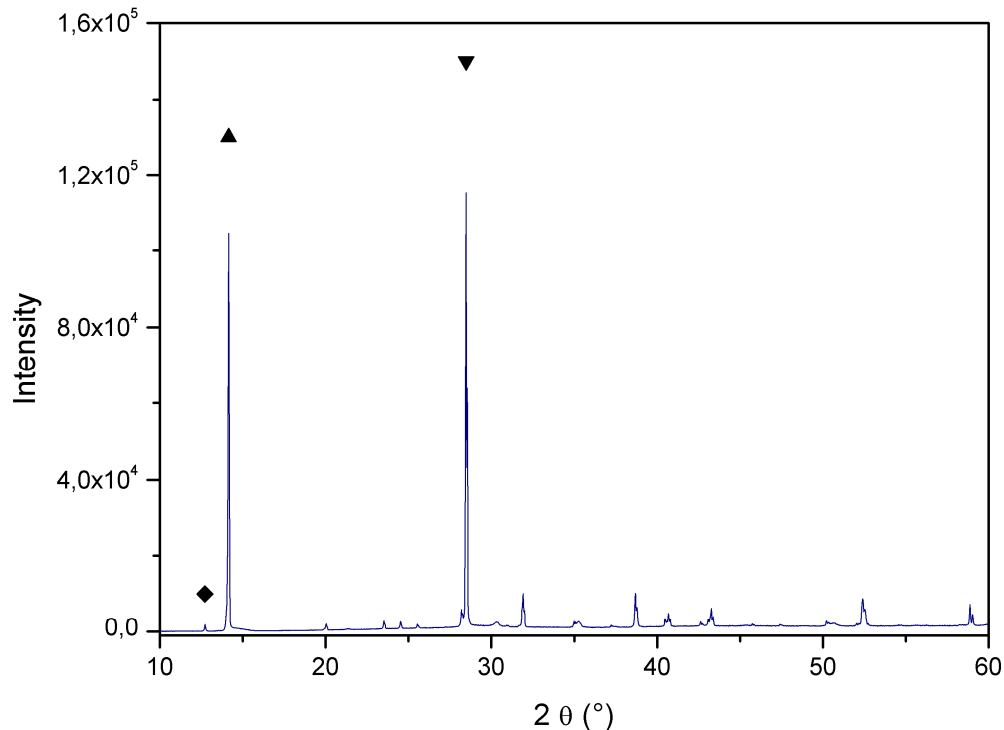


Figure IV.24 - XRD patterns corresponding to printed perovskite films

vi. Perovskite solar cells with printed WO_3 and printed perovskite layers

The best cell obtained with printed WO_3 and printed perovskite layer reached 8.1 % in backward measurements, with a V_{OC} of 745 mV a J_{SC} of $21 \text{ mA}\cdot\text{cm}^{-2}$ with a FF a 52 % (Figure IV.8). This PCE has been obtained after 7 months of work on the printing of perovskite. As stated in the previous section the critical steps were the evolution of the perovskite layer before the annealing. Furthermore, a new bottle of WO_3 solution delivered during this work forced us to optimize again the printing of the WO_3 layer. However, the critical evolution during this printing optimisation was to evolve from a 40 % weight perovskite ink to a 50 % weight concentration. This allowed to increase the PCE from 6.2 % to 7.6 % in the first time. Furthermore, with this new formulation, the printing was more stable and the layer more homogeneous.

PRINTED PEROVSKITE SOLAR CELLS

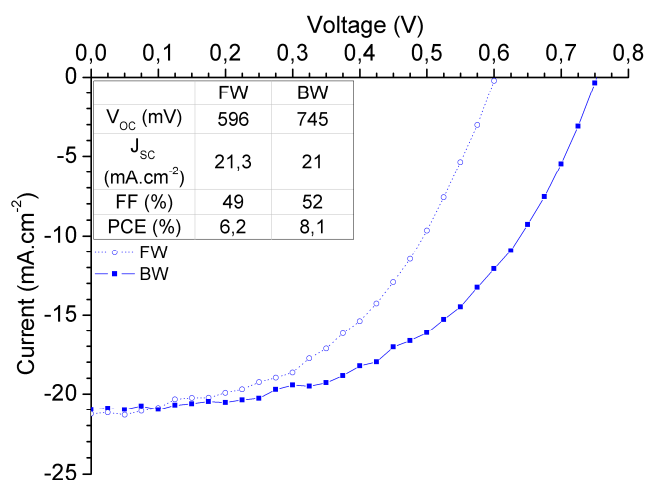


Figure IV.25 - JV curves of the best WO_3 -based PSC with printed WO_3 and printed perovskite

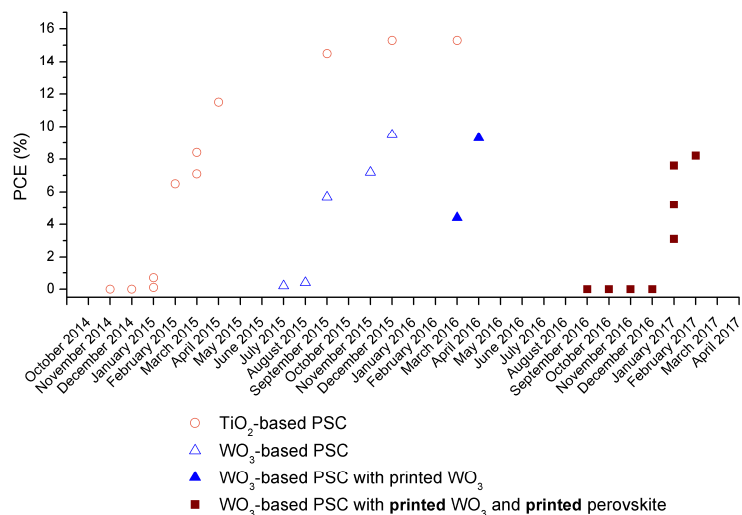


Figure IV.26 - PCE evolution of the best perovskite solar cells

Compared to the objectives the V_{OC} is still in an acceptable range. In fact 795 mV was the best value of the V_{OC} obtained in the case of spincoated WO_3 while we obtain a 745 mV V_{OC} with a printed WO_3 . These PSCs have now two printed layers, and despite its relatively low performances compared to the objective, the decision was taken to continue toward the printing of the HTL. Indeed, since the printing of the Spiro-OMeTAD depends on the layer quality of the printed perovskite the probability that further optimisations of the perovskite printing would be necessary was evaluated as relatively high. This strategy allows also to study the feasibility of the Spiro-OMeTAD printing and its limitations.

	OBJECTIVES	BEST PRINTED WO ₃ AND PRINTED PEROVSKITE CELL COMPARISON
Photovoltaic parameters		
V _{oc} (mV)	830	745
J _{sc} (mA.cm ⁻²)	16	21
FF (%)	75	52
PCE (%)	10	8.1
Fabrication		
Active area	1 cm ²	20 mm ²
Electrode (ITO or FTO)	Non-printable	100 %
ETL	Printed	100 % (printed)
Perovskite	Printed	100 % (printed)
HTL	Printed	50 % (printable)
Top electrode	Printable	0 %
Max annealing temperature	130°C	110 °C

Table IV.12 - Comparison between the objectives and spincoated printable WO₃-based PSC

5. Printing of the hole transporting layer printing

i. HTL ink requirements

This section will briefly present the requirements for the HTM ink. For direct configurations processed from solution using techniques, such as spray-coating, spin-coating or printing, the best HTM are those that do not require strong polar and protic solvent, as such solvents could dissolve the perovskite layer. However, the HTM solvent should exhibit a good affinity with the surface of the perovskites. To get a better understanding of perovskite layer surface energy and its impact on solution-processing of the solar cell, we performed surface energy measurements with three reference liquids on CH₃NH₃PbI_{3-x}Cl_x.

Contact Angles Measurements with Sessile Drop Technique	
<i>Liquid</i>	<i>Contact angle</i>
H ₂ O	49.8°
EG	26.6°
Ethanol	7.3°
Surface Energy (Owens–Wendt Theory) (mJ·m⁻²)	
Total surface energy γ_s ($\gamma_d + \gamma_p$)	51.9
Dispersive component γ_d	6.2
Polar component γ_p	45.7

Figure IV.27 - Contact angle and surface energy of CH₃NH₃PbI_{3-x}Cl_x hybrid perovskite

These measurements have been made on 600 nm-thick CH₃NH₃PbI_{3-x}Cl_x layers, spin coated directly on glass and annealed in air at 90 °C during 120 min. These results show that the surface energy of the perovskite layer is primarily (for about 88%) due to polar interactions. In principle, the solvent of the HTM should have a surface tension energy with a high polar contribution in order to tie in with the polar-oriented profile of the perovskite surface energy. The surface tension of a liquid is defined by its main solvent, but also by the species in suspension or in dilution: in other words, the presence of an HTM can completely modify the surface tension profile of the solvent. Perovskites are also sensitive to humidity, possibly oxygen and doping from other layers: a perfect HTL would be a layer that protects perovskite material from the air and prevents the diffusion of external moieties or elements inside the absorber. Moreover, a perfect HTM would have to properly fill the roughness of perovskite layer. Finally, as the HTM is deposited second to last in the inverted architecture, it should be associated with a low annealing temperature and a short annealing time in order to avoid any degradation of the underlying materials. Typically, the suitable post-processing upper limit is to use an annealing temperature of 60 °C, for less than 1 hour [112].

ii. Spiro-OMeTAD ink

Literature: Spiro-OMeTAD printing and inkjet printing

There is no found studies about the printability of Spiro-OMeTAD despite being known since 1995. This will probably be the first public work on the use of Spiro-OmeTAD for inkjet printing. For this step the Spiro-OmeTAD solution used as ink is the classical solution used previously, it is prepared three days before printing:

In a nitrogen glovebox 106 mg of Bis(trifluoromethane)sulfonimide lithium salt (Li salt) is added in 200 μ l of acetonitrile. Separately, in ambient condition, 73.2 mg of Spiro-OMeTAD

is added to 1 ml of chlorobenzene, then 17.5 μl of the lithium salt/acetonitrile is added followed by 28,8 μl of 4-tert-Butylpyridine (tBP). The solution is then put to be stirred up until its use. Before their printing the Spiro-OMeTAD must be filtered with a 0.2 μm PTFE filter.

Rheological parameters and jettability

The rheological measurements and the calculation of the Re and Oh number (Table IV.13) indicate that the Spiro-OMeTAD is in the limit of stable jettability. The surface tension is lower than the advised 25 $\text{mN}\cdot\text{m}^{-1}$ by the furnisher of the Dimatix printer. The Re number value is superior to 1 but the Oh number value is at that the lowest limit value. The predicted ejection speed is 2.47 $\text{m}\cdot\text{s}^{-1}$.

Density ($\text{kg}\cdot\text{m}^{-3}$)	1117
Viscosity ($\text{mPa}\cdot\text{s}$)	1.3
Surface tension ($\text{mN}\cdot\text{m}^{-1}$)	17.03
Ejection speed ($\text{m}\cdot\text{s}^{-1}$)	2.47
Re	21
Oh	0.1

Table IV.13 - Rheological parameters and jettability of Spiro-OMeTAD

iii. Printing optimisation

Ejection parameters

The speed of ejection measured on the inkjet printing machine is 2.94 $\text{m}\cdot\text{s}^{-1}$. Giving the high evaporation rate of the Spiro-OMeTAD solvent it was not possible to measure the droplets volume.

Splat size

The splat size of the Spiro-OMeTAD printed on perovskite later is not measurable because of the high roughness of the perovskite surface compared to the amount of Spiro-OMeTAD contained in one droplet. Moreover the Spiro-OMeTAD splats are invisible once deposited on the perovskite layer because of the high opacity of the perovskite. Therefore the splat size of the Spiro-OMeTAD was estimated thanks to splat measurements on ITO and WO_3 . The mean splat size on ITO is $103.7 \pm 9.2 \mu\text{m}$ while on WO_3 it is $126.2 \pm 5.7 \mu\text{m}$.

Printing parameters

The drop spacing parameter was optimized from the measure of the thickness of the spincoated Spiro-OMeTAD layer and of the printed Spiro-OMeTAD layer. The tested drop-spacing value were 40, 45 and 50 μm and was chosen arbitrary. However, these values were

found to produce a film thickness close to the one of the spincoated layer, the results are summarized in the Table IV.14. The thickness was in fact measured on the side of the Spiro-OMeTAD layer which is in contact of the glass since it was not possible to measure its thickness on the perovskite layer which is too rough.

	Spincoated	Drop spacing (μm)		
		40	45	50
Average thickness	283	330	277	233
<i>Standard deviation</i>	<i>13</i>	<i>44</i>	<i>13</i>	<i>34</i>

Table IV.14 - Thickness of the printed layer of Spiro-OMeTAD

iv. Perovskite solar cells with three printed layers

The best PSC with three inkjet printed layers was obtained in May 2017 with a PCE of 10.7 %. These three printed layers were WO_3 , $\text{CH}_3\text{NH}_3\text{PbI}_{3-x}\text{Cl}_x$ perovskite and Spiro-OMeTAD. Before to achieve such a high working photovoltaic cell the optimisation of the printing of the Spiro-OMeTAD lasted less than 4 months. In fact, most of the progress were made in the process of the WO_3 and perovskite layers (see next sections).

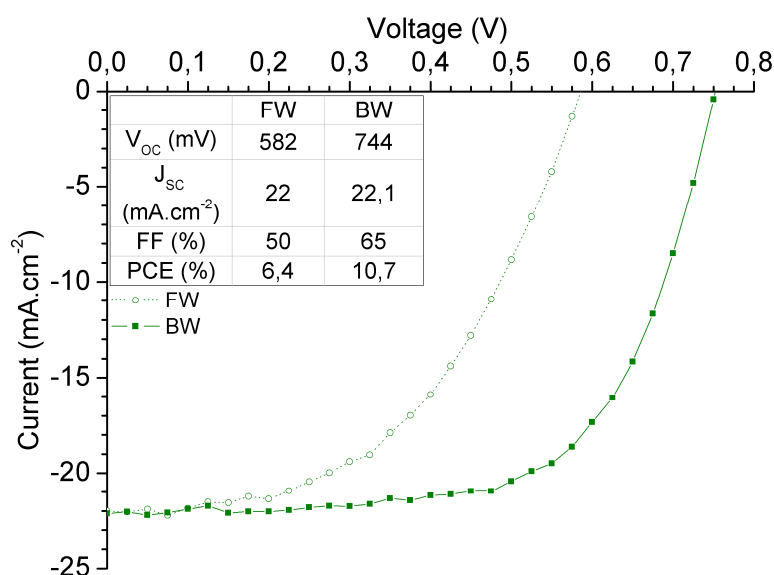


Figure IV.28 - JV curves of the best PSC with three printed layers

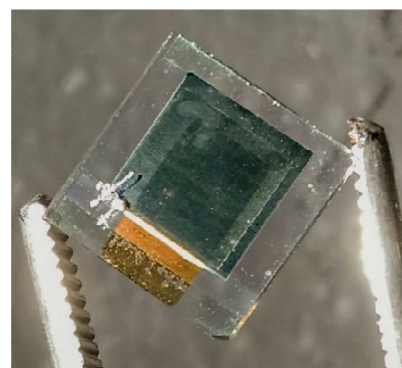


Figure IV.29 - A PSC with printed WO_3 , perovskite, and Spiro-OMeTAD layers

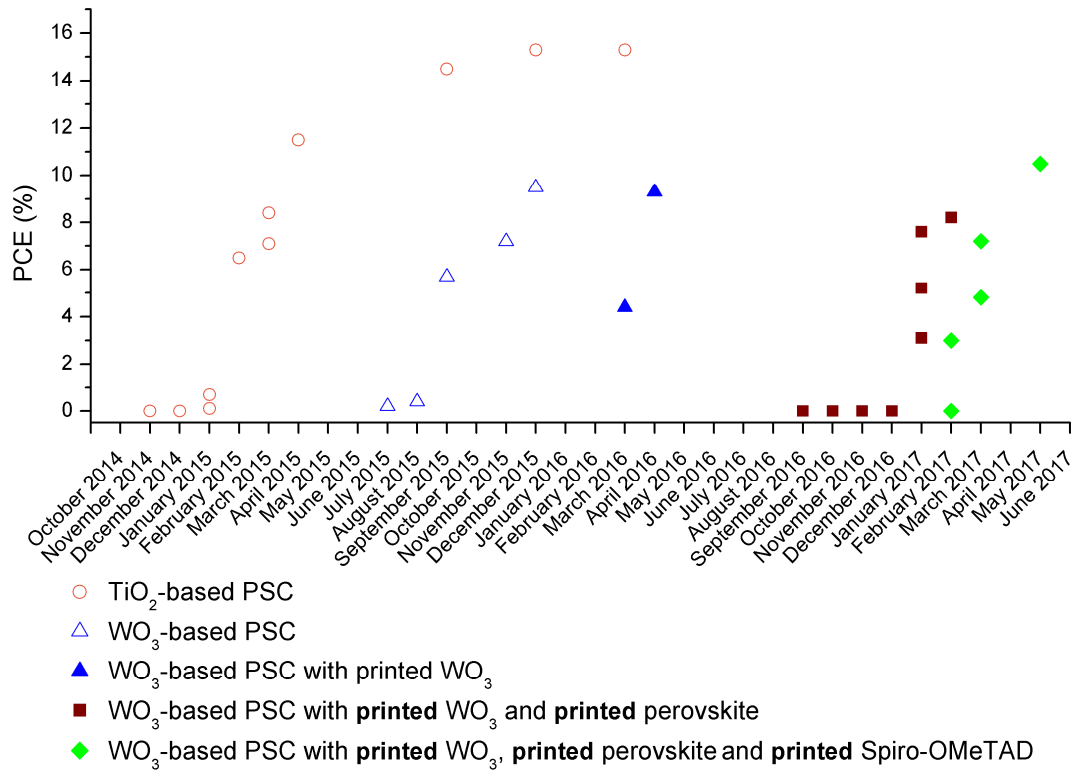


Figure IV.30 - PCE evolution of the best perovskite solar cells

This champion cell is visible in the Figure IV.29 alongside its JV curves of the Figure II.3. Compared to the objectives the V_{OC} of the best cell, which is at 744 mV, is in the acceptable range but still slightly lower. The J_{SC} is high enough at $22 \text{ mA}\cdot\text{cm}^{-2}$. For the first time the resulting PCE is higher than the objective which is of course a very good result. In terms of fabrication the printing is now complete for the three inner layers and the annealing is lower than $130 \text{ }^\circ\text{C}$.

		OBJECTIVES	BEST PRINTED WO ₃ AND PRINTED PEROVSKITE CELL COMPARISON
Photovoltaic parameters			
V _{oc} (mV)	830		744
J _{sc} (mA.cm ⁻²)	16		22
FF (%)	75		65
PCE (%)	10		10.7
Fabrication			
Active area	1 cm ²		20 mm ²
Electrode (ITO or FTO)	Non-printable		Non-printable
ETL	Printed		printed
Perovskite	Printed		printed
HTL	Printed		printed
Top electrode	Printable		Non-printable
Max annealing temperature	130°C		110 °C

Table IV.15 - Comparison between the objectives and spincoated printable WO₃-based PSC

v. LBIC and LBIV

Light Beam Induced Current (LBIC) and Light Beam Induced Voltage (LBIV) was conducted on TiO₂-based PSC and printed WO₃-based PSC (with three printed layer). In this characterisation technic the cell is illuminated locally by a pulsating white light spot which sweeps all the surface of the cell. The acquisition of the resulting current (in short-circuit condition) or the resulting voltage (in open-circuit condition) is proceed synchronously with the pulsating white light.

The LBIC and LBIV characterizations of photovoltaic cell can give insight on the physical default and features as well as the interfacial characteristics of the layers stacking. For the LBIV characterisation technics no current is collected because of the open-circuit condition. In this condition the collected value of V_{oc} gives information about, for example, the local shunt resistance or capacitive effects. For the LBIC, the short-circuit current condition allows to identify the difference in photo-generation trough the layer and interfacial and recombination defects.

The illuminated spot size is $200 \mu\text{m}^2$ with a power illumination of 0.5 mW. The shape of the electrode is visible in the four next figures. In the Figure IV.31 the superposition of the printed perovskite solar cell design and a LBIC/V cartography has been done to help the identification of the electrode.

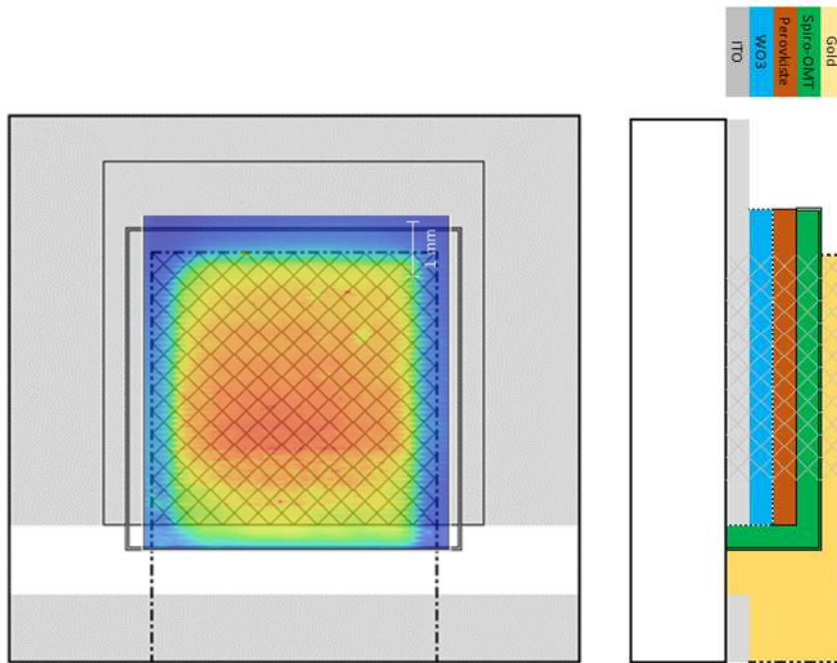


Figure IV.31 - Superposition of LBIC or LBIV cartography with the design of the printed PSC

The LBIC (Figure IV.32) of the spincoated TiO_2 -based PSC shows a relatively homogenous cell in term of photo-generated current. As the spincoating fabrication technic does not produce layer with a preferred orientation we can confirm that the aliasing of the picture is only due to the acquisition sweeping technic. Some defaults can be identified as little yellow dots in the right-top corner of the electrode. These little dots could be low-current-generation areas due to a bad processing of the material (crystallisation defect, foreign element). In the LBIV (Figure IV.33) cartography blurry horizontal lines can be seen and can be due to the acquisition. Furthermore, the dots region of low-current-generation are barely visible, always in the right top corner. As they are not provoking a low voltage area we can conclude that the origin of these dots are not due to a bad processing of the material but rather to a low-current-generation areas, probably due to a thinner zone of perovskite due to a dewetting of the perovskite ink. Always in the LBIV of the TiO_2 -based PSC, the value of the local V_{oc} is higher as we get close to the end of the electrode (low part of the cartography) where the holes are collected. This is due to the fact the conductivity of gold (over 10^7 S.m^{-1}) is higher than that of FTO (over 10^3 S.m^{-1}). The electrons are collected in the other direction (toward the top of the

picture) through the FTO layer and the longer is the path through the FTO the higher is the resistance and the higher is the resulting V_{OC} .

For both LBIC and LBIV of the TiO_2 -based PSC we clearly see the low level (green color) of, respectively, local J_{SC} and V_{OC} in the border of the electrode. Additionally, for the J_{SC} the lower value is in the bottom of the electrode. These low J_{SC} and V_{OC} areas are probably due to diffusion of specie like O_2 or H_2O from the side of the gold electrode.

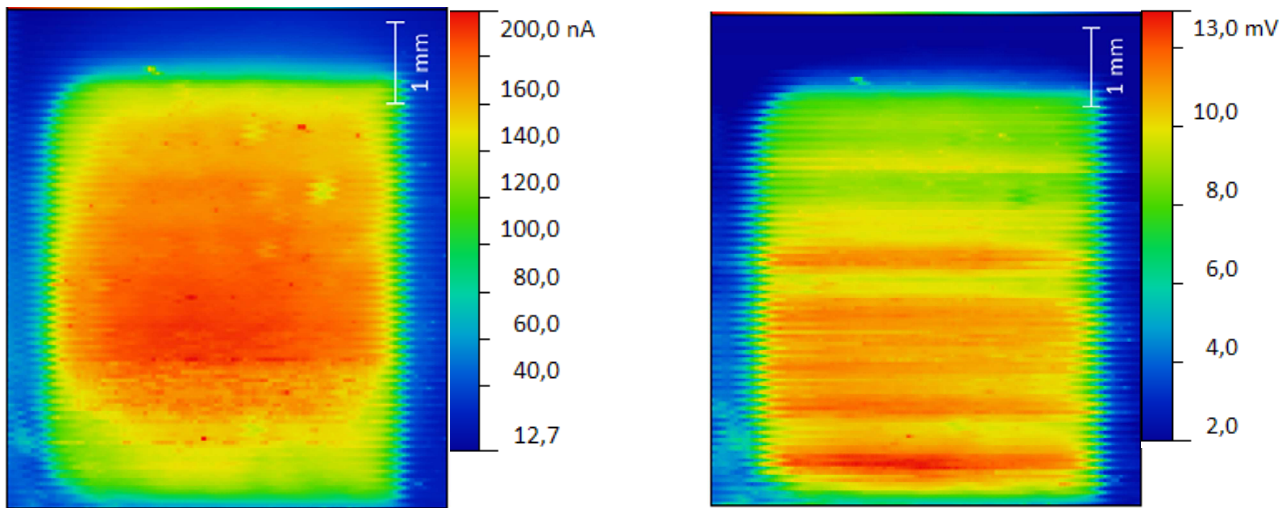


Figure IV.32 - LBIC cartography of TiO_2 -based PSC Figure IV.33 - LBIV cartography of TiO_2 -based PSC

The LBIC (Figure IV.34) and the LBIV (Figure IV.35) of the printed based- WO_3 PSC demonstrate a high heterogeneity. Both cartography show a low quality area in the right top corner of the electrode. This area is probably due to a delamination of the gold electrode from its corner.

The higher voltage area represents less than half of the cell and well defined horizontal lines can be seen. These lines are clearly visible in the LBIC cartography and are probably due to the printing default of the WO_3 layer of the Spiro-OMeTAD. The stronger hypothesis is than the quality of the WO_3 printing is homogenous at the top of the electrode (which is the beginning of the printing) and tends to deteriorate randomly creating these lines. These defaults in the printing produce higher current region. The higher current could be explained by nozzles which clog during printing: therefore, some lines could not be printed which would produce thinner WO_3 layer and promoting a better conductivity of the layer.

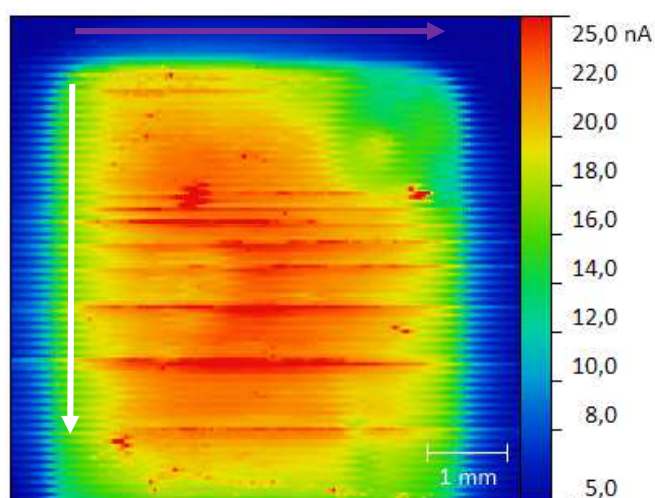


Figure IV.34 - LBIC cartography of printed WO_3 -based PSC (the white arrow indicates the printing direction while the purple one indicates drop deposition direction)

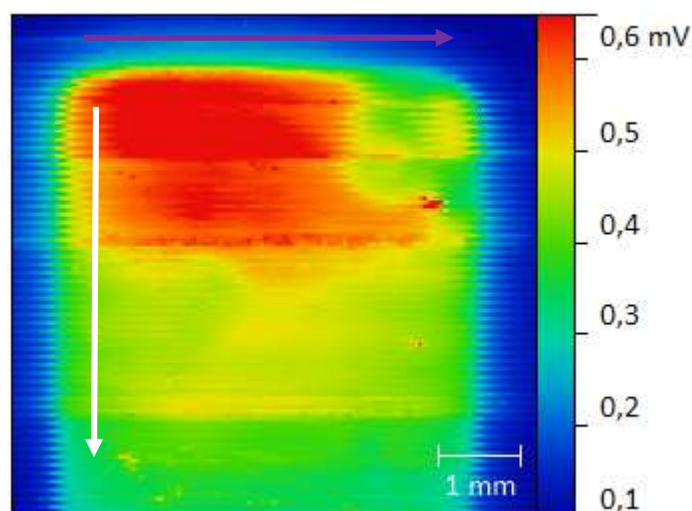


Figure IV.35 - LBIV cartography of printed WO_3 -based PSC (the white arrow indicates the printing direction while the purple one indicates drop deposition direction)

vi. Cause of outstanding working cell

Dewetting of the perovskite ink and influence of device performances

The best printed PSC was obtained after having printed the perovskite layer two days after the printing of the WO_3 layer, between these two steps the substrates were stored in the glovebox in a dry nitrogen atmosphere. In order to determine the effect of this modification in the process we measured the contact angle of three reference liquids (water, DIM and EG, Table IV.5) on WO_3 and ITO depending of the storage condition. Both surfaces were characterized just after the cleaning or the printing and 5 days after, with a storage in the nitrogen dry glovebox or outside in ambient condition. The surface energies were computed and are presented in the Table IV.16.

SURFACE STORAGE CONDITION	ITO			WO_3		
	0 day after cleaning	5 days in air	5 days in nitrogen	0 day after cleaning	5 days in air	5 days in nitrogen
Dispersive component ($\text{mN}\cdot\text{m}^{-1}$)	25.3	30.6	26.8	26.9	35.2	26.6
Polar component ($\text{mN}\cdot\text{m}^{-1}$)	8.0	10.8	16.6	37.1	13.7	38.1

Table IV.16 - Surface energy for ITO and WO_3 depending of the storage condition

The effect of storage is clearly visible on both surfaces. On the ITO the storage in dry nitrogen atmosphere doubles the polar component of the surface energy when the dispersive component stays in the same range. For the WO₃ the effect of storage in air is detrimental in completely reducing the polar component of the surface. In the overall the polar component of both surfaces are the most sensible to storage.

In order to have a better understanding of the consequences of the storage we computed the wetting envelop of each surfaces from this values of surface energy Figure IV.36. Thanks to the diagram the effect of storage is clear. The ITO wetting envelop is larger when stored 5 days after the cleaning, the enhancing is better in the case of nitrogen storage. As such, the perovskite ink has a better wettability on aged ITO than on fresh-cleaned ITO. This could have a positive outcome since it will prevent the dewetting of the perovskite ink on area without WO₃ layer. This situation happens often when the WO₃ is printed: nozzles can randomly clog and this could create area without printed droplets or printed lines. If the ITO is aged during the perovskite printing the perovskite ink will not dewet and this will promote the production of a homogenous film.

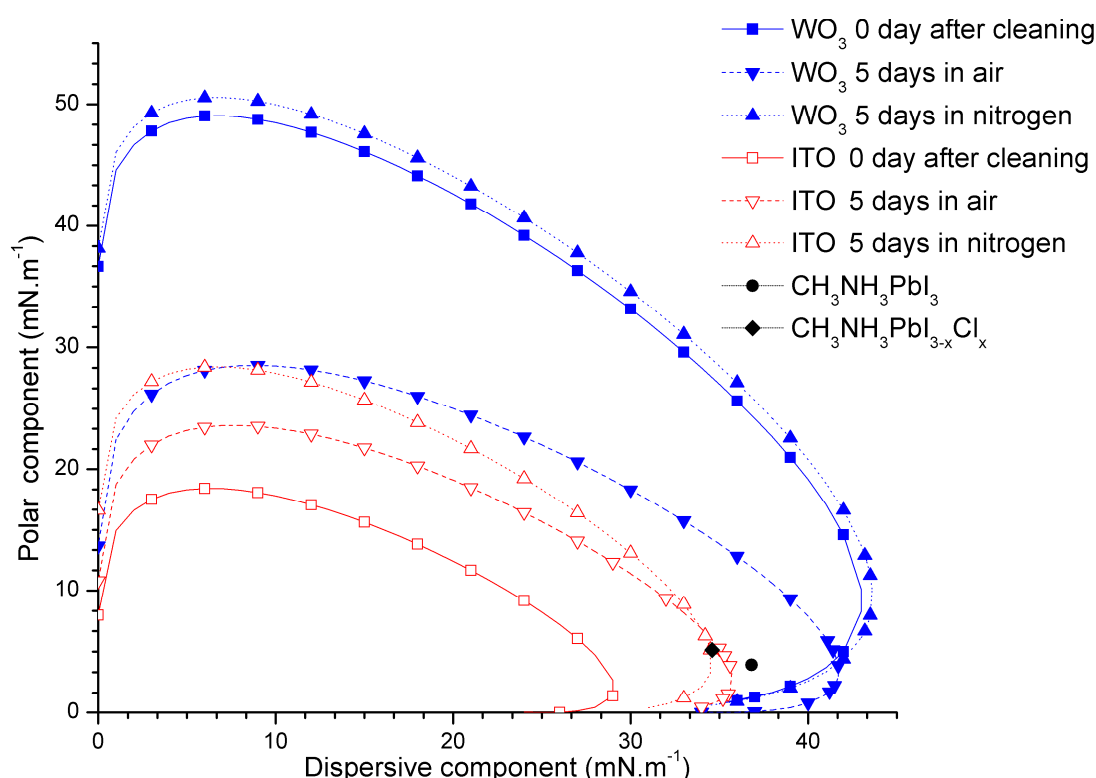


Figure IV.36 - Wetting envelope of ITO and WO₃ depending of the storage condition

Moreover; we can now look at the different formulation of the ink and its impact on wetting on the ITO. In the same Figure IV.36 two different formulations of perovskite ink are

presented: one with only iodine and the other one with chlorine and iodine (the explanation on the ink preparation is explained before on section IV.4.i.). This diagram clearly shows that the use of chlorine will promote a better wettability of the aged ITO compared to the perovskite with only iodine. This result could indicate why chlorine is often used in perovskite solution, indeed this improves the wettability of the ink in certain case where the ITO has been cleaned several days before the use.

In a first conclusion two parameters tend to increase wettability of the ink and promote good quality of the film:

- ITO which has been cleaned then aged during few days
- Use of chlorine in the ink.

The effect of the nature of the aging atmosphere on ITO is now to determine. From the Figure IV.35 we can say that to use nitrogen or ambient atmosphere has few impact on the ITO. At least nitrogen atmosphere tends to improve a little the polar component of the surface. This could be explained by the fact that nitrogen atmosphere is of course deprived of water. Water molecules adsorbed by the ITO are essentially responsible of the dispersive surface energy component and could be the source of the increasing dispersive component of the ITO surface energy when stored in air. At the contrary when the ITO is stored in nitrogen no water is adsorbed, as the atmosphere is almost perfectly dry the remaining water desorbs from the ITO surface which recovers the same value of dispersive component that after the cleaning.

The increase of the polar component of the ITO surface energy during the nitrogen storage is not easily explained. The only hypothesis is that vacancies in the ITO are responsible for the polarity of the surface. Since these vacancies are freed during the storage (by the desorbing of water and oxygen molecules) the polar component would increase as the number of free vacancies increases.

The effect of storage is clear for the WO_3 layer stored in air. As the dispersive component slightly increases (probably due to adsorbed water) the polar completely drops at $13.7 \text{ mN}\cdot\text{m}^{-1}$. The reason of this drop is not clear but can be prevented by storing the WO_3 in the nitrogen atmosphere. This lower surface energy would provoke some dewetting during the perovskite printing. Further investigation with KPFM was conducted in the next section to determine the effect of this degradation on the electrical functioning of the perovskite solar cells.

As a final conclusion the storage of the printed WO_3 in nitrogen is beneficial because it allows to increase the wettability of the ITO without degrading the WO_3 layer. The increase of wettability produce homogenous layer of printed perovskite with chlorine with less pinholes and therefore fewer contact between the ITO and the printed Spiro-OMeTAD.

Effect during printing

When the ITO substrate is not cleaned properly the WO_3 droplets do not fusion and create a regular frame of WO_3 point. This behaviour has already been developed in the IV.3. section. We will now see the direct effect of the cleaning of ITO on the perovskite printing.

In the Figure IV.37 and Figure IV.38 are presented the typical result of a WO_3 printing on an ITO substrate which was not cleaning properly. More precisely the ITO substrate were rub a few second with a paper towel, rinsed with isopropanol then dry with nitrogen. In this situation the quality printing of the WO_3 printing is not sufficient and the droplets do not fusion. The result is a regulate frame with 30 μm droplets separated by a distance of 50 μm between droplets centre.

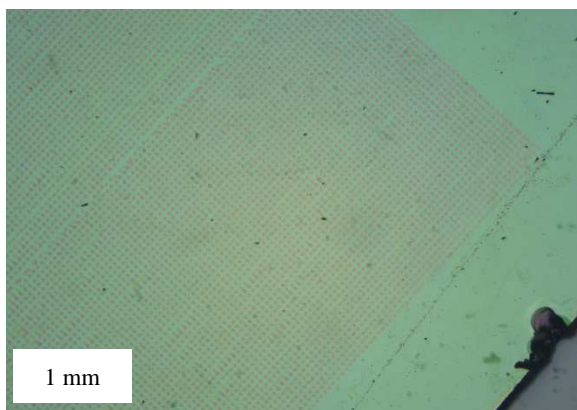


Figure IV.37 - Optical microscopy of the printing of WO_3 without correct cleaning

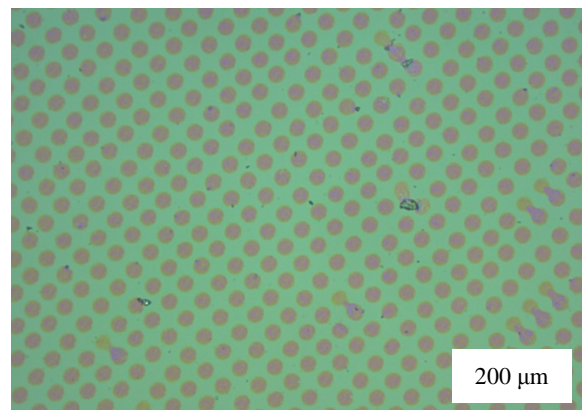


Figure IV.38 - Optical microscopy detail of the printing of WO_3 without correct cleaning

This layer was then printed 3 days later with a perovskite $\text{CH}_3\text{NH}_3\text{PbI}_{3-x}\text{Cl}_x$ ink and the results are visible on the Figure IV.39. The result here is clear: the perovskite ink completely dewets from the ITO and spreads only on WO_3 splats. Since the perovskite ink is in greater amount that necessary to only cover the WO_3 splats the ink tends to form bigger drop which are visible in the Figure IV.40. This tends to happen when some WO_3 droplets manage to fuse to form a continuous path that the perovskite ink runs up by capillarity.

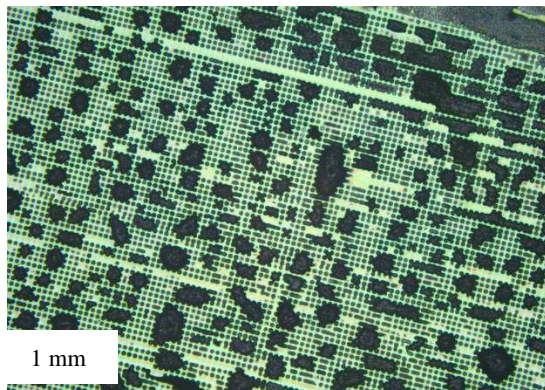


Figure IV.39 - Optical microscopy of the perovskite printed on a WO_3 splat frame

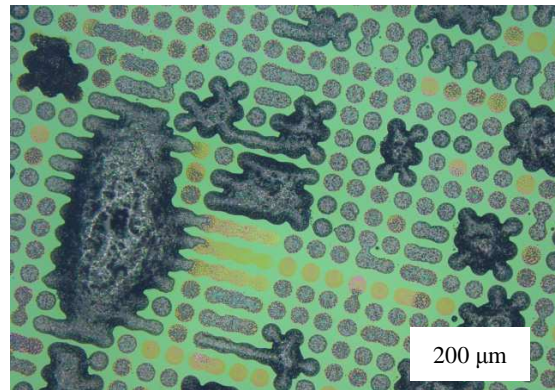


Figure IV.40 - Optical microscopy detail of the perovskite printed on a WO_3 splat frame

In term of PSC this dewetting is detrimental for the solar cell operations. In these conditions the ITO and Spiro-OMeTAD layers are in contact and this could provoke recombination between the electrons collected by ITO and the holes extracted by the HTL. This clearly shows that in this process the cleaning of the ITO and the printing of the WO_3 are the most sensible steps and must be preciously followed.

This phenomenon also shows the possibility to use this dewetting effect to produce by inkjet printing an array of photoelectric micro-devices (PV, photodiode, LED...) on a single substrate. To do so technological challenges must be first investigated, such as the design of an efficient ITO electrodes and top electrodes (probably by photolithography) and the efficient drying of such small droplets of perovskite ink at ambient temperatures.

Work function

KPFM measurements were performed on the printed WO_3 in function of the storage condition in order to determine the effect of storage on the WO_3 energy level. The results are presented in the Table IV.17. The same value of -4.8 eV is found for each condition. The same value has already been found few months before (Table IV.2).

The storage has no effect on the work function of the WO_3 layer. This result with the previous one on the wetting envelope indicate that the effect on storage in the WO_3 is not trivial. The surface of the WO_3 is modified upon storage which modifies the wettability but no effect on electron extraction is found.

CONTROL LAYERS		MEASURED WORK FUNCTION (eV)
ITO		-4.9
FTO		-4.8
STACKING		MEASURED WORK FUNCTION (eV)
Glass/ITO/printed WO ₃	0 day after cleaning	-4.8
	5 days in air	-4.8
	5 days in nitrogen	-4.8

Table IV.17 - Work function of printed WO₃ depending of storage conditionvii. WO₃ annealing temperature*Effect on photovoltaic parameters*

After the production of PSC with three printed layers further optimisation of the layers were performed. One of the parameters which was not deeply investigated was the annealing temperature of the WO₃. For this experiment PSC were produced with spincoated layer of WO₃, perovskite and Spiro-OMeTAD, the WO₃ layer was annealed at 80°C, 110 °C and 140°C during 10 minutes. For the other parts of the fabrication the same procedures as presented previously were followed. For each temperature three cells were produced and the average value for each electrical parameter (PCE, FF, J_{SC}, V_{OC}) was calculated.

In term of PCE (Figure IV.41) the annealing temperature of 110 °C normally used is in fact the annealing temperature that produced the least efficient PSC for both backward and forward measurements. As such, both temperature of 80°C and 140°C produce WO₃-based PSC with the highest mean efficiencies. In order to determine which temperature is the best it is interesting to look at the other electrical parameters such as FF, J_{SC} and V_{OC}.

For a 140°C annealing temperature the mean J_{SC} (Figure IV.43) of the FW and BW measurements is almost the same around 20 mA.cm⁻², almost the same value is obtained for 80°C only for the BW measurement. Interestingly the average value of the short-circuit current in backward measurement increases with the annealing temperature. This can be explained by the increasing amount of oxygen vacancies with higher annealing temperature [89]. Indeed as the amount of oxygen vacancies increases the WO_x is getting closer of the metallic tungsten therefore increasing the conductivity of the layer. Anyhow from the point view of the J_{SC} the best temperature to use is 140°C.

In term of FF (Figure IV.42) the higher average value is 66% obtained for an annealing 80°C in backward measurements The other value of average FF for 110°C and 140°C in

backward measurement are close to one another and their variation are in the range of the standard deviation. The three values of FF in FW measurement for each annealing temperature are in the same situation and are not discernible.

The best annealing temperature for the average V_{OC} is $80^{\circ}C$ (Figure IV.44). The highest mean V_{OC} is obtained at 693 mV for backward measurement, for the forward measurement the highest mean V_{OC} is still obtained for the annealing temperature of $80^{\circ}C$ despite a high hysteresis.

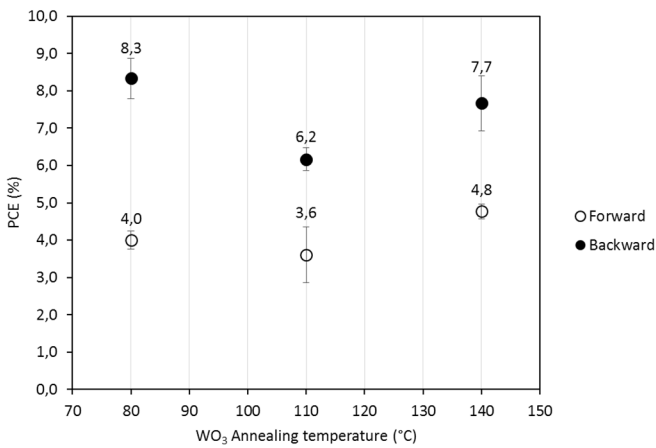


Figure IV.41 - Average PCE of WO₃-based PSC depending of the WO₃ annealing temperature

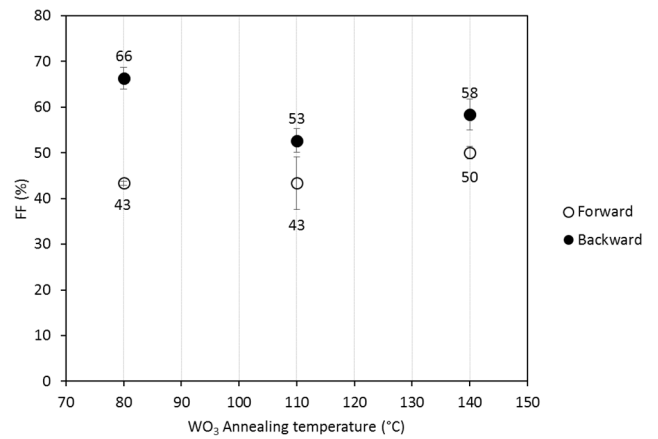


Figure IV.42- Average FF of WO₃-based PSC depending of the WO₃ annealing temperature

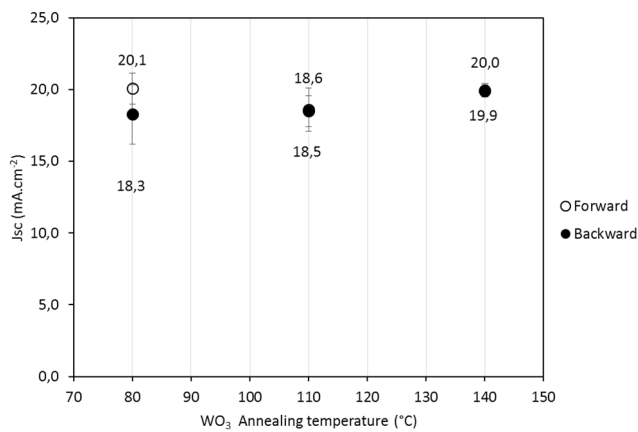


Figure IV.43- Average J_{sc} of WO₃-based PSC depending of the WO₃ annealing temperature

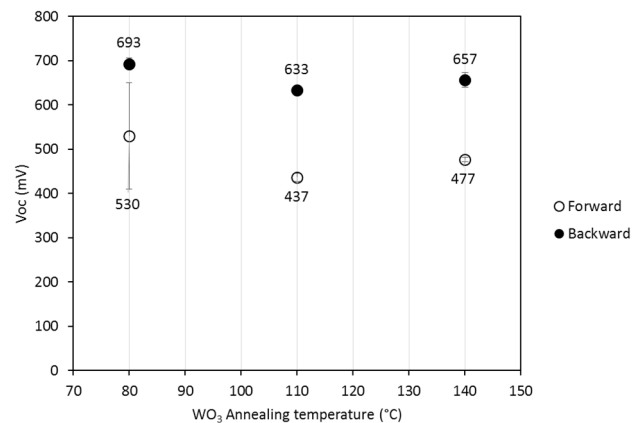


Figure IV.44- Average V_{oc} of WO₃-based PSC depending of the WO₃ annealing temperature

Compared to the objectives (Table IV.15) the short-circuit current is already high enough and the enhancing should be focused on FF and V_{OC} . In term of average value the highest FF and V_{OC} was obtained for $80^{\circ}C$. Furthermore, in this experiments the best V_{OC} at 710 mV and the highest FF at 68 % was also obtained for $80^{\circ}C$. Therefore, the temperature of annealing of the printed WO₃ was lowered from $110^{\circ}C$ to $80^{\circ}C$.

Effect on WO₃ work function

KPFM measurement were conducted on spincoated layers of WO₃ annealed at three different temperatures: 80, 110 and 140 °C. The results of the work function measurements are presented in the Table IV.18

CONTROL LAYERS		MEASURED WORK FUNCTION (eV)
ITO		-4.9
FTO		-4.8
REFERENCE LAYER		MEASURED WORK FUNCTION (eV)
Glass/FTO/TiO ₂ /TiO ₂ -mp		-4.5
LAYER	ANNEALING TEMPERATURE	MEASURED WORK FUNCTION (eV)
Glass/ITO/WO ₃	80 °C	-4.7
	110 °C	-4.9
	140 °C	-4.9

Table IV.18 - Work function of spincoated WO₃ depending of annealing temperature

Here we find that the WF of the WO₃ annealed at 80°C has a higher work function than the one annealed at 110°C. The WF of the WO₃ layer increases from -4.9 eV to -4.7 eV. This is beneficial since the WF value approaches the one of the stacking of FTO and TiO₂ layers. The conditions of the 80°C annealed WO₃ is closer of the condition of the TiO₂-based PSC. It seems that the annealing temperature has a high impact of the electron extraction of the WO₃ layer as it has an impact of the conductivity of the same layers.

For a better comprehension of the mechanism other measurement should be conducted. These measurements should be done on WO₃ layer annealed at different temperature from ambient temperature to at least 150 °C. KPFM would be very interesting to investigate, conductivity measurements (with the 4 probes technique) would be mandatory. Hall measurements are currently on the way, we hope that this characterization will give us insight on the doping level of level, notably regarding the density of oxygen vacancies and their roles in the conductivity.

6. Perspectives for a printable top electrode

The next step for the design of the printed cell is to replace the evaporated gold by a printable electrode. The process and the nature of the electrode must follow some requirements:

- The energy level of the conduction band of the materials must be slightly superior to the one of the Spiro-OMeTAD which is -5.22 eV [113]. In term of

metal the most suitable is of course the gold (-5.1 eV), then silver (-4.6 eV), copper (-4.4 eV), and aluminium (-4.3 eV).

- The process of the electrode should have an annealing lower than 90°C during less than 10 minutes.
- The solvent of the electrode ink should be compatible with the Spiro-OMeTAD. This layer has been processed with chlorobenzene so this solvent must be avoided.

As the objective is to produce low-cost printed perovskite solar cell the strategy would be to choose a low-cost material which is already well known for the printing of electrodes. Silver nanoparticles inks are already widely used in a lot of applications and particularly in the printing of organics solar cells, therefore this material could be a good choice to replace the top electrode.

However, silver is known to react with perovskite $\text{CH}_3\text{NH}_3\text{PbI}_{3-x}\text{Cl}_x$ to form AgI [114] in the case of evaporated silver. During evaporation hot silver atoms can easily diffuse through the Spiro-OMeTAD (which is also heated) and react with the perovskite. We hope that this phenomenon will not occur for the printing of the silver top electrode. Indeed, the ink is a nanoparticle suspension and the nanoparticles would have more difficulty to go through the Spiro-OMeTAD than an atom. Furthermore, if the printing is processed at ambient temperature the diffusion of nanoparticle would be considerably slowed down. Upon annealing of the top electrode the nanoparticle will be partially sintered, thus reducing the chance of diffusion of silver nanoparticle in the Spiro-OMeTAD. Previous work from Brabec. Et al [115] showed that sprayed silver nanowires electrode allow the production of efficient and stable perovskite solar cell.

General conclusion

The principal goals of this work of thesis were the mastery of the fabrication process of these new perovskite solar cells in XLIM and the feasibility demonstration of the printability of such solar cells.

After these three years of work the fabrication of the perovskite solar cell has been adapted for the needs and the objectives of the Elite team of XLIM. It allowed the production of state-of-the-art perovskite solar cell with TiO₂ electron transporting layer with a champion cell at 15.3%. The first important achievement was the design and fabrication of a printable perovskite solar cell. This solar cell was also annealable at low-temperature, showing its versatility for every substrate such as PET or even paper. This WO₃-based perovskite solar cell was also at the state-of-the-art level with a photo-conversion efficiency of 9.3 %.

The most important achievement of this work is the production an actual printed perovskite solar cell, all in ambient atmosphere. If at the beginning of the research project the objective was to print only the perovskite absorbing layer this work showed in fact that three of the solar cell layers was in fact printable. With a WO₃ printed layer, a perovskite printed layer and a Spiro-OMeTAD layer a 20 mm² champion solar cell with an efficiency over 10.7 % was produced. This result is one of the best in term of printed solar cell. This inkjet process used in the work is a true printing and without any utilisation of a mask.

The printed perovskite solar cells are now able to supply in energy at low-cost condition an autonomous sensor. From the first work on stability effectuated in this thesis the remaining work is clear: perovskite solar cell must be protected of the UV and the atmosphere by an efficient encapsulating layer. The next big step is the enlargement of the printed area. This is the biggest challenge for the printing of the perovskite solar cell: despite the large area to print the perovskite layer must remain wet and homogenous in thickness, furthermore if the WO₃ layer is kept as an electron transporting layer its printing process must be stabilized in term of ejection and wettability on ITO.

At last, this work opens opportunities for the creation of new shape of perovskite solar cell. Of course, the feasibility to print the perovskite solar cell on flexible substrates such as PET or paper should be considered. This work gives many insights about stability, and on the importance of the rheology investigations. It notably brings new arguments on the role of chloride on the perovskite mixture. Thanks to the variation of the wetting of the substrate it is now even possible to print different kind of perovskite side by side in order to create frame and

GENERAL CONCLUSION

modulate the colour of the absorbing layer, or the transparency of the cell. One of the new and exciting possibilities would be to print array of micro-perovskite solar cell, in order to increase the stability (each active layer will be fully surrounded by a protecting interfacial layer) and to tailor the electrical parameters for the each application.

V. References and tables

1. Figures table

FIGURE I.1 – THE FUTURE AS SEEN BY SYD MEAD, THE FIRST PUBLICATION OF ASIMOV’S « ...THAT THOU ART MINDFUL OF HIM » AND CAPTAIN JAMES TIBERIUS KIRK USING HIS OMNIPOTENT COMMUNICATOR.....	12
FIGURE I.2 – SCHEMATIC REPRESENTATION OF AN AUTONOMOUS SENSOR	13
FIGURE I.3 – SCHEMATIC ILLUSTRATION OF THE ENERGY MANAGEMENT IN THE SENSOR.	15
FIGURE I.4 – FROM LEFT TO RIGHT ALEXANDRE EDMOND BECQUEREL, CHARLES FRITT, ALBERT EINSTEIN AND ALEXANDER GRAHAM BELL	19
FIGURE I.5 - GENERIC PEROVSKITE STRUCTURE.....	21
FIGURE I.6 - ABSORPTION SPECTRUM OF $\text{CH}_3\text{NH}_3\text{PbI}_{3-x}\text{Cl}_x$ PEROVSKITE	23
FIGURE I.7 - TAUC FIT FOR $\text{CH}_3\text{NH}_3\text{PbI}_{3-x}\text{Cl}_x$ LAYER.....	24
FIGURE I.8 - THE EVOLUTION OF PEROVSKITE SOLAR CELLS FROM THE DYE SENSITIZED SOLAR CELLS TECHNOLOGY [113]	25
FIGURE I.9 - CHART OF THE BEST PHOTOVOLTAIC RESEARCH-CELL EFFICIENCIES (JANUARY 2017).....	26
FIGURE II.1 - PIEZOELECTRIC ELEMENT DEFORMATION PROVOKING THE DROPLET JETTING	30
FIGURE II.2 - PIEZOELEMENT JETTING WAVEFORM.....	31
FIGURE II.3 - EXAMPLE OF A GOOD AND REPEATABLE JETTING: FORMING A UNIQUE DROP, WITHOUT DROPLETS, IN A STRAIGHT TRAJECTORY AND WITH TAILS RETRACTING INTO THE DROP’S HEAD. [111]	31
FIGURE II.4 - RE/WE GRAPH FOR INK JETTABILITY [46].....	34
FIGURE II.5 - INTERACTION PHASES BETWEEN DROP AND SURFACE.	35
FIGURE II.6 - A VARIETY LIQUID DROP IMPACT ON TO A SURFACE [112, 45]	36
FIGURE II.7 - INTERACTION FORCES AT THE GAS/SURFACE/LIQUID INTERFACES	36
FIGURE II.8 - DRYING MODE AND CONTACT LINE MOVES.....	37
FIGURE II.9 - DROP DISPOSITION ON A RECTANGLE.....	38
FIGURE II.10 - SCHEMATIC REORIENTATION OF THE FORCES ACTING ON THE INTERNAL AND SUPERFICIAL MOLECULES	40
FIGURE II.11 - WETTING ENVELOP LOOK	44
FIGURE II.12 - DROP SCHEMATISATION FOR SURFACE ENERGY MEASUREMENT.....	45
FIGURE II.13 - LAMINAR SHEAR OF FLUID BETWEEN TWO PLATES: COUETTE FLOW.....	47
FIGURE II.14 - THE AM1.5 GLOBAL SPECTRUM IS DESIGNED FOR FLAT PLATE MODULES, AM1.5 FOR SOLAR CONCENTRATOR, THE AM0 IS THE EXTRATERRESTRIAL SOLAR SPECTRA	49
FIGURE II.15 - J(V) CURVE SCHEMATIC REPRESENTATION OF AN ILLUMINATED PHOTOVOLTAIC CELL	50
FIGURE III.2 - SCHEMATIC REPRESENTATION OF THE TiO_2 REFERENCE PEROVSKITE SOLAR CELL DIRECT STRUCTURE	53
FIGURE III.2 - WORKING PRINCIPLE OF PEROVSKITE SOLAR CELL IN DIRECT ARCHITECTURE.....	53
FIGURE III.3 - TiO_2 -BASED PEROVSKITE SOLAR CELL FABRICATION DESIGN (VERTICAL SCALE NOT RESPECTED)..	54
FIGURE III.4 - JV CURVES OF THE BEST TiO_2 -BASED PSC : BACKWARD (BW) MEASUREMENTS IS FROM 1.5 V TO -0.1 V AND FORWARD (FW) IS FROM -0.1 V TO 1.5V	55
FIGURE III.5 - JV CURVE IN DARK OF A PEROVSKITE SOLAR CELL.....	55

REFERENCES AND TABLES

FIGURE III.6 - PCE EVOLUTION OF THE BEST PEROVSKITE SOLAR CELLS	55
FIGURE III.7 - A TiO_2 -BASED PEROVSKITE SOLAR CELL.....	55
FIGURE III.8 - PSC PERFORMANCES MEASURED IN BACKWARD JV DEPENDING OF THE ATMOSPHERE DURING PEROVSKITE SPINCOATING.....	59
<i>FIGURE III.9 - TiO_2-MP SURFACE AFM CHARACTERIZATION</i>	63
<i>FIGURE III.10 - $\text{CH}_3\text{NH}_3\text{PbI}_{3-x}\text{Cl}_x$ PEROVSKITE SURFACE AFM CHARACTERIZATION</i>	63
FIGURE III.11 - TWO DIFFERENT SHOTS OF OPTICAL MICROSCOPY OF THE PEROVSKITE LAYER FROM COMPARABLE PEROVSKITE SOLAR CELL.....	63
FIGURE III.12 - POST-ANNEALING UV-VISIBLE TRANSMISSION AND REFLECTION SPECTRA FOR COMPACT AND MESOPOROUS TiO_2 ON GLASS, ABSORPTION OF $\text{CH}_3\text{NH}_3\text{I}_x\text{Cl}_{3-x}$ ON GLASS.....	64
FIGURE III.13 - IPCE OF A TiO_2 - BASED PEROVSKITE SOLAR CELL	65
FIGURE III.14 - JV CURVES OF THE BEST TiO_2 -BASED PSC: BACKWARD (BW) MEASUREMENTS IS FROM 1.5 V TO - 0.1 V AND FORWARD (FW) IS FROM -0.1 V TO 1.5V.....	66
FIGURE III.15 - INFLUENCE OF MOVING CHARGE CARRIERS ON BAND ENERGIES OF A PEROVSKITE THIN FILM.	67
FIGURE III.16 - INFLUENCE OF THE VOLTAGE SWEEP STARTING POINT ON THE FORWARD SCAN	67
FIGURE III.17 - FORWARD (TOP) AND BACKWARD (BOTTOM) JV CURVES DEPENDING OF THE DELAY BETWEEN VOLTAGE IMPOSITION VALUES. FOR CLARITY ONLY THE POSITIVE STANDARD DEVIATION VALUES ARE DISPLAYED	69
FIGURE III.18 - SHORT-CIRCUIT CURRENT, OPEN-CIRCUIT VOLTAGE, FF AND PCE DEPENDING OF THE ILLUMINATION LEVEL.....	70
FIGURE III.19 - SUMMARIZING SCHEME OF DEGRADATION IN PSC	72
FIGURE III.20 - STEADY-STATE PL MEASUREMENTS OF PEROVSKITE LAYERS 2 DAYS AND 11 DAYS AFTER THE PRODUCTION ON TiO_2 ETL.....	73
FIGURE III.21 - STABILITY OF TiO_2 -BASED PEROVSKITE SOLAR CELLS	73
FIGURE III.22 - BACKWARD JV MEASUREMENTS FOR TiO_2 -BASED PSC AT THEIR PRODUCTION DAY AND 9 DAYS LATER.....	74
FIGURE III.23 - WO_3 NANOPARTICLE SOLUTION USED FOR PSC FABRICATION	76
FIGURE III.24 - WO_3 -BASED PEROVSKITE SOLAR CELL FABRICATION DESIGN (VERTICAL SCALE NOT RESPECTED)	77
FIGURE III.25 - JV CURVES OF THE BEST WO_3 -BASED PSC : BACKWARD (BW) MEASUREMENTS IS FROM 1.5 V TO - 0.1 V AND FORWARD (FW) IS FROM -0.1 V TO 1.5V.....	78
FIGURE III.26 - JV CURVE IN DARK OF A PEROVSKITE SOLAR CELL.....	78
FIGURE III.27 - PCE EVOLUTION OF THE BEST PEROVSKITE SOLAR CELLS	79
<i>FIGURE III.28 - A WO_3-BASED PEROVSKITE SOLAR CELL</i>	79
FIGURE III.29 - POST-ANNEALING UV-VISIBLE TRANSMISSION AND REFLECTION SPECTRA FOR COMPACT AND MESOPOROUS WO_3 ON GLASS, ABSORPTION OF $\text{CH}_3\text{NH}_3\text{I}_x\text{Cl}_{3-x}$ ON GLASS.....	81
FIGURE III.30 - UV-VISIBLE ABSORPTION SPECTRA FOR PSC WITH WO_3 OR TiO_2 AS ETL (WITHOUT THE GOLD TOP ELECTRODE)	81
FIGURE III.31 - IPCE OF A WO_3 - BASED PEROVSKITE SOLAR CELL	82
FIGURE III.32 - SHORT-CIRCUIT CURRENT, OPEN-CIRCUIT VOLTAGE, FF AND PCE DEPENDING OF THE ILLUMINATION LEVEL.....	83

REFERENCES AND TABLES

FIGURE III.33 - REFRACTIVE (N) AND EXTINCTION (K) INDEX OF THE WO ₃ LAYER DEPENDING OF THE RADIATION ENERGY	84
FIGURE III.34 - WO ₃ SURFACE AFM CHARACTERIZATION.....	85
FIGURE III.35 - OPTICAL MICROSCOPY OF CH ₃ NH ₃ PbI _{3-x} Cl _x PEROVSKITE SPINCOATED ON A WO ₃ LAYER.....	85
FIGURE III.36 - ILLUSTRATION OF THE EXISTENCE OF A CORRELATION BETWEEN THE VALUES OF THE ETL WF AND THE V _{OC} OF THE PSC.....	86
FIGURE III.37 - STEADY-STATE PL MEASUREMENTS OF PEROVSKITE LAYERS ON ETL AND ON THEIR RESPECTIVE TRANSPARENT CONDUCTIVE LAYER	88
FIGURE III.38 - TRPLD CURVES OF PEROVSKITE LAYERS ON ETL ON THEIR RESPECTIVE TCL.....	89
FIGURE III.39 - K _{CT} CURVES OF PEROVSKITE LAYER ON TiO ₂ AND WO ₃ , AFTER 3 DAYS (A) AND 11 DAYS (B)	91
FIGURE III.40 - STEADY-STATE PL MEASUREMENTS OF PEROVSKITE LAYERS 2 DAYS AND 11 DAYS AFTER THE PRODUCTION ON WO ₃ ETL	93
FIGURE III.41 - SUMMARIZING SCHEME OF DEGRADATION IN PSC	94
FIGURE III.42 - STABILITY OF TiO ₂ -BASED PEROVSKITE SOLAR CELLS	95
FIGURE III.43 - BACKWARD JV MEASUREMENTS FOR WO ₃ -BASED PSC AT THEIR PRODUCTION DAY AND 9 DAYS LATER.....	96
FIGURE III.44 - NITZ MOLECULE.....	96
FIGURE III.45 - EXCITATION (MAGENTA LINE) AND EMISSION (ORANGE LINE) SPECTRUM OF NITZ MOLECULE, PS/NITZ FILM TRANSMISSION (BLACK LINE). IPCE SPECTRUM (CYAN LINE) OF OUR PSC.....	98
FIGURE III.46 - MEAN EVOLUTION OF PCE OF 5 PSC DURING NINE MINUTES UNDER AN AM 1.5 100 W.m ² ILLUMINATION, BEING ALTERNATIVELY EXPOSED TO UV-CONTAINING LIGHT (Q) AND NITZ-FILTERED LIGHT (N)	99
FIGURE III.47 - IPCE OF TiO ₂ PSC WITH OR WITHOUT NITZ FILM	100
FIGURE III.48 - GRAPHICAL REPRESENTATION OF THE X CALCULATION FOR TWO VALUE OF THE IPCE OF THE PSC (70 AND 90 %) IN THE EMISSION RANGE, DEPENDING OF THE EFFICIENCY (FROM 5 TO 100 %) IN THE EXCITATION RANGE AND THE EQY. THE SITUATION OF OUR PSC/NITZ SYSTEM IS FRAMED IN YELLOW...	101
FIGURE III.49 - J _{SC} OF TiO ₂ -BASED PSC PROTECTED WITH UV FILTER (WITHOUT UV), WITH NITZ OR NOT UV-PROTECTED (WITH UV)	103
FIGURE III.50 - FF OF TiO ₂ -BASED PSC PROTECTED WITH UV FILTER (WITHOUT UV), WITH NITZ OR NOT UV-PROTECTED (WITH UV)	103
FIGURE III.51 - V _{OC} OF TiO ₂ -BASED PSC PROTECTED WITH UV FILTER (WITHOUT UV), WITH NITZ OR NOT UV-PROTECTED (WITH UV)	103
FIGURE III.52 - J _{SC} OF WO ₃ -BASED PSC PROTECTED WITH UV FILTER (WITHOUT UV), WITH NITZ OR NOT UV-PROTECTED (WITH UV)).....	103
FIGURE III.53 - FF OF WO ₃ -BASED PSC PROTECTED WITH UV FILTER (WITHOUT UV), WITH NITZ OR NOT UV-PROTECTED (WITH UV)	104
FIGURE III.54 - V _{OC} OF WO ₃ -BASED PSC PROTECTED WITH UV FILTER (WITHOUT UV), WITH NITZ OR NOT UV-PROTECTED (WITH UV)	104
FIGURE III.55 - PCE OF PSC PROTECTED WITH UV FILTER (WITHOUT UV), WITH NITZ OR NOT UV-PROTECTED (WITH UV) WITH TiO ₂ (A) AND WO ₃ (B) AS ETL	105

REFERENCES AND TABLES

FIGURE III.56 - EQY OF NITZ FILM AFTER 4 H OF SOLAR LIGHT EXPOSITION	105
FIGURE IV.1 - PRINTED WO ₃ -BASED PEROVSKITE SOLAR CELL FABRICATION DESIGN (VERTICAL SCALE NOT RESPECTED).....	109
FIGURE IV.2 - WAVEFORM APPLIED FOR THE WO ₃ INK EJECTION.....	111
FIGURE IV.3 - DROP PROFILES OF THE WO ₃ EJECTION THROUGH TIME, FROM THE BEGINNING OF THE JETTING (A), TO THE INTERMEDIATE STEP (B) THEN TO THE FINAL DROP (C)	112
FIGURE IV.4 - SPLAT SIZE OF WO ₃ PRINTED ON ITO DEPENDING OF THE SURFACE TREATMENT.....	113
FIGURE IV.5 - WETTING ENVELOPE OF THE ITO BEFORE AND AFTER THE ACETONE/ETHANOL/ISOPROPANOL/UV/ISOPROPANOL TREATMENT	114
FIGURE IV.6 - WO ₃ LAYER PRINTED ON ITO BEFORE TREATMENT.....	115
FIGURE IV.7 - WO ₃ LAYER PRINTED ON ITO AFTER TREATMENT	115
FIGURE IV.8 - DROP SPACING OPTIMISATION WITH PEROVSKITE SOLAR CELL.....	115
FIGURE IV.9 - AFM CHARACTERIZATION OF PRINTED WO ₃ LAYER.	116
FIGURE IV.10 - JV CURVES OF THE BEST WO ₃ -BASED PSC WITH PRINTED WO ₃	117
FIGURE IV.11 - PCE EVOLUTION OF THE BEST PEROVSKITE SOLAR CELLS	117
FIGURE IV.12 - WAVEFORM APPLIED FOR THE PEROVSKITE INK EJECTION	120
FIGURE IV.13 - DROP PROFILES OF THE PEROVSKITE INK EJECTION THROUGH TIME, FROM THE BEGINNING OF THE JETTING (A), TO THE INTERMEDIATE STEP (B) THEN TO THE FINAL DROP (C)	121
FIGURE IV.14 - PEROVSKITE PRINTED DROPS ANNEALED AT AMBIENT TEMPERATURE	122
FIGURE IV.15 - PEROVSKITE PRINTED DROPS ANNEALED AT 90°C	122
FIGURE IV.16 - NOT STABILIZED PRINTING OF PRINTED PEROVSKITE LAYER ON PRINTED WO ₃ LAYER.....	125
FIGURE IV.17 - PROFILE VIEW OF THE SUBSTRATE AND STEPS OF THE PEROVSKITE PRINTING (VERTICAL AND HORIZONTAL SCALES NOT RESPECTED).....	127
FIGURE IV.18 - PEG INFLUENCE ON VISCOSITY AND SURFACE TENSION ON 30 % WEIGHT CONCENTRATION PEROVSKITE INK.	129
FIGURE IV.19 - WETTING ENVELOPE OF THE ETL AND WETTABILITY OF VARIOUS PEROVSKITE INKS	135
FIGURE IV.20 - OPTICAL MICROSCOPY PICTURE OF PRINTED PEROVSKITE LAYER ON PRINTED WO ₃ LAYER.	137
FIGURE IV.21 - AFM CHARACTERIZATION OF THE PRINTED PEROVSKITE LAYER.....	137
FIGURE IV.22 - STEADY-STATE PL MEASUREMENTS OF THE PRINTED PEROVSKITE LAYERS ON PRINTED WO ₃ LAYER	138
FIGURE IV.23 - TRPLD CURVES OF THE PRINTED PEROVSKITE LAYER ON PRINTED WO ₃ LAYER.....	138
FIGURE IV.24 - XRD PATTERNS CORRESPONDING TO PRINTED PEROVSKITE FILMS	139
FIGURE IV.25 - JV CURVES OF THE BEST WO ₃ -BASED PSC WITH PRINTED WO ₃ AND PRINTED PEROVSKITE.....	140
FIGURE IV.26 - PCE EVOLUTION OF THE BEST PEROVSKITE SOLAR CELLS	140
FIGURE IV.27 - CONTACT ANGLE AND SURFACE ENERGY OF CH ₃ NH ₃ PbI _{3-x} Cl _x HYBRID PEROVSKITE	142
FIGURE IV.28 - JV CURVES OF THE BEST PSC WITH THREE PRINTED LAYERS	144
FIGURE IV.29 - A PSC WITH PRINTED WO ₃ , PEROVSKITE, AND SPIRO-OMETAD LAYERS	144
FIGURE IV.30 - PCE EVOLUTION OF THE BEST PEROVSKITE SOLAR CELLS	145
FIGURE IV.31 - SUPERPOSITION OF LBIV OR LBIC CARTOGRAPHY WITH THE DESIGN OF THE PRINTED PSC	147
FIGURE IV.32 - LBIC CARTOGRAPHY OF TiO ₂ -BASED PSC	148

REFERENCES AND TABLES

FIGURE IV.33 - LBIV CARTOGRAPHY OF TiO ₂ -BASED PSC	148
FIGURE IV.34 - LBIC CARTOGRAPHY OF PRINTED WO ₃ -BASED PSC (THE WHITE ARROW INDICATES THE PRINTING DIRECTION WHILE THE PURPLE ONE INDICATES DROP DEPOSITION DIRECTION)	149
FIGURE IV.35 - LBIV CARTOGRAPHY OF PRINTED WO ₃ -BASED PSC (THE WHITE ARROW INDICATES THE PRINTING DIRECTION WHILE THE PURPLE ONE INDICATES DROP DEPOSITION DIRECTION)	149
FIGURE IV.36 - WETTING ENVELOPE OF ITO AND WO ₃ DEPENDING OF THE STORAGE CONDITION	150
FIGURE IV.37 - OPTICAL MICROSCOPY OF THE PRINTING OF WO ₃ WITHOUT CORRECT CLEANING	152
FIGURE IV.38 - OPTICAL MICROSCOPY DETAIL OF THE PRINTING OF WO ₃ WITHOUT CORRECT CLEANING	152
FIGURE IV.39 - OPTICAL MICROSCOPY OF THE PEROVSKITE PRINTED ON A WO ₃ SPLAT FRAME.....	153
FIGURE IV.40 - OPTICAL MICROSCOPY DETAIL OF THE PEROVSKITE PRINTED ON A WO ₃ SPLAT FRAME	153
FIGURE IV.41 - AVERAGE PCE OF WO ₃ -BASED PSC DEPENDING OF THE WO ₃ ANNEALING TEMPERATURE.....	155
FIGURE IV.42- AVERAGE FF OF WO ₃ -BASED PSC DEPENDING OF THE WO ₃ ANNEALING TEMPERATURE.....	155
FIGURE IV.43- AVERAGE J _{sc} OF WO ₃ -BASED PSC DEPENDING OF THE WO ₃ ANNEALING TEMPERATURE	155
FIGURE IV.44- AVERAGE V _{oc} OF WO ₃ -BASED PSC DEPENDING OF THE WO ₃ ANNEALING TEMPERATURE	155

2. Tables table

TABLE I.1 - OBJECTIVES FOR THE PRINTED SOLAR CELL	16
TABLE I.2 - AVAILABLE SOLAR CELL TECHNOLOGIES	17
TABLE III.1 - COMPARISON BETWEEN THE OBJECTIVES AND THE TiO ₂ -BASED PEROVSKITE SOLAR CELL	56
TABLE III.2 - TiO ₂ FABRICATION PROCEEDING EFFECT ON THE ELECTRICAL PARAMETERS OF TiO ₂ -BASED PSC ...	61
TABLE III.3 - TiCl ₄ TREATMENT EFFECT ON THE ELECTRICAL PARAMETERS OF TiO ₂ -BASED PSC	62
TABLE III.4 - COMPARISON BETWEEN THE OBJECTIVES, THE TiO ₂ -BASED AND WO ₃ -BASED PSC	80
TABLE III.5 - WORK FUNCTION MEASUREMENTS WITH KPFM TECHNIQUE	86
TABLE III.6 - LIFE TIME CONSTANTS OF PEROVSKITE ON THE DIFFERENT ETL AND ON GLASS.....	89
TABLE III.7 - PHOTOVOLTAIC PARAMETERS OF PSC BEFORE THE STABILITY MEASUREMENTS.....	102
TABLE IV.1 - COMPARISON BETWEEN THE OBJECTIVES AND SPINCOATED PRINTABLE WO ₃ -BASED PSC	107
TABLE IV.2 - WORK FUNCTION MEASUREMENTS WITH KPFM TECHNIQUE	116
TABLE IV.3 - PCE OF PSC WITH PRINTED WO ₃ LAYER AND PRINTED PEROVSKITE LAYER, DEPENDING OF THE DROP SPACING OF THE PEROVSKITE PRINTING AND PEROVSKITE WEIGHT CONCENTRATION, PCE MEASURED WITH A AM 1.5 G 100 mW.cm ⁻² ILLUMINATION SOURCE, MASKED AT 0.20 cm ²	123
TABLE IV.4 - EJECTION PARAMETERS OF THE PEROVSKITE INKS DEPENDING OF THE CH ₃ NH ₃ PbI _{3-x} Cl _x WEIGHT CONCENTRATION. ^A SURFACE TENSION OF THE PEROVSKITE INK WITHOUT DIODOOCTANE.....	128
TABLE IV.5 - TENSION SURFACE COMPONENTS OF THE REFERENCE LIQUIDS	132
TABLE IV.6 - CONTACT ANGLE OF REFERENCE LIQUIDS ON REFERENCE SOLID.	132
TABLE IV.7 - SURFACE ENERGY FOR REFERENCE SURFACES.....	133
TABLE IV.8 - CONTACT ANGLE OF PEROVSKITE INK ON REFERENCE SURFACES.	134
TABLE IV.9 - SURFACE ENERGY OF THE ETLs	134
TABLE IV.10 - SURFACE TENSION COMPONENT OF THE PEROVSKITE INKS.	135

REFERENCES AND TABLES

TABLE IV.11 - LIFE TIME CONSTANTS OF PRINTED AND SPINCOATED PEROVSKITE ON WO ₃ BOTH SPINCOATED AND PRINTED.....	138
TABLE IV.12 - COMPARISON BETWEEN THE OBJECTIVES AND SPINCOATED PRINTABLE WO ₃ -BASED PSC	141
TABLE IV.13 - RHEOLOGICAL PARAMETERS AND JETTABILITY OF SPIRO-OMeTAD.....	143
TABLE IV.14 - THICKNESS OF THE PRINTED LAYER OF SPIRO-OMeTAD.....	144
TABLE IV.15 - COMPARISON BETWEEN THE OBJECTIVES AND SPINCOATED PRINTABLE WO ₃ -BASED PSC	146
TABLE IV.16 - SURFACE ENERGY FOR ITO AND WO ₃ DEPENDING OF THE STORAGE CONDITION	149
TABLE IV.17 - WORK FUNCTION OF PRINTED WO ₃ DEPENDING OF STORAGE CONDITION	154
TABLE IV.18 - WORK FUNCTION OF SPINCOATED WO ₃ DEPENDING OF ANNEALING TEMPERATURE	156

3. References

- [1] G. Trousdale and K. Wise, Directors, *Beauty and the Beast*. [Film]. Walt Disney Feature Animation, 1991.
- [2] I. Asimov, "...That Thou Art Midfoul of Him," *Fantasy and Science Fiction*, 1974.
- [3] W. Gibson, *Neuromancer*, Ace Books, 1984.
- [4] *Star Trek*. [Film]. Paramount Television, 1966.
- [5] M. Chui, M. Löffler and R. Roberts, "The Internet of Things," *McKinsey Quarterly*, no. 2, 2010.
- [6] Z. L. Wang, "Self-Powered Nanosensors and Nanosystems," *Adv. Mater.*, vol. 24, pp. 280-285, 2012.
- [7] S. Kim, R. Vyas, J. Bito, K. Niotaki, A. Collado, A. Georgiadis and M. M. Tentzeris, "Ambient RF Energy-Harvesting Technologies for Self-Sustainable Standalone Wireless Sensor Platforms," *P. IEEE*, 2014.
- [8] M. Kemell, M. Ritala and M. Leskelä, "Thin Film Deposition Methods for CuInSe₂ Solar Cells," *Crit. Rev. Solid. State*, vol. 30, pp. 1-31, 2005.
- [9] R. Steim, T. Ameri, P. Schilinsky, C. Waldauf, G. Dennler, M. Scharber and C. J. Brabec, "Organic photovoltaics for low light applications," *Sol. Energ. Mat. Sol. C.*, vol. 95, pp. 3256-3261, 2011.
- [10] C. L. Cutting, M. Bag and D. Venkataraman, "Indoor Light Recycling: A New Home for Organic Photovoltaics," *J. Mater Chem. C*, 2016.
- [11] C.-Y. Chen, J.-H. Chang, K.-M. Chiang, H.-L. Lin, S.-Y. Hsiao and H.-W. Lin, "Perovskite Photovoltaics for Dim-Light Applications," *Adv. Funct. Mater.*, vol. 25, p. 7064–7070, 2015.
- [12] Wikipedia, "Lead poisoning," May 2017. [Online]. Available: https://en.wikipedia.org/wiki/Lead_poisoning. [Accessed May 2017].
- [13] A. Babayigit, D. D. Thanh, A. Ethirajan, J. Manca, M. Muller, H.-G. Boyen and B. Conings, "Assessing the toxicity of Pb- and Sn-based perovskite solar cells in model organism *Danio rerio*," *Nature*, vol. 6, no. 18721, 2016.
- [14] N. Espinosa, L. Serrano-Luján, A. Urbina and F. C.Krebs, "Solution and vapour deposited lead perovskite solar cells: Ecotoxicity from a life cycle assessment perspective," *Sol. Energ. Mat. Sol. C*, vol. 137, pp. 303-310, 2015.

- [15] European Union, "Journal officiel de l'Union européenne," June 2011. [Online]. Available: <http://eur-lex.europa.eu/legal-content/FR/TXT/?uri=CELEX%3A32011L0065>. [Accessed may 2017].
- [16] A. Becquerel, "Recherches sur les effets de la radiation chimique de la lumiere solaire au moyen des courants electriques," *Comptes Rendus de L'Academie des Sciences*, vol. 9, pp. 145-149, 1839.
- [17] J. Even, L. Pedesseau and C. Katan, "Analysis of Multivalley and Multibandgap Absorption and Enhancement of Free Carriers Related to Exciton Screening in Hybrid Perovskites," *J. Phys. Chem. C*, vol. 118, no. 22, p. 11566–11572, 2014.
- [18] A. M. Green, A. Ho-Baillie and H. J. Snaith, "The emergence of perovskite solar cells," *Nature Photonics*, vol. 8, pp. 506-5014, July 2014.
- [19] P. Gao, M. Grätzel and M. K. Nazeeruddin, "Organohalide lead perovskites for photovoltaic applications," *Energy & Environmental Science*, vol. 7, pp. 2448-2463, Avril 2014.
- [20] G. E. Eperon, S. D. Stranks, C. Menelaou, M. B. Johnston, L. M. Herz and H. J. Snaith, "Formamidinium lead trihalide: a broadly tunable perovskite for efficient planar heterojunction solar cells," *Energy & Environmental Science*, 2014.
- [21] W.-J. Yin, J.-H. Yang, J. Kang, Y. Yan and S.-H. Wei, "Halide Perovskite Materials for Solar Cells: A Theoretical Review," *Journal of Materials Chemistry A*, vol. 3, pp. 8926-8942, 2014.
- [22] J. L. Miller, "Unusual defect physics underlies perovskite solar cells' exceptional performance," *Physique Today*, vol. 67, no. 5, p. 13, 2014.
- [23] J. Even, L. Pedesseau, C. Katan, M. Kepenekian, J.-S. Lauret, D. Saporì and E. Deleport, "Solid-State Physics Perspective on Hybrid Perovskite," *The Journal of Physical Chemistry C*, vol. 119, p. 10161–10177, April 2015.
- [24] S. Luo and W. A. Daoud, "Recent progress in organic-inorganic halide perovskite solar cells: mechanisms and materials design," *J. Mater. Chem.*, vol. 7, pp. 2448-2463, 2014.
- [25] S. Colella, E. Mosconi, P. Fedeli, A. Listorti, A. Rizzo, F. Gazza, F. Orlandi, P. Ferro, T. Besagni, G. Calestani, F. De Angelis, R. Mosca and G. Gigli, "MAPbI₃-xCl_x mixed halide perovskite for hybrid solar cells: the role of chloride as dopant on the transport and structural properties," *Mater. Res. Soc. Symp. Proc.*, vol. 1667, 2014.
- [26] G. Xing, N. Mathews, S. Sun, S. S. Lim, Y. M. Lam, M. Grätzel, S. Mhaisalkar and 3. T. C. Sum, "Long-Range Balanced Electron-and Hole-Transport Lengths in Organic-Inorganic CH₃NH₃PbI₃," *Science*, vol. 342, pp. 344-347, 2013.
- [27] P.-M. Geffroy, S. Vedraïne, F. Dumas-Bouchiat, S. K. Saha, A. Gheno, F. Rossignol, P. Marchet, R. Antony, J. Bouclé and B. Ratier, "Electrical and Optical Properties of La_{1-x}A_xFe_{1-y}ByO_{3-δ} Perovskite Films (with A = Sr and Ca, and B = Co, Ga, Ti): Toward Interlayers for Optoelectronic Applications," *J. Phys. Chem. C.*, vol. 120, no. 50, p. 28583–28590, 2016.
- [28] S. Stranks, G. Eperon, G. Grancini, C. Menelaou, M. Alcocer, T. Leijtens, L. Herz, A. Petrozza and H. Snaith, "Electron-Hole Diffusion Lengths Exceeding 1 Micrometer in an Organometal Trihalide Perovskite Absorber," *Science*, vol. 342, pp. 341-344, 2013.
- [29] A. Gheno, T. T. T. Pham, C. Di Bin, J. Bouclé, R. Bernard and S. Vedraïne, "Printable WO₃ electron transporting layer for perovskite solar cells: influence on device performance and stability," *Sol. Energ. Mat. Sol. C*, vol. 161, pp. 347-354, March 2017.

- [30] J.-H. Im, H.-S. Kim and N.-G. Park, "Morphology-photovoltaic property correlation in perovskite solar cells: One-step versus two-step deposition of CH₃NH₃PbI₃," *APL Materials*, vol. 2, no. 081510, pp. 1-8, 2014.
- [31] C. Wehrenfennig, G. E. Eperon, M. B. Johnston, H. J. Snaith and L. M. Herz, "High Charge Carrier Mobilities and Lifetimes in Organolead Trihalide Perovskites," *Advanced materials*, vol. 26, p. 1584–1589, December 2013.
- [32] A. Miyata, A. Mitioglu, P. Plochocka, O. Portugall, J. T.-W. Wang, S. D. Stranks, H. J. Snaith and R. J. Nicholas, "Direct measurement of the exciton binding energy and effective masses for charge carriers in organic–inorganic tri-halide perovskites," *Nature Physics*, vol. 11, pp. 582-587, 2015.
- [33] J. Even, L. Pedesseau, J.-M. Jancu and C. Katan, "DFT and k.p modelling of the phase transitions of lead and tin halide perovskites for photovoltaic cells," *Phys. Status Solidi RRL*, vol. 8, pp. 31-35, 2013.
- [34] U. Bach, D. Lupo, P. Compte, J. Moser, F. Weissörtel, J. Salbeck, H. Spreitzer and M. Grätzel, "Solid-state dye-sensitized mesoporous TiO₂ solar cells with high photon-to-electron conversion efficiencies," *Nature*, pp. 583-585, 1998.
- [35] L. Schmidt-Mende, U. Bach, R. Humphry-Baker, T. Horiuchi, H. Miura, S. Ito, S. Uchida and M. Grätzel, "Organic Dye for Highly Efficient Soli-State Dye-Sensitized Solar Cells," *Advanced Materials*, vol. 17, no. 7, pp. 813-815, 2005.
- [36] A. G. Chynoweth, "Surface Space-Charge Layers in Barium Titanate," *Phys.Rev.*, vol. 102, no. 3, pp. 705-714, may 1956.
- [37] A. Kojima, K. Teshima, Y. Shirai and T. Miyasaka, "Novel Photoelectrochemical Cell with Mesoscopic Electrodes Sensitized by Lead-halide Compounds," in *212th ECS Meeting*, 2006.
- [38] A. Kojima, K. Teshima, Y. Shirai and T. Miyasaka, *J. Am. Chem. Soc.*, vol. 131, pp. 6050-6051, 2009.
- [39] H.-S. Kim, C.-R. Lee, J.-H. Im, K.-B. Lee, T. Moehl, A. Marchioro, S.-J. Moon, R. Humphry-Baker, J.-H. Yum, J. E. Moser, M. Grätzel and N.-G. Park, "Lead Iodide Perovskite Sensitized All-Solid-State Submicron Thin Film Mesoscopic Solar Cell with Efficiency Exceeding 9%," *Nature*, vol. 2, no. 591, pp. 1-7, august 2012.
- [40] M. M. Lee, J. Teuscher, T. Miyasaka, T. N. Murakami and H. J. Snaith, "Efficient Hybrid Solar Cells Based on Meso-Superstructured Organometal Halide Perovskites," *Science*, vol. 338, pp. 643-647, Octobre 2012.
- [41] H. Zhou and Q. Chen, "Interface engineering of highly efficient perovskite solar cells," *Science*, vol. 354, no. 6196, pp. 542-546, August 2014.
- [42] M. Saliba, T. Matsui, J.-Y. Seo, K. Domanski, J.-P. Correa-Baena, M. K. Nazeeruddin, S. M. Zakeeruddin, W. Tress, A. Abate, A. Hagfeldt and M. Grätzel, "Cesium-containing Triple Cation Perovskite Solar Cells: Improved Stability, Reproducibility and High Efficiency," *Energy Environ. Sci.*, 2016.
- [43] NREL, "Photovoltaic Research," [Online]. Available: <https://www.nrel.gov/pv/>. [Accessed Mars 2016].
- [44] L. Scriven, "Physics and Applications of Dip Coating and Spin Coating," in *Mat. Res. Soc. Symp. Proc.*, 1988.
- [45] Fujifilm, "Dimatix Materials Printer DMP-2850," 2017. [Online]. Available: http://www.fujifilmusa.com/products/industrial_inkjet_printheads/deposition-products/dmp-2800/index.html. [Accessed Fevrier 2017].
- [46] S. D. Hoath, *Fundamentals of Inkjet Printing*, Weinheim: Wiley-VCH, 2016.

- [47] B. Derby, "Inkjet Printing of Functional and Structural Materials: Fluid Property Requirements, Feature Stability, and Resolution," *Annu. Rev. Mater. Res.*, vol. 40, pp. 395-414, 2010.
- [48] C. Stow and M. Hadfield, "An Experimental Investigation of Fluid Flow Resulting from the Impact of a Water Drop with an Unyielding Dry Surface," *Proc. R. Soc. Lond. A*, vol. 373, pp. 419-441, 1981.
- [49] J. Briant, *Phénomènes d'interface, Agents de surface, Principes et modes d'action*, Paris: Technip, 1989.
- [50] A&D Company, Limited, "Tuning Fork Vibro Viscometer SV-A Series," 2016. [Online]. Available: http://www.aandd.jp/products/test_measuring/pdf/sv-a_brochure.pdf.
- [51] J. Kroon, M. Wienk, W. Verhees and J. Hummelen, "Accurate efficiency determination and stability studies of conjugated polymer/fullerene solar cells," *Thin Solid Films*, Vols. 403-404, pp. 223-228, 2002.
- [52] V. Shrotriya, G. Li, Y. Yao, T. Moriarty, K. A. Emery and Y. Yang, "Accurate Measurement and Characterization of Organic Solar Cells," *Adv. Func. Mater.*, vol. 16, pp. 2016-2023, 2006.
- [53] H. J. Snaith, "How should you measure your excitonic solar cells?," *Energ. Environ. Sci.*, vol. 5, no. 4, pp. 6513-6520, 2012.
- [54] G. E. Eperon, V. M. Burlakov, P. Docampo, A. Goriely and H. J. Snaith, "Morphological Control for High Performance, Solution-Processed Planar Heterojunction Perovskite Solar Cells," *Advanced Functional Materials*, vol. 24, pp. 151-157, 2014.
- [55] K. Wojciechowski, M. Saliba, T. Leijtens, A. Abate and H. J. Snaith, *Energy Environmental Science*, vol. 1142, 2014.
- [56] Dyesol, "18NR-T Transparent Titania Paste," [Online].
- [57] Ossila, "I101 Perovskite Precursor Ink," 2015. [Online]. Available: http://www.ossila.com/oled_opv_ofet_catalogue3/Perovskites/I101-perovskite-ink.php. [Accessed April 2015].
- [58] H. Gao, C. Bao, F. Li, T. Yu, J. Yang and W. Zhu, "Nucleation and Crystal Growth of Organic-Inorganic Lead Halide Perovskite under Different Relative Humidity," *ACS Appl. Mater. Interfaces*, vol. 7, no. 17, pp. 9110-9117, 2015.
- [59] G. E. Eperon, S. N. Habisreutinger, T. Leijtens, B. J. Bruijnaers, J. J. v. Franeker, D. W. deQuilettes, S. Pathak, R. J. Sutton, G. Grancini, D. S. Ginger, R. A. J. Janssen, A. Petrozza and Snaith, "The Importance of Moisture in Hybrid Lead Halide Perovskite Thin Film Fabrication," *ACS Nano*, vol. 9, no. 9, pp. 9380-9393, 2015.
- [60] F. Knorr, D. Zhang and J. McHale, "Influence of TiCl₄ treatment on surface defect photoluminescence in pure and mixed-phase nanocrystalline TiO₂," *Langmuir*, vol. 23, no. 17, pp. 8686-8690, 2007.
- [61] G. Richardson, S. E. J. O'Kane, R. G. Niemann, T. A. Peltola, J. M. Foster, P. J. Cameron and A. B. Walker, "Can slow-moving ions explain hysteresis in the current-voltage curves of perovskite solar cells?," *Energ. Environ. Sci.*, vol. 9, no. 1476, 2016.
- [62] C. Eames, J. M. Frost, P. R. Barnes, B. C. O'Regan, A. Walsh and M. S. Islam, "Ionic transport in hybrid lead iodide perovskite solar cells," *Nat. Commun.*, vol. 6, no. 7497, 2015.

- [63] J. Y. Luo, S. Z. Deng, Y. T. Tao, F. L. Zhao, L. F. Zhu, L. Gong, J. Chen and N. S. Xu, "Evidence of Localized Water Molecules and Their Role in the Gasochromic Effect of WO₃ Nanowire Films," *J. Phys. Chem. C*, vol. 2009, no. 11, p. 15877–15881, 2009.
- [64] T. Leijtens, G. E. Eperon, S. Pathak, A. Abate, M. M. Lee and H. J. Snaith, "Overcoming ultraviolet light instability of sensitized TiO₂ with meso-superstructured organometal tri-halide perovskite solar cells," *Nat. Commun.*, vol. 4, no. 2885, 2013.
- [65] K. Schwanitz, U. Weiler, R. Hunger, T. Mayer and W. Jaegermann, "Synchrotron-Induced Photoelectron Spectroscopy of the Dye-Sensitized Nanocrystalline TiO₂/Electrolyte Interface: Band Gap States and Their Interaction with Dye and Solvent Molecules," *J. Phys. Chem.*, vol. 111, no. 2, pp. 849-854, 2007.
- [66] G. Lu, A. Linsebigler and J. T. J. Yates, "The adsorption and photodesorption of oxygen on the TiO₂(110) surface," *J. Chem. Phys.*, vol. 102, no. 11, pp. 4657-4662, 1995.
- [67] G. Niu, X. Guo and L. Wang, "Review of recent progress in chemical stability of perovskite solar cells," *J. Mater. Chem. A*, 2015.
- [68] G. Grancini, V. D'Innocenzo, E. R. Dohner, N. Martino, A. R. S. Kandada, E. Mosconi, F. D. Angelis, H. I. Karunadasa, E. T. Hoke and A. Petrozza, "CH₃NH₃PbI₃ perovskite single crystals: surface photophysics and their interaction with the environment," *Chem. Sci.*, vol. 6, pp. 7305-7310, 2016.
- [69] S. D. Stranks, P. K. Nayak, W. Zhang, T. Stergiopoulos and H. J. Snaith, "Formation of Thin Films of Organic–Inorganic Perovskites for High-Efficiency Solar Cells," *Angewandte*, vol. 54, no. 11, pp. 3240-3248, 2015.
- [70] J. H. Heo, H. J. Han, D. Kim, T. K. Ahn and S. H. Im, "18.1 % hysteresis-less inverted CH₃NH₃PbI₃ planar perovskite hybrid solar cells," *Energy & Environmental Science*, vol. 8, pp. 1602-1608, april 2015.
- [71] M. Antoniadou, E. Siranidi, N. Vaenas, A. G. Kontos, E. Stathatos and P. Falaras, "Photovoltaic Performance and Stability of CH₃NH₃PbI₃-xCl_x Perovskites," *Journal of Surfaces and Interfaces of Materials*, vol. 2, no. 4, pp. 1-5, 2014.
- [72] S. Allaman, G. Desie, D. Vadillo and A. Soucemarianadin, "Impact and spreading of micro-drops onto solid substrates," *Mec. Ind.*, vol. 4, p. 443–455, 2003.
- [73] G. Desie, G. Deroover, F. D. Voeght and A. Soucemarianadin, "Printing of Dye and Pigment-Based Aqueous Inks Onto Porous Substrates," *J. Imaging Sci. Technol.*, vol. 48, no. 5, p. 389–397, 2004.
- [74] W. Ke, G. Fang, Q. Liu, L. Xiong, P. Qin, H. Tao, J. Wang, H. Lei, B. Li, J. Wan, G. Yang and Y. Yan, "Low-Temperature Solution-Processed Tin Oxide as an Alternative Electron Transporting Layer for Efficient Perovskite Solar Cells," *J. Am. Chem. Soc.*, vol. 137, no. 21, pp. 6730-6733, 2015.
- [75] Q. Liu, M.-C. Qin, W.-J. Ke, X.-L. Zheng, Z. Chen, P.-L. Qin, L.-B. Xiong, H.-W. Lei, J.-W. Wan, J. Wen, G. Yang, J.-J. Ma, Z.-Y. Zhang and G.-J. Fang, "Enhanced Stability of Perovskite Solar Cells with Low-Temperature Hydrothermally Grown SnO₂ Electron Transport Layers," *Adv. Funct. Mater.*, vol. 26, no. 13, pp. 6069-6075, 2016.
- [76] J. Song, E. Zheng, X.-F. Wang, W. Tian and T. Miyasaka, "Low-temperature-processed ZnO–SnO₂ nanocomposite for efficient planar perovskite solar cells," *Sol. Energ. Mater.*, vol. 144, pp. 623-630, 2016.

- [77] D. Liu and T. L. Kelly, "Perovskite solar cells with a planar heterojunction structure prepared using room-temperature solution processing techniques," *Nat. Photonics*, vol. 8, pp. 133-138, 2014.
- [78] J.-C. Obscur, T. Trigaud, C. Arrive and B. Ratier, "Organic solar cells : Oxide nanoparticles materials for PEDOT:PSS replacement," in *ESOS*, Cargese, 2015.
- [79] S. Han, W. S. Shin, M. Seo, D. Gupta, S.-J. Moon and S. Yoo, "Improving performance of organic solar cells using amorphous tungsten oxides as an interfacial buffer layer on transparent anodes," *Org. Electron.*, vol. 10, no. 5, pp. 791-797, 2009.
- [80] T. Stubhan, N. Li, N. A. Luechinger, S. C. Halim, G. J. Matt and C. J. Brabec, "High Fill Factor Polymer Solar Cells Incorporating a Low Temperature Solution Processed WO₃ Hole Extraction Layer," *Adv. Energy Mater.*, vol. 2, no. 12, pp. 1433-1438, 2012.
- [81] K. Mahmood, B. S. Swain, A. R. Kirmani and A. Amassian, "Highly efficient perovskite solar cells based on a nanostructured WO₃-TiO₂ core-shell electron transporting material," *J. Mater. Chem. A*, vol. 3, pp. 9051-9057, October 2014.
- [82] K. Wang, Y. Shi, Q. Dong, Y. Li, S. Wang, X. Yu, M. Wu and T. Ma, "Low-Temperature and Solution-Processed Amorphous WOX as Electron-Selective Layer for Perovskite Solar Cells," *J. Phys. Chem. Lett.*, vol. 6, p. 755-759, February 2015.
- [83] Y. Hou, C. O. R. Quiroz, S. Scheiner, W. Chen, T. Stubhan, A. Hirsch, M. Halik and C. J. Brabec, "Low-Temperature and Hysteresis-Free Electron-Transporting Layers for Efficient ,Regular, and Planar Structure Perovskite Solar Cells," *Adv. Energy Mater.*, vol. 5, no. 1501056.
- [84] Avantama, "Prod. 6040: Avantama P-10," 2017. [Online]. Available: <http://avantama.com/shop/p-10/>.
- [85] R. Schlaf, H. Murata and Z. H. Kafafi, "Work function measurements on indium tin oxide films," *J. Electron. Spectrosc.*, vol. 120, no. 1, pp. 149-154, 2001.
- [86] M. G. Helander, M. T. Greiner, Z. B. Wang, W. M. Tang and Z. H. Lu, "Work function of fluorine doped tin oxide," *J. Vac. Sci. Technol.*, vol. 29, p. 011019, 2011.
- [87] D. Aldakov, M. Sajjad, V. Ivanova, A. Bansal, J. Park, P. Reiss and I. Samuel, "Mercaptophosphonic acids as efficient linkers in quantum dot sensitized solar cells," *J. Mater. Chem. A*, vol. 3, pp. 19050-19060, 2015.
- [88] T. Sum, S. Chen, G. Xing, X. Liu and B. Wu, "Energetics and dynamics in organic-inorganic halide perovskite photovoltaics and light emitters.," *Nanotechnology*, vol. 26, no. 34, p. 342001, 2015.
- [89] Z. Zhang, H.-X. Wei, G.-F. Ma, Y.-Q. Li, S.-T. Lee and J.-X. Tang, "Interface energetics at WOX/organic interfaces: The role of oxygen vacancies," *Appl. Phys. Lett.*, vol. 103, no. 133302.
- [90] M. Qiu, D. Zhu, X. Bao, J. Wang, X. Wang and R. Yang, "WO₃ with surface oxygen vacancies as an anode buffer layer for high performance polymer solar cells," *J. Mater. Chem. A.*, vol. 4, pp. 894-900, 2016.
- [91] H. Chen, N. Xu, S. Deng, D. Lu, Z. Li, J. Zhou and J. Chen, "Gasochromic effect and relative mechanism of WO₃ nanowire films," *Nanotechnology*, vol. 18, pp. 205701-205707, 2007.
- [92] J. M. Frost, K. T. Butler, F. Brivio, C. H. Hendon, M. v. Schilfhaarde and A. Walsh, "Atomistic Origins of High-Performance in Hybrid Halide Perovskite Solar Cells," *Nano. Lett.*, vol. 14, p. 2584-2590, 2014.

- [93] S.-H. Lee, R. D. e, P. A. Parilla, K. M. Jones, B. To, A. H. Mahan and A. C. Dillon, "Crystalline WO₃ Nanoparticles for Highly Improved Electrochromic Applications," *Adv. Mater.*, vol. 18, pp. 763-766, 2006.
- [94] S.-H. Baeck, K.-S. Choi, T. F. Jaramillo, G. D. Stucky and E. W. McFarland, "Enhancement of Photocatalytic and Electrochromic Properties of Electrochemically Fabricated Mesoporous WO₃ Thin Films," *Adv. Mater.*, vol. 15, no. 15, pp. 1269-1273, 2003.
- [95] D. Chen and J. Ye, "Hierarchical WO₃ Hollow Shells: Dendrite, Sphere, Dumbbell, and Their Photocatalytic Properties," *Adv. Funct. Mater.*, vol. 18, pp. 1922-1928, 2008.
- [96] N. Chander, A. F. Khan, P. S. Chandrasekhar, E. Thouti, S. K. Swami, V. Dutta and V. K. Komarala, "Reduced ultraviolet light induced degradation and enhanced light harvesting using YVO₄:Eu³⁺-down-shifting nano-phosphor layer in organometal halide perovskite solar cells," *Appl. Phys. Lett.*, vol. 105, no. 033904, 2014.
- [97] F. Bella, G. Griffini, J.-P. Correa-Beana, G. Saracco, M. Grätzel, A. Hagfeldt, S. Turri and C. Gerbaldi, "Improving efficiency and stability of perovskite solar cells with photocurable fluoropolymers," *Science*, 2016.
- [98] F. Bella, G. Leftheriotis, G. Griffini, G. Syrokostas, S. Turri, M. Grätzel and C. Gerbaldi, "new design paradigm for smart windows: Photocurable polymers for quasi-solid photoelectrochromic devices with excellent long-term stability under real outdoor operating conditions," *Adv. Funct. Mater.*, vol. 26, no. 7, 2015.
- [99] Y.-H. Gong, F. Miomandre, R. Méallet-Renault, S. Badré, L. Galmiche, J. Tang, P. Audebert and G. Clavier, "Synthesis and Physical Chemistry of s-Tetrazines: Which Ones are Fluorescent and Why?," *Eur. J. Org. Chem.*, p. 6121-6128, 2009.
- [100] U. Caglar, "Studies of Inkjet Technology with Focus on Electronic Materials," *Tampere University of Technology*, vol. 863, 2009.
- [101] J. Burschka, N. Pellet, S.-J. Moon, R. Humphry-Baker, P. Gao, M. K. Nazeeruddin and M. Grätzel, "Sequential deposition as a route to high-performance perovskite-sensitized solar cells," *Nature*, vol. 499, pp. 316-320, 2013.
- [102] Y. Zhao and K. Zhu, "CH₃NH₃Cl-Assisted One-Step Solution Growth of CH₃NH₃PbI₃: Structure, Charge-Carrier Dynamics, and Photovoltaic Properties of Perovskite Solar Cells," *J. Phys. Chem. C*, vol. 118, pp. 9412-9418, 2014.
- [103] H. Yu, F. Wang, F. Xie, W. Li, J. Chen and N. Zhao, "The Role of Chlorine in the Formation Process of "CH₃NH₃PbI_{3-x}Cl_x" Perovskite," *Adv. Funct. Mater.*, vol. 24, no. 45, pp. 7102-7108, 2014.
- [104] Q. Chen, H. Zhou, Y. Fang, A. Z. Stieg, T.-B. Song, H.-H. Wang, X. Xu, Y. Liu, S. Lu, J. You, P. Sun, J. McKay, M. S. Goorsky and Y. Yang, "The optoelectronic role of chlorine in CH₃NH₃PbI₃(Cl)-based perovskite solar cells," *Nat. Commun.*, vol. 6, no. 7569, 2015.
- [105] E. Mosconi, E. Ronca and F. D. Angelis, "First-Principles Investigation of the TiO₂/Organohalide Perovskites Interface: The Role of Interfacial Chlorine," *J. Phys. Chem. Lett.*, vol. 5, pp. 2619-2625, 2014.
- [106] E. Edri, S. Kirmayer, S. Mukhopadhyay, K. Gartsman, G. Hodes and D. Cahen, "Elucidating the charge carrier separation and working mechanism of CH₃NH₃PbI_{3-x}Cl_x perovskite solar cells," *Nat. Commun.*, vol. 5, no. 3461, 2014.
- [107] D. E. Starr, G. Sadoughi, E. Handick, R. G. Wilks, J.-H. Alsmeier, L. Köhler, M. Gorgoi, H. Snaith and M. Bär, "Direct Observation of an Inhomogeneous Chlorine

- Distribution in $\text{CH}_3\text{NH}_3\text{PbI}_3\text{-xCl}_x$ Layers: Surface Depletion and Interface Enrichment,” *Energ. Environ. Sci.*, vol. 8, pp. 1609-1615, 2015.
- [108] R. K. Fu, Y. Mei, G. Wan, G. Siu, P. K. Chu, Y. Huang, X. Tian, S. Yang and J. Chen, “Surface composition and surface energy of Teflon treated by metal plasma immersion ion implantation,” *Surf. Sci.*, vol. 573, pp. 426-432, 2004.
- [109] S. Wu, *J. Polym. Sci.*, vol. C34, no. 19, 1971.
- [110] D. K. Owens and R. C. Wendt, “Estimation of the Surface Free Energy of Polymers,” *J. Appl. Polym. Sci.*, vol. 13, pp. 1741-1747, 1969.
- [111] Q. Chen, H. Zhou, Y. Fang, A. Z. Stieg, T.-B. Song, H.-H. Wang, X. Xu, Y. Liu, S. Lu, J. You, P. Sun, J. McKay, M. S. Goorsky and Y. Yang, “The optoelectronic role of chlorine in $\text{CH}_3\text{NH}_3\text{PbI}_3(\text{Cl})$ -based perovskite solar cells,” *Nat. Commun.*, vol. 6, no. 7269, 2015.
- [112] A. K. Jena, M. Ikegami and T. Miyasaka, “Severe Morphological Deformation of Spiro-OMeTAD in $(\text{CH}_3\text{NH}_3)\text{PbI}_3$ Solar Cells at High Temperature,” *ACS Energy Lett.*, vol. 2, pp. 1760-1761, 2017.
- [113] H. Zhou, Q. Chen, G. Li, S. Luo, T.-b. Song, H.-S. Duan, Z. Hong, J. You, Y. Liu and Y. Yang, “Interface engineering of highly efficient perovskite solar cells,” *Science*, vol. 345, pp. 542-546, 2014.
- [114] Y. Kato, L. K. Ono, M. V. Lee, S. Wang, S. R. Raga and Y. Qi, “Silver Iodide Formation in Methyl Ammonium Lead Iodide Perovskite Solar Cells with Silver Top Electrodes,” vol. 2, no. 13.
- [115] F. Guo, H. Azimi, Y. Hou, T. Przybilla, M. Hu, C. Bronnbauer, S. Langner, E. Spiecker, K. Forberich and C. J. Brabec, “High-performance semitransparent perovskite solar cells with solution-processed silver nanowires as top electrodes,” *Nanoscale*, vol. 7, pp. 1642-1649.
- [116] A. v. d. Bos, M.-J. v. d. Meulen, T. Driessen, M. v. d. Berg, H. Reinten, H. Wijshoff, M. Versluis and D. Lohse, “Velocity Profile inside Piezoacoustic Inkjet Droplets in Flight: Comparison between Experiment and Numerical Simulation,” *Phys. Rev. Applied*, vol. 1, no. 014004, 2014.
- [117] R. Rioboo, M. Marengo and C. Tropea, “Time evolution of liquid drop impact onto solid, dry surfaces,” *Experiments in Fluids*, vol. 3, pp. 112-124, 2002.
- [118] M. K. Nazeeruddin, “Twenty-five years of low-cost solar cells,” *Nature*, vol. 538, no. 463, 2016.

4. Notations table

<i>a</i>	<i>Characteristic dimension</i>
<i>AFM</i>	<i>Atomic Force Microscopy</i>
<i>AM</i>	<i>Air Mass</i>
<i>BW</i>	<i>Backward</i>
<i>c</i>	<i>Light velocity in vacuum</i>
<i>CB</i>	<i>Conduction Band</i>
<i>DIM</i>	<i>Diiodomethane</i>

<i>DIO</i>	<i>Diiodooctane</i>
<i>DMF</i>	<i>N,N-Dimethylformamide</i>
<i>DOD</i>	<i>Drop-On-Demand</i>
<i>DSSC</i>	<i>Dye Sensitized Solar Cell</i>
<i>E</i>	<i>Energy</i>
e^-	<i>Electron</i>
<i>EHC</i>	<i>Energy Harvesting Component</i>
<i>EQE</i>	<i>External Quantum Efficiency</i>
<i>EQY</i>	<i>Emission Quantum Yield</i>
<i>ETL</i>	<i>Electron Transporting Layer</i>
<i>ETM</i>	<i>Electron Transporting Material</i>
<i>FF</i>	<i>Fill Factor</i>
<i>FTO</i>	<i>Fluorine-doped Indium Tin Oxide</i>
<i>FW</i>	<i>Forward</i>
<i>g</i>	<i>g-force</i>
<i>h</i>	<i>Planck constant</i>
h^+	<i>Hole</i>
<i>HSC</i>	<i>Hybrid Super-Capacitor</i>
<i>HTL</i>	<i>Hole Transporting Layer</i>
<i>HTM</i>	<i>Hole Transporting Material</i>
<i>IoT</i>	<i>Internet of Things</i>
<i>IPCE</i>	<i>Incident photon to converted electron</i>
<i>IRF</i>	<i>Instrument Response Function</i>
<i>ITO</i>	<i>Indium Tin Oxide</i>
J_{sc}	<i>Short-circuit current</i>
<i>JV</i>	<i>Current-Voltage characterization</i>
k_{CT}	<i>charge transfer rate</i>
<i>KPFM</i>	<i>Kelvin-probe Force Microscopy</i>
<i>LBIC</i>	<i>Light Beam Induced Current</i>
<i>LBIV</i>	<i>Light Beam Induced Voltage</i>
<i>m</i>	<i>Mass</i>
<i>MAI</i>	<i>Methylammonium Iodide</i>
<i>NITZ</i>	<i>naphthalimide-tetrazine</i>
<i>Oh</i>	<i>Ohnesorge number</i>
<i>OWRK</i>	<i>Owens-Wendt-Rabel-Kaelble</i>
<i>P</i>	<i>Power</i>
<i>PCE</i>	<i>Photo-Conversion Efficiency</i>
<i>PEG</i>	<i>polyethylene glycol</i>
<i>PEN</i>	<i>polyethylene naphthalate</i>
<i>PET</i>	<i>polyethylene terephthalate</i>
<i>PL</i>	<i>Photoluminescence</i>
<i>PMMA</i>	<i>Poly(methyl methacrylate)</i>
<i>PS</i>	<i>Polystyrene</i>

REFERENCES AND TABLES

<i>PSC</i>	<i>Perovskite Solar Cell</i>
<i>PTFE</i>	<i>Polytetrafluoroethylene</i>
<i>PVDF</i>	<i>Polyvinylidene fluoride</i>
<i>Re</i>	<i>Reynolds number</i>
<i>RMS</i>	<i>Root Mean Square</i>
<i>rpm</i>	<i>revolutions per minute</i>
<i>S</i>	<i>Surface of the nozzle section</i>
<i>SD</i>	<i>Standard Deviation</i>
<i>sDSSC</i>	<i>solid Dye Sensitized Solar Cell</i>
<i>T</i>	<i>Transmission</i>
<i>tBP</i>	<i>4-tert-Butylpyridine</i>
<i>TRPLD</i>	<i>Time-resolved PL decay</i>
<i>UV</i>	<i>Ultra-Violet</i>
<i>v</i>	<i>Drop velocity</i>
<i>VB</i>	<i>Valence Banf</i>
<i>V_{oc}</i>	<i>Open-circuit Voltage</i>
<i>We</i>	<i>Weber number</i>
<i>XRD</i>	<i>X-Ray Diffraction</i>
<i>Z</i>	<i>Inverse of Oh</i>
<i>α</i>	<i>Absrobance</i>
<i>γ</i>	<i>Surface Tension and Surface Energy</i>
<i>η</i>	<i>Diynamic velocity</i>
<i>θ</i>	<i>Drop contact angle</i>
<i>λ</i>	<i>Wavelength</i>
<i>ρ</i>	<i>Bulk density</i>
<i>τ</i>	<i>Time constant</i>
<i>v</i>	<i>Period</i>

VI. Acknowledgements

The author would like to thank his two financers: the Labex Σ - Lim (ANR-10-LABX-0074-01) and the French ministry of defense's DGA (DGA 2014 60 0041).

VII. Résumé en français

Ce travail de thèse a pour sujet la conception des cellules solaires photovoltaïques à base de pérovskite hybride par le biais de la technologie d'impression jet d'encre. Les deux premiers chapitres font la présentation du contexte de la thèse, à savoir l'alimentation d'un réseau autonome de capteur, et passent en revue les aspects scientifiques des technologies jet d'encre et photovoltaïque de nouvelle génération. Le troisième chapitre présente la mise au point d'une cellule photovoltaïque à l'état de l'art et son évolution vers une architecture imprimable à basses températures de recuit. La problématique de la stabilité des cellules photovoltaïques à pérovskite est aussi abordée. La dernière partie présente les différents aspects et problématiques de l'impression par jet d'encre des trois couches internes d'une cellule solaire pérovskite. Au terme de ce travail la possibilité d'imprimer des cellules solaires pérovskites avec des rendements supérieurs à 10 % a été démontrée, le tout en condition ambiante et à basse température.